HYDRODYNAMICS AND SEDIMENT TRANSPORT IN THE INNER SURF AND SWASH ZONES

By

JACK ANTHONY PULEO

A DISSERTATION PRESENTED TO THE GRADUATE SCHOOL
OF THE UNIVERSITY OF FLORIDA IN PARTIAL FULFILLMENT
OF THE REQUIREMENTS FOR THE DEGREE OF
DOCTOR OF PHILOSOPHY

UNIVERSITY OF FLORIDA

2004

ACKNOWLEDGMENTS

I am indebted to my advisor, Dr. Don Slinn who suggested that I work as his student (first at Florida Atlantic and then at the University of Florida). Because of Don, I was given an outstanding opportunity to study under an excellent selection of professors using cutting edge numerical models and data sets. I also thank my committee members. Their effort made this manuscript more readable and easier to understand. My colleagues at the Naval Research Laboratory provided a sound home base where scientific thoughts are freely shared and exchanged; furthering my knowledge in certain areas and providing new avenues of pursuit for this dissertation and other work undertaken during my time enrolled at UF.

My wife, Liles; and sons, Anthony and Carlos, happily supported me during my time at UF. Their smiles and love kept me going. My parents and extended family continued their support and encouragement through this adventure,always asking when I would finish. Last (really first!), I thank the Lord for giving me the intelligence and desire to further my education. Without His blessing, I would not be where I am.

This work was supported by the Office of Naval Research (ONR) through funding to the Naval Research Laboratory and by grants to Dr. Don Slinn,through ONR.

Chapters 1-6 are published or will be submitted to peer-reviewed journals. Chapter 1 serves as a background for (and thorough review of) swash zone studies that have been completed over the last few decades. The sediment transport portions of this chapter are to be included in a special issue on swash processes in Continental Shelf Research.

Chapter 2 uses field data collected from a high energy steep beach to try to better understand the processes driving sediment transport. Comments on this chapter were provided by Dr. Todd Holland, Dr. Nathaniel Plant, Dr. Donald Slinn and Dr. Dan Hanes. This work has since been published in the Journal of Geophysical Research (vol 108, C11, 3350, doi:10.1029/2003JC001943, 2003) and is included here with permission from the American Geophysical Union.

Chapter 3 presents a remote sensing technique using video cameras to determine the spatial field of surface velocity vectors. The well-known statistical technique, particle image velocimetry (PIV), was adapted for the swash zone at the Naval Research Laboratory by Dr. Todd Holland and myself. The chapter here includes, work that was not included in the original study, comparing the optical technique to that of a radar-based system. This was necessary to further validate the optical technique used in chapter 4 to obtain velocity fields as the forcing for a morphodynamic model. Comparisons were made to radar-based data collected by fellow student Gordon Farquarhson and his advisor Dr. Steve Frasier of the University of Massachusetts, Amherst. This work has since been published in the Journal of Geophysical Research (vol 108, C3, 3100, doi:10.1029/2002JC001483, 2003), and is included here with permission from the American Geophysical Union.

After accepting the PIV technique as a viable option to in situ sensors, PIV estimations were used in conjunction with various sediment transport models to predict three-dimensional foreshore evolution. Dr. Todd Holland and Dr. Tony Butt provided comments and suggestions on this chapter. A revised version of this chapter will be submitted to Marine Geology.

A departure from sediment transport is taken in Chapter 5, where the small-scale hydrodynamics are investigated using a fully nonlinear numerical model based on the Navier-Stokes equations (previously developed at Los Alamos National Laboratory). Dr. Donald Slinn originally modified the model for use in the swash zone. Bret Webb made modifications to account for falling water droplets and air bubbles. The model has since been modified (by me) to include a new forcing algorithm, a turbulence closure scheme, a velocity correction algorithm, and numerous other changes. This chapter will be submitted to the Journal of Fluid Mechanics.

Chapter 6 further uses the hydrodynamic model to investigate velocity and shear stress variability in the swash zone under various hydrodynamic conditions. Dr. Don Slinn provided comments and suggestions. This chapter will be submitted to Coastal Engineering.

TABLE OF CONTENTS

page

APPENDIX

LIST OF TABLES

LIST OF FIGURES

Abstract of Dissertation Presented to the Graduate School
of the University of Florida in Partial Fulfillment of the
Requirements for the Degree of Doctor of Philosophy

HYDRODYNAMICS AND SEDIMENT TRANSPORT IN THE INNER SURF AND SWASH ZONES

By

Jack A. Puleo

August 2004

Chair: Donald Slinn
Department: Civil and Coastal Engineering

Hydrodynamic and morphodynamic processes occurring in the swash zone control the erosional and accretional patterns of the foreshore, the last line of natural defense for the back beach from the full brunt of ocean waves. Our study focuses on inner surf and swash motions through remote sensing, field data collection, and numerical modeling efforts. Data obtained from these endeavors are used to better predict and understand sediment transport in this region, through modeling efforts and through kinematic and statistical relationships.

The first portion of this dissertation provides a thorough background on the studies that have been undertaken in the swash zone in the last few decades. Following this review, several field studies are explored with the aim to better predict sediment transport, specifically erosion, on the foreshore. Initially, flow velocity and suspended sediment concentration (SSC) measurements are used to show that SSC depends on both fluid velocity and fluid acceleration leading to an additional term in a typically used sediment transport formulation. It is proposed, however, that the inclusion of this term, while being a function of acceleration, likely serves as some parameterization for the

turbulence generated in the bore. Armed with this new formulation, an experiment was carried out to further validate an optical remote sensing technique for estimating the surface fluid velocities in the swash zone over a large spatial region that could be used in a three-dimensional model of sediment transport and foreshore change. We found that the formulations with an acceleration term increased the predictive skill of the beach change, while at the same time reducing the error between the predicted and true bathymetry.

Finally, we focused on high resolution numerical modeling of inner surf and swash zone hydrodynamics over a fixed bed. The model solves the Navier-Stokes equations, and is able to accurately reproduce the sea surface elevation and fluid velocities across the inner surf and swash zones, in addition to giving detailed information on pressure gradients and bed shear stress.

CHAPTER 1
THE SWASH ZONE: A REVIEW OF HYDRODYNAMICS, SEDIMENT TRANSPORT AND FORESHORE CHANGE PROCESSES

Introduction

Wind stresses whether generated by large-scale planetary circulation cells, medium scale atmospheric disturbances such as storms, or small scale sea breezes resulting from inland heating provide a mechanism whereby energy is transferred to the ocean surface resulting in the formation of surface gravity waves that propagate energy in all directions. When the waves approach a coastline (Figure 1-1), they begin to dissipate their energy at the sea bed through frictional processes and eventually break. Even after these processes, the wave form continues its migration toward land until the majority of its energy is finally expended in the region where the land meets the sea. This region, where water rushes up and down the beach face is termed the swash zone and is important for a variety of reasons.

The swash zone comprises the most seaward reach of exposed beachfront property and therefore acts as the final buffer for any shoreline erosive processes that may encroach landward. On the other hand, sediment transport through the swash zone may build out the foreshore, further protecting the upper beach. Therefore, the swash zone acts as a sediment gateway between the upper beach and offshore, where swash processes determine the net erosion or accretion of the foreshore region.

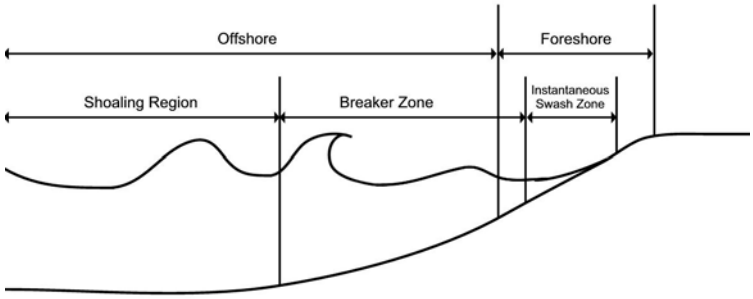

Figure 1-1. Schematic of offshore and foreshore regions showing shoaling, breaking and swash zones.

Buffering provided by the foreshore also translates to monetary aspects (such as tourism revenue and beachfront property protection) and erosion mitigation. For instance, the swash zone is where vacationers wade into the ocean, make sand castles, and (for the romantic types) walk off into the sunset; but is also where some nourishment and/or beach dewatering projects are located. While this is only a limited list on the importance of the swash zone, it does point to its importance as related to both physical processes and civil aspects in terms of shoreline erosion and tourist revenue.

Perhaps surprisingly, based on the importance of this region, scientific understanding of the physical processes occurring here is improving but still remains poor in comparison to oceanic processes occurring in, for instance, the surf zone or larger scale circulation. One reason understanding is poor is the complex nature of processes and scales that meet in the swash zone. As an example, swash motions are highly turbulent, direction-reversing flows that collide with one another, experience high water column and bed shear, and are capable of transporting quantities of sediment that may exceed those in the surf zone by up to a factor of nine [*Beach and Sternberg*, 1991]. The fact that the water depth in the swash zone can range from zero to over a meter with changes in depth occurring on time scales as short as several seconds makes measurements both discontinuous and difficult to obtain and further complicates understanding.

The purpose of this review chapter (see *Butt and Russell* [2000] or *Elfrink and Baldock* [2002] for other swash zone reviews) is to give details on fluid and sediment transport processes that occur in the swash zone, to provide a review of the research that has been undertaken in this region over the last several decades and to suggest some of

the necessary steps to gaining a better understanding in the future. The following sections introduce swash zone hydrodynamic generalities, differences from the surf zone, the scales of motion relating to shoreline oscillations and those that would be measured by a fixed point current meter, studies of cross-shore flows, shear stress, and alongshore motions. Through bed flows that are typically ignored in many swash studies are then addressed. Simple to complex numerical models are discussed, with an implication for future understanding of the relevant physics that need to be studied to better understand swash hydrodynamics. Next sediment transport discussed including transport observations, predictions, and estimates based on elevation changes. Then foreshore change measurements and predictions through conceptual, kinematic and statistical descriptions as well as direct modeling efforts are discussed.

Swash Zone Fluid Dynamics

General Description of Swash Motions

There is no precise definition of the seaward edge of the swash zone although it has been suggested that the seaward edge of the swash starts where bore turbulence begins to significantly affect the sea bed [*Puleo et al.*, 2000]. *Brocchini and Peregrine* [1996] also give definitions of average parameters in the swash zone based on their analysis of numerical model results. Most researchers, however, reference the swash zone as either the region of the beach profile where there is intermittent fluid coverage or the time varying region extending from the point of bore collapse on the beach face to the maximum uprush limit. Adopting the latter definition, Figure 1-2 shows an idealized time history of swash motions for a monochromatic wave train on a planar sloping permeable beach. Initially, a bore is approaching the point of fluid intersection with the foreshore and a sensing device such as a current meter (represented by the solid circle)

may be just out of the fluid domain leading to discontinuous measurements. High onshore-directed fluid velocities are associated with the bore in the upper portion of the water column, whereas strong offshore-directed flows occur near the bed. The turbulence associated with the bore and the water column shear owing to flow convergence is responsible for high vertical mixing. The thin uprush motion after the bore has collapsed at the beach face, (the beginning of uprush) has been accelerated in the shoreward direction as a result of the pressure push of the collapse itself and is shown in the next panel. Here, the fluid velocities are all essentially onshore and the permeability, largely dependent on grain size and saturation, has allowed for fluid to infiltrate the foreshore surface (denoted by grey arrows). By the third panel, the uprush has already reached its maximum landward extent, the flow has passed through reversal and started to head offshore as backwash. Difficulties can arise even with these simple definitions because of cross-shore variations in the flow field (mentioned below). At this time, the flow accelerates downslope and fluid may still be infiltrating the beach. Finally the backwash begins to be affected by the next bore in the inner surf zone and swash zone transition causing the outer swash flow to decelerate. Meanwhile, further shoreward, a retrogressive bore may develop [*Shen and Meyer*, 1963b and *Hibberd and Peregrine*, 1979] and fluid may exfiltrate the foreshore surface. The approach of the inner surf bore may also cause a hydraulic jump to form in the lower swash zone particularly on shallow sloping beaches.

Comparison of the Surf and Swash Zones

As suggested above swash zone time series tend to be discontinuous, unlike their continually submerged surf zone counterparts. This difference is only one of many that distinguish the swash zone from the surf zone.

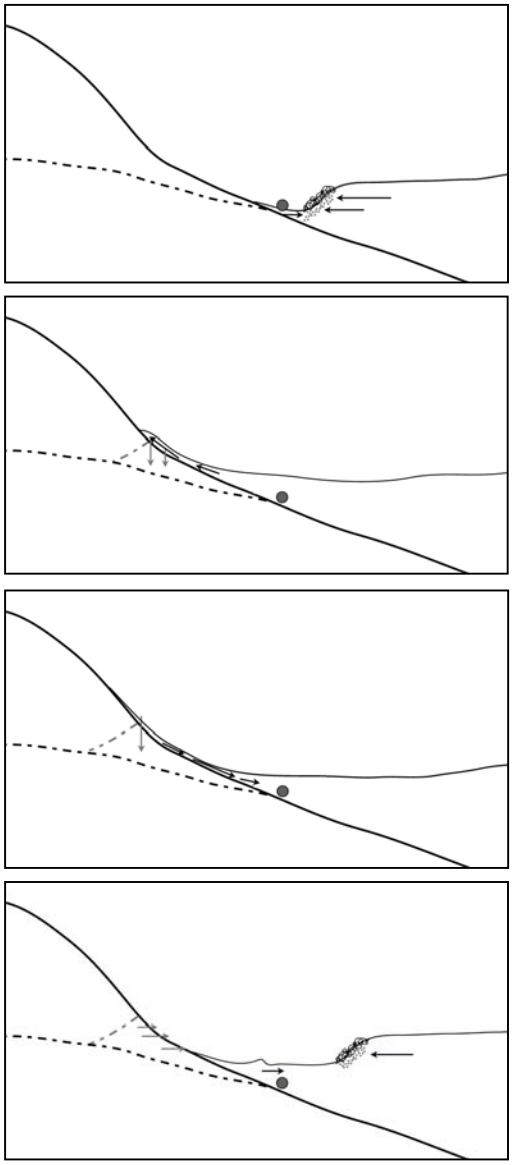

Figure 1-2. Schematic of swash cycle. Thick solid curve is the foreshore surface. Thin solid curve is the water surface. Black dashed curve is the water table elevation. Grey dashed curve is the water table level due to runup. Solid circle represents location where an in situ sensing device may be placed. Arrows indicate flow direction and relative magnitudes (after *Osborne and Rooker* [1997]).

Basic definitions such as wave height (distance from trough to crest), wavelength (distance between wave crests) and wave period (time required for two successive waves to pass a fixed point) do not have a simple mapping into the swash zone. As an example, one may define the beginning of the uprush occurring as the instant the bore reaches the time varying shoreline location and the end of the backwash as the instant just before the next uprush begins. While these notions make sense conceptually, the time between these occurrences is not as constant as, say, the peak period in the surf zone because of interactions of the natural (random) wave field and swash motions. Hence, the observed swash period, (more correctly, duration) cannot generally be assumed representative for a series of swash motions on a natural beach. Because the swash duration varies over time, a range of swash excursion distances (analog to surf zone wavelength?) is also expected to be quite variable. Similarly, the analog to surf zone wave height may be the runup elevation, but the latter is a measure of the distance above the still water level (see *Butt and Russell* [2000] for more definitions used in the swash zone) as opposed to the distance between wave troughs and crests that do not exist in the swash zone. Within the swash zone, after bore collapse at the beach, the resulting fluid motion becomes a thin sheet of runup [*Shen and Meyer*, 1963b] and has been likened to a rarefaction (or expanding) wave [*Freeman and Le Méhauté*, 1964 and *Miller*, 1968] that no longer exhibits the characteristics of a combined longitudinal/transverse wave or shock wave (bore) observed in the surf zone. Hence, the concept of water particles having an orbital trajectory is no longer applicable to swash flows.

Eulerian vs. Lagrangian Observations

Based on Figure 1-2 it is also apparent that in situ measurements made with a current meter, pressure sensor or sediment sensing device will be subjected to

intermittent emergence from the water column if they are truly placed in the swash zone. Not only does this intermittency affect statistical analysis procedures, it may complicate understanding of the swash processes because the sampling occurs in an Eulerian frame of reference. Because the swash zone continually migrates up and down the foreshore in response to tidal motions (and the swash motions themselves), the swash zone actually represents a Lagrangian region of the nearshore. For instance, simple models (next section) describe the motion of the leading edge of the swash and its velocity without reference to the physical processes in the swash interior. With the Lagrangian aspect of swash motions noted, the field study portion of this review is still largely based on Eulerian measurements, because of the difficulty associated with trying to measure the motion of individual fluid parcels. Explanations of leading edge motions and swash oscillations, however, are still given in the Lagrangian time frame, since the leading edge is more easily monitored as a function of space and time.

Infra-Gravity and High Frequency Scales of Motion

It was mentioned previously that the swash zone serves as a buffer between the back beach and the full brunt of ocean waves. It also acts to modify or accept the inner surf zone modification of energy from offshore, and may act as a low pass filter for the energy reaching the beach face [*Emery and Gale*, 1951 and *Sonu et al.*, 1974]. There are generally two approaches to describing swash motions. The first is that swash flows are dominated by low frequency infragravity motions and the second is that swash motions are dominated by individual bores [*Baldock et al.* 1997].

Low Frequency Motions

Low frequency scales of motion are most easily analyzed by monitoring the swash oscillations obtained from the leading edge. For instance, runup measurements

have been made using resistance wires aligned parallel to the beach face and digitized video recordings [*Aagaard and Holm*, 1989]. Care must be taken in recording these measurements, as varied conclusions can be obtained based on the mode of collecting [*Holland et al.*, 1995]. As an example, it has been reported that resistance wire elevation changes on the order of just a few centimeters can cause variance differences as great as 25% [*Holman and Guza*, 1984].

It has been proposed that the amplitude of swash motions for monochromatic waves are proportional to the standing wave amplitude and hence saturated [*Miche*, 1951] such that increasing the incident wave height does not increase the incident energy at the shoreline. Swash motions at lower frequencies, however, appear to be unsaturated, such that increasing the offshore incident wave energy causes swash oscillations to increase at infragravity time scales [*Huntley et al.*, 1977; *Holman*, 1981; *Guza and Thornton*, 1982; *Holman and Guza*, 1984; *Holman and Sallenger*, 1985; *Huntley et al.*, 1993; *Holland et al.*, 1995; *Raubenheimer and Guza*, 1996 and *Baldock et al.*, 1997]. For instance, *Suhayda* [1974] showed that low-frequency energy associated with swash oscillations was attributed to linear standing waves. On the other hand, *Guza and Thornton* [1982] and *Raubenheimer and Guza* [1996] found a linear relationship between low frequency swash oscillations and the offshore significant wave height, whereas *Holman and Sallenger* [1985] and *Ruessink et al.* [1998] showed that the ratio of low frequency swash motions to incident wave height depends on the Iribarren number, a function of beach slope and offshore wave steepness [*Iribarren and Nogales*, 1949].

The finding regarding low frequency swash oscillations and Iribarren number points to the importance of beach slope, or more importantly the dissipative nature of the

beach. Another way to classify the dissipative nature of the beach is through the surf similarity parameter [*Guza and Inman*, 1975]

$$\xi = \frac{H_b \omega^2}{2g \tan^2 \beta}, \quad (1\text{-}1)$$

where H_b is the breaker height and ω is the radian frequency. Values of ξ>20 indicate dissipative conditions, whereas values of ξ<2.5 indicate reflective conditions [*Wright and Short*, 1984].

In many of the aforementioned studies, the swash motions were observed on low sloping beaches with very wide swash zones (indicative of small Iribarren numbers and large ξ) and it was shown that the standing wave hypothesis likely explained some of the swash variance at low frequencies [*Holland et al.*, 1995]. Thus, it may be expected that on steeper beaches where much of the incoming energy approaches shore before being dissipated, swash oscillations would be dominated by incident energy [*Butt et al.* submitted]. However, this has been shown to not always be the case by analyzing swash motions on steep laboratory beaches. *Shah and Kamphuis* [1996] and *Baldock and Holmes* [1999] found that swash motions were still low frequency dominated but that the low frequency motions were associated with the incoming wave groups rather than a cross-shore standing wave phenomenon. This finding was further supported by *Mase* [1995] when the energy at the shoreline was weak. In contrast, field studies have shown that low frequency motions in the swash zone could be generated by uprush/backwash interaction [*Carlson*, 1984] and bore overtake and capture [*Bradshaw*, 1982]. *Mase* [1988] confirmed this to some extent by modeling swash runup oscillations as a series of overlapping parabolas. *Mase* [1995] went on to simulate waves in a laboratory flume, to show that there is a frequency down shift, from incident to low frequency, of swash

motions that can be driven by uprush-backwash interaction when the power of the incident waves is large. Yet, these findings are in contrast to the statements of *Guza and Thornton* [1982] who state that if the downshift in energy is due to bore capture, there should be a continuous shift toward lower frequency motions from the breakpoint to the shoreline. They support their comments based on the field data of *Suhayda* [1974] and *Huntley* [1976] where no continuous down-shifting of energy was observed.

In summary, it appears that both long waves (standing waves, or motions attributed to wave groupiness) and bore capture are both important in initiating low frequency motions in the swash zone. Figure 1-3 shows a schematic of the incoming wave energy and that observed at the shoreline (after *Mase*, [1995]). In the simplest case, monochromatic waves shoal and break in the surf zone and drive swash oscillations at a frequency similar to the incident frequency. It has been suggested that swash oscillations in this case will have the same frequency as the incident waves [*Mase*, 1995], but this is not necessarily the case as the swash oscillations also depend on the foreshore slope. Note, however, that this case does not occur for natural swash as monochromatic wave fields are only approachable in a laboratory setting. In the random wave case, both short and long (free and bound) waves affect swash oscillations. In the long wave case, the motions are generally manifested as shoreline reflections and observed as a standing wave component to the low frequency swash signal. Short waves can contribute to both the low frequency and incident frequency oscillations where the low frequency oscillations are driven by wave groups due to variability in the breakpoint [*Symonds et al.*, 1982] and due to uprush/backwash interactions.

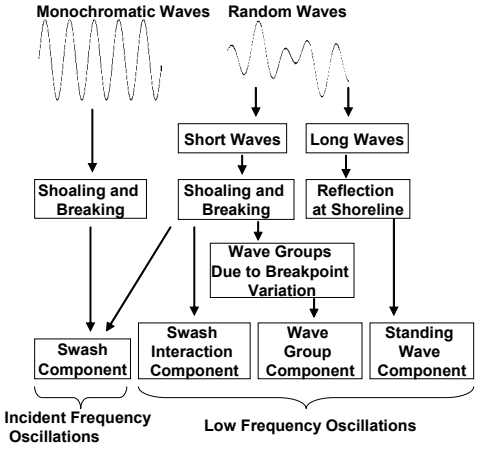

Figure 1-3. Schematic showing transfer of offshore energy into swash zone oscillations (adapted from *Mase*, [1995]).

Bores and Turbulence

The highest frequency motions in the swash zone occur as turbulence is generated at the bed by frictional processes and more readily by the churning of water in the leading edge and bore motions. For instance, *Yeh et al.* [1989] observed bore collapse in a flume using laser-induced fluorescence to show that that the turbulence generated near the shoreline is not only highly three-dimensional, but that the turbulence is advected with the bore front, spreads downward toward the bed [*Madsen and Svendsen*, 1983 and *Svendsen and Madsen*, 1984] and ultimately acts on the unwetted beach face. Therefore, one may expect this to be a dominant supply of energy delivered to the bed. In fact, *Miller* [1968], using high speed motion imagery in a laboratory channel, found a large vortex-like internal swirl formed at the front of the bore that then lags behind the bore but is successively replaced at the front by new vortices. These newly formed vortices extend to the bottom of the water column but progressively die out near the rear of the bore as the energy imparted to the vortex dissipates. *Rodriguez et al.* [1999] measured turbulence levels in the inner surf and swash zones in a laboratory flume and found that the distribution of swash zone turbulent kinetic energy varied linearly with depth, consistent with the notion of vortices extending down to the bed. *Petti and Longo* [2001a] and *Petti and Longo* [2001b] have further extended our knowledge of turbulence in the swash zone through laboratory studies using laser and acoustic Doppler velocimeters. They concluded that 1) the turbulent energy flux is shore–directed, 2) that the turbulence is controlled by the bore during uprush and the bed during backwash, and 3) the Kolmogorov length scale increases towards the bed indicating dissipation is less important near the bottom than near the surface during uprush. Finally, the most detailed laboratory data to date on internal swash zone flows were collected by *Cowen et al.*

[2003] using PIV techniques with a high speed video camera mounted below a clear, smooth, planar-sloping laboratory beach. Their study corroborated the results of *Petti and Longo* [2001a] and *Petti and Longo* [2001b] and in that the uprush turbulence is dominated by bore-generated and bore-advected turbulence which evolves analogous to grid turbulence, whereas the backwash turbulence is dominated by the growing boundary layer and compares well to the classic flat plate boundary theory near the bed.

Field studies of high frequency swash motions using hot film probes indicate the turbulence length scales depend on the bore height (local depth), but may decrease sharply under the bore itself [*Flick and George*, 1990]. *Osborne and Rooker* [1999] used an acoustic Doppler velocimeter to show that the turbulent kinetic energy is large and nearly equal during uprush and backwash. In contrast, *Butt et al.* [in press] found high levels of turbulence associated with the bore front that were largest during the backwash/uprush transition. Furthermore, the highest values of turbulent kinetic energy estimates occurred while the near bed velocity was still offshore-directed in line with the idea of the surface-generated turbulence penetrating towards the bed (the internal vortex described by *Miller* [1968]). *Longo et al.* [2002] provide further details on turbulence measurements and characteristics in the swash zone.

Field and Laboratory Studies of Cross-shore Swash Flows

The previous section focused on low or high frequency aspects of swash motions typically tied to swash oscillations or the turbulence within the bore respectively. Many studies have addressed interior swash motions, those behind the leading edge or in front of/behind the bore in the incident band (even though measurements with fixed instruments in the swash zone are difficult to obtain). For instance, rapidly changing velocities and water depths, scour and burial, shallow water depths, intermittently

exposed instruments, turbulence and air entrapment all act to interfere or contaminate swash signals.

One of the first studies of swash zone flows measured mean uprush and backwash velocities using the time and distance over which floats traveled [*Miller and Zeigler*, 1958]. Other early swash studies used devices such as a dynamometer [*Schiffman*, 1965] or a swinging vane [*Hardisty et al.*, 1984], where the accuracy was likely questionable, to monitor swash velocities. In recent studies, more accurate instruments such as the electromagnetic current meter (EMCM) [*Butt and Russell*, 1999; *Butt et al.*, 2001 and *Butt et al.*, in press], acoustic Doppler velocimeter (ADV) [*Baldock and Holmes*, 1997; *Osborne and Rooker*, 1999; *Blewett et al.*, 2000; *Puleo et al.*, 2002; *Raubenheimer*, 2002 and *Butt et al.*, in press], laser Doppler velocimeter (LDV) [*Cox et al.*, 2000; *Cox and Hobensack*, submitted; *Petti and Longo*, 2001a and *Petti and Longo*, 2001b] and ducted impellor current meter (DICM) [*Sonu et al.*, 1974; *Hughes et al.*, 1997b; *Masselink and Hughes*, 1998; *Puleo et al.*, 2000 and *Puleo et al.*, 2003b] have been used to record swash velocities in a variety of conditions and beach types. Remote sensing has also been used to measure swash velocities. The first attempts appear to be that of *Speranskiy* [1972] and *Wright* [1976] who used a photographic technique to determine the distance the leading edge or foam traveled between successive photographic frames and the time separation of the frames to estimate the velocity. *Holland et al.* [2001] used particle image velocimetry (PIV) and *Puleo et al.* [2003a] used PIV and radar techniques to measure the surface flow fields in a natural swash zone while *Cowen et al.* [2003] and *Jensen et al.* [2003] measured the near bed velocity profile within a laboratory swash zone using PIV.

While each of these methods is likely more accurate and easily deployed than the instruments of the past, they all have some difficulty tied to the problems with swash measurements mentioned above (Table 1-1). For instance, all in situ instrumentation is subject to water depth and distance above the bed constraints whereas the field remote sensing methods cannot extract subsurface information. In addition, the acoustic devices can be noisy due to intermittent emergence from the water column and air bubbles, whereas the DICM's are known to have a short flow response time and can be hindered by sediment laden flows.

Regardless of how measurements are collected, studies have repeatedly shown some general features of the swash zone internal flows and highlight the significant differences between uprush and backwash [*Hughes et al.*, 1997a]. During uprush the flows are typically originated by the collapsing bore, that may have a history through collision with the preceding backwash, accelerating the initial fluid motion [*Hibberd and Peregrine*, 1979; *Puleo et al.*, 2003b and *Jensen et al.*, 2003]. This collision can result in a nearly stationary bore or hydraulic jump [*Nelson and Miller*, 1974; *Brenninkmeyer*, 1976a; *Brenninkmeyer*, 1976b; *James and Brenninkmeyer*, 1977; *Broome and Komar*, 1979; *Bradshaw*, 1982; *Osborne and Rooker*, 1999 and *Butt et al.*, 2002] where the incoming bore is roughly held in place by the rapidly accelerating offshore flows, or results in a slight bore retreat. The uprush/backwash collision may also create backwash vortices that are efficient suspension mechanisms and may be responsible for the formation of beach steps [*Miller and Zeigler*, 1958; *Matsunaga and Honji*, 1980; *Matsunaga and Honji*, 1983 *Larson and Sunamura*, 1993 and *Bauer and Allen*, 1995]. Note that these two opposing flows are also likely to generate strong mid-water column

shear [*Cowen et al.*, 2003 and *Butt et al.*, in press] that may complicate advection based sediment transport models using a single current meter because the transport could occur in both the offshore and onshore directions simultaneously depending on elevation [*Butt et al.*, in press]. Also, after the initiation of uprush motion, the turbulence likely acts to homogenize much of the water column such that the flow becomes nearly depth uniform [*Larson and Sunamura*, 1993; *Petti and Longo*, 2001a; *Petti and Longo*, 2001b and *Cowen et al.*, 2003] because any turbulence near the bore tends to smooth out variations that begin to grow in the flow field. This is not the case behind the bore where the turbulence has been observed to decay moderately [*Cowen et al.*, 2003] to rapidly [*Yeh et al.*, 1989]. Furthermore, *Madsen and Svendsen* [1983] and *Svendsen and Madsen* [1984] found that the bottom boundary layer will be weak at the bore front and will not be significant until well behind the bore further suggesting that the flow is essentially depth uniform after uprush initiation.

The bore driven uprush process more rapidly loses its signature on dissipative beaches because of the energy dissipation over a wider surf zone, shallower swash depths allowing more dissipation at the bed, and the distance over which the uprush travels through a wide swash zone. For instance, *Miller* [1968] showed that bore motion was strongly affected by beach slope and bottom roughness indicating that gravity and grain size in addition to turbulence generation play a key role in bore dissipation on beaches.

Maximum uprush velocities observed on shallow sloping natural beaches have approached 2 m s^{-1} [*Beach and Sternberg*, 1991; *Beach et al.*, 1992; *Butt and Russell*, 1999].

Table 1-1. Limitations on typical swash zone current meters

Instrument	**Limitations**
DICM	Impellor inertia may alter signal
	Sediment laden flows can slow impellor
	Hysteresis in response to direction reversing flows
	Scouring if placed too close to bed
	Two instruments required to obtain cross-shore and alongshore motions
	Interfere with flow field
Two-component ADV (horizontal looking)	Signal contaminated by air entrained bubbles
	Cannot have sensing volume interfere with bed
	Noise observed upon intermittent submergence
	Interfere with flow field
	Minimum water depth constraints
Three-component ADV	Restricted height above bed requirements
	Noise observed upon intermittent submergence
	Interfere with flow field
	Minimum water depth requirements
LDV	Not presently possible in field setting
	Signal unlocking from intermittent coverage
	Signal contaminated by air bubbles
Miniature EMCM	Restricted height above bed requirements
	Interfere with flow field
PIV (below beach mounting)	Not possible in field setting
	Algorithm intensive
PIV (surface velocity fields)	Cannot estimate sub-surface flows
	Natural image texture required
	Algorithm intensive

In contrast, measurements on steeper beaches generally range up to 3.5 m s^{-1} [*Masselink and Hughes*, 1998 and *Holland et al.*, 2001] but have been reported to exceed 5 m s^{-1} [*Hughes et al.*, 1997b]. The timing of maximum velocities recorded by a current meter can vary depending on the history of the current meter location with respect to the swash zone. For instance, if the current meter is 'dry' before being inundated by the uprush, the maximum velocity occurs nearly instantaneously [*Hughes et al.*, 1997b; *Masselink and Hughes*, 1998; *Puleo et al.*, 2000], whereas if the current meter is already submerged, the maximum uprush velocity may occur shortly after the uprush passes [*Butt and Russell*, 1999 and *Osborne and Rooker*, 1999] because it takes time for the mostly surface associated flow to affect the current meter (generally placed near the bed). In either event, the rapid rise in velocity suggests that cross-shore variations in the flow field and/or fluid accelerations exist during uprush. Another explanation, however, is that the current meters are incapable of responding to a rapidly changing velocity signal. In the case of DICM's, *Masselink and Hughes* [1998] corrected their raw velocity signal using the correction for frequency response suggested by *Nielsen and Cowell* [1981] to account for this incapability. Yet, this apparent rapid acceleration during the initial stages of uprush has been observed in laboratory settings using remote sensing techniques [*Jensen et al.*, 2003] and in two dimensional numerical model simulations [*Puleo et al.*, submitted] where a current meter cannot be blamed for the response implying accelerating uprush (see *Hibberd and Peregrine*, [1979]), albeit short-lived, is possible in swash zone flows near the bore collapse point.

Flow reversal, generally associated with maximum runup levels, is relatively uneventful, but normally corresponds to maximum water depths on dissipative beaches

[*Zelt*, 1991] and occurs after maximum water depth is obtained on steeper beaches [*Hughes*, 1992 and *Hughes et al.*, 1997b]. It is also important to understand that the initiation of flow reversal and backwash motion is dependent upon the collection location on the foreshore. For instance, it has been reported that the backwash motion well behind the leading edge may actually start before the uprush reaches its maximum landward extent [*Raubenheimer et al.*, 1995; *Raubenheimer and Guza*, 1996; *Hughes et al.*, 1997a; *Puleo and Holland*, 2001 and *Cox and Hobensack*, submitted] resulting in a thinning of the swash tongue. This has implications when trying to ascertain the importance of uprush versus backwash flow durations as well as net sediment transport since these estimates will depend heavily on foreshore location.

While the uprush motion is dominated by the bore and turbulent flows originating in the bore or leading edge, backwash motion is dominated by shear derived at the bed [*Petti and Longo*, 2001b and *Cowen et al.*, 2003]. As a result it has been found that longer duration backwashes have an associated boundary layer growth *Raubenheimer* [2002] that is more distinct than during uprush. Backwash flows accelerate under the forces of gravity, frictional processes and cross-shore pressure gradients such that they increase their rate of speed but not to their full downslope gravitational potential [*Puleo et al.*, 2003b]. In fact, it has been found that swash flows might decelerate at the end of backwash (evident from the time series presented in, for instance, *Hughes et al.* [1997b] and *Masselink and Hughes*, [1998]) due to the horizontal pressure gradient and shore-directed force supplied by the next bore [*Puleo et al.*, 2003b]. Like the beginning of the uprush, the end of the backwash is a fuzzy concept and depends on the definition used and how the motions are recorded.

It is generally found that the duration of uprush flow tends to be less than backwash flows [*Hughes et al.*, 1997b; *Masselink and Hughes*, 1998 and *Cowen et al.*, 2003] with the typical uprush and backwash maximum velocity magnitudes being roughly equal [*Masselink and Hughes*, 1998; *Holland and Puleo*, 2001; *Raubenheimer*, 2002; *Cowen et al.*, 2003 and *Puleo et al.*, 2003b]. Individual swash events, however, can show variability in the ratio between uprush and backwash velocity maxima and flow durations analogous to skewed waves in the surf zone, but the concept of skewness becomes complicated due to the discontinuous nature of typical swash measurements. If sediment transport is assumed to be dominated by velocity moments, then backwash duration exceeding uprush duration leading to offshore-directed skewness would suggest a bias towards offshore transport [*Elfrink and Baldock*, 2002] especially if the fact that sediment is more easily transported downslope is considered. Yet, if this were the typical case, beaches should always be in an eroding state. Hence, even if the swash tends to be skewed offshore some other mechanism must exist to enhance the uprush transport to counteract this potential offshore bias.

Shear Stresses and Friction Coefficients

Most sediment transport models rely on the bed shear stress as the mobilizing force. Yet, direct measurements of shear stresses are rarely obtainable in the field or in the laboratory because they require precise, detailed measurements of the near bed flow field or other robust instrumentation. *Conley and Griffin* [2003] used a hot film anemometer flush mounted to a permeable brick and emplaced it in the swash zone of a natural beach. They observed a rapid rise and gradual decline in bed shear stress during uprush and a more symmetric rise and fall of shear stress during backwash. The peak uprush shear stress was nearly twice that of the peak backwash shear stress with the

overall ensemble averaged shear stress time series being skewed onshore. Shear stress estimates based on the Law of the Wall and LDV data collected in a rough bottom laboratory flume [*Cox et al.,* 2000] and through the use of numerical model simulations on a smooth slope [*Puleo et al.*, 2002] displayed similar time series.

Rather than basing shear stress estimates from velocity profile data or a numerical model, the typical approach relies on the quadratic drag law from an approximation using the free stream velocity, U, rather than the friction velocity, u^* as

$$\tau = \rho u^* |u^*| = \frac{1}{2}\rho f U |U|, \quad (1\text{-}2)$$

where ρ is the fluid density and f is an empirical friction factor. In field studies, knowledge of the boundary layer is often unknown so a single point current meter measurement independent of the boundary layer height is often used in place of U. The use of equation 1-2 presents another difficulty in terms of the appropriate value for f. However, because of the importance of f for estimating the shear stress, much effort has gone into its estimation. Using depth dependent velocity data, *Cox et al.* [2000] obtained f values between 0.032 and 0.054 during uprush and 0.013 and 0.038 during backwash on a rough slope whereas *Cowen et al.* [2003] found values between roughly 0.01 and 0.1 during uprush and 0.006 and 0.01 during backwash on a smooth slope. Estimates of f from shear stress sensor data [*Conley and Griffin*, 2003] yielded values of about 0.002 to 0.01 during uprush and 0.001 to 0.005 during backwash. Finally, estimates from ADV measurements yielded values around 0.01 to 0.03 for uprush and backwash [*Archetti and Brocchini*, 2002 and *Raubenheimer et al.*, in review]. The general consensus based on these studies is that the uprush friction coefficient is equal to or greater than the backwash friction coefficient.

Friction estimation based on leading edge force balances (Lagrangian as opposed to the Eulerian estimates mentioned previously) found uprush values on the order of 0.007 to 0.1 [*Hughes*, 1995 and *Puleo and Holland*, 2001] whereas backwash values ranged between 0.01 and 0.07 and showed considerable variability over a high tide cycle. Furthermore, *Puleo and Holland* [2001] and *Butt et al.* [2001] have suggested that the friction coefficient may even be time dependent through its relation to water depths. The larger backwash f values in the *Puleo and Holland* [2001] study are in direct contrast to the estimates from the aforementioned studies. The differences may result from the estimation technique, the use of leading edge rather than internal swash velocities and the exclusion of other forces on the leading edge such as pressure gradients and any infiltration or exfiltration modification of the swash flow.

The generalities obtained from swash zone velocity measurements are that the uprush and backwash are physically different. The uprush is dominated by (more so for steeper beaches) bore turbulence that tends to make the velocity profile nearly depth uniform after uprush initiation. Backwash flows are dominated by turbulent dissipation resulting from boundary layer formation near the bed. Flow durations are typically unequal with a slightly longer backwash but this can be dependent on the cross-shore location of the measuring instrument and forcing conditions. Flow accelerations tend to be less than gravitational acceleration throughout much of the swash duration with a short burst of accelerating uprush during the "collapse" process and a short section of decelerating backwash during the backwash/uprush collisional process. For the most part, shear stresses tend to be about twice as large during uprush than during backwash

but of a shorter duration. Friction coefficients tend to be equal to or larger during uprush than backwash and may vary throughout the swash duration.

Alongshore Swash Motions

Little attention has been specifically paid to alongshore swash motions, because many past experiments focused on cross-shore measurements. The effect of alongshore motions in the swash zone may be of vital importance accounting for a large portion of the total alongshore sediment transport [*Kamphuis*, 1991; *Van Wellen et al.*, 2000; *Wang et al.*, 2002 and *Smith et al.*, 2003], representing one of the peaks in the typical bi-modal cross-shore distribution of the alongshore sediment transport (the other being at the breaker zone) [*Kraus et al.*, 1981; *Kraus et al.*, 1982; *Bodge and Dean*, 1987; *Wang et al.*, 1998 and *Wang et al.*, 2002] and utilized in models related to beach cusp formation [*Dean and Maurmeyer*, 1980; *Werner and Fink*, 1993 and *Coco et al.*, 1999]. For instance, *Thornton and Abdelrahman* [1991] found a non-vanishing alongshore current in the swash zone that occurred as a result of obliquely incident wind waves interacting with long standing waves, while non-zero alongshore swash velocities from video based field measurements have also been observed (chapter 4). Other studies focused on alongshore flows in the swash zone have also shown them to be significant [*Asano et al.*, 1994; *Kobayashi and Karjadi*, 1996; *Brocchini and Peregrine*, 1996 and *Brocchini*, 1997]. Fortunately, the increasing use of side and downward looking ADV's allows for the use of a single *in situ* instrument to record both the cross-shore and alongshore velocities. Hence, it is likely that more knowledge on alongshore flows will be gained during even typical swash laboratory and field deployments.

Influence of Groundwater and Through Bed Flow in the Swash

So far, swash hydrodynamics have generally been discussed in relation to motions over an impermeable bed. In reality, groundwater dynamics are part of the swash zone hydrodynamic regime because of potential exchanges between the subsurface aquifer and the flow above. The location of the water table with respect to oceanic fluid levels helps determine the degree of saturation of the beach face and potentially the ease with which fluid can enter or leave the foreshore through the bed [*Baird and Horn* 1996; *Turner* 1998 and *Butt and Russell* 2000]. Field studies have addressed the motion of the water table in response to long period motions such as infragravity motions and tides [*Waddell*, 1973; *Waddell*, 1976; *Lanyon et al.*, 1982; *Nielsen*, 1990; *Turner*, 1990; *Metcalf et al.*, 1995; *Raubenheimer et al.*, 1999], as well as water table variability on swash duration time scales [*Hegge and Masselink*, 1991; *Turner*, 1993; *Kang et al.*, 1994 and *Turner and Masselink*, 1998]. On tidal frequencies which appear to dominate the water table elevation in many instances [*Gourlay*, 1992], rise and fall of the water table is damped with distance inland of the beach face [*Ericksen*, 1970; *Harrison et al.*, 1971; *Lanyon et al.*, 1982; *Nielsen*, 1990 and *Raubenheimer et al.*, 1999], generally lags the phase of the tide [*Emery and Foster*, 1948 and *Nielsen*, 1990] and is asymmetric [*Lanyon et al.*, 1982; *Nielsen*, 1990 and *Raubenheimer et al.*, 1999]. Because of the lag during ebbing tide, a seepage face, often described as having a ‘glassy’ appearance, may form between the shoreline and exit point of the water table on the foreshore [*Turner*, 1993].

One dimensional models based on mass continuity and Darcy’s law [*Dominick et al.*, 1971 and *Harrison et al.*, 1971] have shown good agreement with the measured time variation of the water table elevation. *Nielsen* [1990] gives an analytic solution to the one dimensional Boussinesq equation for finite amplitude water table fluctuations for a

sloping beach whereas *Baird et al.* [1998] and *Raubenheimer et al.* [1999] solved the equations numerically. The Boussinesq model equations were able to predict the tidal water table fluctuations with some lag between model and data noted, and adverse effects after seepage face formation *Nielsen* [1990], and in the *Baird et al.* [1998] study showed improvement when the wave runup was included.

None of the above studies included the capillary fringe, the region above the water table that still contains moisture due to capillarity between individual grains, in their models. Hence it was assumed that the sand drains instantaneously. It has been shown, however, that at tidal frequencies, capillarity effects have little effect to the overall rise and fall of the water table [*Li et al.*, 1997a]. Recent advances, though, have included the use of two dimensional models with capillarity [*Li et al.*, 1997b; *Li et al.*, 2000] and the use of non linear shallow water equations for driving swash motions coupled with groundwater flow equations [*Li et al.*, 2002] .

Through Bed Flow Effects on Swash Zone Hydrodynamics

The aforementioned models and study of groundwater flow typically focused on the effect of tidal modulations rather than individual swash motions that, in themselves, can affect through bed flow. A simple explanation of through bed flow during a swash cycle can be related to the instantaneous swash edge position with respect to the location of the exit point, where the water table intersects the foreshore. As swash flows reach landward of the exit point where it is often assumed to be ‘dry’, fluid may infiltrate the bed and reduce uprush volume. Conversely, below the exit point, where the foreshore is saturated, backwash flows may be enhanced by fluid exiting the foreshore. It turns out that the concept of ‘wet’ and ‘dry’ depending on location with respect to the exit point is fuzzy because of the height of the capillary fringe with respect to the foreshore surface.

Turner [1993] states that pore spaces within the capillary fringe are generally 100% saturated but they are not considered part of the water table because the pore pressure is less than atmospheric. A rapid water table rise can occur in a short amount of time by increasing the pore pressure or slight infiltration by addition of a thin lens of water (the reverse Wieringermeer effect) supplied by swash rather than a large upward fluid flow [*Turner*, 1993]. This water table rise may in turn affect the infiltration capacity and exfiltration potential for the rest of the swash duration if the water table coincides with the foreshore surface. *Waddell* [1973], *Waddell* [1976], *Hegge and Masselink* [1991] and *Turner and Masselink* [1998] have further confirmed that the water table responds to individual swash events.

While it has been shown that the water table can fluctuate on swash time scales, infiltration appears to be more significant on coarse grained beaches where the subsurface pressures respond rapidly to swash flows and infiltration [*Blewett et al.*, 2000]. For instance, *McLachlan et al.* [1985] found volume infiltration rates to be on the order of 20-70 $m^3\ m^{-1}\ day^{-1}$ for grain sizes of 0.3 to 0.6 mm. *Turner and Masselink* [1998] estimated the infiltration/exfiltration exchange using pore pressure and hydraulic gradients on a foreshore with a median grain diameter of about 0.5 mm to be $O(10^{-3}\ m\ s^{-1})$, whereas *Blewett et al.* [2000] estimated infiltration velocities using hydraulic gradients (of between 0.3 to 2.2) on beaches with grain sizes between roughly 0.2-200 mm to be $O(10^{-2}$ to $10^{-4}\ m\ s^{-1})$. Similarly, *Baldock et al.* [2001] found swash-induced hydraulic gradient magnitudes just below the foreshore surface (mean grain size of 0.24 mm) to be on the order of 1.0.

These studies have shown that the fluid exchange between the swash flows and those subsurface for fine grained beaches is quite small and based on numerical models has little effect on swash hydrodynamics [*Packwood and Peregrine*, 1980 and *Packwood*, 1983].

Through Bed Flow Effects on Swash Zone Sediment Transport

Even though through bed flow is often small (specifically on sandy beaches), its effect in sediment transport models seems warranted since it is generally assumed (perhaps incorrectly) that infiltration during uprush promotes deposition while exfiltration during backwash promotes erosion. Models such as those of *Turner* [1995] and *Quick* [1991] included the effect of infiltration. In the *Turner* [1995] model simulation over medium to coarse sand, the upper foreshore profile steepened while the lower foreshore profile lowered resulting in a break in swash zone/inner surf morphology. *Quick* [1991] found that infiltration during uprush increased the shear stress while exfiltration during backwash tended to dislodge or destabilize sediment particles. These finding suggest opposing effects on sediment transport and have been recast into a modified Shield's parameter [*Nielsen*, 1998 and *Turner and Masselink*, 1998]. On the one hand, infiltration can modify the boundary layer, increasing shear stresses [*Watters and Rao*, 1971; *Oldenziel and Brink*, 1974 and *Conley and Inman*, 1994], by allowing for streamlines to squeeze closer to the bed. On the other hand, infiltration imparts a stabilizing force by inducing a downward pressure on the sediment grains [*Martin and Aral*, 1971 and *Watters and Rao*, 1971]. Conversely, exfiltration reduces boundary shear stresses by dilating the boundary layer and destabilizes the bed by imparting an upward force on sand grains promoting bed fluidization. *Baldock and Holmes* [1998] suggest

that sediment transport over a fluidized bed may differ only slightly from that over a non-fluidized bed, but may increase significantly if the sediment is transported as sheet flow (a transport mode likely to occur during backwash), further justifying the need to study infiltration/exfiltration effects on sediment transport in the swash zone.

With the opposing infiltration/exfiltration effects on hydrodynamic and bed stabilization noted, analysis has been directed at determining when one effect should dominate over the other. *Nielsen* [1998] suggested that medium grained sands (0.58 mm) would be stabilized by infiltration with altered bed shear stresses becoming more important as grain size is increased. In using their modified Shields parameter and measurements of the vertical pore pressure gradients in the beach, *Turner and Masselink* [1998] found that changes in bed stress dominated over any stabilizing effects for a median grain size of 0.5 mm and that these were most important during uprush. Their simulated sediment transport rates showed an increase by up to 40% during uprush and a reduction by 10% during backwash when through bed effects were included. Using a similar modification of the Shields parameter and vertical pore pressure gradients, *Butt et al.* [2001] found contradictory results with a decrease in uprush transport on the order of 10.5% and an increase in backwash transport on the order of 4.5% for a median grain size of 0.24 mm. *Karambas* [2003] also found contradictory results to those of *Turner and Masselink* [1998] using a coupled Boussinesq hydrodynamic model and porous flow model to determine the effect of through bed flow on sediment transport. Results showed that uprush transport is enhanced for coarser grains and decreased for smaller grains, whereas for backwash the opposite was found. Some of the differences could be attributed to the formulation for the friction factor in the model [*Butt et al.*, 2001 and

Karambas, 2003]. Sensitivity tests [*Butt et al.*, 2001 and *Karambas*, 2003] suggested that there is a critical grain size when the influence of infiltration or exfiltration changes sign from offshore to onshore. They reported values of about 0.55 mm and between 0.4 to 0.6 mm (in close agreement with the suggestion by *Nielsen* [1998]) respectively, where below this cutoff, stabilizing and destabilizing forces are more important than boundary layer modification to sediment transport while above this cutoff, boundary layer modification should dominate. Finally, *Masselink and Li* [2001] investigated the role of swash infiltration on altering the foreshore slope. They used a numerical model to show that the accretionary effects of swash infiltration are only manifested when the total volume of infiltration over a swash cycle is about 2%. This is approximated to occur when the grain size is roughly 1.5 mm. Therefore, they conclude that the correlation between foreshore slope and grain size on sandy beaches is not related to swash infiltration, but is likely the dominant factor controlling the slope of gravel beaches.

Based on these works, it appears that through bed flow in the swash zone tends to be negligible unless the grain size is medium sand or larger. In these instances, through bed flow appears to alter the swash hydrodynamics by serving as a potential source or sink for fluid and affects sediment transport in the swash zone through boundary layer modifications and stability effects on sediment grains. As a result (even though the effects may be small), groundwater processes should be included in future hydrodynamic and sediment transport models and studies as more ground truth validation of the groundwater effect on these processes is needed.

Numerically Modeling Cross-shore Swash Motions

Shoreline (leading edge) Models

A simple method of modeling leading edge swash motions is to model only the motion after bore collapse and to assume no swash interactions or through bed flow [*Shen and Meyer*, 1963b; *Meyer*, 1972; *Kirkgöz*, 1981; *Bradshaw*, 1982; *Hughes*, 1992; *Hughes*, 1995 and *Puleo and Holland*, 2001]. The bore can be modeled through the non linear shallow water equations, but care must be taken because the bore itself represents a shock wave where mass and momentum are conserved either side of the bore but that energy may not be conserved. Conservation results when the losses in mechanical energy are accounted for by production of heat and turbulence in the bore front [*Stoker*, 1948] requiring bore relations in the form of internal boundary conditions [*Hibberd and Peregrine*, 1979]. Therefore, the simple model described below is only applicable once the bore has collapsed at the beach face. The leading edge of the runup tongue is divided into individual fluid elements bounded by vertical planes, the sea bed and the free surface. If it is assumed that each fluid element contains the same mass then the leading edge fluid element acts analogous to a block on a frictional incline as

$$m\frac{d^2X}{dt^2} = -mg\sin(\beta) - \tau\delta l, \tag{1-3}$$

where X is the instantaneous shoreline position, m is the mass of the leading edge fluid element, β is the angle the foreshore makes with the horizontal, τ is the bed shear stress and δl is the width of the leading edge fluid element. *Hughes* [1992] provides the inviscid analytic solution to the ballistic uprush equation (*Peregrine and Williams* [2001] have also given a solution for the time dependent shoreline location for uprush and backwash based on characteristics). The solution including friction was first presented

by *Kirkgöz* [1981] for uprush and *Puleo and Holland* [2001] for backwash. *Kirkgöz* [1981] showed that results using this simple theory are sensitive to the shear stress formulation and *Hughes* [1992] found that the inviscid predictions were typically in error by 65% for some swash parameters. That study attributed the discrepancy to the effects of friction and infiltration the latter of which seems important given that the field studies occurred on beaches with grain sizes ranging from 0.31-2.00 mm. Recall, however, that even the viscid solutions assume only gravity and friction are the driving forces for the fluid element such that any other unaccounted hydrodynamic processes could also contribute to the discrepancies observed. As an example, if the quadratic drag law is adopted for the shear stress term, then any processes, other than gravity and friction, that act to transfer fluid momentum become incorrectly incorporated into the only free parameter, f [*Puleo and Holland*, 2001].

Figure 1-4 shows the theoretical Lagrangian position and velocity time series for the leading swash edge using equation (1-3) and friction values of 0, 0.01 and 0.1. It can be seen that friction acts to reduce the maximum backwash velocity, the swash duration and shape of the water particle trajectory. It is also evident that the swash excursion profile can become asymmetric solely by including friction.

It was mentioned previously that the Eulerian fixed point time history of swash velocity had a short-duration accelerating portion during uprush [*Jensen et al.*, 2003 and *Puleo et al.*, 2003b] and a decelerating portion during backwash [*Puleo et al.*, 2003b] that cannot be predicted by this simple ballistic theory (Figure 1-4) because the theory only simulates flow after the uprush initiation without interactions.

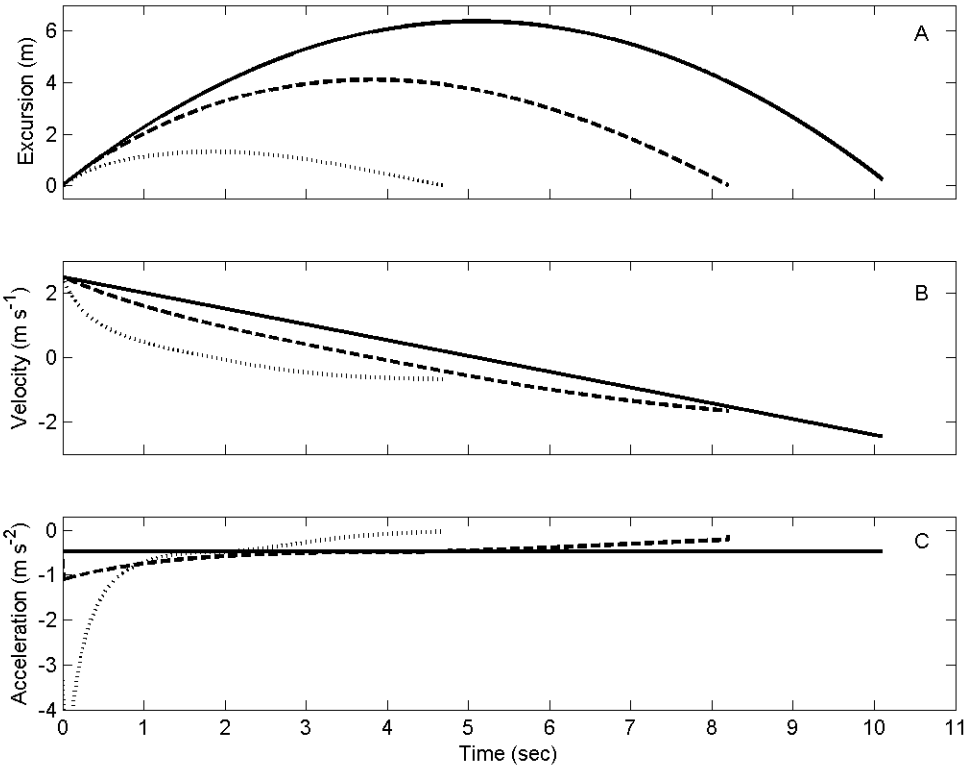

Figure 1-4. Ballistic theory for leading edge swash motions for the excursion trajectory (A), cross-shore velocity (B) and cross-shore acceleration (C). Solid curves are for the inviscid case, dashed curves for $f = 0.01$ and dotted curves for $f = 0.1$. Swash conditions are a beach slope of 1:20, initial velocity of 2.5 m s^{-1} and $\delta h = 0.05$m.

Furthermore, visual observations as well as estimates of the horizontal pressure gradients [*Puleo et al.*, 2003b] have shown that the swash tongue is not uniformly deep such that the initial assumption of friction and gravity as the only important processes may be violated. To address this, Figure 1-5 shows a schematic of the time history of the swash acceleration near the collapse point for a relatively steep, impermeable beach (analogous to field data [*Puleo et al.*, 2003b], laboratory data, numerical model results *Puleo et al.*, [submitted] and for acceleration in sawtooth waves *Drake and Calantoni* [2001]) but pointing to the important processes when the acceleration deviates from that expected if gravitational acceleration was the only important force. The solid curve is for a location just seaward of the uprush start location, while the dashed curve is for a location just landward of the uprush start location. The swash cycle starts in the lower left hand quadrant and proceeds clockwise (denoted by circular arrow). At the beginning of uprush, the onshore flow is accelerating (rather than decelerating) due to a strong shore-directed pressure gradient provided by the bore. Shortly after (quadrant 2), the flow is decelerating at a magnitude less than gravitational potential. Note that gravity and friction are still acting in unison so an onshore force, a pressure gradient, must exist else the acceleration magnitude would be larger than the downslope component alone. After flow reversal, (quadrant 3), the backwash flow begins to accelerate downslope, but again does not reach its full downslope potential. At this time, both friction and any pressure gradient from a sloping swash surface are acting in opposition to gravity in the seaward directed flow. Finally, the next bore supplies a large shore-directed pressure gradient so as to slow the backwash flow causing deceleration.

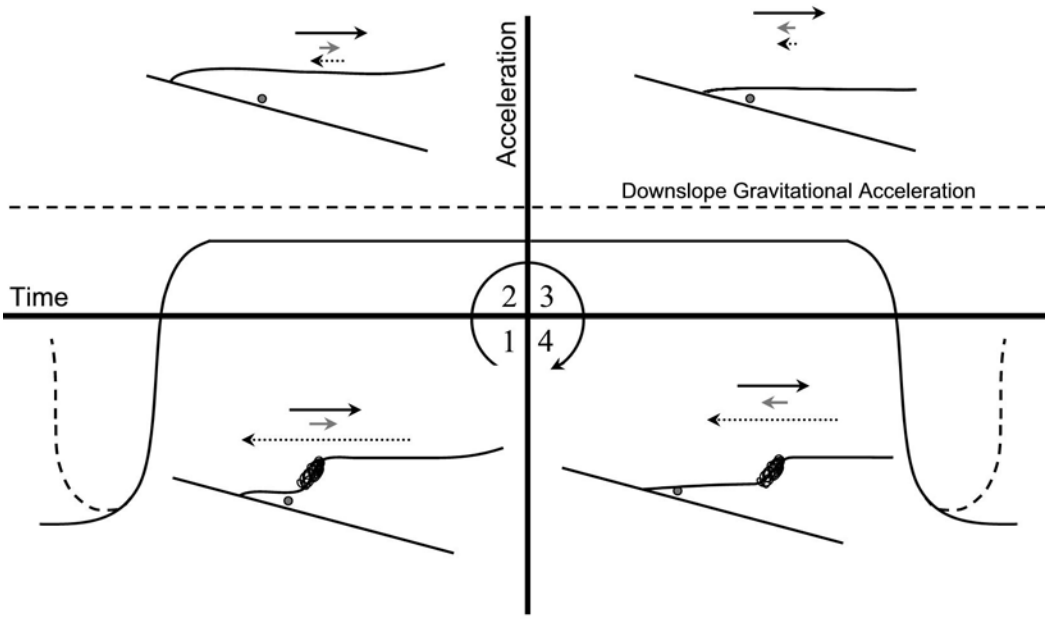

Figure 1-5. Eulerian swash flow acceleration schematic. Solid curve is for a location just seaward of the seaward edge of the swash zone. Dashed curve is for a location slightly landward of the seaward edge of swash zone. The horizontal dotted line represents the downslope gravitational component. Based on a coordinate system with cross-shore distance increasing offshore, quadrant 1 represents accelerating uprush, quadrant 2 represents decelerating uprush, quadrant 3 represents accelerating backwash and quadrant 4 represents decelerating backwash. Corresponding swash schematics from lower foreshore denote location of current meter (dot) and swash flow scenarios. Arrows in scenario represent direction and relative magnitude of forces responsible for net acceleration (Bold arrow – gravity, dashed arrow – pressure gradient, gray arrow – friction).

The two deviations from the nearly flat curve, namely the short accelerating portion of uprush and decelerating portion of backwash, diminish in the landward direction in the swash zone such that a short distance away from the seaward edge of the swash zone the acceleration curve is likely to be flat.

For the most part the frictional ballistic theory is reasonable except for the beginning of the uprush and end of the backwash. During these times, deviation from a flow solely controlled by gravity and friction causes the simple model to over predict a more rapidly decelerating uprush flow and a more rapidly accelerating backwash flow. As mentioned earlier, the ballistic model can be a good predictor of these motions if one calibrates the model with data through the free friction parameter, but the main drawback to the ballistic model is that only yields information pertaining to the leading edge unless one uses approaches similar to those outlined by *Peregrine and Williams* [2001].

One-Dimensional Models

Typical one-dimensional models follow the initial work of *Stoker* [1948] and *Carrier and Greenspan* [1958] (*Meyer* [1972] gives an early review on modeling beach runup) who modeled wave motions on planar impermeable beaches using the inviscid nonlinear shallow water equations. The latter study showed that there are standing waves that can climb a sloping beach without breaking whereas the former study focused on the motion of breaking waves and bores. *Whitham* [1958], *Keller et al.* [1960], *Ho and Meyer* [1962] and *Freeman and Le Méhauté* [1964] modeled the propagation of bores over a planar sloping bed. Theoretical solutions showed that the bore height tended to zero as the initial shoreline is approached and the particle velocity and bore velocity approach the same value as the shoreline is reached [*Keller et al.*, 1960]. *Shen and Meyer* [1963a] extended the work of *Ho and Meyer* [1962] to include a non-uniform beach slope. These

previous studies focused on the motion of the bore until it reached the shoreline whereas *Shen and Meyer* [1963b], *Amein* [1966] and *Hibberd and Peregrine* [1979] performed theoretical investigations as to the fluid flow after the shoreline is reached. They give approximate solutions of the leading edge location as a function of time, the shape of the runup tongue as a function of time and distance behind the leading edge, show that the trajectory of the leading edge is roughly parabolic and predict the formation of a backwash (retrogressive) bore.

More recently, Kobayashi and his colleagues [*Kobayashi and DeSilva*, 1987; *Kobayashi et al.*, 1987; *Kobayashi et al.*, 1989; *Kobayashi et al.*, 1990a; *Kobayashi et al.*, 1990b; *Kobayashi and Wurjanto*, 1990; *Wurjanto and Kobayashi*, 1991 *Kobayashi and Wurjanto*, 1992 and *Kobayashi and Johnson*, 2001] have utilized the depth averaged non linear shallow water equations (DNLSWE) over arbitrary bathymetry including friction to model wave shoaling and transformation across surf and swash zones. The DNLSWE equations are given as

$$\begin{aligned} &\frac{\partial h}{\partial t}+\frac{\partial}{\partial x}(hu)=0 \\ &\frac{\partial}{\partial t}(hu)+\frac{\partial}{\partial x}\left(hu^2\right)=-gh\frac{\partial \eta}{\partial x}-\frac{1}{2}f|u|u \end{aligned} \qquad (1\text{-}5)$$

where h is the water depth, u is the depth averaged cross-shore velocity, g is gravitational acceleration, η is the sea surface, f is an empirical friction factor, x is the cross-shore distance and t is time. The first relationship in equation 1-5 represents conservation of mass and the second conservation of momentum. The last term in the second equation is the bottom shear stress parameterized through a quadratic drag law. In this model broken waves are modeled as shocks (bores) and hence the sea surface cannot be multi-valued at

any given cross-shore location. In other words, plunging breakers and wave faces curling over prior to breaking cannot be visualized with this model.

RBREAK simulations on rough slopes have compared well with laboratory simulations [*Kobayashi et al.*, 1989 and *Kobayashi et al.*, 1990a] and were able to reproduce field measurements of: 1) shape and horizontal excursion of runup, 2) the increase in infragravity and decrease in incident energy as the waves propagate across the surf zone into the swash zone, 3) the total variance in runup with less than 20% error, and 4) third moments of the wave field velocity in the inner surf zone [*Raubenheimer et al.*, 1995; *Raubenheimer and Guza*, 1996 and *Raubenheimer*, 2002]. While RBREAK has been found to be a good predictor of the above hydrodynamic observations, it over predicts the swash zone velocity skewness, sea swell asymmetry and the maximum uprush to maximum backwash velocity ratio [*Raubenheimer*, 2002] suggesting that the model performs more poorly in predicting the cross-shore swash zone fluid velocity. Other work on smooth slopes using a derivative of RBREAK known as IBREAK [*van der Meer and Breteler*, 1990] showed that only the backwash velocities and runup levels compared well with measurements.

Navier-Stokes Solvers

Recently, the advent of faster and more readily available computing power has allowed for numeric solutions to the full Navier-Stokes (NS) equations rather than using DNLSWE. The 2D mass and momentum equations are

$$\frac{\partial u}{\partial x}+\frac{\partial w}{\partial z}=0$$
$$\frac{\partial u}{\partial t}+u\frac{\partial u}{\partial x}+w\frac{\partial u}{\partial z}=-\frac{1}{\rho}\frac{\partial p}{\partial x}+\frac{1}{\rho}\frac{\partial \tau}{\partial x}+g_x+\frac{1}{\rho}F_{bx} \quad (1\text{-}6)$$
$$\frac{\partial w}{\partial t}+u\frac{\partial w}{\partial x}+w\frac{\partial w}{\partial z}=-\frac{1}{\rho}\frac{\partial p}{\partial z}+\frac{1}{\rho}\frac{\partial \tau}{\partial z}+g_z+\frac{1}{\rho}F_{bz}$$

where u and w are the depth dependent velocity components, p is the pressure, τ, is the shear stress tensor, ρ is the fluid density, F_b is a body force, and subscripts x,z denote direction. In using the full Navier-Stokes equations (unlike DNLSWE), the pressure is not required to be hydrostatic, the vertical velocity remains in the equations, the model is not restricted to shallow water and the horizontal velocity is not depth averaged. *Raubenheimer et al.* [1995] suggest that the effect of the non hydrostatic assumption and lack of vertical flow information in using the DNLSWE may be small based on qualitative agreement between field data and RBREAK. It seems likely, however, that the vertical flow and strong turbulence generated in the bore would suggest that these effects are still important at least in the vicinity of the bore.

The use of the full NS equations for modeling swash flows was performed by *Lin et al.* [1999] for breaking and nonbreaking solitary waves on sloping beaches. They utilized the volume of fluid (VOF; *Hirt and Nichols* [1981]) method in an extension of a pre-existing model known as RIPPLE [*Kothe et al.*, 1991] whereby the fluid domain is modeled using appropriate force balances in each control volume and the flux of water across each of the control volume surfaces. The addition of a k-ε turbulence closure scheme that depends on the turbulent kinetic energy and energy dissipation yields a time and space varying turbulent eddy viscosity. Flow patterns during runup and rundown from the model showed strong vertical variations in the horizontal velocity at times,

implying the shallow water approximation may be inaccurate even for nonbreaking runup. Their use of the NS equations showed better agreement with data than the DNLSWE and was able to simulate the breaking process reasonably well. *Puleo et al.* [2002] also used RIPPLE but without the k-ε turbulence closure scheme to predict swash flows. It was shown that the gross features of the breaking bore on a steep beach were similar to RBREAK simulations, but as previously mentioned, were able to better describe the overturning process. Furthermore, sea surface elevations in the outer swash/ inner surf zone area were predicted equally well by the two models, but variations in predicted runup and fluid velocities were evident. Potential discrepancies between the two simulations may be attributed to the use of a constant kinematic eddy viscosity, the forcing methods and a smooth surface in the RIPPLE simulation. To address some of these potential discrepancies, *Puleo et al.* [submitted] included large eddy simulation (LES) which results from calculating the stresses at the resolvable scales and modeling them at the sub grid scales (SGS), to describe the turbulent eddy viscosity (see *Rogallo and Moin* [1984]; *Shyy et al.* [1996]; *Ferziger and Peric* [1999] or *Wilcox* [2000] for VOF, LES and other computational fluid dynamics topics potentially related to swash flows), and altered the forcing mechanism using an open boundary in the offshore. The improved model showed excellent correlation for both sea surface and velocities in the inner surf and swash zones, but the effect of the LES was minimized due to the small grid scales used. Lastly, *Wood et al.* [2003] modeled runup of steep non-breaking waves using the VOF procedure in a commercially available code called FLUENT. The model qualitatively reproduced the evolution of the wave front and the magnitude of fluid velocities and accelerations during the initial runup, but had more difficulty in later

stages. A false surface boundary layer was observed that likely affected the velocity distribution in the body of the fluid. Other NS solvers have been used in the surf zone without specific application to the swash zone but the extension seems logical [*Lemos*, 1992; *Petit et al.*, 1994; *Sabeur et al.*, 1996; *Lin and Liu*, 1998b; *Lin and Liu*, 1998a; *Zhao and Tanimoto*, 1998; *Chen et al.*, 1999; *Bradford*, 2000 and *Mayer and Madsen*, 2000].

The VOF approach has been extended to three dimensions to better describe the inherent 3D nature of the turbulence associated with wave breaking [*Christensen and Deigaard*, 2001]. Rather than using a k-ε turbulence closure scheme which is known to have difficulty in complex flows and under adverse pressure gradients [*Rodi and Scheuerer*, 1986 and *Pope*, 2000], they utilized LES. They included the swash zone in their model but like other surf zone studies, focused on the wave breaking processes in the upper part of the water column. Future extensions of models based on these NS-type solvers should lead to a much better understanding of the highly turbulent breaking process in the swash zone bore as well as boundary layer structure throughout the uprush and backwash.

Sediment Mobilization and Transport Processes

Observations

Recalling that the uprush and backwash flows differ in their physical description, it seems logical that the uprush and backwash sediment transport processes would also be different. Past work has assumed [*Hughes et al.*, 1997a and *Elfrink and Baldock*, 2002], perhaps incorrectly, that the runup is a solely decelerating flow while the backwash is a solely accelerating flow and reaches a maximum in acceleration in the final stage of run down. As was shown in Figure 1-5, the runup can be characterized by a short duration

burst of acceleration associated with the collapsing bore [*Hibberd and Peregrine*, 1979]. It is this collision/collapsing process leading to highly turbulent motion that is likely responsible for much of the suspended sediment that is observed in the swash zone [*Butt and Russell*, 1999 and *Puleo et al.*, 2000]. The bore motion can supply high shear stresses to the bed which are an efficient sediment suspending mechanism that has been likened to a bulldozer effect [*Nelson and Miller*, 1974]. *Brenninkmeyer* [1976a] found what he termed 'sand fountains', large plumes of high suspended sediment concentration to occur in the region where the uprush and backwash meet (the incoming bore or hydraulic jump). These finding have also been corroborated by more recent work of *Osborne and Rooker* [1999], *Voulgaris and Collins* [2000], *Puleo et al.* [2000] and *Butt et al.* [in press] who obtained suspended sediment concentrations on a natural beach and showed that the concentration was highest and nearly depth uniform at the bore and leading edge of the swash where the turbulence is generated.

Based on this past work it appears that much of the sediment that is transported during uprush occurs as suspended load, loosely defined as mobilized sediment that is supported by turbulent fluctuations rather than grain to grain interactions (bedload). Most works assume, without explicitly stating, that the suspended sediment at a given location comes from the bed directly below that location rather than being advected from further shoreward or seaward (depending on flow direction). The effect of advection of pre-suspended sediment has been directly addressed in field studies by *Jackson et al.* [2004] and in a sediment transport model *Kobayashi and Johnson* [2001]. It has been suggested to be important to swash zone sediment transport [*Hughes et al.*, 1997a and *Elfrink and Baldock*, 2002] specifically near the early stages of uprush [*Jackson et al.*,

2004] but the rapid decrease in measured sediment concentrations behind the bore seems to suggest otherwise for the remainder of the swash cycle [*Puleo et al.*, 2000 and *Butt et al.*, in press]. Regardless, further understanding of any potential advective processes of previously suspended sediment on transport in the swash zone warrants further investigation.

Unlike uprush, the backwash is not dominated by surface generated turbulence (except during hydraulic jump formation or during collision processes) but instead the bulk of the turbulence supplied to the flow originates at the bed. Because of this origination, it is expected that sediment mobilization and transport during backwash typically occurs near the bed [*Horn and Mason*, 1994]. Logic also suggests that backwash should be bedload dominated because the swash zone tends to be void of surface features such as ripples that would be destroyed during the rapidly thinning flows. Field studies of sediment transport showed that the suspended load was highly suppressed, and moving near the bed during backwash [*Butt and Russell*, 1999 and *Puleo et al.*, 2000] pointing towards bedload dominance. Measurements of bedload dominated backwash sediment transport was found by *Horn and Mason* [1994] using sediment traps (bedload was defined as transport occurring below 1 cm) on four separate beaches. Other work such as that by *Hughes* [1992] observed a 'slurry' of sand and water during backwash that is more analogous to debris flow and may more readily be described by sheet flow conditions where the excess shear stress is large [*Wilson*, 1987] and the flow thickness is on the order of 10-30 times the grain diameter for the swash zone of sandy beaches [*Hughes et al.*, 1997b]. If this is the case, then *Hughes et al.* [1997b] suggest

that the measurements of *Horn and Mason* [1994] may actually have been suspended load rather than bedload if the transport was occurring under sheet flow conditions.

The above findings have pointed to two main difficulties with regards to sediment transport in the swash zone. The first is being able to accurately measure the sediment transport signal and the second is being able to partition the sediment transport into suspended load and bedload components. Overcoming the latter difficulty is highly dependent on the definition of bedload or suspended load used and even the device. For instance bulk measurements can be made with total load sediment traps [*Hardisty et al.*, 1984; *Jago and Hardisty*, 1984; *Horn and Mason*, 1994; *Hughes et al.*, 1997b and *Masselink and Hughes*, 1998], profile traps [*James and Brenninkmeyer*, 1977], and pump samplers [*Kroon*, 1991], whereas time dependent sediment loads can be obtained using optical devices [*Brenninkmeyer*, 1976b; *Kroon*, 1991; *Beach and Sternberg*, 1991; *Beach et al.*, 1992; *Osborne and Rooker*, 1997 *Butt and Russell*, 1999; *Osborne and Rooker*, 1999; *Puleo et al.*, 2000; *Butt et al.*, in press and *Puleo et al.*, 2003b] or acoustic devices (the author knows of no attempt to use acoustical backscatter devices in the swash zone; see *Thorne and Hanes* [2002] for a review on acoustic measurements for sediment transport). Note that some of the devices also attempt to partition the suspended load and bedload [*Horn and Mason*, 1994]. Table 1-2 gives the typical swash zone sediment transport/concentration devices along with their limitations. Based on some of these limitations, it appears that our knowledge of sediment transport in this region is severely hampered by inadequate field measurements.

Table 1-2. Limitations on typical swash zone sediment sensors

Instrument	**Limitations**
Bulk Trap	No time dependent knowledge
	No depth dependent knowledge
	No bedload/suspended load partitioning
Profile Trap	No time dependent knowledge
	No bedload/suspended load partitioning
Single Point OBS	No depth dependent knowledge
	No bedload information
	May be affected by bubbles (no consensus in literature)
	Affected by debris and foam
Vertical OBS Array	May be affected by bubbles (no consensus in literature)
	No bedload information
	Affected by debris and foam
Acoustic Backscatter	Affected by bubbles and intermittent submergence
	No bedload information
	Affected by debris and foam

Rather than focusing on net sediment transport, some studies have focused on individual sediment particle motion. *Williams* [1982] used two sizes of tracer sand to show that, as may be expected, smaller sized grains tended to move alongshore faster than larger grains. With respect to downslope motion, however, both particle size classes had roughly a simultaneous arrival of a maximum number of particles, suggesting a more uniform movement of the two size classes in the cross-shore direction.

Individual sediment particle motion (space-time trajectory) in the swash zone has been shown to have a roughly parabolic shape [*Kobayashi and DeSilva*, 1987], whereas the motion of large cobbles appeared to have a more linear path during uprush with only slight curvature [*Luccio et al.*, 1998]. A more precise understanding of cobble motion in the swash zone could not be had during that investigation because backwash motions were not studied. Understanding particle motion cannot be tied solely to size and hence shape and density must play a role. Based on findings that more rounded grains were transported to the back of the swash zone, *Trenhaile et al.* [1996] noted, in support of *Shephard and Young* [1961] assertion, that sand grain roundness can have a significant effect on cross-shore sorting (particle movement) in the swash zone. In addition, *Hughes et al.* [2000] suggest that heavy minerals, with smaller grain size and settling velocity than light-mineral grains, in their study area were hydraulically shear sorted as opposed to selective entrainment sorting [*Komar* 1987 and *Komar* 1998] because the flow velocities were expected to always be large enough to cause the particles to be in motion. Differences between these findings and those of entrainment sorting owing to skewed fluid motions that are typically associated with ‘black sand’ or ‘placer deposits’ could be due to beach type at a given location [*Hughes et al.*, 2000], but also the shape and density

of the heavy mineral particles with respect to the lighter mineral particles. In any event, motions of particles with different size, density or shape adds an additional layer of complexity to the already difficult problem of swash zone sediment transport and points to a need for a better understanding of sediment transport in heterogeneous sedimentary environments [*Holland et al.*, 2003].

Sediment Transport Predictions

Even though the sediment transport mechanisms are clearly different during the uprush and backwash, our understanding of these processes is limited, leading to the use of potentially inappropriate sediment transport models. The most often used sediment transport model is the velocity-moment-based energetics model [*Bagnold*, 1963; *Bagnold*, 1966; *Bailard*, 1981 or *Bowen*, 1980]. The model of *Bailard* [1981] a derivative of Bagnold's original work is given as

$$q = \left[\frac{\varepsilon_b \rho f}{2 \tan \phi} \left\{ u |\vec{u}|^2 - \frac{\tan \beta}{\tan \phi} |\vec{u}|^3 \right\} + \frac{\varepsilon_s \rho f}{2w} \left\{ u |\vec{u}|^3 - \frac{\varepsilon_s \tan \beta}{w} |\vec{u}|^5 \right\} \right], \quad (1\text{-}7)$$

where q is the total load cross-shore sediment transport rate related to a portion of the fluid power delivered to the bed through shear stresses, w is the sediment fall velocity, ε_b and ε_s are bedload and suspended load efficiency factors, $\tan\varphi$ is the internal friction angle of sand and the vector sum of both horizontal velocity components is used to determine the shear stress. The formulation contains two parts, one for bedload and one for suspended load. Each of these has a downslope term such that sediment transport has a downslope component regardless of the direction in which the motion was initiated. Studies in the surf zone relating to sand bar motion, however, have shown that the downslope term is small and often negligible [*Gallagher et al.*, 1998; *Thornton et al.*, 1996 and *Plant et al.*, 2004].

Before proceeding it is important to consider several assumptions that went into the original derivation of Bagnold's model and where violations occur in the use of this model in the swash zone. *Bagnold* [1966] gave several "Restrictions of conditions to be considered" when his model was developed. One restriction is to steady open-channel liquid flow by gravity which is violated in the swash zone where unsteady flows governed by processes in addition to gravity prevail. Although *Bagnold* [1963] gives a formulation for a purely sinusoidal oscillatory flow, he probably never envisioned his model being used in the swash zone with sawtooth waves, breaking bores and surface generated turbulence. This steady restriction is further violated by the existence of a pressure gradient that can occur in the swash zone. His reasoning for violation was arrived by the impulsion of flow in closed pipes being driven by a pressure gradient. Another assumption is that the thickness of the carpet of bedload material in motion to water depth is small. When this assumption is violated the bedload efficiency factor can approach 0.3 rather than the typically used value of about 0.1. It seems likely that in the thin swash flows, specifically during backwash, this assumption is violated. The fact that some of the assumptions of the original model may be violated in the swash zone should be kept in mind when comparing measurements to predictions.

Tests of the energetics-type model are obtained using some measure of the total suspended load either from a depth integration of sediment concentration measurements [*Puleo et al.*, 2000; *Puleo et al.*, 2003b and *Butt et al.*, in press], from sediment traps [*Hardisty et al.*, 1984; *Hughes et al.*, 1997b and *Masselink and Hughes*, 1998]; coupled with a velocity measurement (usually from a single point) or from elevation change measurements [*Holland et al.*, 1998; *Puleo and Holland*, 2000 and chapter 4].

Immediately we recognize that should strong shear in the water column exist, the use of a single point measurement will cause errors due to the transport direction obtained from a single current meter (recall the strong water column shear mentioned in the vicinity of the bore). Analysis has shown that this type of model has a moderate to good predictive skill at times. This should not be surprising provided much of the appropriate physics are included and because instantaneous correlation tests end up relating the measured flux to an estimate of the flux that also includes the fluid velocity [*Puleo et al.*, submitted]. In using this model, validation is obtained by fitting either the friction coefficient and/or the efficiency factor through the calibrating coefficient, k, that incorporates these values in addition to the fluid density and often the fall velocity [*Hughes et al.*, 1997b; *Masselink and Hughes*, 1998; *Puleo et al.*, 2000; *Evans et al.*, 2003; *Puleo et al.*, 2003b; *Butt et al.*, in press and *Butt et al.*, submitted]. These studies have shown that values for k can vary by up to an order of magnitude. Part of this difference can be ascribed to the use of instantaneous versus time averaged models, but could still suggest that the use of the energetics-type model may yet have some difficulty in the swash zone (see *Butt et al.* [submitted] for an overview of the use of the energetics model in the swash zone). In addition, because it is known that the flow characteristics are different for uprush and backwash, equation 1-7 or simplifications thereof are often fit separately for each phase of flow further suggesting that the varying efficiency factor helps to account for un-modeled sediment transport physics.

Field measurements have shown that phase shifts in the observed velocity or sediment suspension peaks could lead to errors in the prediction of sediment transport [*Osborne and Rooker*, 1999 and *Butt et al.*, in press]. This is likely to occur in regions

where flow directions are rapidly changing under conditions of high sediment suspension such as near the uprush/backwash interaction. This phase shift is similar to but not identical to the phase shift between the free stream velocity and the bed shear stress in a pure oscillatory flow (swash is not a pure oscillatory flow). As such, using a phase shift in a sediment transport formulation may be able to account for instances such as the scenario described above. *Nielsen* [2002] has incorporated a phase shift into a sediment transport model and showed that the new formulation could better predict the shift in the maximum suspension peak during uprush than a sediment transport model without the shift. Other sediment transport models have used the fluid acceleration or statistics related to the fluid acceleration in addition to the velocity moments, which may account for this phase shift (*Drake and Calantoni* [2001]; their method accounts for horizontal pressure gradients). *Puleo et al.* [2003b] and *Butt et al.* [in press] have extended energetics models to include the fluid acceleration and the turbulent kinetic energy (TKE) respectively. The former model used the fluid acceleration to alter the shear stress to include both drag and inertia forces while the latter included the TKE to potentially include the importance of the bore which was shown to be important in a previous sediment transport model [*Puleo et al.*, 2000]. Both the *Puleo et al.* [2003b] and *Butt et al.* [in press] models showed increases in predictive skill over the energetics model alone but it was suggested that the inclusion of the fluid acceleration likely only serves as a proxy for the bore effect rather than serving as a separate mechanism driving sediment transport in the swash zone [*Puleo et al.*, 2003b]. In fact, *Kobayashi and Johnson* [2001] suggest that the correlation between sediment transport and fluid acceleration may be difficult to establish due to the shifted response of the instantaneous sediment

concentration owing to advection and water column storage. The effect of fluid acceleration on swash zone sediment transport is an active area of research and will hopefully lead to a better understanding of its importance.

Estimation from Elevation Changes

Relative estimates of total load sediment transport can be obtained with no knowledge of the flow field provided time-spaced bathymetric measurements are made. Exact estimates cannot be made because elevation changes arise from gradients in transport and not the transport rates themselves, unless one integrates from above the shoreline (where the transport rate is known to be zero) to some location on the foreshore. Nevertheless, *Holland et al.* [1998] used the method of *Holland and Holman* [1997] to estimate foreshore surfaces roughly every 15 minutes and upon subtraction of successive surface elevations, estimated erosion rates of over 0.25 m^3 hr^{-1} per meter beach corresponding to offshore-directed transport. Other studies have also inferred the direction of net transport based on bathymetric measurements [*Waddell*, 1976; *Sallenger and Richmond*, 1984; *Howd and Holman*, 1987 and *Nordstrom and Jackson*, 1990] but actual transport values were generally not reported.

Foreshore Change Measurements and Predictions

Conceptual models

Conceptual models of foreshore change have been devised based on the combined effects of swash motions, through bed flow and tidal variations [*Grant*, 1948; *Duncan*, 1964; *Strahler*, 1966 and *Eliot and Clarke*, 1988]. In summary, these models state that the foreshore steepens on the rising tide due to sediment deposition as the uprush is able to reach landward of the water table/foreshore intersection. This allows infiltration of the uprush and a corresponding reduction of its transporting capacity leading to deposition.

Conversely, during the ebbing tide, the foreshore is saturated permitting a larger volume of fluid to remain (less infiltration) or even allowing water to exfiltrate out of the beach face causing beach flattening. These conceptual models must be viewed in light of the recent work on groundwater and exfiltration which have suggested that on sandy beaches through bed flow is relatively small [*Turner and Masselink*, 1998] or has a small net effect on sediment transport [*Butt et al.*, 2001] or beach change [*Masselink and Li*, 2001].

Kinematic relationships

Rather than addressing foreshore change as a result of variations in groundwater and through bed processes, some works have suggested kinematic relationships based on the swash flows. For instance, *Holland and Puleo* [2001] related the change in foreshore slope to an inequality between the swash duration and the significant wave period measured in the trough of an intermediate beach. It was found that the foreshore slope responded rapidly to a decrease in significant wave period through erosion. Other kinematic relationships have related the foreshore change to an inequality between uprush and backwash energy dissipation [*Inman and Bagnold*, 1963], to the phase difference defined as the ratio of uprush time to the total wave period [*Kemp and Plinston*, 1968] or to the swash flow asymmetry parameter, the ratio between uprush and backwash swash edge velocities [*Hardisty*, 1986].

Foreshore slope predictions and change can also be estimated by comparison to dimensionless parameters obtained from dimensional analysis of the important variables. *Harrison* [1969] and *Sunamura* [1984] showed that the foreshore slope or change in foreshore slope is a function of $H_b/(g^{1/2}D^{1/2}T)$ where H_b is the breaker height, g is gravitational acceleration, D is the grain size and T is the wave period. Similarly, the

foreshore slope has been related to the offshore wave steepness [*Rector*, 1954 and *Doornkamp and King*, 1971]. In contrast, *Smith* [1990] compared the foreshore slopes from various beaches to the Iribarren number and some dimensional parameters such as the breaker energy, the wave period and the significant wave height to name a few, but all showed poor correlations. Perhaps the latter studies were flawed because the comparisons to foreshore slope were related solely to hydrodynamic conditions and did not include any sediment characteristics such as the grain diameter that likely help govern the beach slope (*Bascom* [1951] and *Dubois* [1972]; *Sunamura* [1984] provides an extended reference list of sediment grain size effects and other factors affecting foreshore slope).

Swash Flow Statistics

Similar to kinematic relationships, swash flow statistics can be used to estimate the erosive or accretive nature of the foreshore. Since it is generally observed that the foreshore erodes during large wave and storm events (the winter and summer profile scenario described by *Shephard* [1950] and *Bascom* [1953]) that likely cause low frequency motions in the swash zone, one may expect that low frequency dominated swash zones would be in an erosive state. However, *In situ* velocity measurements, even from high energy beaches, have shown, that the swash is typically low frequency dominated [*Butt and Russell*, 1999; *Osborne and Rooker*, 1999 and *Puleo et al.*, 2000 and chapter 4] regardless of the erosive nature. Low frequency motions have been tied to sediment level oscillations on the order of 1-6 cm with typical time scales of about 10 minutes arising from upslope sand wave migration of a perturbation landward of the beach step [*Sallenger and Richmond*, 1984 and *Howd and Holman*, 1987] and to the potential low frequency wave effect on beach saturation [*Nordstrom and Jackson*, 1990].

Yet, a shift to lower frequency motions over time did not appear to affect the foreshore slope [*Puleo et al.*, 2000], rather foreshore erosion appears to be tied to the total amount of energy contained in the flow field and the shape of the swash velocity time series [*Butt and Russell*, 1999; *Butt et al.*, submitted and chapter 4].

Higher order statistics other than the simple ones described above have also shown relationships to foreshore change. Two such statistics are the velocity skewness, characterized by velocity time series with narrow high-velocity peaks and wide low-velocity troughs and acceleration skewness (an estimate of the flow asymmetry) characterized by a sawtooth shape with a steep sloping rear face and gentle sloping front face with equal velocity magnitudes [*Butt and Russell*, 1999]. In the swash zone, skewness results from the rapid change in flow direction during backwash/uprush collision, or the inundation of an initially unwetted foreshore location. For instance, during eroding conditions on the foreshore, the normalized velocity skewness, $\langle u^3 \rangle / \langle u^2 \rangle^{3/2}$, was offshore-directed for low frequency (cutoff at 0.05 Hz) swash motions potentially enhancing offshore transport and onshore-directed for both low and high frequency motions during stable conditions [*Butt and Russell*, 1999]. The concept of offshore-directed swash velocity skewness may be difficult to visualize as it would suggest a broad low-velocity uprush followed by a pronounced high velocity backwash. On infragravity time scales, however, this generally corresponds to several swashes moving up the foreshore where each swash overtakes the preceding one before it has completed its cycle (or even before it has started backwash) leading to a "piling" of water on the foreshore and a corresponding high velocity backwash resulting from the ensuing

infragravity time scale return flow. During the same studies, acceleration skewness, $-\langle a^3 \rangle / \langle a^2 \rangle^{3/2}$ where a is flow acceleration, was nearly always onshore-directed but was larger during stable conditions, potentially biased towards onshore transport. While these non-dimensional flow descriptors are not normally used to directly predict sediment transport in the swash zone [*Butt and Russell*, 1999], their use as an indicator as to the erosive or accretive nature of the foreshore appears useful [*Butt et al.*, submitted].

Foreshore Change Modeling

Many cross-shore profile models exist for predicting the time evolution of profile change in the surf and swash zones, but are often incapable of accurately modeling swash zone flows and sediment transport processes [*Broker-Hedegaard et al.*, 1992 and *Schoonees and Theron*, 1995]. Therefore, foreshore changes are often modeled as a separate section of the nearshore using swash zone measurements or within a larger framework where the swash flows and resulting transport are driven from either a model or measurements made in the inner surf zone. Regardless of how the sediment transport is determined, foreshore evolution arises from gradients in the sediment transport rates through the continuity equation as

$$\frac{\partial z}{\partial t} = -\frac{1}{\alpha}\frac{\partial \vec{q}}{\partial \vec{x}}, \quad (1\text{-}8)$$

where z is the elevation and α is a factor accounting for sediment packing efficiency.

Swash flows, sediment transport and foreshore change represent a feedback system because while swash flows drive the sediment transport, gradients of which lead to elevation changes, the flows themselves are altered based on the bed beneath them. With this in mind, there are a variety of ways to model foreshore change (Figure 1-6).

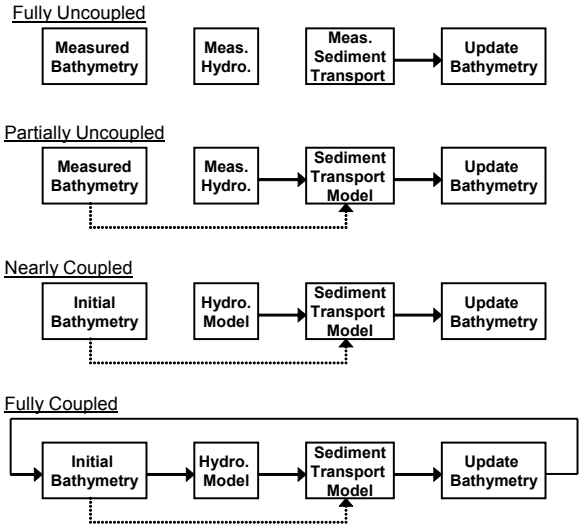

Figure 1-6. Flow chart for various methods of modeling foreshore bathymetric change.

In the first scenario, only the bathymetric evolution is modeled. The nearbed velocity and suspended sediment concentrations are measured and are fully uncoupled from the bathymetric predictions (Figure 1-6; fully uncoupled). This type of analysis is generally concerned with how well the measurements can conserve sediment mass in the model domain. For instance, *Puleo et al.* [2000] used two current meters and optical backscatter data to calculate elevation changes over a 5 m section of foreshore. In general, they were able to match the observed foreshore elevations within several centimeters of discrepancy. Errors increased when they tried to account for sediment that was not measured above the highest sensor. Other reasons for the discrepancies could be attributed to the use of only two current meters instead of a vertical velocity profile.

In the next approach, nearbed velocities and bathymetric evolution are measured and used to drive the sediment transport model (Figure 1-6; partially uncoupled). In this scenario, the measured velocities incorporate the variations caused by the true bathymetric changes, but are uncoupled from the modeled bathymetric changes. Hence, the downslope terms in equation 1-7 use the measured bathymetry at each model time step (or downslope terms may be omitted). This method is often used so that instability growth in the predicted bathymetry does not create large positive or negative gradients which swamp the sediment transport calculation. *Holland et al.* [1998] utilized a simple video-based current meter, stereometrically generated foreshore surfaces [*Holland and Holman*, 1997] and an energetics formulation to predict the foreshore profile change over time during a highly erosive condition. Only qualitative agreement could be found between measurements and predictions with differences being hypothesized to rely on through bed flows, sediment advection and the possible use of varying efficiency

coefficients in the sediment transport model. *Puleo and Holland* [2000] performed a similar test, but over a cross-shore and alongshore region of foreshore rather than for a cross-shore profile. In that study, cross-shore and alongshore surface PIV velocities were used to drive the sediment transport model while the foreshore surfaces were collected in the same manner as *Holland et al.* [1998]. Similar to the previous study, the energetics formulation could only qualitatively reproduce the observations. In chapter 4 we returned to the data used in the *Holland et al.* [1998] study and performed further tests again using PIV and the collected foreshore surfaces rather than a cross-shore profile. In addition to using the standard energetics-type formulations, we also included the acceleration extensions developed by *Drake and Calantoni* [2001] and *Puleo et al.* [2003b]. Again, the standard energetics-type models had difficulty predicting the observed foreshore evolution. The model even had difficulty in some instances predicting the correct sign of foreshore change. The addition of the acceleration modification by *Puleo et al.* [2003b] improved the predictions, but some discrepancies still arose. The extension developed by *Drake and Calantoni* [2001] most accurately reproduced the observed foreshore erosion with root mean square elevation errors over the domain of 0.17 m as compared to 0.34 m for the energetics model alone. It appears that these models can in the least, qualitatively predict the foreshore evolution, but measurement errors are probably restricting true tests of these models. As an example, in the studies by Puleo, the surface velocity, as opposed to a velocity measured at a constant nearbed elevation, was used in the sediment transport formulation. It is not clear how these measurements may have adversely affected the computations since they are sure to lie in the boundary layer at some phases of swash and outside it at others.

In the third approach the hydrodynamics and sediment transport are modeled but the bathymetric change from the initial conditions does not influence the modeled hydrodynamics (Figure 1-6; nearly coupled). The only difference between this approach and the partially uncoupled approach is that the hydrodynamics are modeled rather than measured and hence move toward a more enclosed modeling system. *Kobayashi and Johnson* [2001] used the DNLSWE to test a model of this nature, but rather than referring to the oft used energetics approach they approached the sediment transport aspect of the model using an equation based on water column storage of sediment and sediment advection being balanced by sediment suspension and settling. The model has a reasonable predictive capability with some slight elevation overprediction in accretive areas and underprediction in erosive areas, although the amount of discrepancy is dependent on values used for the two suspension efficiency coefficients.

Finally, the most physically correct approach is to model all three processes (Figure 1-6; fully coupled), such that the whole feedback loop is linked. Early attempts at this approach used energetics-type models for the sediment transport aspect and somewhat crude estimates of the velocity field in the swash zone. *Howd and Holman* [1987] used a velocity equation that related the time rate of change of the cross-shore velocity to the downslope gravity and a friction velocity product (contrast with the typical quadratic drag law that has a friction, velocity-squared product). The model showed the landward migration and amplitude decay of a foreshore perturbation that qualitatively matched observations, but no direct comparisons were made. *Hardisty* [1986] developed a morphodynamic model for beach gradients using a bedload based energetics equation and only the maximum uprush and backwash velocities for the hydrodynamic modeling

(no location dependent velocities were used). The results were compared to the data of *Doornkamp and King* [1971] and showed close correlation for offshore wave steepness of 0.06 or less. For larger wave steepness, the simple model severely under predicted the measured foreshore slope. Suspended load transport was later added to this model [*Hardisty*, 1990], but no comparisons were made to measurements. A Boussinesq hydrodynamic model coupled with a bedload formulation to calculate changes across the beach profile showed reasonable agreement with observed elevation changes but under predicted the observations in an accretive case [*Rakha et al.*, 1997]. While the swash zone was included in this model, little foreshore change was observed in either the measurements or predictions.

A numerical model for simulating storm-induced beach change was developed by *Larson and Kraus* [1989] for monochromatic waves and later extended to random waves [*Larson and Kraus*, 1995 and *Larson*, 1996]. All the studies included modeling the wave decay across the surf zone and up to a point on the foreshore. From that point forward, the velocity is used to drive the sediment transport based on a linear increase with distance offshore the maximum runup limit [*Larson and Kraus*, 1991] and later modified for non-linear increases with distance (or elevation) [L*arson and Kraus*, 1995]. Although, the models have been compared to laboratory and field data with fairly good visual and statistical skill, the lack of a swash hydrodynamic model and the basic distance-dependent sediment transport formulation that relies on the predicted transport at the surf zone boundary seem overly simplified for such a dynamic region.

In a similar model *Plant et al.* [2004] calculated the wave transformation across the surf zone using the relationship of *Thornton and Guza* [1983]. They supplied a

quadratic shape function to account for the sediment transport in the swash zone where the transport was set to zero at 2 m above the mean tide level and equal to the level in the surf zone where the wave energy is reduced 10% of its deep water value. Comparisons to field data over a variety of conditions showed that the prediction error was largely unaffected by this swash formulation but that the swash zone must bear importance as sediment from this region was eroded and distributed further offshore. Note that the last two models are placed in the fully coupled category because the hydrodynamics and sediment transport outside the swash zone are still fully coupled even though a specific swash zone hydrodynamic model is lacking and the sediment transport models in the swash zone are somewhat ad hoc.

Other fully coupled models have included the effects of through bed flow. For instance, *Turner* [1995] used a simple estimate of the swash velocity based on the time varying location of the leading edge to drive an energetics sediment transport model. The model could reproduce the gross behavior of observations on natural beaches in that an elevated water table led to foreshore erosion whereas a lower water table led to foreshore accretion. No direct comparisons to data were made in that study. More detailed studies that lead to the same general conclusions involved the modeling of the hydrodynamics using the non-linear shallow water equations or higher order Boussinesq models [*Masselink and Li*, 2001 and *Karambas*, 2003 respectively]. The former study assumed saturated flow conditions (Laplace equation) whereas the latter used a complete porous flow model for the subsurface flow. These models represent the few that exist in the literature that specifically model swash zone flows and sediment transport in a fully coupled manner.

Summary

This review of swash zone research has detailed some of the present accepted knowledge on sediment transport, hydrodynamics and foreshore change. Yet, the main conclusion from this exhaustive literature review is that the swash zone remains poorly understood. If the scientific community, specifically engineers who require knowledge of these processes for design and estimation of the survivability of projects, desires an improved knowledge of this region, more effort will have to be made not only in measuring the hydrodynamic and sediment transport processes, but understanding the link between the two.

CHAPTER 2
FLUID ACCELERATION EFFECTS ON SUSPENDED SEDIMENT TRANSPORT IN THE SWASH ZONE

Introduction

The swash zone is one of the most scientifically challenging oceanic environments for describing sediment transport. Here, uprush and backwash motions mobilize and transport large quantities of sediment compared to other regions [*Beach and Sternberg*, 1991; *Hughes et al.*, 1997; *Masselink and Hughes*, 1998; *Butt and Russell*, 1999; *Osborne and Rooker*, 1999 and *Puleo et al.*, 2000]. Gradients in the relatively small time integrated transport drive morphological change. In order to predict changes in beach morphology, an understanding of the physical processes is needed to develop an accurate mathematical description of sediment transport mechanisms in the swash zone.

Sediment transport in the swash zone has generally been described with an energetics type formulation originally derived by *Bagnold* [1966] for steady unidirectional flows and later adapted by *Bowen* [1980] and *Bailard* [1981] (hereafter referred to as B3 models) for time-dependent flows and used in several studies [*Hardisty et al.*, 1984; *Hughes et al.*, 1997; *Masselink and Hughes*, 1998 and *Puleo et al.*, 2000 among others]. Although the range of observations supporting these descriptions in the swash zone is somewhat limited, B3-type relationships have occasionally shown some significant correlation between predicted and measured sediment transport rates [*Masselink and Hughes*, 1998]. In addition, several studies have modified the original B3 equations in the hope of increasing the predictive skill at matching measurements. For

instance, *Puleo and Holland* [2001] and *Butt et al.* [2001] have suggested that the friction coefficient, f, varies between uprush and backwash and may even be a function of water depth. Since B3 models depend linearly on f, inclusion of this uprush-backwash variation could lead to improvement of sediment transport predictions either directly or indirectly by accounting for unrelated physical processes.

The B3 type models rely on velocity moments and hence do not explicitly account for flow unsteadiness that has been shown to affect boundary layer structure and hence energy dissipation at the bed. An example was given by *King* [1991] who showed, that the boundary layer development is slowed in an accelerating flow, implying the thickness is less than that for a steady flow (further described by *Nielsen* [1992]). The delayed development is easily understood for a laminar flow where rapid velocities may remain closer to the bed than in steady flow thereby increasing the bed shear stress. This explanation is less clear in a fully turbulent boundary layer where more mixing is likely to occur. Also, there is a phase lag between the free stream velocity and that in the boundary layer. These unsteady boundary layer effects are not incorporated into the B3 models, even though they appear to have a significant influence on sediment transport [*Hanes and Huntley*, 1986 and *Jaffe and Rubin*, 1996 among others]. For instance, *Drake and Calantoni* [2001] adapted a sheet flow model and added an extra term to the B3 bedload formula to account for acceleration effects (manifested through horizontal pressure gradients). Their numerical results showed that the inclusion of acceleration effects significantly improved the skill of the sediment transport model. Fluid accelerations have also been related to sandbar morphology [*Elgar et al.*, 2001 and *Hoefel and Elgar*, 2003] where it was shown that the peak in acceleration skewness of

surf zone flows was well correlated to onshore sand bar motion. *Admiraal et al.* [2000] developed relationships based on fluid accelerations and sediment response to predict the phase lag between maximum shear stress and peak suspended sediment concentrations from laboratory measurements in a flume.

While several studies have addressed the effect of fluid acceleration either from a theoretical viewpoint or for the surf zone, fewer studies have applied these concepts to the swash zone. *Nielsen* [2002] adopted the *Meyer-Peter and Muller* [1948] sediment transport model for swash by including a phase shift in the shear stress term. This phase shift accounts for greater bed shear stresses for a given velocity during accelerating flow. In the swash zone, this is most important to the accelerating portion of the uprush where peak velocities are higher and sediment tends to be more concentrated than during backwash [*Butt and Russell*, 1999 and *Puleo et al.*, 2000]. In fact, *Butt and Russell* [1999] used field data to show that sediment suspension events coincided with periods of large onshore-directed fluid acceleration.

The primary aim of this chapter is to describe the link between fluid acceleration and sediment transport in the swash zone, using field observations from a natural beach. The secondary aim is to use the new understanding of swash zone sediment transport to make a modification to the B3 model and to test this modification. The following describes the expected fluid motions based on idealized models. The B3-type sediment transport equation and the modification caused by including acceleration are then presented followed by a brief description of the field set up and data collected. Observations of suspended loads in velocity-acceleration space and comparisons between observations and model predictions are given in the results section. Discussion and

conclusions are then presented with respect to the effect of acceleration on observed sediment transport.

Idealized Swash Motions and Sediment Transport

Before developing the acceleration-based modification for the swash zone application of the Bailard model, it is important to understand the context to which this acceleration may play a role in swash zone suspended sediment transport. Technically, the swash motion begins after bore collapse into very shallow water [O(mm - cm)] or exposed (possibly wetted) bed. The inertia of the shoaling wave and the pressure force from the collapse accelerate the mass of water up the beach face. Towards the end of the backwash the seaward directed flow collides with the next incident bore (decelerates) leading to the ensuing swash event.

Frictional ballistic motion often applied to describe the swash cycle [*Ho and Meyer*, 1962; *Shen and Meyer*, 1963 and *Kirkgöz*, 1981] balances fluid acceleration against gravity and friction (see *Puleo and Holland* [2001] for analytic formulation). An example showing a Lagrangian velocity and acceleration time history for the leading edge and solely cross-shore flow is given in Figure 2-1 (defining the cross-shore direction, x, to be positive offshore). The flow is modeled analogous to a block moving up and down a frictional incline with a beach slope of 1:12, initial velocity, u_0, of 4 m s^{-1}, friction factor of 0.01 and a leading edge water depth of 0.05 m. An instantaneous increase in velocity would be expected as the uprush begins, followed by uprush deceleration, flow reversal and backwash acceleration during the seaward phase.

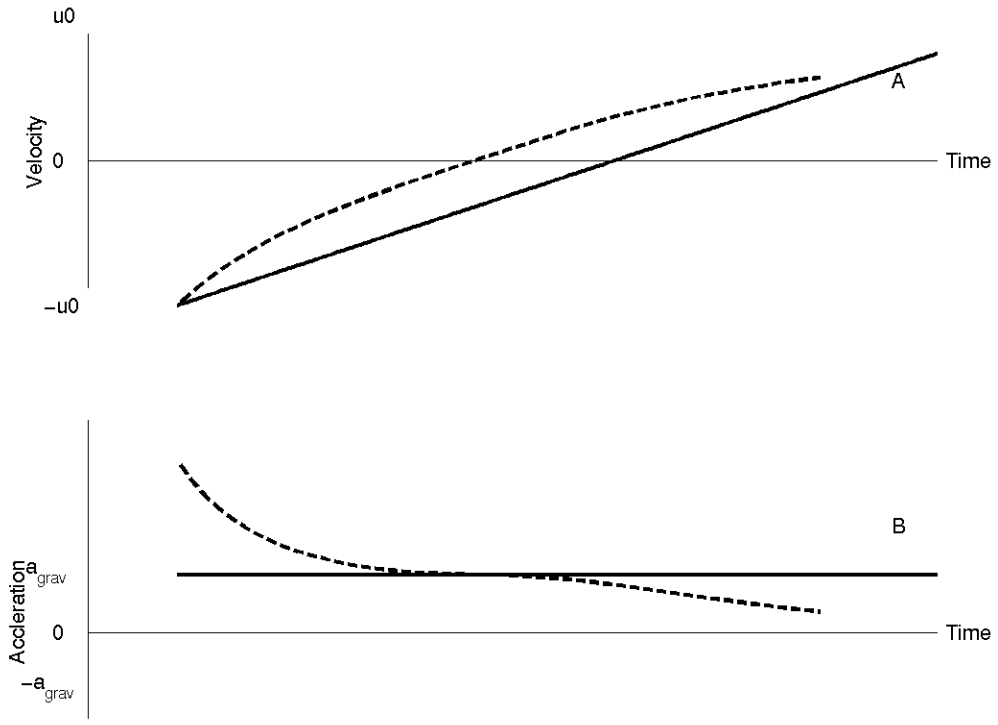

Figure 2-1. Theoretical ballistic motion for leading edge velocity (A) and acceleration (B) without (solid) and with friction (dashed). The initial velocity, u_0, is 4.0 m s^{-1} and a_{grav} is the downslope gravitational acceleration for a beach slope of 1:12. Inviscid swash duration is roughly 9.8 seconds.

Note also, that the theory does not describe the swash motion before the leading edge reaches the collapse point such that it only applies just after uprush initiation and just before the next uprush starts. Throughout chapter 2 and the rest of the dissertation, the term acceleration is used to refer to a flow with increasing velocity magnitude. The term deceleration is only used for referencing a flow whose rate of speed is decreasing. This is simpler terminology than using the term negative acceleration because in swash studies, fluid motions occur in both the positive and negative directions.

The effect of friction is indicated in the velocity time series (Figure 2-1A) by the swash duration being shortened and by flow velocities nearly always being less than frictionless motion (after accounting for swash phase due to differences in duration). The figure shows that the flow is decelerating throughout uprush and accelerating throughout backwash (Figure 2-1B). Near the initiation of the swash motion, the flow decelerates faster than downslope gravitational acceleration, a_{grav}, because both gravity and friction forces are acting together against the flow in the downslope direction. Acceleration values are only close to a_{grav} during times of small fluid velocity when the friction force is also small. After flow reversal, the acceleration is less than a_{grav} because friction and gravity forces are opposing each other. In short, the simple frictional theory for Lagrangian swash edge motion predicts a decelerating uprush and accelerating backwash during their respective cycles.

While the Lagrangian description of leading edge fluid motion is often applied in the swash zone, observations of Eulerian swash motions sampled with a current meter may yield a different typical time series for the interior (behind the leading edge) flow (Figure 2-2, from ducted impellor current meter data, *Puleo et al.* [2000], and similar to

that used by *Nielsen* [2002]). Here, the velocity does not increase instantaneously to its maximum, but does a short time after the sensor is inundated (Figure 2 in *Nielsen* [2002]). The inundation by swash at a given point represents a large onshore-directed acceleration (Figure 2-2A,B) as expected, but is not predicted by the simple ballistic model (which always predicts decelerating uprush flow). The swash flow then decelerates roughly according to gravity and friction (and likely horizontal pressure gradients). This is evident from Figure 2-2B where the acceleration curve approaches but does not quite reach downslope gravitational acceleration (denoted by dotted line). After flow reversal, the seaward-directed flow accelerates under gravity and friction, but does not continue to accelerate according to those processes alone, because the seaward flow is resisted by fluid mass offshore creating an adverse pressure gradient. Hence, backwash flow is not entirely ballistic as offshore fluid levels cause deceleration in the backwash. This is evidenced in Figure 2-2B where the acceleration curve becomes negative while the flow velocity is still in the positive (offshore) direction. Because of this, the maximum observed backwash velocity within a single swash cycle may not occur at the last value recorded by the sensor (Figure 2-2A) except at times, when the sensor emerges from the water column. While this schematic may not apply to all natural swash events it does point to differences between Lagarangian and Eulerian velocity and acceleration time series.

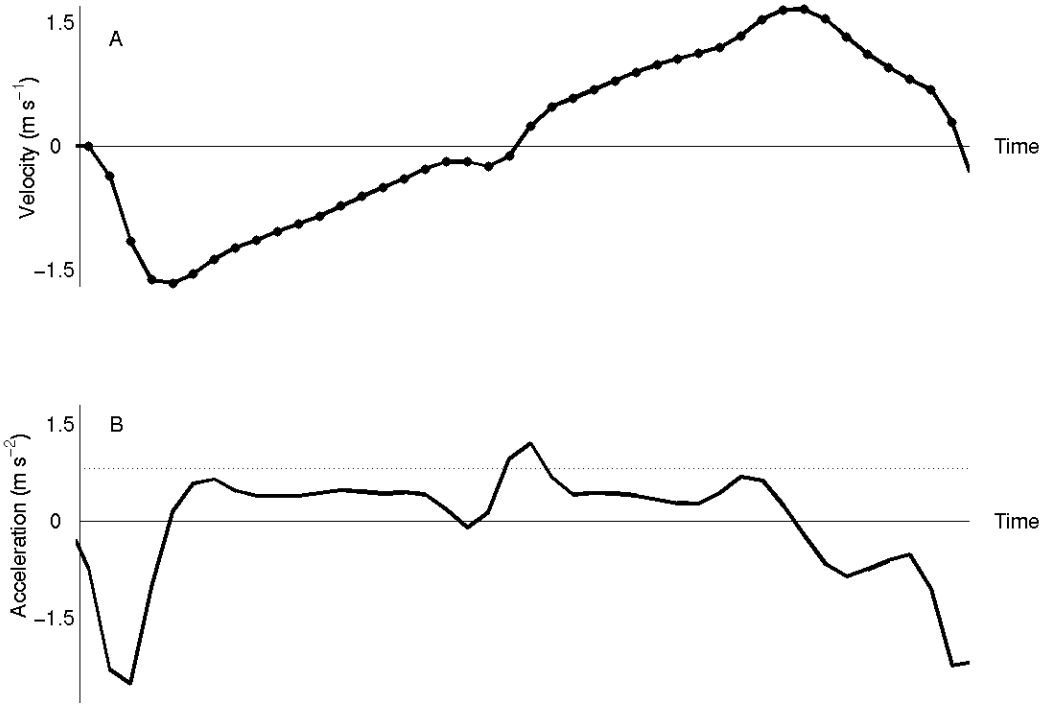

Figure 2-2. Swash schematic from current meter data showing velocity (A) and acceleration (B) profile. The solid horizontal lines represent zero velocity and acceleration. Dotted line in (B) is downslope gravitational acceleration on a 1:12 sloping beach. Swash duration is roughly 10 seconds.

The differences mentioned above may have a potential effect on swash zone sediment transport. For instance, even though swash velocity time series can be roughly symmetric (Figure 2-2A, and *Holland and Puleo* [2001]) or have slightly longer backwash durations with roughly equal velocity magnitudes [*Masselink and Hughes*, 1998], several studies have shown the dominance of suspended sediment during uprush [*Masselink and Hughes*, 1998; *Butt and Russell*, 1999 and *Puleo et al.*, 2000]. Yet, the rough velocity symmetry used in a velocity-based suspended sediment transport model with a bed slope effect would suggest continual foreshore erosion (same conclusion arrived at if a velocity-based bedload model is used). Based on these previous findings and because beaches cannot continually erode, another mechanism, not tied solely to velocity, should exist to balance this apparent deficiency in uprush transport. Large onshore-directed turbulence associated with the swash zone bore [*Butt and Russell*, 1999 and *Puleo et al.*, 2000] is the likely mechanism and including the fluid acceleration, a potential proxy for this bore turbulence, in a sediment transport formulation may lead to improved predictions.

Suspended Sediment Transport Equations and the Development of the Acceleration

The *Bailard* [1981] suspended load formulation (hereafter referred to as the Bailard model) relates the immersed weight suspended sediment transport to the fluid power as

$$q_B = K_d \omega_d = \frac{\varepsilon_s u}{w} \omega_d \quad (2\text{-}1)$$

where q_B (kg s^{-3}) is the time-dependent immersed weight suspended sediment transport rate, u is the cross-shore velocity, ε_s is a suspended load efficiency, w is the sediment fall

velocity, and ω_d is the local rate of energy dissipation per unit surface area (a portion of which is available to transport sediment), given by

$$\omega_d = \tau_d u \ . \qquad (2\text{-}2)$$

Here τ_d is the bed shear stress and can be expressed by a quadratic drag law

$$\tau_d = \frac{1}{2}\rho f |u| u \ , \ (2\text{-}3)$$

where ρ is the fluid density and f is an empirical friction factor. Incorporating equation 2-3 into equation 2-1 leaves

$$q_B = \frac{\varepsilon_s \rho f}{2w} u|u|^3 = ku|u|^3 \ , \ (2\text{-}4)$$

Note that in this formulation we have not included the downslope term as it has been previously disregarded in sediment transport studies in the swash zone [*Hughes et al.*, 1997 and *Masselink and Hughes*, 1998] and shown to be minimal in predictions of sand bar motion [*Thornton et al.*, 1996 and *Gallagher et al.*, 1998].

Since arguments given in the previous section suggested that sediment transport may depend on acceleration, a simple modification will be made to equation 2-4 to incorporate acceleration effects. Furthermore, since the Bailard model given here is time-dependent it is consistent to use an acceleration modification that may also be time dependent unlike the acceleration skewness proposed by *Drake and Calantoni* [2001] and *Elgar et al.* [2001] that are statistics derived from a velocity time series but cannot be used to investigate the phase-dependent nature of swash zone sediment transport.

The effect of fluid acceleration on sediment transport is not well understood, but thought to alter the force on the bed through strong horizontal pressure gradients [*Drake and Calantoni*, 2001 parameterized through fluid accelerations]. The total force on

sediment particles on the bed can, therefore, be recast to include parameterizations of drag and inertia forces (the latter containing acceleration). The drag force on a sand grain and that extrapolated to the bed are both given through a quadratic drag law. In a crude manner, we also assume the inertial forces on a sand grain can be similarly extrapolated to the bed yielding a combined force as

$$F = F_d + F_p = \frac{1}{2}\rho f|u|uA + \rho V k_m a \quad , (2\text{-}5)$$

where A is the bed surface area, V the volume, a the local fluid acceleration and k_m is a constant coefficient. The convective acceleration, normally included in the inertia force, has not, to our knowledge, been studied in the swash zone, but future work may show its importance. It is excluded in this formulation since field measurements were obtained from only a single location in the cross-shore (see section on field set up and data collection). Furthermore, particle inter-granular forces normally included in sediment transport models that operate at the particle scale are not included here. The intent is to use a simple approach guided by some physical justification to determine the form of the acceleration term for the "macro" scale affect of acceleration on sediment transport akin to the drag-law-driven energetics approach that is similarly focused on predicting bulk sediment transport rather than grain-to-grain interactions and individual particle motions. If one wishes, the acceleration modification in equation 2-5 can be viewed similarly to the pressure gradient force extension used in the *Drake and Calantoni* [2001] model but for instantaneous rather than time averaged transport predictions.

The total shear stress is then given by the total force per unit area of bed as

$$\tau = \frac{1}{2}\rho f|u|u + \rho k_m d a \quad , (2\text{-}6)$$

where upon division by the surface area, A, a vertical length scale, d, is needed. If the length scale is assumed to be constant, then the logical choice for the length scale when applied to a single grain is the grain diameter. It is not clear, however, that the grain diameter is the appropriate length scale in this formulation for shear stress and hence it should not be assumed that the inertia force is negligible when applied to the bed. Regardless, a constant length scale would become incorporated into the leading coefficient and would not need to be specified *a priori*. If on the other hand, one assumes that the acceleration in the swash zone is largely associated with the turbulent leading edge and bore [*Butt and Russell*, 1999] then a logical choice for the length scale would be the water depth since the turbulence is able to extend from the water surface to the bed [*Petti and Longo*, 2001 and *Cowen et al.*, 2003]. For the time being, the model will, for simplicity, include the length scale in the leading coefficient (assumes a constant value). Variations arising from using the time dependent water depth, however, are mentioned in the results section.

Using equation 2-6 for the bed shear stress, a new formulation for suspended sediment transport becomes

$$q_{pred} = k_b u|u|^3 + k_a |u|^2 a \quad . \text{(2-7)}$$

where subscripts b and a represent coefficients for the Bailard model and the added acceleration effect respectively. Throughout this chapter, equation 2-7 is referred to as the modified model. Transport relationships like equation 2-7 are often utilized in a time averaged form such that a transport rate is determined per swash cycle or for a length of time series. Time averaging erases all phase information. Here, we are interested in the

phase dependent nature of sediment transport throughout a swash cycle and will use ensemble averages of swash events instead.

Field Study

Data were collected at Gleneden Beach, OR in February 1994. This beach is intermediate to steep with a foreshore beach slope of roughly 1:12 and a median grain size of 0.44 mm. Complete details of the data collection, reduction and experimental setup are in *Puleo et al.* [2000]. Briefly, two ducted impellor current meters (initially 4 and 8 cm above bed), a pressure sensor (initially at bed level), and a fiber optic backscatter system (FOBS) to measure suspended sediment concentrations (penetrates the bed so that bed level and suspension concentration to within 1 cm of the bed can be obtained) were deployed at three locations on the foreshore separated by 5 m in the cross-shore direction.

Data used in our study were obtained from the most landward location on February 27, 1994 and were collected during a high tide cycle (data from the other two locations on this day were not utilized due to intermittent current meter difficulty). Only several centimeters of bed level change occurred over the course of the run at this location. While the original sampling rate was 16 Hz, data were subsequently block averaged to 4 Hz to reduce noise. A 4-minute time series on the rising tide is shown in Figure 2-3. Discontinuities in the η time series (Figure 2-3A) show that during this portion of the run, the sensors were intermittently immersed. The lower current meter velocity (Figure 2-3B) can be seen to increase rapidly (onshore is negative due to coordinate system), but as stated earlier, the increase is not always instantaneously to a maximum. At times the velocity reaches the current meter maximum threshold of (± 1.67 m s^{-1}).

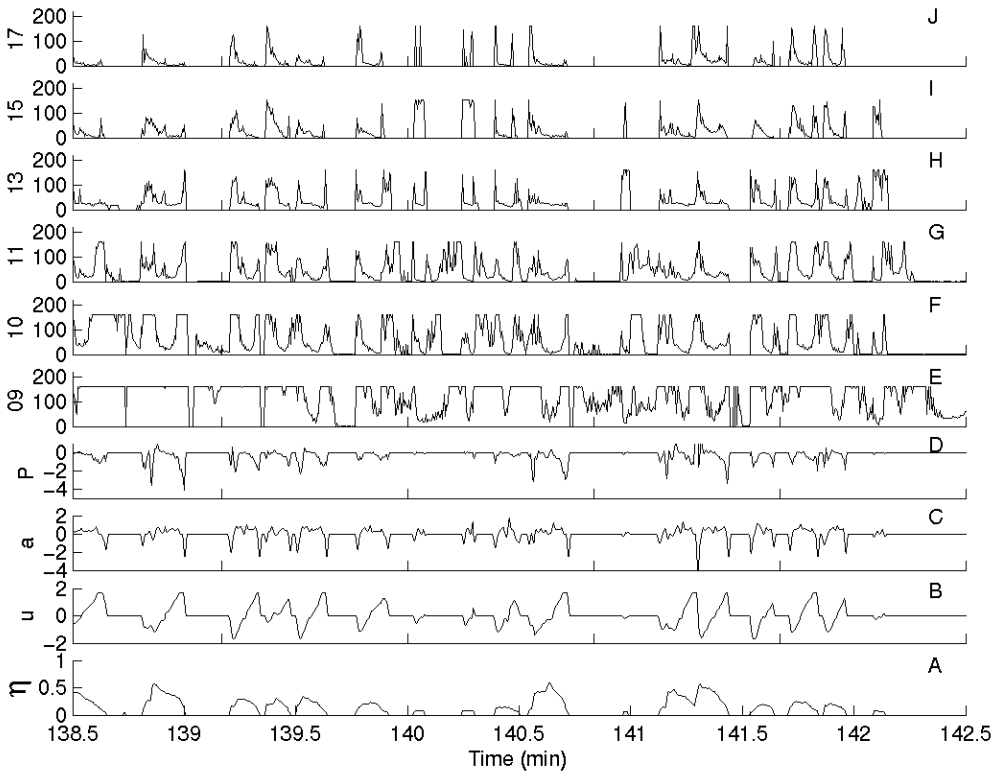

Figure 2-3. 4-minute swash time series. A) Sea surface (m). B) Swash zone fluid velocity (m s^{-1}) at 4 cm above the bed. C) Swash zone fluid acceleration (m s^{-2}). D) An estimate of the horizontal pressure gradient, P (m s^{-2}). E-J) Suspended sediment concentration output from FOBS (g l^{-1}). Number on y-axis is FOBS sensor number. The bed level is roughly at sensor 09 for this section of time series.

Swash events containing velocities beyond this artificial cutoff are excluded in all forthcoming analyses. The fluid acceleration, a (Figure 2-3C), was determined by a centered difference approximation using the measured velocity time series. Figure 2-3D shows that the estimate of the horizontal pressure gradient (using Taylor's hypothesis)

$$P = -g\frac{\partial \eta}{\partial x} = \frac{1}{u} g \frac{\partial \eta}{\partial t} \quad , (2\text{-}8)$$

is onshore during the entire swash event but strongest near the beginning of uprush and end of backwash. Equation 2-8 is only a rough estimate of the true horizontal pressure gradient because it inherently assumes that velocities are steady over the 0.5 s time period for which the value is calculated. This assumption may be violated at times in the swash zone where flows are expected to be highly variable. Taylor's hypothesis, however, has been used in previous swash studies [*Puleo et al.*, 2000] and for theoretical descriptions of bores and hydraulic jumps [*Johnson*, 1997]. Also, the use of the fluid velocity rather than wave celerity in equation 2-8 is more appropriate because within the swash zone, after bore collapse, the flow no longer represents a combined longitudinal/transverse wave or bore that would be observed further seaward. Hence, the concept of wave celerity for true swash flows is no longer applicable and the use of u is more appropriate.

The correspondence in Figures 2-3C and 2-3D imply that the fluid acceleration may also serve as a surrogate for the pressure gradient estimate. Suspension pulses tend to occur during sudden onshore-directed acceleration events as the swash reaches the sensors and during decelerating backwash. Individual suspension pulses (Figure 2-3E-2-3J) can be seen with the passing of each swash event. The suspension pulses extend at least 10 cm into the water column and likely higher for some swash events. The suspension data indicate that more sediment is generally carried as suspended load during

the uprush than during the backwash as evidenced by the often asymmetric suspension peaks.

Results

Suspended Sediment Transport Calculation

Dry mass suspended sediment loads, C, were calculated by taking the vertical integral of the suspended sediment concentration time series. The integral was carried to the water surface or to the highest FOBS sensor if the water elevation was above the highest sensor. Potential error does exist in this calculation since suspended sediment above the highest sensor is not included in addition to any noise from the measuring devices including signal saturation.

The measured instantaneous immersed weight sediment transport rate, q_{meas}, is determined from the calculated dry mass suspended load and fluid velocity as

$$q_{meas} = \frac{\rho_s - \rho}{\rho_s} guC \text{ , (2-9)}$$

where u is the lower current meter (used in all calculations), ρ_s and ρ are the sediment and fluid densities respectively. Since velocities are thought to be essentially depth uniform except for very close to the bed [*Petti and Longo*, 2001], then using a uniform velocity to calculate the suspended load transport rates will not introduce significant error into the calculation.

Ensemble-Averaged Swash Events

The velocity, acceleration, pressure gradient estimate, suspended load and sediment transport time series were separated into individual swash events based on zero crossings of the velocity record. Swash events with a current maximum less than the cutoff and durations greater than 4 s were retained for a total of 314 events. As

mentioned in, *Puleo et al.* [2000] the depiction of a swash events captured by the current meter at some distance above the bed misses the thin swash lens typically at the latter stage of backwash.

Individual swash events were linearly interpolated to a normalized (by the duration of each swash event) time grid, t_{norm} = 0 to 1 such that ensemble averages of the measurements could be determined (Figure 2-4). In Figure 2-4A the ensemble averaged velocity time series is roughly symmetric with maximum speeds of 0.91 m s^{-1} during uprush and 0.89 m s^{-1} during backwash. The grey lines represent the 5th and 95th percentiles of the individual events that were used for the ensemble average. The corresponding ensemble-averaged accelerations (even though the derivative process may amplifiy noise, we use $< a >=< \frac{\partial u}{\partial t} >$ rather than $< a >= \frac{\partial < u >}{\partial t}$; Figure 2-4B) show a handlebar shape similar to Figure 2-1, with a short lived onshore-directed acceleration during uprush and deceleration during backwash. The acceleration magnitude (~0.5 m s^{-2}) is about half that of downslope gravity (~0.82 m s^{-2}) for the rest of the ensemble average duration. Horizontal pressure gradient estimates are roughly symmetric and largest during times of strong onshore-directed acceleration and smallest when acceleration is offshore-directed (Figure 2-4C). The large spread in *P* during the beginning and end of the cycle likely results from the estimation method since the velocity (used in Taylor's hypothesis to convert a spatial gradient to a temporal gradient) can be either positive or negative.

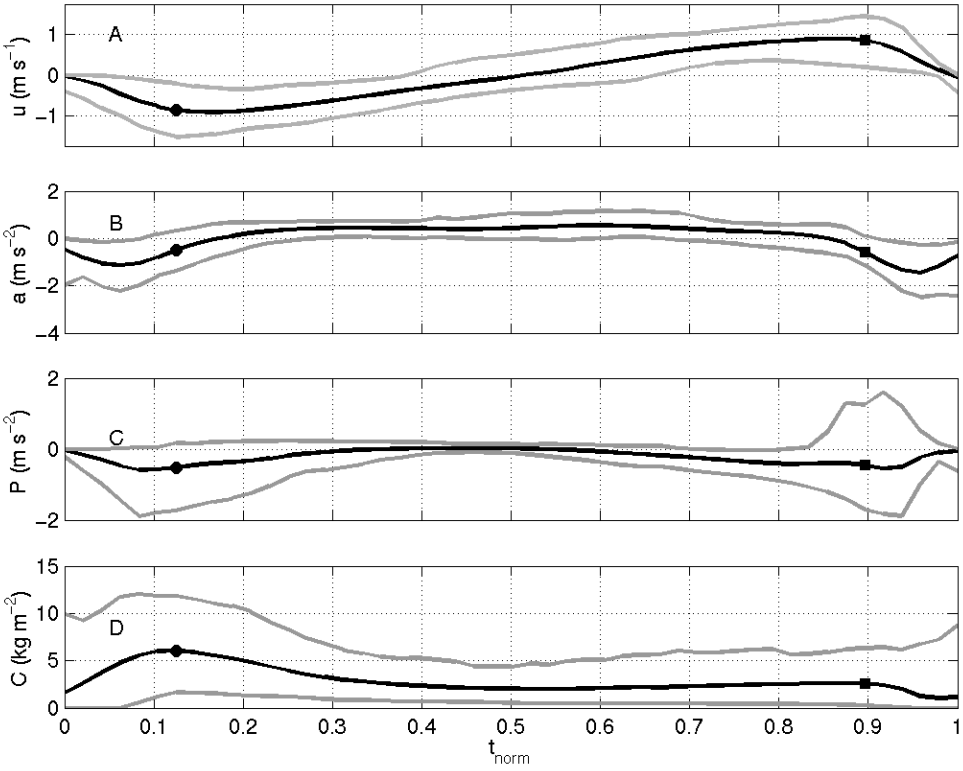

Figure 2-4. Ensemble average swash time (normalized) series; A) velocity, B) acceleration C) Horizontal pressure gradient estimate (P), and D) suspended load. Solid circles and squares denote timing of suspended load maxima for uprush and backwash respectively.

Unlike the velocity magnitude, acceleration, and pressure gradient time series, ensemble averaged suspended loads are asymmetric and indicate uprush suspended loads are typically twice that of backwash suspended loads (Figure 2-4C). Solid circles (squares) in Figure 2-4 indicate the timing of the uprush (backwash) suspended load maximum. During uprush, the suspended load maximum tends to lag the acceleration magnitude maximum by 0.06 (normalized time, e.g. for a 10 second swash event, by 0.6 s or ~22°) and slightly lead the velocity magnitude maximum (0.04 normalized time). Conversely, during backwash, the suspended load maximum leads the onshore-directed backwash acceleration maximum by 0.08 (normalized time) but does not lag or lead the backwash velocity maximum.

Suspended Sediment Observations

Suspended load measurements from the 314 un-normalized instantaneous swash events were interpolated to an equally spaced 0.2 m s^{-1} by 0.2 m s^{-2} velocity–acceleration grid using the technique described in *Plant et al.* [2002] to show the importance of fluid acceleration (Figure 2-5). Since onshore flow is negative in this coordinate system, the lower left quadrant (QA) represents onshore-directed uprush acceleration (The vertical axis was clipped at -2.5 m s^{-2} because the number of observations below this cutoff was sparse causing the interpolation to have errors larger than estimated values), the upper left (QB) represents uprush deceleration, the upper right (QC) corresponds to offshore-directed backwash acceleration, and the lower right (QD) corresponds to backwash deceleration (quadrants are separated by solid black lines). The symbols in the upper panel describe the mean swash velocity time series to assist the reader in interpreting the relationship between each quadrant and the phase of swash flow.

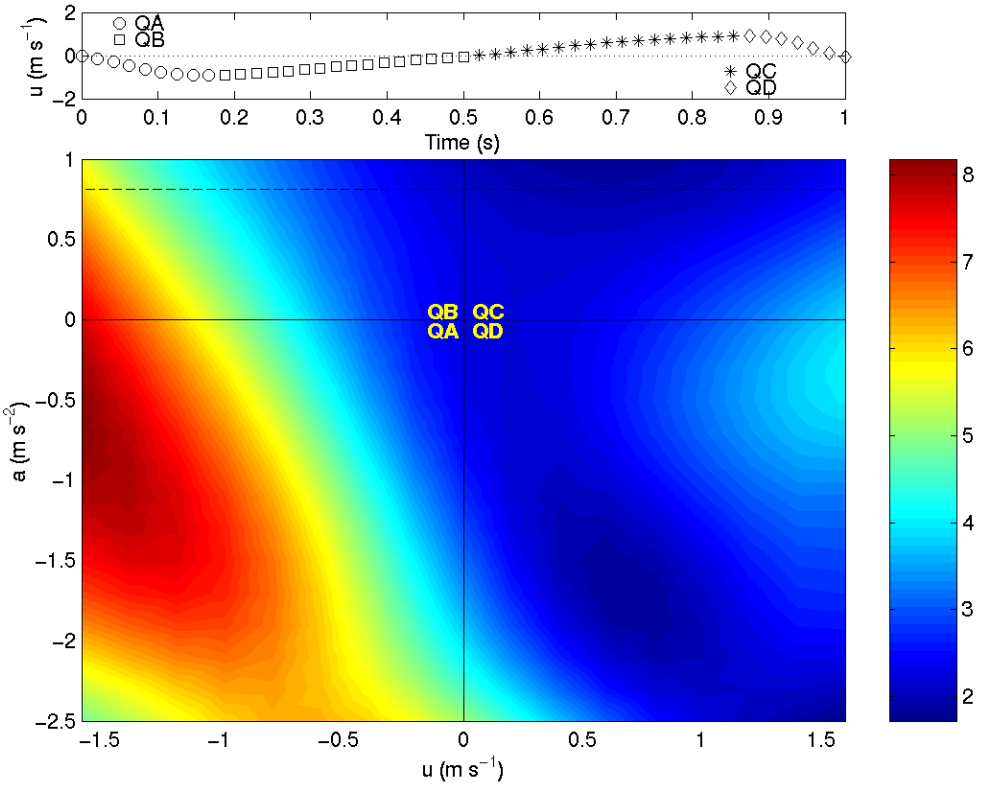

Figure 2-5. Interpolated suspended load (kg m^{-2}) as a function of velocity and acceleration. Dotted line is downslope gravitational acceleration and solid horizontal and vertical lines separate quadrants. Upper panel shows a velocity time history of an ensemble-averaged swash event with symbols corresponding to the 4 quadrants.

The plot shows that most of the high suspended sediment concentrations (over 7 kg m^{-2}) occur during uprush where high velocities and onshore-directed accelerations are largest. It is also clear, however, from the slopes of the color contours that for a given velocity the suspended load also increases as a function of *a*. In contrast, the backwash suspended loads are typically smaller at 1-3 kg m^{-2} and the largest suspended loads are confined to times when the backwash flow is decelerating.

Suspended Sediment Transport Predictions

Linear regression between ensemble averages of the measured suspended sediment transport rates and predictions was performed using

$$q_B = k_b \left\langle u|u|^3 \right\rangle + b_B \quad (2\text{-}10)$$

$$q_{pred} = k_b \left\langle u|u|^3 \right\rangle + k_a \left\langle |u|^2 a \right\rangle + b_{pred} \quad , (2\text{-}11)$$

where angle brackets denote ensemble averaging of the time stretched values and a constant term (bias) is added to maintain the definition of the squared correlation coefficient (the model is not forced through zero). It is necessary to calculate ensemble averages in this manner (e.g. $< u|u|^3 >$ rather than $< u > |< u >|^3$) due to the nonlinear nature of the velocity and acceleration products. Similarly, ensemble averages of the sediment transport rates utilized $< uC >$ rather than $< u >< C >$.

Suspended sediment transport rate predictions indicate that the modified model more accurately predicts the timing of the uprush suspended sediment transport maximum (Figure 2-6A). Both models predict essentially the same maximum suspended sediment transport rate during uprush, however, the Bailard model lags the modified model.

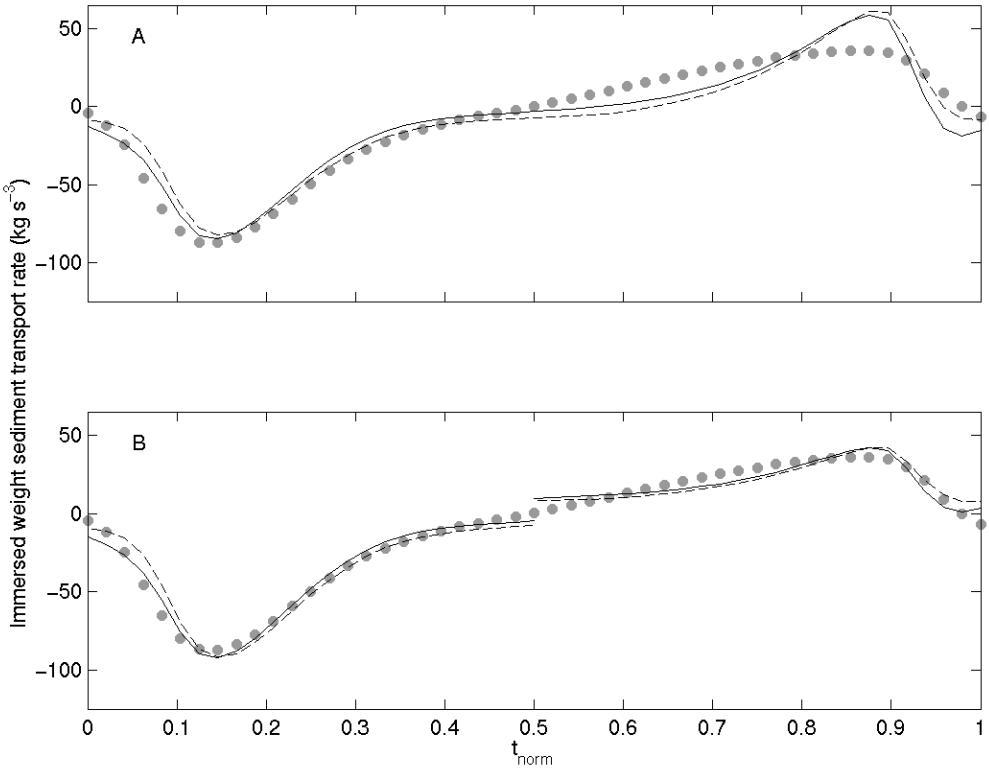

Figure 2-6. Suspended sediment transport rate measurements (circles) and predictions [dashed (q_B); solid (q_{pred})]. A) For the entire swash cycle. B) For uprush (negative values) and backwash (positive values) portions of the swash cycle fitted separately.

The modified model shifts the uprush peak to occur earlier in the swash cycle more closely matching the observations. The Bailard model and the modified model are nearly coincident throughout backwash and over predict the suspended sediment transport rate by about 30%. Net predicted transport rates are roughly -445 kg s^{-2} or approximately 0.03 m^3 per m beach width per swash cycle. A very rough estimate of the predicted elevation change per swash cycle can be obtained by dividing this value by the maximum distance the swash reached beyond the sensor. Using a value of 3 m leaves 0.01 m of accretion per swash cycle. Over many cycles this would suggest severe foreshore accretion that was not observed during our study [*Puleo et al.*, 2000]. It should be noted though, that this simple calculation incorporates only suspended load transport whereas the unmeasured bedload transport, specifically during the backwash, likely counterbalances the suspended load transport predicted during uprush.

Coefficients (Table 2-1) on the first term of the Bailard or modified model have the same value of 56.0. A typically used estimate of this coefficient based on values of 1025 kg m^{-3} for ρ, 0.01 for f, 0.01 for ε_s, and 0.065 m s^{-1} for the sediment fall velocity, w, is 0.79. This estimate is two orders of magnitude smaller than the coefficients determined from the regression and raises concerns about the "efficiency" concept in the B3 models (see discussion). The constant of -8.3 for both models shows that there is a slight bias. The fact that this bias is negative means that suspended sediment transport is not predicted to occur until the velocity moment and acceleration terms reach some threshold values, analogous to the threshold criterion in a Shield's stress formulation.

Table 2-1. Coefficients with 95% confidence intervals for linear regressions.

	q_B (Bailard, no acceleration terms)	q_{pred} (Bailard + acceleration terms)
k_b, b	56.0±5.4 , -8.3±3.4	56.0±4.7 , -8.3±3.0
k_a,	----	9.3±4.9
k_b, b uprush only	62.4±6.5 , -9.1±4.2	60.2±4.4 , -10.1±2.9
k_a, uprush only	----	9.7±3.7
k_b, b backwash only	27.8±6.5 , 7.8±3.8	29.4±5.8 , 7.0±3.4
k_a, backwash only	----	5.0±3.7

Although less desirable than calibrating coefficients for the entire swash cycle, the models can be split into uprush and backwash components allowing predictions and coefficients to be determined for each portion. Performing this decomposition causes the modified model to match the uprush observations both in magnitude and phase more closely (Figure 2-6B). During backwash, the Bailard model and modified model are again nearly coincident and match the backwash maximum more closely than in Figure 2-6A. Because the uprush and backwash are fit separately, there is a discontinuity in the predictions at $t_{norm} = 0.5$ for the models.

One to one comparisons between the measured suspended sediment transport rates and those predicted by the models show increased correlation when acceleration effect is included and when the models are decomposed into their uprush and backwash components (Figure 2-7). The R^2 value for the whole swash cycle increases from 0.90 to 0.93 for the Bailard, and modified model respectively (significant at the 99% level). In decomposing the swash cycle, the R^2 values for both the Bailard and modified model increase for the uprush portion but decrease for the backwash portion (Table 2-1). Because some studies have found that the energetics model using the velocity to third power had better predictive skill even for suspended sediment transport [*Butt et al.*, in press] we tested equation 2-10 using $< u|u|^2 >$ rather than $< u|u|^3 >$ and found the R^2 value increased by only a few percent depending on whether or not it was used for the entire swash event or for the uprush or backwash decompositions. This suggests that, at least for our study, the predictive capability using the energetics model was less sensitive to the power of the velocity component than including an acceleration term.

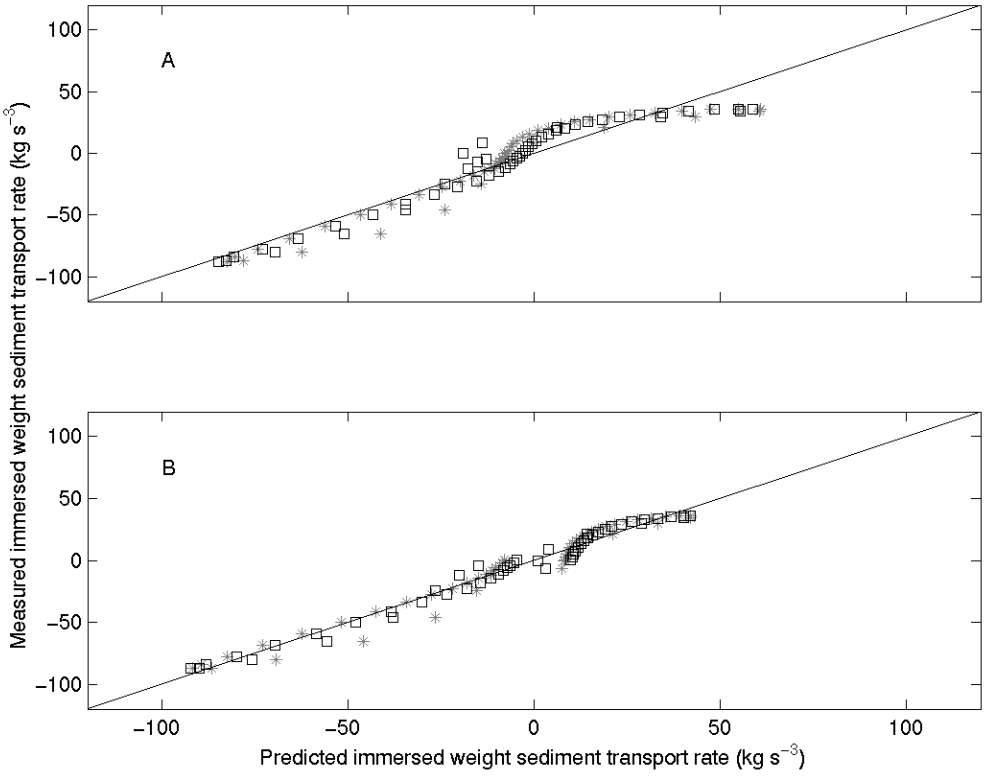

Figure 2-7. One to one comparison between measured suspended sediment transport rates and those predicted by the Bailard model (A) and the modified Bailard model including acceleration effects (B). Solid line denotes perfect correlation. Grey dots are for the entire cycle and black dots for values fit individually to the uprush and backwash components.

Root-mean-square errors between model predictions and observations show that the inclusion of the acceleration term reduces the overall error by 13%. When the ensembles are decomposed into uprush and backwash components, the error reduction becomes 35% for uprush and 14% for backwash (Table 2-2). The error reduction in the modified model is largely due to correcting the timing mismatch that exists between the Bailard model predictions and observations. Re-analysis using the time dependent water depth as the length scale rather than a constant value included in the regression coefficient, causes the k_a value to change but only slightly increases the correlation coefficient. Therefore, using a constant length scale did not adversely affect the predictive capability of the model.

Discussion

Typical swash events on this steep beach display acceleration time series that are not consistent with flows governed solely by gravity and friction. Strong onshore-directed uprush acceleration and backwash deceleration that are not included in typical sediment transport models likely affect sediment transport. As a result, the Bailard model based on fluid velocities was modified to include terms accounting for the fluid acceleration. The effect of fluid acceleration is normally assumed to produce delayed boundary layer growth and hence higher velocities near the bed than flows with weaker acceleration after the same duration of boundary layer development [*King*, 1991 and *Nielsen*, 1992]. In the swash zone, however, it is felt that the modification likely accounts for the disproportionate onshore-directed accelerations (as compared to backwash) observed in the shoreward propagating bore and swash front and the associated horizontal pressure gradients and not due to delayed boundary layer growth.

Table 2-2. Skill and prediction error for linear regressions.

	q_B (Bailard)	q_{pred} (Bailard + acceleration terms)
Skill (R^2)	0.90	0.93
Skill (R^2) uprush only	0.94	0.98
Skill (R^2) backwash only	0.77	0.84
Root-mean-square error (kg s^{-3})	11.5	10.0
Root-mean-square error (kg s^{-3}) uprush only	7.0	4.6
Root-mean-square error (kg s^{-3}) backwash only	6.2	5.3

Nielsen [2002] showed by theoretical arguments and field data that incorporating a phase shift in the shear stress term of a typical sediment transport model could account for the larger amount of sediment transport observed within the beginning of the uprush. *Puleo et al.* [2000] analyzed sediment transport in the swash zone bore (using this data set) and concluded that turbulent energy dissipation across the bore was a better descriptor for sediment transport across the bore than a bed shear type model. Combining the statements above suggests that the bore dissipation and fluid acceleration may be related. For instance, the bore dissipation observations from *Puleo et al.* [2000] are plotted against the fluid acceleration and show that the two fluid descriptors are related (Figure 2-8). While this figure does not prove that turbulent dissipation and acceleration are interchangeable, it does show that using the acceleration modification may account for the turbulent bore dissipation in a proxy form.

The rather high R^2 values observed in our study, even for the Bailard model, seem to contradict the findings by *Puleo et al.* [2000] using this same data set. In that study, it was found that the bed shear type model was typically a poorer predictor of observed sediment transport rates (maximum R^2 was 0.6), whereas our study showed that with or without an acceleration modification, the Bailard model more accurately predicted suspended sediment transport.

The difference between the two studies is important. The present study used ensemble averages of a set of swash events, so that the aim was to predict a time dependent sediment transport rate for an "average" swash event and determine the effect of fluid acceleration from a typical swash event on suspended sediment transport.

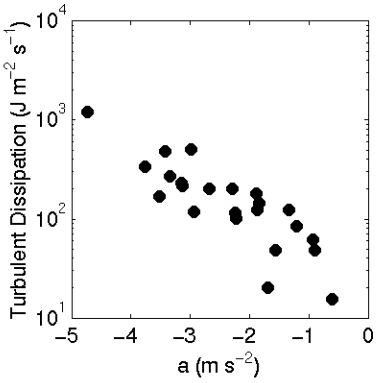

Figure 2-8. Turbulent bore dissipation from the bores in the *Puleo et al.* [2000] study as a function of fluid acceleration.

The prior study [*Puleo et al.*, 2000] analyzed the bed shear type model for instantaneous and time averaged transport which is different from ensemble averaging unless every swash event is nearly identical. Nevertheless, re-analysis of the data in the *Puleo et al.* [2000] study but using the acceleration term incorporated here slightly increased the R^2 value.

Since backwash flows are mostly controlled by gravity and friction, it would have been expected that offshore-directed accelerations would be important to backwash suspended sediment transport similar to onshore-directed uprush accelerations. It has been shown that long duration backwashes, presumably able to reach near gravity acceleration are effective at suspending and transporting sediment [*Butt and Russell*, 1999; *Puleo et al.*, 2000; *Holland and Puleo*, 2001 and *Butt et al.*, 2002]. The sensor location in the upper swash zone during our study meant that many of the observed swashes were of short (<8 s) duration implying that long duration backwashes were not observed and may have masked the importance of offshore-directed accelerating backwash. Accelerating backwash flow, however, is also thinning in its seaward retreat, and potentially hampers the acceleration effect on suspended sediment transport. Because the flow is thinning, there is less water column to suspend sediment and it is likely that during much of the backwash flow sediment is transported as bed load [*Horn and Mason*, 1994] or sheet flow. Hence, an offshore-directed acceleration (as opposed to deceleration) effect cannot be confirmed or contradicted with data from our study.

It was observed that decelerating backwash (Figure 2-5; QD) had larger sediment transport rates than did accelerating backwash (Figure 2-5; QC) at a given velocity. This implies that some mechanism is entraining more sediment during this latter portion of

backwash. When the backwash is decelerating, it must be acted upon by an adverse pressure gradient and to a lesser extent friction, since gravity is acting to accelerate the flow. The decelerating backwash often collides with the next uprush resulting in a hydraulic jump or backwash vortex that has been shown to be an effective suspending mechanism [*Matsunaga and Honji*, 1980 and *Butt et al.*, 2002] and may help explain the large values observed here. Also, *Hanes and Huntley* [1986] suggested that boundary layer separation during decelerating flow may be associated with sediment suspension.

Although the notions of hydraulic jumps and boundary layer separation could not be readily investigated with this data set, the suggestion by *Hanes and Huntley* [1986] that boundary layer separation may be associated with sediment suspension can be addressed through horizontal pressure gradients since boundary layer separation can occur under conditions of an adverse pressure gradient. It was shown that during decelerating backwash, when backwash suspended sediment transport was largest, the horizontal pressure gradient estimate was large and onshore-directed (Figure 2-4), consistent with the notion of an adverse pressure gradient. Other studies have also shown that strong horizontal pressure gradients at the bed are able to influence sediment transport [*Drake and Calantoni*, 2001]. Thus, it is felt that suspended sediment transport during decelerating backwash is likely enhanced by these mechanisms (hydraulic jump/backwash vortex, boundary layer separation and adverse pressure gradients), but warrants further investigation.

While the Bailard model had high R^2 values regardless of whether or not it was used for the entire swash cycle or for the uprush and backwash portion individually, several inadequacies may exist. First, the k_B coefficients were large and implied an

efficiency factor of about 0.7. Similar to previous studies [*Masselink and Hughes*, 1998; *Puleo et al.*, 2000 and *Drake and Calantoni*, 2001] the efficiency factor was predicted to be more than an order of magnitude larger than typically used values. So, it is likely that if the B3 type model is accepted for the swash zone, the efficiency factor for these highly turbulent, time-dependent flows must be necessarily larger than the originally proposed value for time averaged flows [*Bagnold*, 1963 and *Bagnold*, 1966], or it may suggest that the use of an efficiency factor in the sediment transport formulation is undesirable. Second, the B3 type model, assumes that instantaneous sediment transport rates are a function of instantaneous flow conditions. Because of this assumption, pre-suspended sediment advection (from the inner surf zone or the bore) is not accounted for. Unfortunately, in the swash zone, where hydraulic jumps and bore collapse appear to be dominant sediment suspending mechanisms, the exclusion of advected sediment and water column storage of sediment [*Kobayashi and Johnson*, 2001] should be expected to cause errors in the B3 approach. Studies by *Puleo et al.* [2000] and *Butt et al.* [in press] however, showed that sediment tends to settle out quickly behind the shoreward propagating bore such that the lack of pre-suspended sediment advection in the B3 type swash zone sediment transport model may not represent a significant source of error.

Conclusions

Suspended sediment concentrations and fluid velocities collected in the swash zone of a high energy, steep beach showed that high values of suspended sediment concentration (over 7 kg m^{-2}) were observed during times of rapid velocities, uprush acceleration and onshore directed pressure gradients during uprush associated with the shoreward propagating bore. Maximum suspended sediment concentrations reached 3 kg m^{-2} during backwash but occurred during decelerating flow, when the backwash is likely

slowed by adverse pressure gradients from the ensuing uprush. An energetics model for sediment transport was modified to include the effect of fluid acceleration and was able to reduce the root-mean-square prediction error by up to 35% over the energetics model without the modification suggesting that the inclusion of the acceleration term may account for the additional sediment transporting mechanisms during the unsteady flow conditions observed in the swash zone.

CHAPTER 3
COMPARISON OF OPTICAL AND RADAR MEASUREMENTS OF INNER SURF AND SWASH ZONE VELOCITY FIELDS

Introduction

The coastal ocean is a dynamic region where breaking waves and currents mobilize and transport sediments reshaping the underlying bathymetry and coastal morphology. These sediment processes in turn influence the wave and current patterns inducing a feedback mechanism. An understanding and predictive capability of these processes is necessary for engineering practices in coastal land use policy and erosion mitigation. Typical field studies involve the emplacement of several current meters or wave gauges. While it is known that nearshore fluid motions and wave fields are typically non-uniform in the alongshore direction (three-dimensional), cost and deployment logistics tend to force sparse cross-shore arrays. In order to increase the sampling region, remote sensing methods that are cost effective and can sample large spatial regions are required. Two such methods include radar and video-based imaging.

The use of video methods for nearshore processes research has gained increasing interest and acceptance in the scientific community [*Holman et al.*, 1993 and *Holland et al.*, 1997]. The thrust of video-based research has focused on describing the nearshore morphology such as sandbar migration [*Lippmann and Holman*, 1989 and *Lippmann and Holman*, 1990], beach configuration [*Holman et al.*, 1991; *Holland and Holman*, 1997], bathymetry estimation [*Stockdon and Holman*, 2000; *Dugan et al.*, 2001b] and wave information such as phase speed, period and direction [*Lippmann and Holman*, 1991;

Dugan et al., 1996 and *Dugan et al.*, 2001a]. Video data has also been used to estimate the mean alongshore current in the nearshore [*Chickadel and Holman*, 2001]. Comparisons with near-bottom-mounted current meters have shown high correlations, but these were restricted to mean flows rather than instantaneous motions. Video-based methods have also included the use of particle image velocimetry (PIV) which has been used to investigate the vertical flow structure under breaking and non-breaking waves [*Gray and Greated*, 1988; *She et al.*, 1997 and *Chang and Liu*, 1998] and the fluid motion over a rippled bed [*Earnshaw et al.*, 1994]. More recently, PIV has been used to extract instantaneous surface current velocities in the swash zone of a high energy beach [*Puleo and Holland*, 2000 and *Holland et al.*, 2001].

Similarly, microwave radar has been used extensively in remote sensing of the ocean surface. Airborne along-track interferometric synthetic aperture radar (InSAR) has been used to measure energy density spectra and to derive current estimates for the ocean surface in the nearshore region [*Marom et al.*, 1991 and *Shemer et al.*, 1993] and for current estimation in deeper water [*Graber et al.*, 1996]. From surface based radars, time series of radar intensity images have been used to produce frequency-wavenumber spectra using standard marine navigation radars [*Young et al.*, 1985 and *Wolf and Bell*, 2001] and attempts have been made to estimate surface currents from the sequences by measuring the deformation of the frequency-wavenumber dispersion relationship [*Frasier and McIntosh*, 1996 and *Senet et al.*, 2001]. However, in the surf and swash zones where the waves refract and shoal over varying bathymetry, these traditional techniques are suspect as they rely on a statistically homogeneous wave field. Other methods involving image analysis have also been used to obtain wave direction and celerity from marine

navigation intensity images [*Bell*, 1999]. However, standard marine navigation radars use horizontally polarized electromagnetic radiation to minimize sea clutter, which, for wave studies, is the desired signal. Horizontally polarized backscattered energy is also highly non-linear at low grazing angles making it difficult to directly relate intensity to the wave spectrum. In contrast, direct measurement of the Doppler shift due to line of sight velocities with a vertically polarized microwave Doppler radar provides a more direct method of estimating surface currents and directional wave spectrum [*Frasier et al.*, 1995; *Poulter et al.*, 1995; *Frasier and McIntosh*, 1996 and *McGregor et al.*, 1997]. This technique has also been used to measure the relationship between surface currents and subsurface current structure [*Moller et al.*, 1998] and to estimate bathymetry and wave energy fluxes and dissipation across an offshore bar [*McGregor et al.*, 1998] in water depths of several meters. Microwave Doppler radar techniques have occasionally been used inside the surf zone [*Ruessink et al.*, 2002], but only in relation to sand bar crest position.

The measurements presented in this paper were used to compare and interpret both PIV and microwave Doppler radar measurements of nearshore currents and waves. In this paper, we present observations of the nearshore region incorporating the surf and swash zones using both techniques. The following sections describe the field experiment, site layout and the principles of video and radar imaging. Next, we detail the methods used for extracting velocities from imagery. Velocity measurements, results and validation are then given followed by discussion and conclusions.

Field Experiment

Site Layout

A nearshore field experiment was conducted at Scripps Beach in La Jolla, CA from October 2 to October 10, 2000. The beach is situated south of the Scripps Canyon and north of the pier at the Scripps Institute of Oceanography. Scripps Beach is a shallow sloping (gradient ~ 1/50) fine sand beach. Semi-diurnal tidal range is about 1.5 m and wave heights are typically much smaller than 1 m. During the experiment, radar and video measurements overlapped for several 20-minute data segments between October 8 and October 10. A representative 20-minute segment of data collected on October 10th, when wave heights and wind speeds were sufficient for both techniques to be utilized, is presented. Specifically, the significant wave height (measured at the pier end) was roughly 1 m with a peak period of about 5 s (wave heights for the previous days were typically less than 0.5 meters). The wind speed averaged 4.5 m s-1 and was roughly onshore from 283° true North.

Two analog video cameras were fixed atop the Center for Coastal Studies (CCS) building overlooking the area of interest with a total coverage of about 100 m in the alongshore and 250 m in the cross-shore. The pixel footprint in the near field was roughly 0.1 x 0.1 m. The radar system was located on the roof just south of the camera location. The radar field of view (which significantly over lapped that of the cameras) covered a 30° azimuthal sector with a resolution of 0.5° and 384 m in range with a resolution of 3 m. Figure 3-1 shows the position of the footprints for each of the sensors. The alongshore coordinate increases to the north and the cross-shore coordinate in the offshore direction.

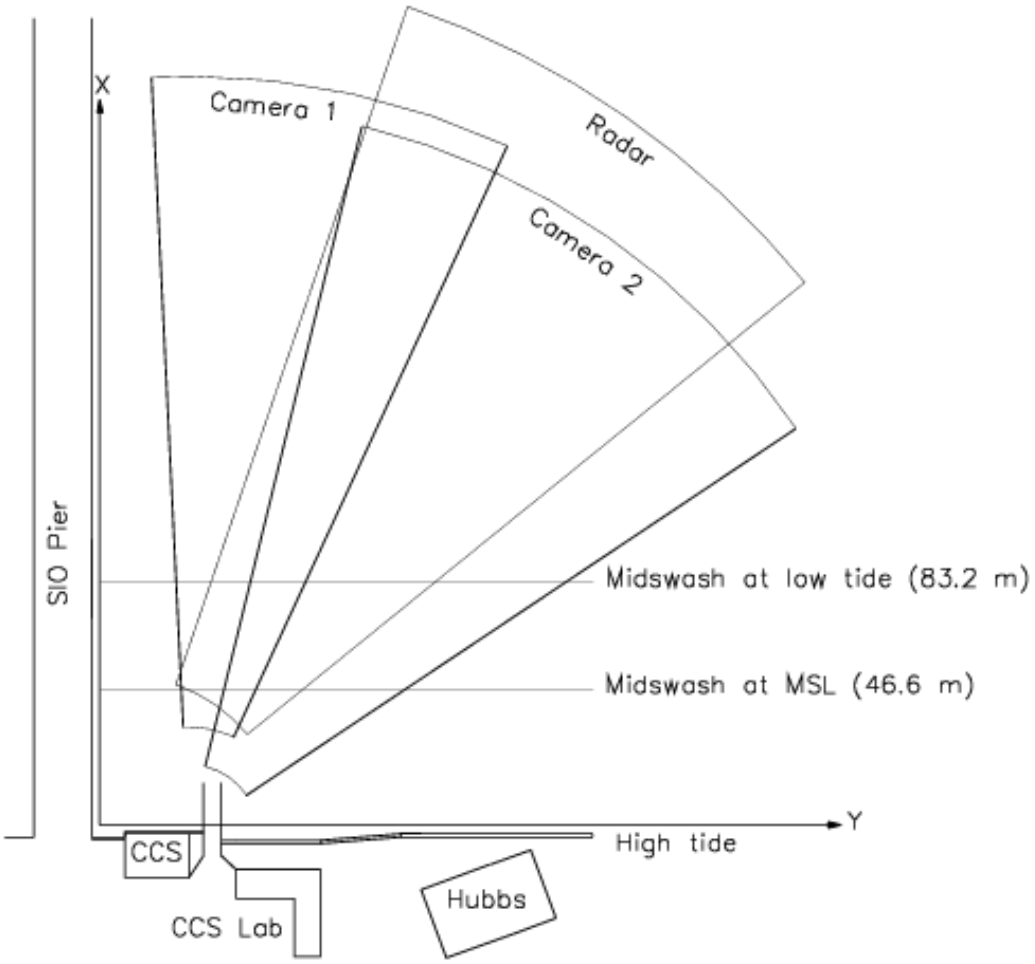

Figure 3-1. Schematic of Scripps Beach showing the imaging footprints for the two analog cameras and the radar system. The radar was positioned on top of the top left hand corner of the CCS building and the cameras on the top right hand corner.

Beach and offshore bathymetry surveys were obtained with a kinematic GPS system onboard a subaerial profiling pushcart or jet ski water craft.

Radar and Video Imagery

Figure 3-2A shows a relative backscattered power image collected from the radar system. The bright areas correspond to regions of high backscatter and the darker regions to areas of low backscatter. The dashed line is the radar centerline for which range-time comparisons will later be made. A corresponding geo-rectified camera snapshot image is shown in Figure 3-2B, where, for clarity, the portion of the image outside the radar field of view has been removed. Here, the dark regions correspond to areas with little wave breaking whereas the brighter region, especially between x = 100 to x = 120 m corresponds to the wave breaking and foam generation. The regions of breaking and high backscatter show a strong visual correlation giving confidence that the two methods are sampling similar features. Radar is also capable of observing unbroken waves as shown by the high backscatter intensity observed in the radar image near x = 140 m. Unbroken waves are not as readily discernible in the geo-rectified video image as only a weak increase in image intensity is observed near x = 140 m.

In Figure 3-3, two oblique video images separated by roughly 2 seconds are shown. The colored lines are the contours of backscattered radar power at 90 (blue) and 100 (red) dB. In both images, high backscattered power is recorded where the shoreward propagating bores are located as evidenced by the red contours overlaying the landward edges of the bright regions in the image.

In the image at 17:32:54.66, a wave is seen offshore that has an unbroken section. The backscattered power is higher at the broken sections and is less in the unbroken section where the wave is steepening.

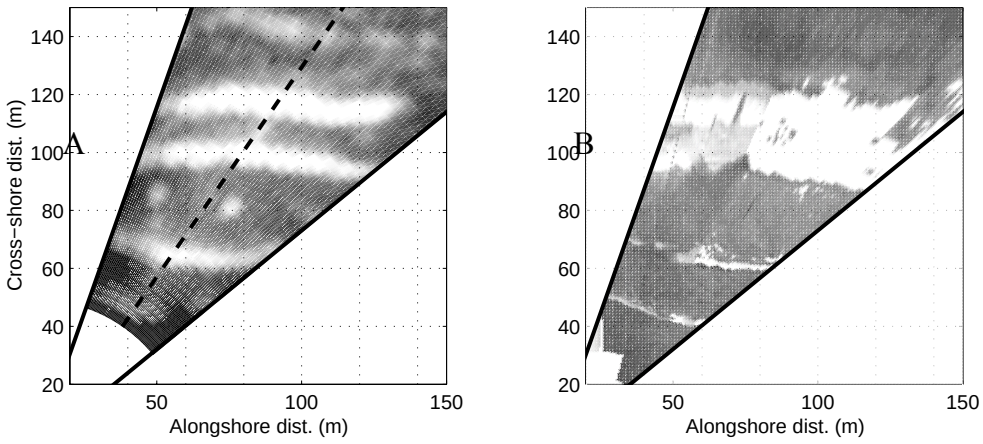

Figure 3-2 A) Radar snapshot of the backscattered power and the radial centerline (dashed). Solid lines demarcate radar field of view. B) Merged video snapshot from both analog cameras excluding the portion outside radar field of view.

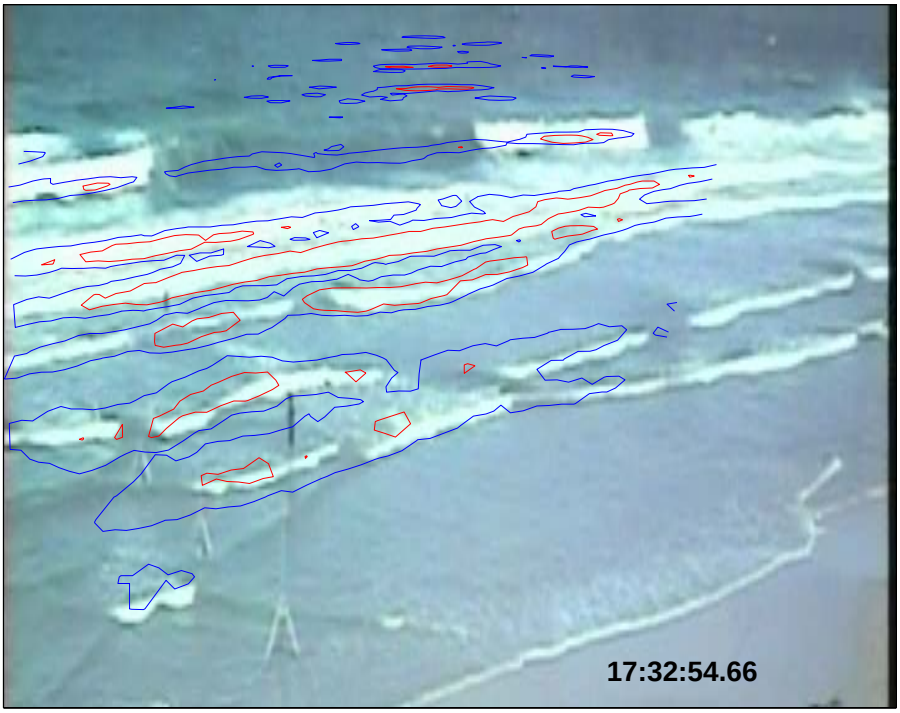

Figure 3-3. Oblique video images with backscattered radar power contour levels of 90 (blue) and 100 (red) dB superimposed. Wave height was not taken into account when overlaying the contour levels, causing some of the mis-registration. Image times are shown as hours:minutes:seconds in GMT.

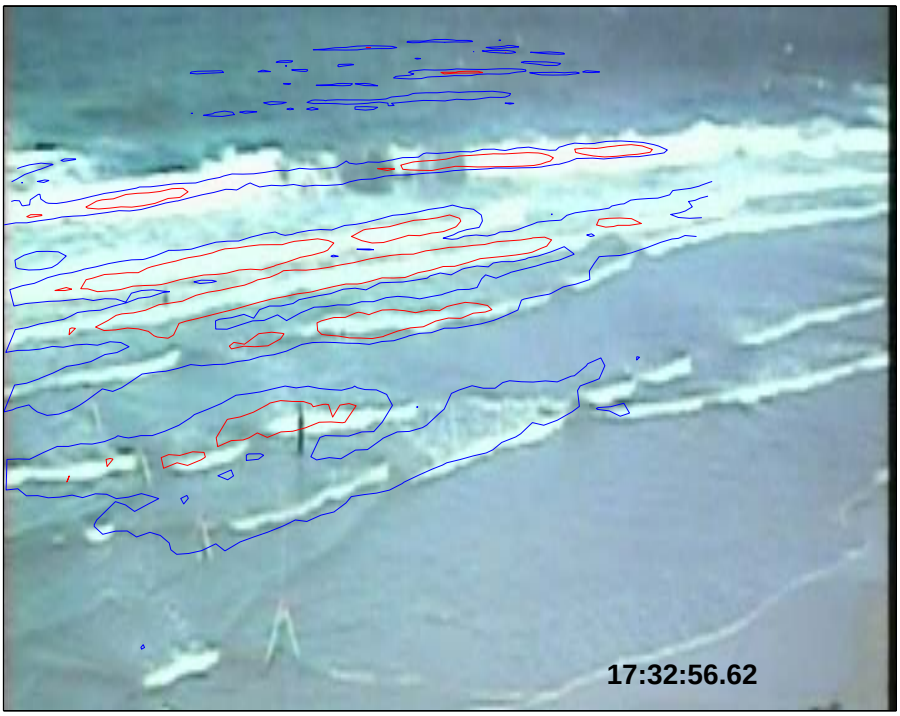

Figure 3-3. Continued.

In the second image at 17:32:56.62, where most of the wave has broken, the high power contours extend through a larger region of breaking and the 90 dB contour is more continuous across the wave front. Offshore of this wave there are still areas of high backscatter, but because of the obliquity of the image, individual waves are difficult to see in the video view at this distance. These images suggest that the radar system measures wave steepening and wave breaking that is simultaneously observed by the video system.

Further qualitative comparison between the two methods can be obtained using a range-time image (Figure 3-4). A range-time image is created by plotting the backscattered (or image) intensity along a single transect (the radial centerline in Figure 3-2) over time and is useful for tracking wave crest propagation across the surf zone. Further, since the data are in time-distance space, the slope of the features represents a component of the bore phase velocity which will be larger than the shoreward directed phase velocity of the bore. Individual waves can be seen as the brighter curved features. The patterns have curvature because the wave celerity decreases with decreasing water depth. The color bar represents the radar relative backscattered power (dB) or the dimensionless image intensity.

Although the patterns observed with the two methods are similar, individual waves are more readily visible in the radar range-time image because the backscatter is related to the bore elevation and slope of the water surface whereas for the video range-time image, the relation between pixel intensity and bore location depends on lighting angles and contrast changes in remnant surface foam, which causes the wave features to appear less distinct.

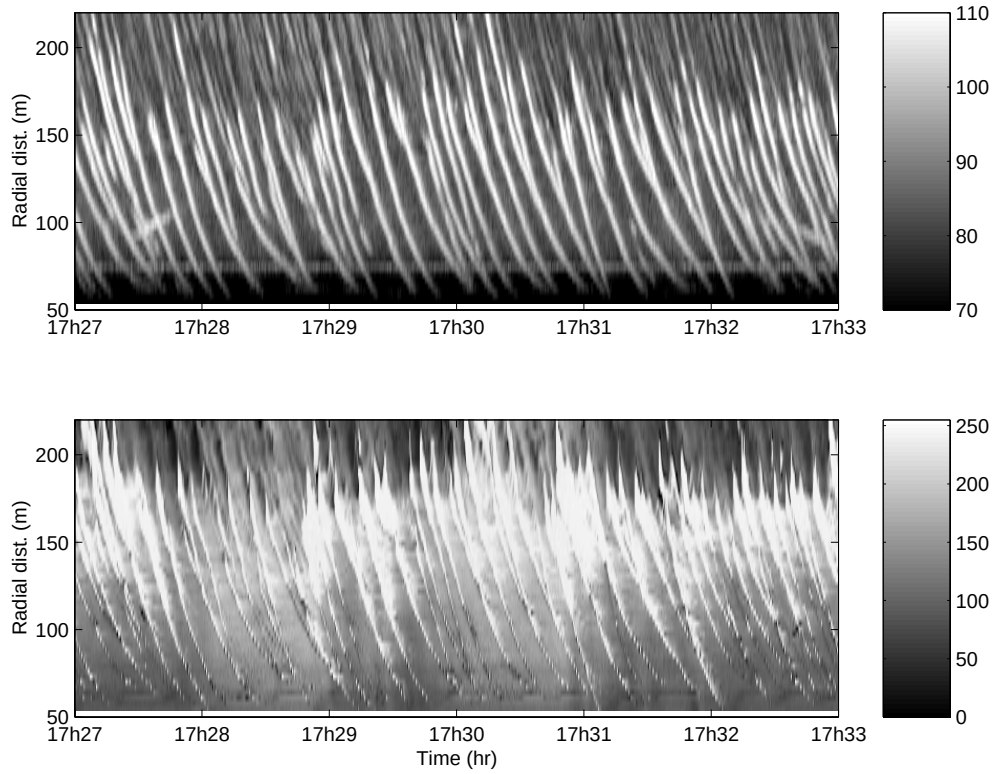

Figure 3-4. Range-time images for radar [top panel] and PIV [bottom panel] generated along the radial centerline of the radar footprint. The color bar represents the relative backscattered power (dB) for the radar and the scaled image intensity for the video image.

Both techniques, however, clearly record the same wave fronts and are able to capture wave interactions. An example of these wave interactions can be seen just prior to t = 17h32 (GMT) where two features merge due to a second wave front overtaking the preceding one. The breaking region is also captured in both images as evidence by the rapid change in intensity indicating wave breaking at a radial distance of approximately 175 m. The physical reason for a change in the video signal is obvious because the sea surface intensity actually changes from dark to light due to foam and bubble generation. The change in backscattered radar intensity is an increase in surface roughness to scales comparable to or larger than the electromagnetic wavelength. Although neither technique estimates wave amplitude directly, the comparisons between radar and video imagery suggest that these remote sensing techniques image similar surface features, such as wave crests, in the nearshore region.

Methods of Velocity Extraction

Radar

The radar used in our study is the Focused Phased Array Imaging Radar (FOPAIR) [*McIntosh et al.*, 1995], a dual-polarized X-band (10 GHz) Doppler radar designed to image the sea surface with meter scale spatial resolution. The radar uses a linear receive array and digital beamforming techniques to obtain azimuth resolution of 0.5°, and pulse compression to achieve range resolution of 3 m. The radar is capable of both vertical and horizontal polarization measurements. However, only vertically polarized measurements are considered in here.

At incidence angles sufficiently removed from nadir, the microwave (> 1 GHz) reflectivity of the ocean waves with small surface slopes compared to the electromagnetic wavelength, is dominated by resonant interaction between the incident electromagnetic

waves and small capillary and capillary-gravity waves (Bragg scattering) [*Wright*, 1968]. Contrast in microwave radar images is obtained through the modulation of this mean reflectivity through tilting of the local incidence angle (tilt modulation) and straining and compressing of the shorter waves (hydrodynamic modulation). Surface fluid velocities are measured from the line of sight Doppler shift due to the wave velocity. In the Bragg scattering model the velocity measured by the radar is comprised of the phase velocity of the resonant capillary waves superimposed on any surface current that might be present. When the spatial resolution of the radar is sufficient to resolve long wave features such as gravity waves, the velocity measurement also includes the radial component of the instantaneous orbital velocity of the longer waves in addition to the capillary wave velocity.

The Doppler shift in the received electromagnetic wave is estimated by the FOPAIR system through a covariance or "pulse pair" technique applied to successive radar images. The pulse pair calculation is an estimation of the first moment of the Doppler spectrum [*Miller and Rochwarger*, 1972]. The radar forms an image of the ocean surface over a period of approximately 0.64 ms, which is well within the decorrelation time for microwave backscatter at X-band [*Plant et al.*, 1994]. A second image is captured about τ = 1.5 ms later and the covariance $C(t,\tau)$ of the images is formed. The covariances for several image pairs are averaged over a period of 0.5 seconds to obtain Doppler radar velocity estimates using

$$v(t) = \frac{\lambda}{2\pi} \frac{\phi(t)}{2\tau \sin\theta_i} \quad (3\text{-}1)$$

where λ is the wavelength of the transmitted electromagnetic wave, θ_i is the angle of incidence from the antenna to the ocean surface. The argument of the covariance

function, $\varphi(t)$, is the phase difference of the radar return between successive radar pulses and is proportional to the change in distance that the scattering feature has moved over the time period τ.

Particle Image Velocimetry

In a similar way to radar, PIV uses correlation of image pairs to measure wave propagation. However, rather than electromagnetic backscatter, the image intensity represents a combination of brightness changes due to wave breaking and changes resulting from light reflection off the slope of the water surface relative to the sun angle as viewed from the camera. The assumption is that the motion of the image texture (tracer) created by spatial variations in the image intensity travels at the flow velocity. Somewhat analogous to the radar system's dependence on a sloped surface (capillary or gravity waves), difficulties for PIV result when insufficient texture is recorded by the imagery.

The PIV technique used is fully described in [*Holland et al.*, 2001] and only a brief description will be given here. Two images separated in time by Δt are digitized from time sequence imagery and geo-rectified to a common ground plane [*Holland et al.*, 1997]. A small interrogation window, I, is selected about the grid point in the first image and compared to many search windows, S, of the same size in the second image. Comparisons are made using an error correlation function, Φ, [*Hart*, 1998],

$$\Phi_{\Delta x,\Delta y} = 1 - \frac{\sum_{1}^{a}\sum_{1}^{b}\left(|I - S|\right)}{\sum_{1}^{a}\sum_{1}^{b}\left(I + S\right)}, \quad (3\text{-}2)$$

where a and b are the dimensions of I and Δx and Δy are the spatial offsets.

The peak in the correlation matrix is fitted with a 2D Gaussian shape to yield the horizontal offsets to sub-pixel accuracy. When these offsets are divided by the image separation time, 2D surface velocity vectors are obtained. As with most PIV approaches, post-processing is applied to the velocity field to remove spurious vectors [*Holland et al.* 2001].

Results

Radar-PIV comparisons

PIV and radar velocities were collected between 17:19 and 17:39 (GMT) from several locations across the surf zone at cross-shore positions x = 50, 60, 70, 75, 80, 90, and 100 m from the shoreline. The PIV data were collected at 3.5 Hz and the radar data at roughly 2 Hz. The radar Doppler velocities were subsequently linearly interpolated to the same 3.5 Hz sampling times as the PIV data. The velocity component in the direction of the radar line of sight was computed from the PIV velocity vectors through a coordinate system rotation. As a consequence of the coordinate system, negative velocities are directed toward the radar system and positive velocities away from the radar system. Six minutes of the time series are shown in Figure 3-5. The gray lines are radar and the black lines are PIV with each successive pair of time series offset by 5 m s^{-1}. The time series show the maximum radial velocities increasing in the offshore direction and ranging from about -3.5 to -5 m s^{-1}. In both cases, the velocities generally do not become positive, thus indicating movement away from the sensor is infrequently measured. At all cross-shore locations except at x = 50 and x = 100 m the time series are well correlated (Table 3-1) and indicate that peak radar and PIV velocities are nearly equal. The highest correlations (all are significant at the 95% level) are observed between x = 60 and x = 90 m with a decrease in correlation for the swash zone and

offshore positions. When high frequency noise (> 0.25 Hz) was excluded from the calculation of the correlation coefficient, the R^2 values increased slightly (Table 3-1).

Mean PIV velocities calculated from the 7 locations, however, show that mean radar velocity magnitudes are consistently larger than PIV velocity magnitudes (Table 3-2). Mean PIV velocities range from -0.55 to -0.79 m s^{-1} but tend to cluster near -0.75 m s^{-1} (except x = 50 m and x = 100 m) while mean radar velocity magnitudes range between –1.07 to –1.94 m s^{-1}. In all cases PIV standard deviations are roughly equal to the mean PIV velocities indicating the scatter in the data is as large as the velocity estimate whereas radar velocity standard deviations show an increase with offshore distance and are larger than PIV standard deviations.

A measure of the difference between the time series can be determined by,

$$E_{\alpha,\gamma} = \frac{\langle \gamma - \alpha \rangle}{|\langle \gamma \rangle|} \pm \frac{\sigma_{\gamma-\alpha}}{|\langle \gamma \rangle|} \quad , (3\text{-}3)$$

where α,γ are the time series of interest, here PIV and radar respectively, σ is the standard deviation, angle brackets denote averaging and | | denote magnitude. $E\alpha,\gamma$ is a measure of the normalized mean difference and the spread about that mean given by the normalized standard deviation. In a similar way to mean radar Doppler and mean PIV velocities, $E_{PIV,\ Doppler}$ (Table 3-2) tends to increase in the offshore direction and the scatter is nearly as large as the mean difference itself. Note that $E\alpha,\gamma$ can be thought of as a normalized relative error if it is assumed that the variable γ represents the true value.

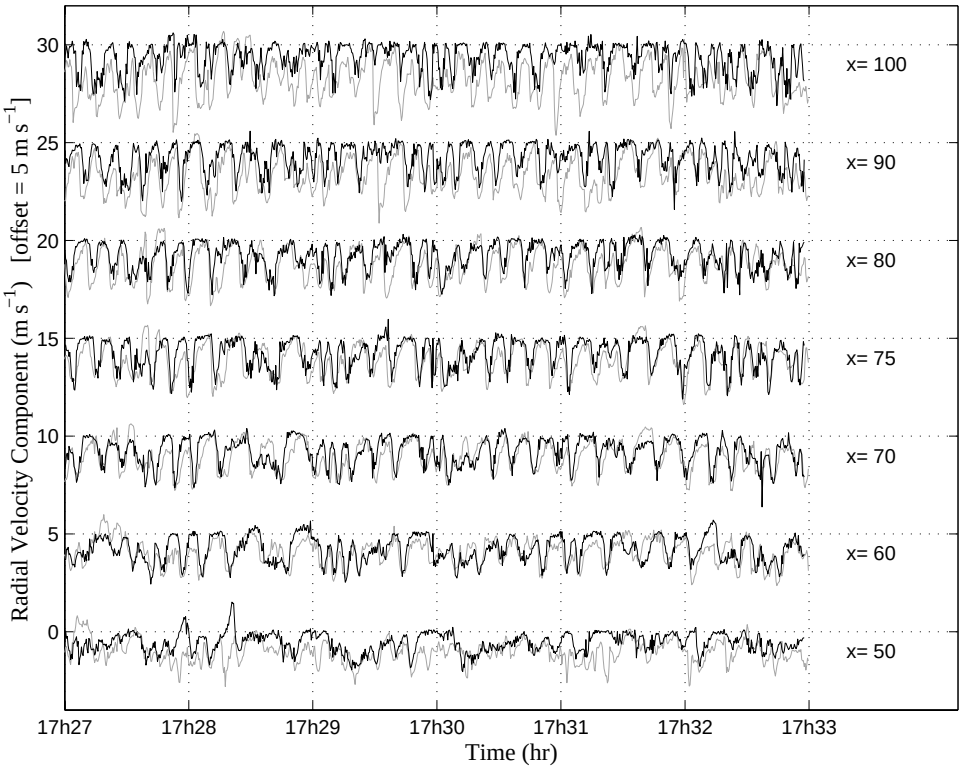

Figure 3-5. Radial velocity time series comparison between radar (gray) and PIV (black) at seven cross-shore locations. Successive time series are vertically offset by 5 m s^{-1}.

Table 3-1. PIV/radar time series correlation

Cross-shore location	R^2 correlation coefficient	R^2 correlation coefficient (after filtering)
x = 50	0.15	0.18
x = 60	0.38	0.43
x = 70	0.48	0.56
x = 75	0.43	0.52
x = 80	0.48	0.59
x = 90	0.46	0.60
x = 100	0.27	0.37

Table 3-2. PIV/radar time series statistics

Cross-shore location (radial distance from radar) (m)	PIV mean ± 1 std (m s^{-1})	Doppler radar mean ± 1 std (m s^{-1})	$E_{PIV,Doppler}$
x =50 (83.9)	-0.55 ± 0.51	-1.07 ± 0.58	-0.49 ± 0.56
x =60 (89.0)	-0.73 ± 0.70	-1.00 ± 0.68	-0.27 ± 0.61
x =70 (95.7)	-0.78 ± 0.72	-1.14 ± 0.81	-0.33 ± 0.53
x =75 (99.2)	-0.79 ± 0.77	-1.23 ± 0.87	-0.36 ± 0.56
x =80 (103.9)	-0.78 ± 0.72	-1.31 ± 0.91	-0.41 ± 0.51
x =90 (110.6)	-0.79 ± 0.74	-1.69 ± 0.98	-0.54 ± 0.43
x =100 (124.6)	-0.70 ± 0.75	-1.94 ± 1.04	-0.65 ± 0.47

Histograms were computed to show similarities and differences in the distribution of surface velocities from the PIV and radar techniques (Figure 3-6). The histograms indicate that both radar and PIV sampled predominantly onshore (negative) velocities with magnitudes increasing with offshore location and showing some variability across the surf zone. At x = 50 m (swash zone) the velocity histograms are shifted with the radar displaying a Gaussian-type shape. From x = 60 to x = 80 m (inner surf zone), the histograms have more similar shapes although PIV tends to be more negatively skewed than the radar and a bimodal structure in the radar histograms becomes apparent. The radar peak near –2 m s^{-1} increases with offshore distance while the peak near zero velocity decreases. In contrast, the PIV peak near zero velocities increases in the offshore direction causing the difference between the peaks of the histograms to increase as well. At x = 90 and x = 100 m (shoaling or breaking region) the radar does not show a clear peak near zero velocity and instead has a broad peak near -3.25 m s-*1*. However, PIV still shows a strong peak near zero velocity.

Velocity difference histograms (Figure 3-7) show that the radar velocity magnitudes are generally larger than those measured by PIV. They also display a trend of increasing difference in the offshore direction (with the exception of the swash zone [x = 50 m]). Hence, radar and PIV velocities are most similar in inner surf zone and differ more throughout the mid surf zone to the breaking region (Table 3-2). Standard deviations of the differences range between 0.60 and 0.73 m s^{-1} except at x = 100 m, where the value is 0.91 m s^{-1}.

In a spectral sense, the velocity signals are also similar. Example energy spectra for x = 70 m are shown in Figure 3-8A for PIV (solid) and radar (dashed).

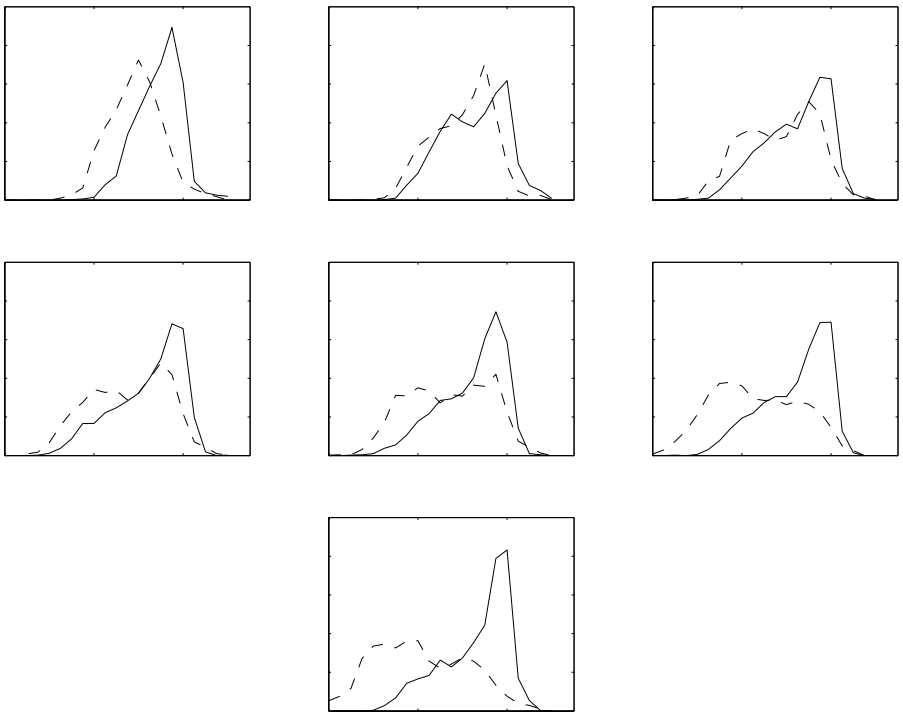

Figure 3-6. PIV (solid) and radar (dashed) velocity histograms for the seven cross-shore locations. Axis labels for lower panel apply to all panels.

Spectra were calculated using a Kaiser-Bessel window on each of 512 ensembles with 50% overlap and band averaged over two adjacent frequency bands. Both plots show a broad spectral peak near 0.071 s^{-1} (~14 s), which is more than double the incident peak period measured at the pier end. Spectral estimates are similar until about $f = 0.7$ s^{-1} when the curves diverge. The squared coherence is shown in Figure 3-8B along with the 95% confidence level (dotted). Over 80% of the spectral energy is contained under the spectral peak from f = 0.02 to 0.25 s^{-1}. The squared coherence is significant at the 95% confidence level in this frequency range with values approaching 0.85 and rapidly decays above incident wave frequencies of 0.25 s^{-1}. Phase estimates with 95% confidence limits span zero phase throughout the region of high coherence (Figure 3-8C). Note that phases are only shown when the coherence exceeds the 95% confidence limit. This analysis indicates that the time series are nearly in phase in low frequency to incident band. Spectra for the other cross-shore locations are similar to the one shown here except at x = 50 and x = 100 m. At x = 50 m the broad spectral peak occurs near $f = 0.03$ s^{-1} (not shown). A broad region of coherence is not observed at this location with the squared coherence being significant at just several frequencies, reiterating the dissimilarity between the time series in the swash zone. At x = 100 m, the spectral peak is near f = 0.085 s^{-1} and the region of high squared coherence is narrower extending from $f = 0.03$ to 0.12 s^{-1} (not shown).

Validation

The range-time image (Figure 3-4) can be used to estimate the radial component of the bore propagation velocities in the surf zone and can be compared with corresponding velocities measured by the radar Doppler and PIV.

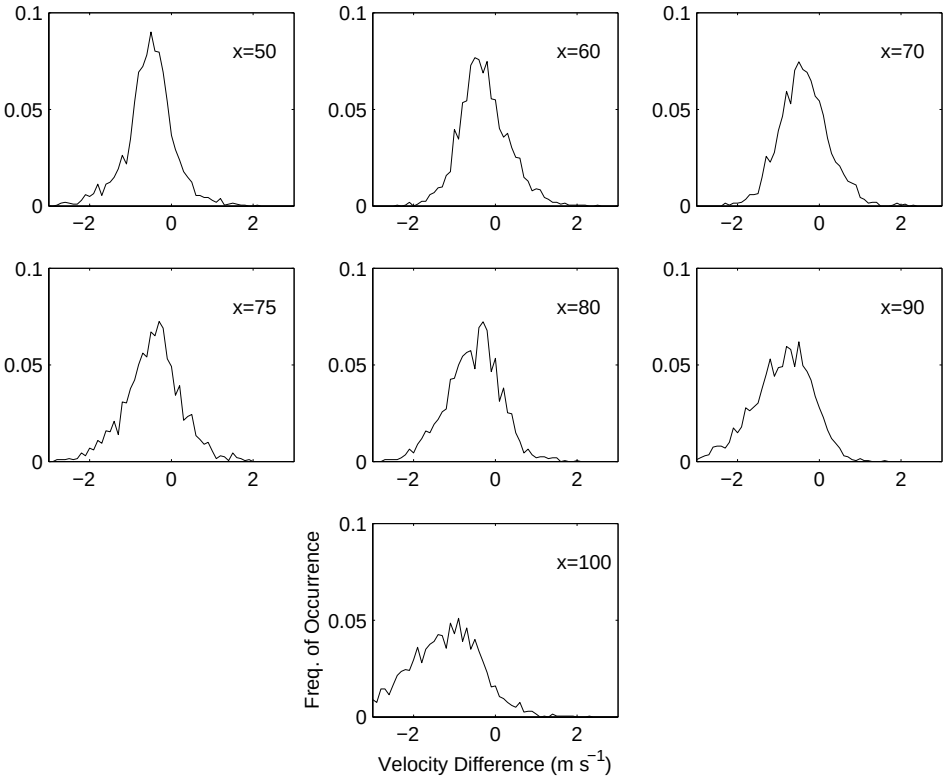

Figure 3-7. Histograms of velocity differences between radar and PIV for the seven cross-shore locations. Axis labels for lower panel apply to all panels.

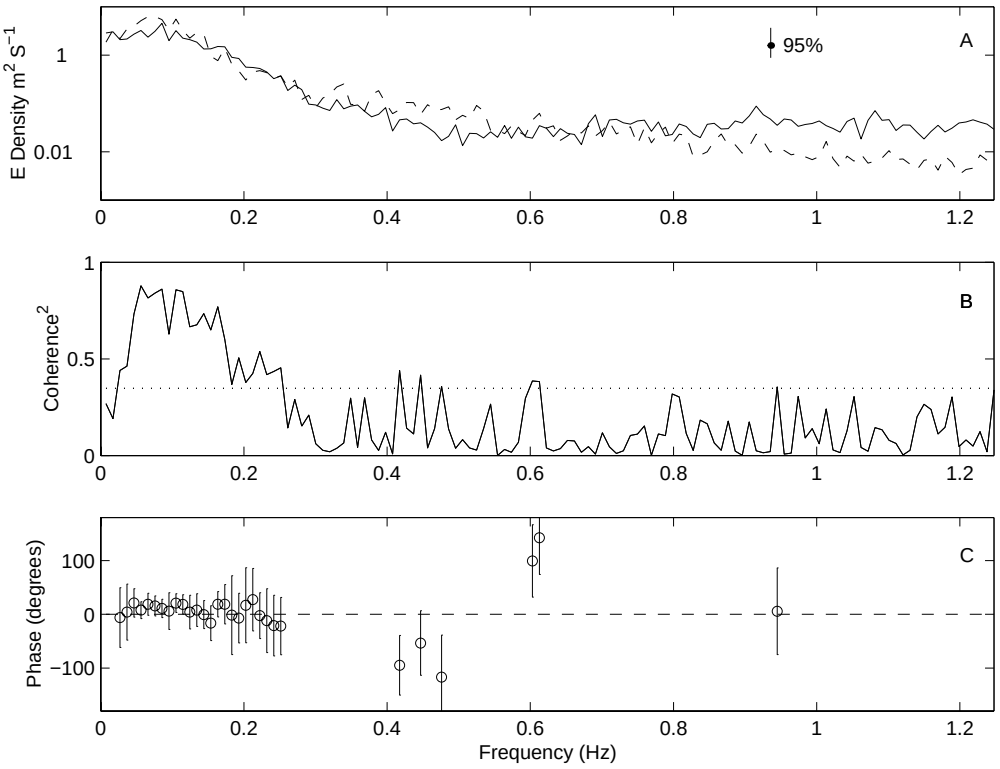

Figure 3-8. A) Auto-spectra of time series collected at x = 70 and y = 60 for radar (dashed) and PIV (solid). 95% confidence bar is also shown. B) Squared coherence values (solid) and 95% confidence level (dotted). C) Phase between the time series with 95% error bars. Note: phases only shown for significant coherence squared.

Although the range-time images are created from data collected by the same remote sensing systems, the manner in which velocities are extracted (slope of trajectory) is different from either the PIV or "pulse pair" radar technique and serves as an independent bore celerity estimate. However, since the range-time data yields only bore celerity information, these data cannot be used to validate the surface velocities between bores.

For comparison, thirty-nine representative bore trajectories determined from the bright curves in the radar range-time data were selected where the bore signature was clearly visible from a radial distance of 75 to 125 m and where shoreward propagating bores did not capture and overtake one another (where bright curves in Figure 3-4 do not coalesce). The bore trajectories were then fit with a 2nd order polynomial and the radial bore velocity was calculated for each radial distance corresponding to the 7 cross-shore locations by taking the derivative of the polynomial, evaluating at each location and accounting for the oblique direction of the radial centerline over which the radar range time-image was created (Table 3-3). The mean range-time derived bore celerities obtained from the polynomial fits decrease (in magnitude) in the landward direction from about –3.4 m s^{-1} to -1.4 m s^{-1} (Table 3-3). PIV and Doppler velocities corresponding to the range-time derived bore celerities at the same cross-shore distance are also given in Table 3-3 (these values differ from those in Table 3-2 since only PIV and Doppler velocities corresponding to the range-time derived bore celerities, rather than the whole time series, are used). In a similar way to the mean range-time bore celerities, the corresponding Doppler velocities tend to decrease (in magnitude) in the landward direction as does PIV except at the offshore location. However, the normalized mean relative error between range-time bore celerities and PIV varied between 1 to 26%

whereas the normalized mean relative error between range-time bore celerities and Doppler varied between 25 to 43%.

PIV and Doppler bore celerities can be further validated by comparison to a shallow water wave dispersion relationship. Dispersion relationships have been previously used to infer the water depth using measurements of wave celerity [*Holland*, 2001]. In this case, however, we estimate bore celerities from measured water depths.

The shallow water dispersion relationship used here accounts for finite amplitude effects and has the form

$$c = \sqrt{g(h+H)} = \sqrt{1+\gamma_H}\sqrt{gh} \quad (3\text{-}4)$$

where c is the theoretical bore celerity, h is the water depth (obtained from bathymetry surveys), H is the wave height, γ_H is a coefficient relating wave height to water depth and g is gravitational acceleration. The constant γ_H was set to a value of 0.5, roughly the value found by *Raubenheimer et al.* [1996] for this beach and similar wave conditions (although choice of other appropriate values for γ_H has little effect on overall trends). For comparison (Figure 3-9), radial Doppler and PIV bore celerities were geometrically transformed to lie along the radial center line. The radial component of the theoretical bore celerity was obtained by assuming shore normal waves. Note again, that celerities are negative due to the coordinate system used in our study. Results indicate that the radar range-time bore celerity estimates (solid dots with 1 standard deviation error bar) closely match those of the shallow water model (solid line) corroborating our use of these estimates as one form of validation (Figure 3-9A). PIV estimates of bore celerities closely match the shallow water dispersion relationship (Figure 3-9B) with normalized relative errors of about 15% excluding the location at x = 100 m.

Table 3-3. Bore celerity statistics for radial range-time, PIV and Doppler bore celerities.

Cross-shore location (radial distance from radar) (m)	Range-time mean ± 1 std (m s^{-1})	PIV mean ± 1 std (m s^{-1})	Doppler mean ± 1 std (m s^{-1})	$E_{PIV, range-time}$	$E_{Doppler, range-time}$
X=50 (83.9)	-1.37 ± 0.36	-1.39 ± 0.45	-1.97 ± 0.47	0.01 ± 0.36	0.43 ± 0.33
X=60 (89.0)	-1.65 ± 0.31	-3.08 ± 0.39	-3.08 ± 0.49	0.26 ± 0.28	0.26 ± 0.32
X=70 (95.7)	-1.88 ± 0.31	-3.14 ± 0.32	-3.35 ± 0.43	0.14 ± 0.19	0.25 ± 0.24
X=75 (99.2)	-1.98 ± 0.32	-3.31 ± 0.35	-3.50 ± 0.39	0.17 ± 0.20	0.27 ± 0.22
x=80 (103.9)	-3.08 ± 0.33	-3.16 ± 0.40	-3.72 ± 0.40	0.04 ± 0.23	0.31 ± 0.22
x=90 (110.6)	-3.26 ± 0.35	-3.16 ± 0.47	-3.00 ± 0.45	-0.04 ± 0.25	0.33 ± 0.17
x=100(124.6)	-3.42 ± 0.39	-1.98 ± 0.41	-3.31 ± 0.49	-0.18 ± 0.27	0.37 ± 0.22

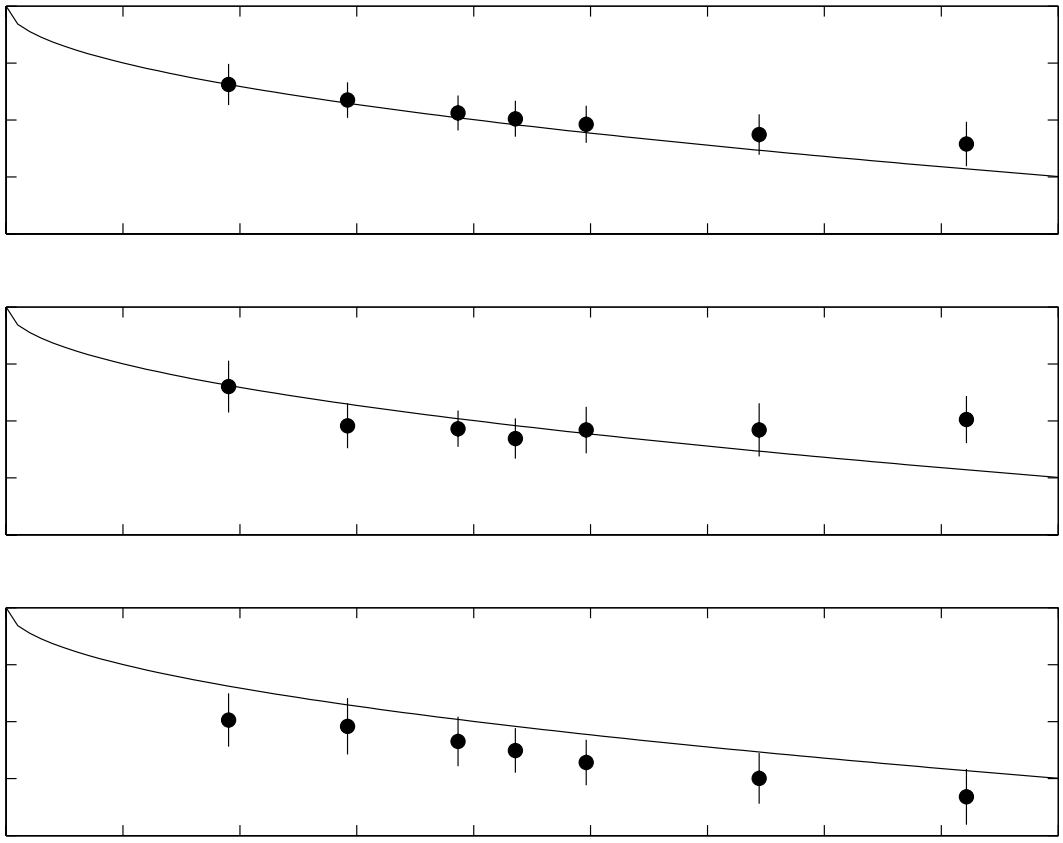

Figure 3-9. Radial range-time (A), PIV (B), and radar (C) bore celerity comparisons to radial component of shallow water dispersion relationship. Dots are mean bore celerities and error bars are 1 standard deviation. The curved line is the bore celerity predicted by equation 3-4.

Conversely, Doppler estimates of bore celerities follow the trend of the shallow water model but tend to over predict at all depths (Figure 3-9C) with normalized relative errors of about 25% excluding the location at x = 50 m.

Discussion

The previous sections have shown PIV and Doppler radar measurements made across the surf and swash zones and comparisons to estimated bore celerities from range-time images and a shallow water model. Although the two techniques often obtained similar velocity estimates, noticeable differences occurred and can generally be related to various subregions of the nearshore as described below.

Offshore (x = 90 and x = 100 m), the lack of significant image texture (frequently unbroken waves) and decreased pixel resolution may yield erroneous results from the PIV. For example, just prior to 17h31 at x = 90 and x = 100 in Figure 3-5, a velocity signal observed in the radar data does not appear in the PIV data. However, using the velocity signature as a wave tracer and invoking a principle of continuity in time and space it is clear from both sensor time series that the wave observed from x = 80 to x = 60 must have also existed at x = 90 and x = 100. This lack of texture was the likely cause of a large number of near zero velocities in the PIV histograms at all locations (Figure 3-6).

Within the surf zone, the onset of breaking and bore propagation changes the nature of the radar backscatter to include more specular or non-Bragg scattering and provides sufficient image texture for PIV such that the instruments measure velocities more indicative of the bore celerity. Also, the change in pixel footprint between the radar and PIV leads to different spatial averaging which may contribute to the differences in the derived velocities. From the inner surf zone to the breaking region, the histogram shapes become less similar as PIV develops a larger peak near zero velocity whereas

radar has a bimodal structure. Changes in the PIV histogram with offshore location result from a decrease in surface texture due to the decrease in broken wave propagation. The decrease or lack of surface texture, and hence a tracer, causes the PIV method to return zero or near zero velocity except when a wave crest is within the interrogation window. The bimodal shape of the radar histograms changes across the surf zone as well. However, from the inner surf zone to the breaking region, the peaks shift with the larger velocity peak becoming more dominant implying two competing scattering mechanisms that vary across the surf zone.

In the swash zone, away from shoreward propagating bores, the radar signal to noise ratio decreased by 10 dB. As radar relies on surface roughness, the water surface may be too smooth to yield a sufficient radar echo to obtain a reliable velocity estimate from the radar causing a large difference between the radar and PIV velocities. In this zone, the histograms consisted of only one peak and the shapes were similar, but because the PIV velocities were typically smaller, the histograms are offset from each other.

To further investigate the bimodal nature of the histograms, the mean values of each modal distribution were estimated. The mean values of the more negative modal distribution decrease (in magnitude) steadily from offshore to onshore from roughly -3.6 to -1.5 m s^{-1}, indicative of the decrease in wave celerity with decreasing depth. This is also consistent with the curved shapes of the shoreward propagating bores (and velocities derived from them; Table 3-3) in the range-time images. Thus, it is likely that the significant mechanism contributing to velocities in this modal distribution is attributed to the phase speed of the bore fronts.

The mean of the less negative (slower) peak in the PIV histograms is constant at around -0.2 m s^{-1}. This can be attributed to the large number of near zero velocities due to a lack of sufficient surface texture as discussed previously. In contrast, the mean values for the slower peak in the radar histograms are roughly constant around -0.5 m s^{-1} for x = 60 to x = 75 m and increase from -0.5 m s^{-1} to roughly -0.9 m s^{-1} for x = 80 to x = 100 m. These velocities are significantly less than the bore speeds and probably indicative of measurements of the water surface between bores. In this region, the surface would not have a dominant scattering feature (a bore) and these velocities would be attributed to a distributed scattering mechanism such as Bragg scattering. In deep water conditions, Doppler velocities are a combination of a surface drift, the phase velocity of the Bragg resonant waves, and any surface current present. However, in the surf and swash zone environments, interpretation of these velocities is more complex. One might expect the largely mechanically generated capillary wave spectrum between bores to be directionally broad and mostly isotropic. This would imply little or no bias due to the Bragg resonant capillary wave velocities. However, the effect of onshore-directed wind on these waves might result in an onshore bias to these velocities. It is therefore not clear whether the measured velocities are dominated by wind or a mean onshore surface current. However, as the water depth decreases, the effect of any subsurface offshore directed current (undertow) "felt" by the surface waves would increase, thus causing the velocities measured by the radar to be less than those further offshore between x = 80 to 100 m.

While these explanations for the observed velocities are plausible, they do not address why the techniques differ from the range-time derived bore celerities or the

shallow water model. Although the range-time derived bore celerities are close to the dispersion relationship, they are slightly lower than predicted values. This could be a result of non-shore normal bore propagation. For example, a mean incident wave angle of 7 degrees from shore normal minimizes the rms difference between the range-time derived bore celerities and the model. It also yields range-time bore celerities that are closer to the Doppler and PIV estimates. Differences between PIV and the model were largest at the offshore locations, likely due to the infrequent occurrence of broken waves and spatial averaging, and decreased in the onshore direction to a minimum in the inner surf zone where broken waves are prevalent.

In contrast to PIV, Doppler radar bore celerities are systematically larger than expected. Since radar velocities are measured from the Doppler shift of the backscattered electromagnetic wave due to ensemble particle motions, the Doppler velocity includes the radial components of both the alongshore current and cross-shore motion of the bores. Any southward propagating alongshore current will therefore increase the Doppler bore estimates. For a bore propagation angle of 7 degrees, an alongshore surface current of 0.44 m s^{-1} is required to minimize the rms difference between the Doppler bore estimates and the range-time derived bore celerities. This current velocity may be too large for the wave conditions during the collection period and thus may not completely explain the difference. Other factors such as the speed of the turbulent water tumbling down the bore face, sea spray and shore-directed water particle ejections resulting from breaking can also contribute to the Doppler velocities.

Conclusions

This study has presented surface velocity measurements from the surf and swash zones using two remote sensing instruments. Comparisons of velocities from various

cross-shore locations have been used to investigate each technique under different nearshore conditions. The study has also attempted to provide an interpretation of the measured velocities in the context of the imaging mechanisms used by each sensor.

Qualitative image comparisons showed excellent agreement in which regions of high radar backscatter corresponded to bores visible in the video imagery. Direct velocity comparisons between the two techniques at several cross-shore locations yielded R^2 correlation coefficients up to 0.60. Spectral decomposition of the times series were also similar as evidenced by high coherence in the low frequency to incident band (roughly 0.02 to 0.25 s^{-1}) with 95% confidence levels for phase shifts spanning 0°. Neither technique observed significant offshore-directed motions either because of a lack of offshore-directed surface motion or because the sensors are incapable of measuring such motions when they existed. PIV was found to be vulnerable to errors in conditions of insufficient surface texture while the radar appeared susceptible to errors close to shore where, away from the bore, water smoothness may adversely affect the measurement. In addition, both techniques are affected by spatial smoothing.

This comparison has shown that care is needed in interpreting microwave radar and PIV remote sensing measurements of the nearshore region. Specifically, the techniques provided estimates of swash zone velocities and surf zone bore celerities with typical relative errors of 15-25% compared to velocities derived from the slope of the range-time bore front trajectory, which in turn compared well with a shallow water dispersion relationship. The most significant difference in the PIV occurred at the two offshore locations whereas the radar showed a consistent over prediction of the bore celerities with the most significant difference in the swash zone. The bimodal

distribution of microwave Doppler radar velocities indicated that the radar measurements were significantly influenced by the bore celerities during bore propagation inside the surf zone and a superposition of capillary, wind-driven and shore-directed wave velocities in between bores. PIV was found to be capable of estimating bore celerities inside the surf zone, and more closely matched the celerity estimates of a shallow water model. Due to intermittent lack of image texture, PIV was often less sensitive than radar at measuring the surface fluid velocities between bore fronts. However, PIV was able to typically track both uprush and backwash swash zone surface velocities when adequate image texture was present, whereas radar infrequently measured backwash velocities.

Measurements made with remote sensors have the potential to further our understanding of nearshore hydrodynamics and wave motions resulting from the larger spatial coverage and non-interference with the flow field. In addition, remote sensors often reduce logistical deployment difficulties, require low maintenance and can be cost-effective. Results from our study offer insight into the use of two remote sensing techniques in the surf and swash zones, which will be important in the interpretation of measurements from future remote sensing studies.

CHAPTER 4
SWASH ZONE FLOW FIELDS AND FORESHORE MORPHODYNAMICS ON A STEEP BEACH

Introduction

Within the swash region, flows wash up and down the foreshore carrying varying quantities of sediment. The cumulative effect of the often small difference between the amount of sediment carried within each phase of the swash drives beach change. Therefore, predicting beach change requires an understanding of each phase of the swash flow and the associated mechanisms for entraining and transporting beach sediment. Yet, while the individual flow and sediment transport signals are visually obvious and typically quite large, scientific understanding of the beach change resulting from these swash processes is still poorly understood.

Many prior studies have attempted to qualitatively relate beach change and beach slope to groundwater and through-bed flow processes that are themselves a function of the sediment grain size. For instance, *Grant* [1948] and *Duncan* [1964] related the beach foreshore change over a tidal cycle to differences in infiltration due to varying beach saturation levels resulting from water table fluctuations. In both cases, beach steepening on the rising tide was attributed to sediment deposition as the uprush drains into the beach face and loses its transporting capacity. Conversely, during ebbing tide, a saturated beach permits a larger volume of water to remain on the beach increasing the backwash transporting capacity, thereby causing beach flattening. More recently, *Turner and Masselink* [1998] measured swash infiltration/exfiltration on a sandy beach and simulated

the effect of this vertical flow and its alteration of the shear stress to show that it enhances net upslope transport of sediment on a saturated beach. *Butt et al.* [2001] also analyzed the effect of swash infiltration/exfiltration and showed that there appears to be a critical grain size at which these influences change the net transport rate from offshore to onshore. Process-based numerical models, however, have shown that the foreshore slope for sandy beaches is not likely due to increased swash asymmetry caused by infiltration [*Masselink and Li*, 2001] such that the concept of *Grant* [1948] and *Duncan* [1964] likely only applies for large grain sizes.

In contrast, other studies have tried to describe foreshore change by analyzing variations in swash flow kinematics. *Holland and Puleo* [2001] related the foreshore slope change to an inequality between the inner surf zone wave period and the swash duration governed by frictional ballistic motion. It was shown that the foreshore slope rapidly decreased such that the difference between the swash duration and wave period was minimized thereby reaching a dynamic equilibrium. Kinematic relationships for foreshore change similar to this were proposed by *Inman and Bagnold* [1963] as resulting from inequality between uprush and backwash energy dissipation, by *Kemp* [1975] resulting from the phase difference between uprush time and wave period and by *Hardisty* [1986] as related to the swash flow asymmetry parameter, the ratio between uprush and backwash swash edge velocities.

In some cases, statistical parameterizations of the flow instead of flow kinematics have been correlated to swash zone sediment transport. For instance, *Butt and Russell* [1999], showed that the normalized skewness of the velocity field (a single point measurement by a miniature electro-magnetic current meter) was related to the observed

foreshore change. During 'storm' conditions when the beach eroded, the normalized skewness was offshore-directed for low frequency motions (potentially enhancing offshore transport) and onshore-directed for both low and high frequency motions (potentially enhancing onshore transport) during 'calm' conditions. The concept of high order flow statistics such as acceleration skewness have also recently been related to bed load transport in the surf zone using a discrete particle model [*Drake and Calantoni*, 2001] and to sand bar migration [*Elgar et al.*, 2001 and *Hoefel and Elgar*, 2003] but are seldom tested in the swash zone.

While some of the aforementioned parameterizations and kinematic descriptions of beach change have proved fruitful, direct predictions based on flow conditions are typically poor and rarely used to predict three dimensional foreshore evolution. This approach generally adopts an energetics transport relationship [*Bagnold*, 1966] for the swash zone. Difficulties arise because the flow field is unsteady, (although *Bailard* [1981] has extended the equations for the unsteady case), and may be significantly affected by strong turbulence and uprush/backwash interactions. The unsteadiness has been further addressed by *Nielsen* [2002] who included a phase shift in the stress term of a sediment transport model similar to Bagnold's to account for the lag between the free stream velocity and the bed shear stress. *Drake and Calantoni* [2001] and *Hoefel and Elgar* [2003] account for the unsteadiness by including a measure of the acceleration skewness (a proxy for the horizontal pressure gradient), but those models were not tested for swash. *Puleo et al.* [2003] showed the fluid acceleration/horizontal pressure gradient concept proposed by *Drake and Calantoni* [2001] makes sense for swash but likely accounts for the turbulent bore rather than being an independent mechanism on its own.

The objectives of this chapter are to relate the flow fields during a highly erosive beach condition that occurred at Duck, NC on October 10, 1994 (previously documented in *Holland and Puleo* [2001]) to the observed foreshore change. To do so, statistical parameters describing the fluid flow including mean flow fields, velocity and acceleration skewness, and incident vs. infragravity energy, are used to determine which parameters are associated with erosive or stable conditions. In addition, spatially dense velocities are used to drive a simplified two dimensional sediment transport model with and without modifications for fluid acceleration to test the skill in modeling beach change. The next section introduces the sediment transport model and extensions to include flow acceleration and acceleration skewness. The field site, environmental conditions and installation of equipment are then described. The following section briefly explains the methods used to extract foreshore elevations and surface velocities from video recordings. Relationships between flow statistics and beach change are addressed. Comparisons between the models and the observed foreshore change are given in the results section. The chapter ends with discussion and conclusion on the findings.

Sediment Transport Model and Acceleration Parameterizations

Much of the direct swash zone sediment transport modeling to date has focused on the energetics approach [*Masselink and Hughes*, 1998; *Puleo et al.*, 2000 and *Butt et al.*, submitted] originally derived by *Bagnold* [1963]. Bagnold's original arguments were that in steady one-dimensional flow, energy expended on the bed through shear stresses supplied the power necessary to transport sediment (both as bed load and suspended load). In other words the depth integrated sediment transport rate was a function of the shear stress at the bed multiplied by the velocity. *Bailard* [1981] followed Bagnold's arguments and derived an equation for the time dependent total sediment transport rate

which also depended on the same shear stress-velocity product. Based on their formulations we adopt a simplified sediment transport equation where the shear stress can be thought of as the mobilizing or stirring mechanism and the velocity as the transporting mechanism such that

$$\vec{q} = k\left(u\hat{i} + v\hat{j}\right)\left|\vec{u}\right|^2 \quad (4\text{-}1)$$

where q is the volumetric total load sediment transport rate obtained from the third velocity moments and is referred to as the velocity-moment-based model. There is no incipient motion criterion such that equation 4-1 predicts transport at all flow velocities and we do not differentiate between bedload and suspended load.

As mentioned earlier energetics models, have recently been extended to include acceleration effects on sediment transport in the swash zone; [chapter 2 and *Puleo et al.*, 2003] and the surf zone [*Drake and Calantoni*, 2001 and *Hoefel and Elgar*, 2003]. Two extensions are applied to the unmodified model given by equation 4-1. The first by *Puleo et al.* [2003] is denoted by subscript *a* on the transport variable and the second by *Drake and Calantoni* [2001] is denoted by subscript *as* on the transport variable. Note that the unmodified model given by equation 4-1 will not carry a subscript on the transport variable.

The *Puleo et al.* [2003] extension in two dimensions yields

$$\vec{q}_a = k\left(u\hat{i} + v\hat{j}\right)\left|\vec{u}\right|^2 + k_a\left(a_x\hat{i} + a_y\hat{j}\right)\left|\vec{u}\right| \ , \quad (4\text{-}2)$$

where u and v are the horizontal velocity components in the cross-shore ($\hat{i}$) and alongshore ($\hat{j}$) directions respectively and a_x and a_y are the corresponding horizontal fluid accelerations. The coefficients k, k_a account for the conversion to volumetric

transport, fluid density, friction factor, and a length scale for the acceleration term. If one wanted to think of this as the Bagnold or Bailard model, then the coefficients would also include an efficiency factor. Note that there is no explicit autosuspension formulation included in equations 4-1 or 4-2 and the effect of a sloping bed and the angle of repose of sediment are incorporated into the leading coefficients.

The *Drake and Calantoni* [2001] extension (denoted by subscript as) in two dimensions yields

$$\vec{q}_{as} = \vec{q} + k_A\left(A_x\hat{i} + A_y\hat{j}\right), \quad (4\text{-}3)$$

where A is the non-dimensional acceleration skewness. *Drake and Calantoni* [2001] use a dimensional acceleration skewness using the root mean square acceleration as a scaling factor and suggest other scaling factors may exist. We choose a scaling factor of unity. Their model also included a critical value such that acceleration induced transport only occurs when this threshold is exceeded. In previous studies the threshold value has ranged from 0.2 to 1 m s^{-2} [*Drake and Calantoni*, 2001and *Hoefel and Elgar*, 2003]. Hence, the value is likely flow and sediment grain size dependent and we choose to disregard the threshold in our model since there is no incipient motion criterion on the velocity moment term.

Once the transport rates are calculated, elevation changes arising from spatial gradients in volumetric sediment transport, are determined by the sediment continuity equation as

$$\frac{\partial \vec{z}}{\partial t} = -\frac{1}{\alpha}\frac{\partial \vec{q}}{\partial \vec{x}} \quad (4\text{-}4)$$

and α accounts for sediment porosity.

In practice, equation 4-4 is often given in the time averaged form solved for the elevation change as

$$\partial\vec{z} = -\frac{1}{\alpha}\left\langle\frac{\partial\vec{q}}{\partial\vec{x}}\right\rangle\partial t \quad (4\text{-}5)$$

where ∂t would now represent the length of time over which the gradient in transport rates are averaged.

Field Site and Installation

Data were collected at the Army Corps of Engineers Field Research Facility (FRF) at Duck, NC. The beach at Duck is barred (often 2 bars present) with a relatively steep foreshore (typically 1:12) and a much shallower sloping offshore section. The grain size on the foreshore at the FRF varies from fine sand to medium gravel with a median grain size of roughly 0.5 mm. Waves at Duck vary with large storms during the late fall and winter months and relatively calm during the summer months. Semi-diurnal tidal range at the FRF is approximately 2 m. The data presented here were collected during an energetic storm on October 10, 1994 when significant wave heights obtained from the 8 m instrument array operated by the FRF were between 0.8 and 1.8 m with a peak period of between 3 and 8 s (Figure 4-1A,B). Figure 4-1C shows the wave direction spanning October 10 rotating from the south (above the shore normal dashed line) to approaching from the north (below shore normal dashed line). The corresponding alongshore current measured offshore (x = 914 m, y = 950 m in the FRF coordinate system) with a Marsh McBirney biaxial current meter shows the alongshore current direction changing from northerly flow (dots) to southerly flow (plus signs) and increased to 0.4 m s^{-1} (Figure 4-1D).

Instrumentation specific to this foreshore study consisted of three high resolution Sony video cameras. The cameras were mounted nearly 8 m above the foreshore on triangular antenna sections that were erected on the dunes backing the beach. Cameras were typically in collection mode during daylight hours from October 9, 1994 to October 20, 1994 and imagery was collected at 30 Hz. However, the data presented here is from October 10, 1994 when the large erosive event was observed. In conjunction with the video data, daily beach surveys were collected using a kinematic GPS mounted on an all terrain vehicle.

Data Extraction Methods and Analysis

Fortunately, data contained within the video signal yields not only the fluid forcing (swash velocities), but the beach change as well. The methods presented below have been fully described elsewhere and as such only a brief description is given here.

Video Stereogrammetry

Holland and Holman [1997] developed a stereometric technique to extract three dimensional (3D) beach coordinates based on video imaging. Multiple camera views of a 20 m alongshore by 20 m cross-shore section of foreshore were imaged synchronously through the three cameras. The imagery shown in Figure 4-2 is obtained from the southern camera (looking North) and the region of interest is denoted by the solid lines. The stereo technique utilizes the swash edge in each camera view found and digitized using standard edge detection algorithms.

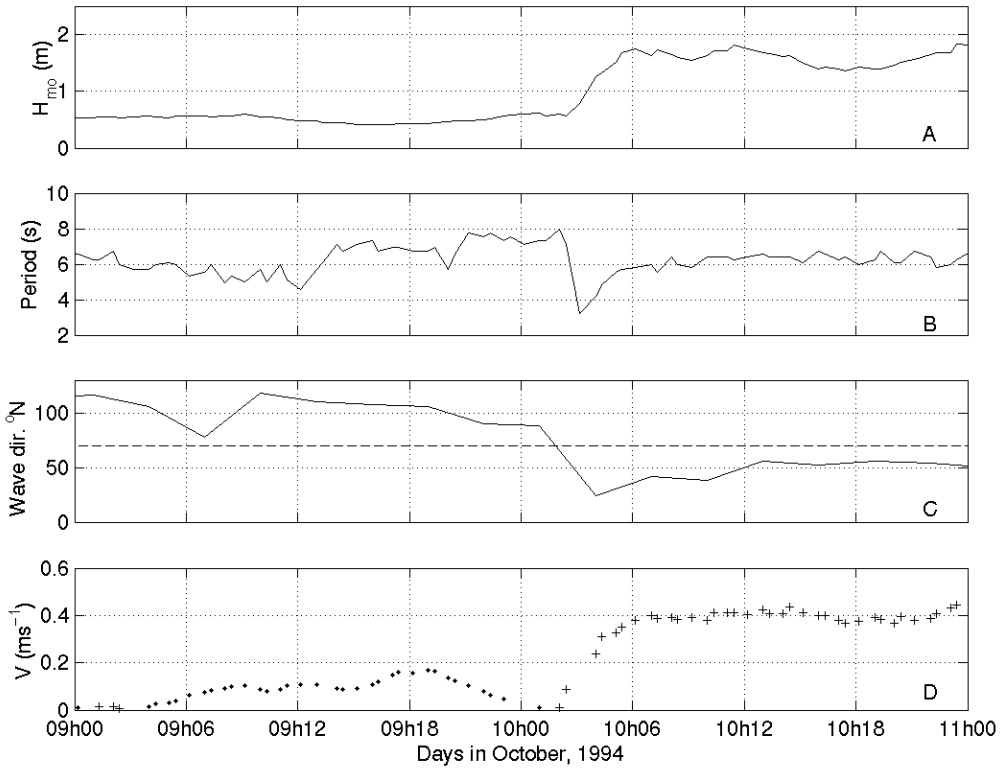

Figure 4-1. Offshore conditions for October 9 through October 11, 1994 at Duck, NC. A) Significant wave height, B) Wave period, C) Wave direction with respect to true North (dashed line is shore-normal incidence), D) Alongshore current speed (southerly flow: plus signs, northerly flow: dots).

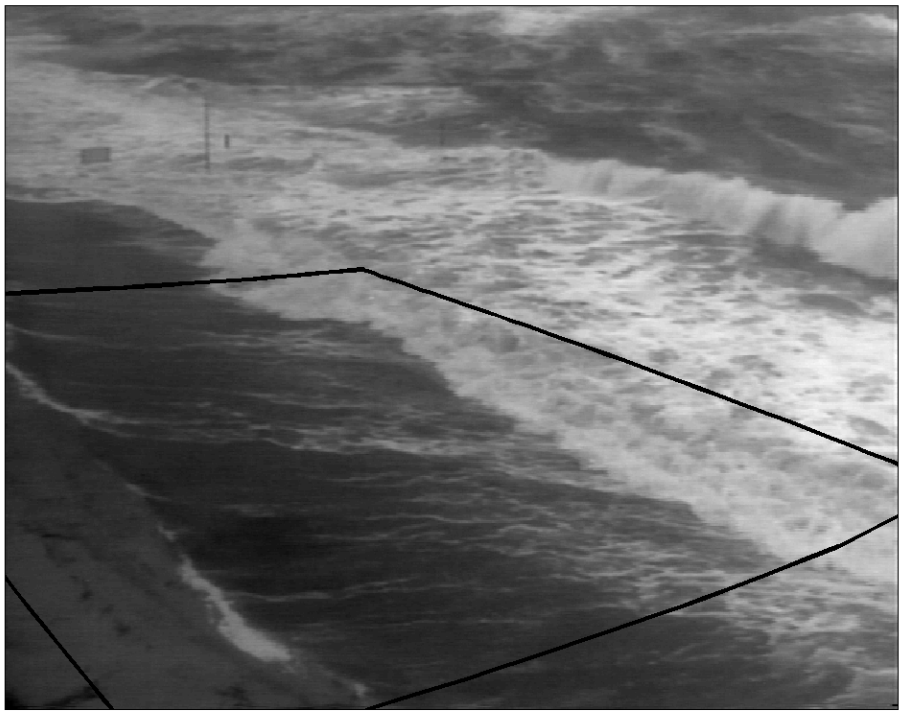

Figure 4-2. Oblique image from the southern camera showing the region of interest denoted by the solid lines.

In order to extract the elevations over time and hence the foreshore change, the mathematical model [*Holland et al.*, 1997] describing each camera's location and orientation (tilt, azimuth and roll) and internal parameters (such as distortion and focal length) is used in conjunction with the digitized edges (at 6 Hz of a 30 Hz video signal) to perform stereometric intersection yielding 3D real world coordinates of a chosen pixel. The technique is completed for each pixel along the swash edge and each edge within the uprush cycle. In this sense, the uprush maps out the foreshore topography during its landward motion and often results in many thousands of estimates of beach elevation in a small region such as the one of interest here. *Holland et al.* [1998] have shown that during this study the error about the elevation estimates was O(1 cm) when compared to standard GPS measurements.

In order to perform inter-comparisons over time, beach surface maps are constructed on a regularly spaced grid. Here we choose a grid with 0.5 m spacings in both the cross-shore and alongshore directions and surfaces are constructed every 15 minutes using the following method. First, several sets of elevation estimates within a 10-minute time bracket around the time of interest (e.g. for a surface at 1000, only elevations determined between 0955 and 1005 are used) are grouped and a quadratic filter (space and time) using Loess interpolation weights is applied to the data points yielding 'smooth' surfaces at the pre-specified grid (see *Plant et al.* [2002] for a complete description of the filtering technique). The smoothing is achieved by selecting cutoff length scales (time and space) of features of interest. Here we use a length scale of 15 m and a time scale of 45 minutes such that short scale features are smoothed. The data used in the interpolation scheme is coupled with supplementary data obtained from GPS

measurements. It should be noted that this GPS data obtained by either the Coastal Research Amphibious Buggy (CRAB) or from the Argo (a small 6-wheeled amphibious vehicle) is generally supplanted outside the region of interest to minimize edge effects in the Loess interpolation method. The interpolation algorithms mentioned above and applied to this data are slightly different than the interpolation scheme previously performed on this data *Holland and Puleo* [2001] by using quadratic Loess interpolation rather than linear interpolation and by allowing for interpolation in both space and time. The differences between the output are small, but the new technique yields smoother beach surface time series.

The result from the interpolation is a four dimensional data set (x,y,z,t) of which various time slices are depicted in Figure (4-3). The initial beach surface at 0900 shows a steep foreshore and a cusp horn centered at roughly $y = 970$. By 1100, the cusp horn has been eroded and the more planar sloping beach has undergone over 0.7 m of erosion. From 1200 to the end of the run, the foreshore is in a relatively stable configuration with only slight elevation changes observed. Expected root-mean-square interpolation errors (not shown) were roughly 0.02 – 0.03 m during the erosive period and approximately 0.01 m during the stable period. These errors are consistent with those reported by *Holland et al.* [1998] in comparison between the stereo technique and standard GPS surveying. The interpolation errors increase to about 0.04-0.05 m at the edges of the interpolation domain in both space and time.

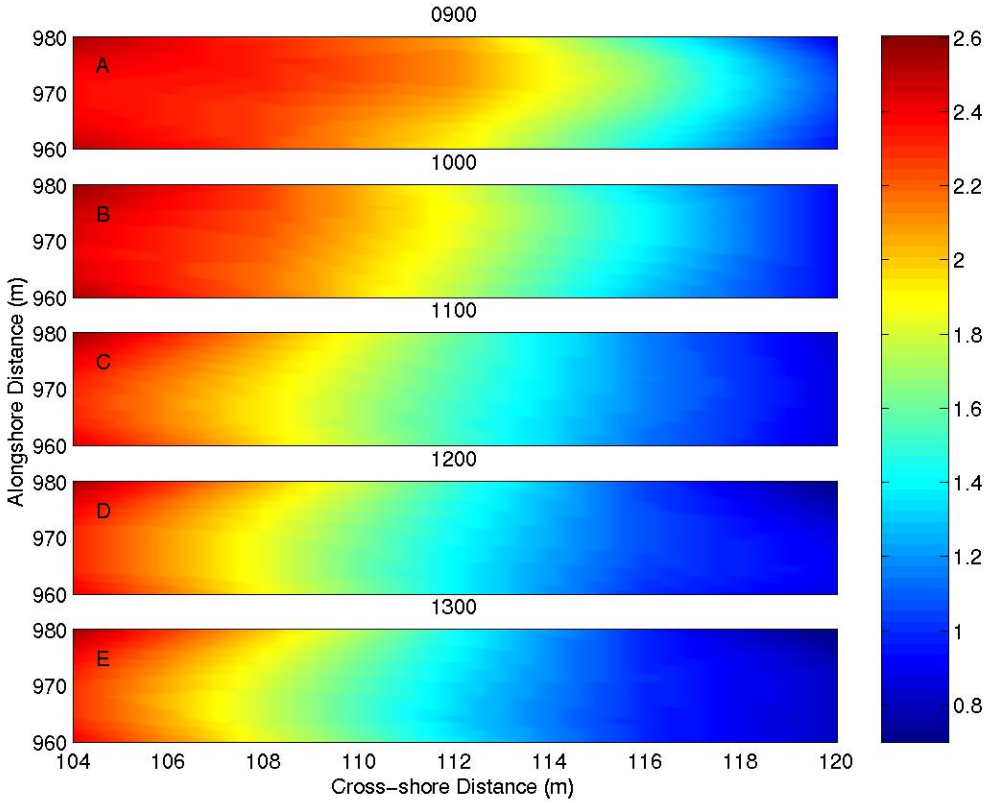

Figure 4-3. Time history of morphologic change on October 10, 1994 from 0900 to 1300 local time. Color shading represents elevation in meters.

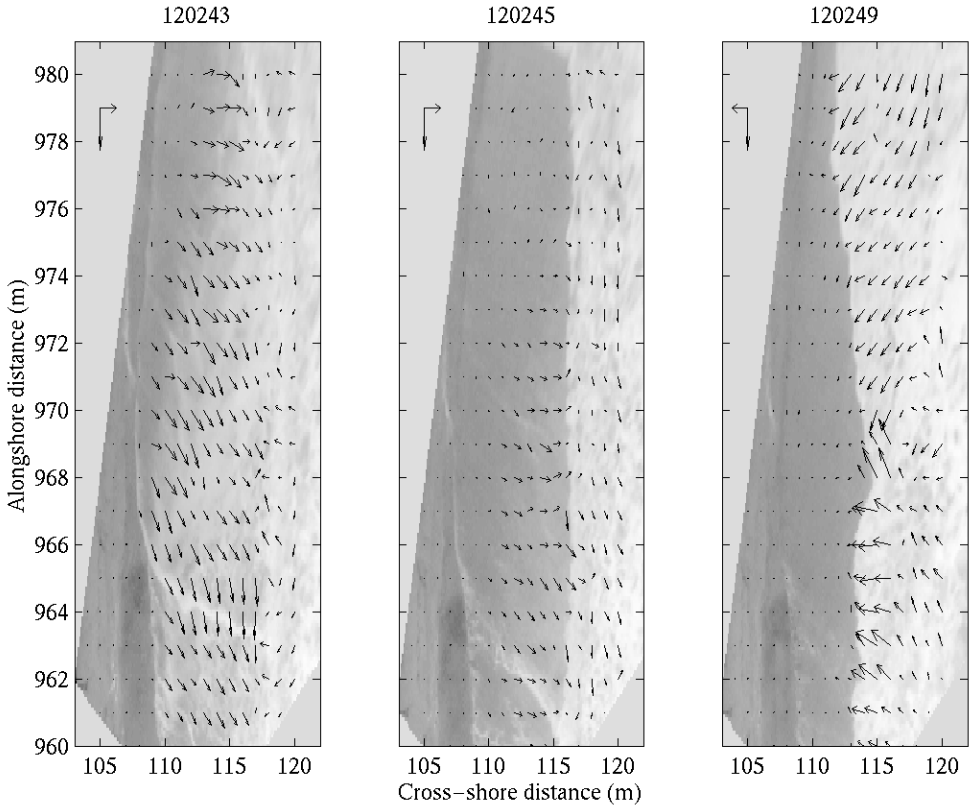

Figure 4-4. Three geo-rectified images with overlain PIV-determined velocity vectors showing the beginning and end of the backwash along with the start of the uprush. Numbers represent the time in hr:min:sec: on October 10, 1994. The velocity scale vectors of 0.5 m s^{-1} are shown in the upper left and the size varies only because of the vertical exaggeration of the figure.

Particle Image Velocimetry (PIV)

The particle image velocimetry technique was described in chapter 2 and is fully described in *Holland et al.* [2001] so no recapitulation is given here. In the usage here, velocity time series from the PIV method are smoothed with a 7 point running average Hanning window filter.

Three geo-rectified snapshots along with the PIV determined surface velocity vectors are shown in Figure 4-4. At 120243 a strong (up to 0.7 m s^{-1}) backwash is moving offshore and it can be seen that there is a dominant southerly alongshore component to the flow. At 120245 (two seconds later), the backwash has nearly reached completion as the velocity magnitudes are only 0.2 m s^{-1} but still have a significant alongshore component. By 120249 the uprush has started with maximum velocity magnitudes of over 0.5 m s^{-1} with the alongshore velocity being a smaller component of the total velocity magnitude.

Swash Flow Statistics in relation to Foreshore Change

Before attempting numerical modeling of the observed foreshore change, flow statistics were analyzed to determine if these statistics show correspondence with the foreshore response. Figure 4-5 shows the hourly mean velocity fields in the cross-shore (Figure 4-5A-E) and alongshore (Figure 4-5F-J) directions, cross-shore flow acceleration (Figure 4-5K-O) and the beach elevation change (Figure 4-5P-T). The color scale gives the velocity (m s^{-1}) with positive velocities being offshore and to the north (negative onshore and to the south), positive acceleration (m s^{-2}) being offshore-directed and negative elevation change (m) indicating erosion. Fluid means were calculated only when the PIV sensor registered a velocity magnitude greater than 0.02 m s^{-1}.

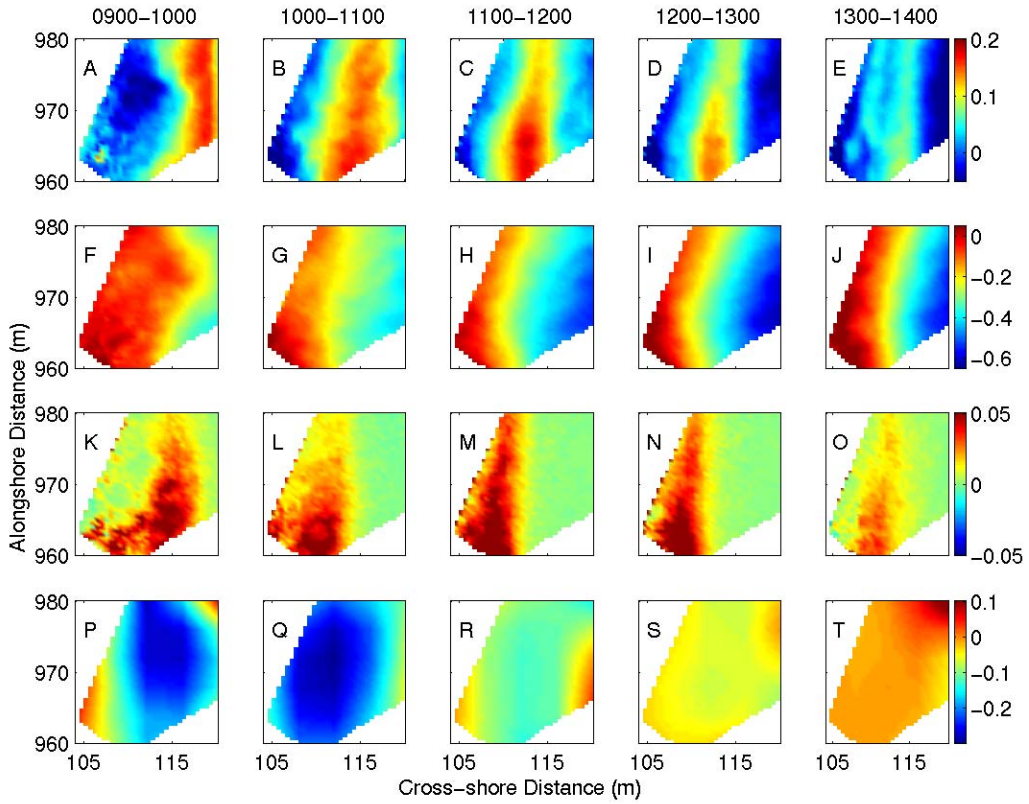

Figure 4-5. One hour time-averaged cross-shore velocity (A-E; m s^{-1}), alongshore velocity (F-J; m s^{-1}), cross-shore acceleration (K-O; m s^{-2}) and beach elevation change (P-T; m). Title for each column denotes times for averaging.

In this way, the means are not biased during times when a section of the foreshore is not covered by swash. It can be seen that the erosion is strongly associated with the landward edge of the band of mean offshore velocities during the rising tide (0900 to 1200). Mean offshore-directed cross-shore velocities exceed 0.2 m s^{-1} during the erosive period and are smaller after the severe erosion. Mean alongshore flow velocities exceed 0.7 m s^{-1}, but no strong alongshore gradients in mean alongshore flow are observed throughout the run except initially (at 0900-1000). The small observed alongshore gradient in the alongshore flow (Figure 4-5F) however, has the correct shape so as to enhance erosion of the cusp horn that existed in the study region (Figure 4-3), but it cannot be ruled out that the observed pattern occurs as a result of the cusp horn. Mean cross-shore flow acceleration is offshore-directed in all cases such that the short-lived onshore-directed acceleration associated with bore motion is minimal, in a time-averaged sense, compared to the offshore directed gravitational effect. Regions of strong cross-shore spatial gradients in flow acceleration also display a visual correspondence to the regions of erosion (Figure 4-5K-M).

Non-dimensional velocity skewness, can be determined from the normalized third moment of the time-averaged velocity by [*Butt and Russell*, 1999 and *Elgar et al.*, 2001]

$$\Gamma = \frac{\langle u^3 \rangle}{\langle u^2 \rangle^{\frac{3}{2}}} \quad . \text{(4-6)}$$

Similarly, non-dimensional acceleration skewness, a rough estimate of velocity asymmetry, can be obtained from acceleration skewness as [*Butt and Russell*, 1999]

$$\mathrm{A} = -\frac{\langle a^3 \rangle}{\langle a^2 \rangle^{\frac{3}{2}}} \quad . \text{(4-7)}$$

Recall that velocity skewness is characterized by a time series with narrow high-velocity peaks and wide low-velocity troughs. Flow asymmetry is characterized by a sawtooth shape with a steep sloping rear face and gently sloping front face having equal velocity magnitudes. Due to the coordinate system used here, a positive value for A means the acceleration skewness is predominantly onshore (larger accelerations associated with the incoming uprush) while a negative value for A means the acceleration skewness is predominantly offshore. Conversely, a positive value for Γ is skewed offshore while a negative value for Γ is skewed onshore.

Time series (~5.25 hours) for each alongshore PIV sensor at cross-shore positions 119 m and 119.5 m (a total of 52 sensors) were extracted for analysis. Locations near the offshore edge of the study area were chosen to minimize discontinuities in the swash velocity time series due to intermittent water coverage in the study area. In a strict sense these measurements would occasionally be located just outside the swash zone, but estimates of Γ and A are difficult to interpret from a time series with numerous discontinuities. Hence we chose locations that had the least amount of discontinuity while still being often located within the swash zone.

After the time series were extracted, they were decomposed into cross-shore and alongshore components, divided into 15 minute segments and then low pass and high pass filtered with a cutoff at a frequency of 0.05 Hz to determine any importance of each component. Mean values for Γ and A (Figure 4-6) were then calculated for each 15 minute time block yielding a time history of each statistic. In each plot, the square symbols are the low frequency (<0.05 Hz) component and the circles represent the high frequency (>0.05 Hz) component.

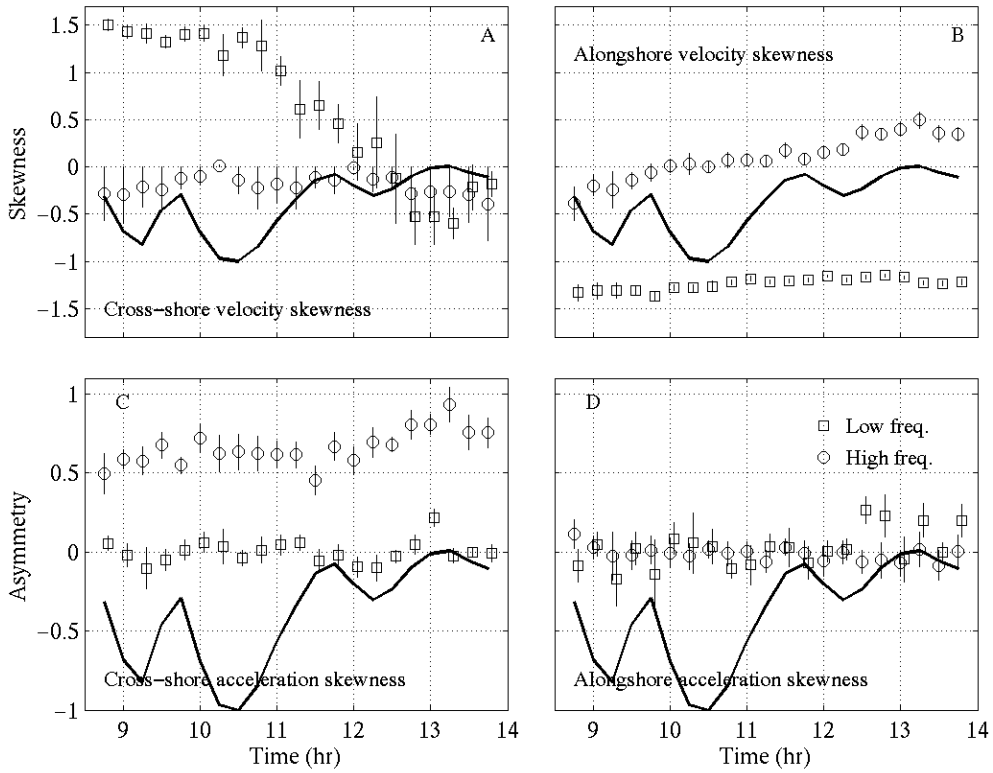

Figure 4-6. Low and high pass filtered velocity and acceleration skewness time series from the seaward edge of domain for cross-shore (A,C) and alongshore (B,D) velocity. The solid curve is the total volumetric change normalized by the magnitude of the maximum volumetric change (~80 m^3 m^{-2} hr^{-1}).

Vertical lines are the two standard deviation spread about the mean of each calculated statistic from the 52 PIV sensors used. The solid curve is the corresponding total volumetric change normalized by the magnitude of the maximum volumetric change for a given 15 minute segment (~80 m^3 m^{-2} hr^{-1}; the actual amount of volumetric change is obtained by multiplying the value from the y-axis by 80 m^3 m^{-2} hr^{-1}). This curve essentially shows that there was severe erosion until approximately 1130 LT and near stable conditions thereafter. In Figure 4-6A, the cross-shore low frequency velocity skewness is related to the observed foreshore change as it is strongly offshore for the first part of the run, and becomes negative (onshore) near the time the foreshore reaches its quasi-equilibrium (~1130 LT). The high frequency alongshore skewness is nearly zero for much of the run but does change signs about 1000 LT. Conversely, the low frequency alongshore Γ is nearly constant(-1.5) throughout the run and strongly to the south (negative) as was the current measured offshore (Figure 4-1) and depicted by the mean PIV velocity fields (Figure 4-5). Cross-shore high frequency acceleration skewness is onshore for the duration of the run but increases during the stable period suggesting an enhancement to onshore-directed transport. The alongshore acceleration skewness is roughly zero for the duration of the run for both the high frequency and low frequency case. In general, qualitative relationships show that the erosive nature of the foreshore during our study occurred when the flow was dominated by low frequency offshore-directed velocity skewness and the stable portion when the onshore acceleration skewness increased.

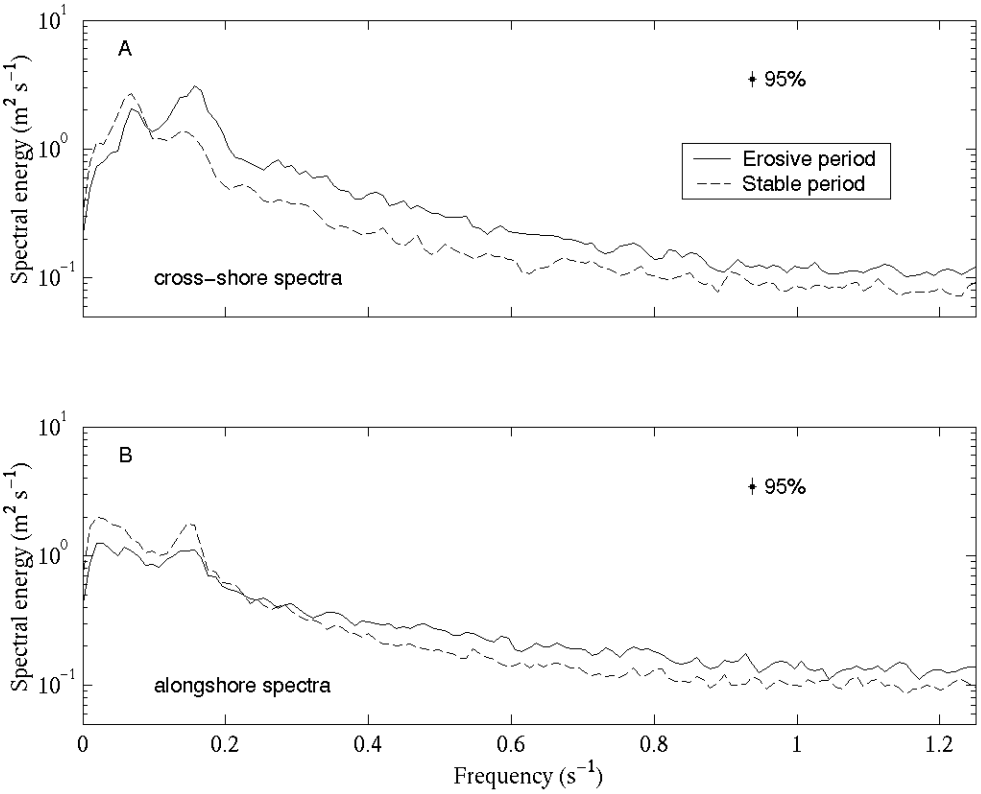

Figure 4-7. Cross-shore (A) and alongshore (B) averaged velocity spectra from 52 time series collected at x = 119 and 119.5 m and y = 960 to 980 in the FRF coordinate system for an erosive and stable period.

Averaged velocity spectra for the "erosive period" (0845-1130 LT, 23933 points for each of the 52 time series) and a "stable period" (1130-1400, 22125 points for each of the 52 time series) were calculated using Welch's averaged periodogram method on 256 tapered (Hanning window) ensembles and band averaged over 50 adjacent frequency bins (Figure 4-7). Only the 95% confidence interval for the erosive case is shown because the confidence intervals for the two cases are nearly equal. Both cross-shore spectra show two broad peaks centered at 14.7s and 6.4 s (only slightly visible during the stable period), the latter is consistent with the offshore incident wave period (Figure 4-7A). In this case, the energy at the 6.4 s peak is greater during the erosive period than the stable period whereas the energy at the 14.7 s peak is slightly greater during the stable period than the erosive period. Alongshore spectra show a similar peak at about 6.4 s and a second peak at a much higher period of about 46.3 s (Figure 4-7B). The overall cross-shore spectral energy, is 36% larger during the erosive period than during the stable period. Low frequency (<0.05 Hz) cross-shore spectral energy, however, is 62% larger during the stable period than the erosive period. These findings suggest that the erosion was tied to the overall larger energy input to the swash rather than being solely related to the low frequency component.

Morphodynamic Model-Data Comparisons

The entire (~5.25 hours) spatial set of velocity time series was used to test the sediment transport model with and without the extensions including acceleration and acceleration skewness. Spatial gradients of $\vec{q}$, $\vec{q}_a$, $\vec{q}_{as}$ and were calculated for the entire run, smoothed with the Loess interpolation filter [*Plant et al.*, 2002] and used to determine mean transport gradients and elevation change via centered differences.

Table 4-1. Coefficients with 95% confidence intervals for linear regressions.

	$\vec{q}$	$\vec{q}_a$	$\vec{q}_{as}$
k (s^3 m^{-1}) x10^{-3}	2.7 ± 0.08	1.7 ± 0.07	0.04 ± 0.06
k_a (s^3) x10^{-3}	---	12.9 ± 0.5	---
k_A (m^3 m^{-1}) x10^{-3}	---	---	0.7 ± 0.01
Model Skill	0.62	0.78	0.90

First order finite spatial differences were used along the domain boundaries. Direct comparisons were performed by linear regression of the estimated foreshore change using the gradients in transport and the actual foreshore change through the free parameters k, k and k_a or k and k_A (Table 4-1). Comparisons between the k_a and k_A values, the coefficients due to the acceleration extensions are difficult to make because of differing units. The k values for the three models, having the same units, can be compared such that any differences can help determine the importance of the acceleration extensions. For instance, the value of k decreased by 38% for the acceleration extension model as compared to k in the unmodified model, but is offset by the large value of k_a. Surprisingly, k decreased by 99% for the acceleration skewness extension as compared to k in the unmodified model suggesting that the acceleration skewness is a dominant descriptor for describing net sediment transport in the swash zone as evidence by the decreased error and increased model skill (see below). These large decreases in k for the acceleration extended models imply the additional term is able to account for a large portion of the total transport gradient.

Overall root-mean-square differences between the predicted elevation change and the measured elevation change over the entire 5.25 hour period were 0.34 m, 0.27 m, and 0.17 m for the velocity-moment-based model (equation 4-1), the model with the acceleration extension (equation 4-2) and the model with the acceleration skewness extension (equation 4-3) respectively. The velocity-moment-based model (equation 4-1, Figure 4-8B) predicts erosion in the upper half of the foreshore region, but unlike the observations, predicts accretion in the lower half resulting in a larger prediction error (compare to the observed beach change in Figure 4-8A).

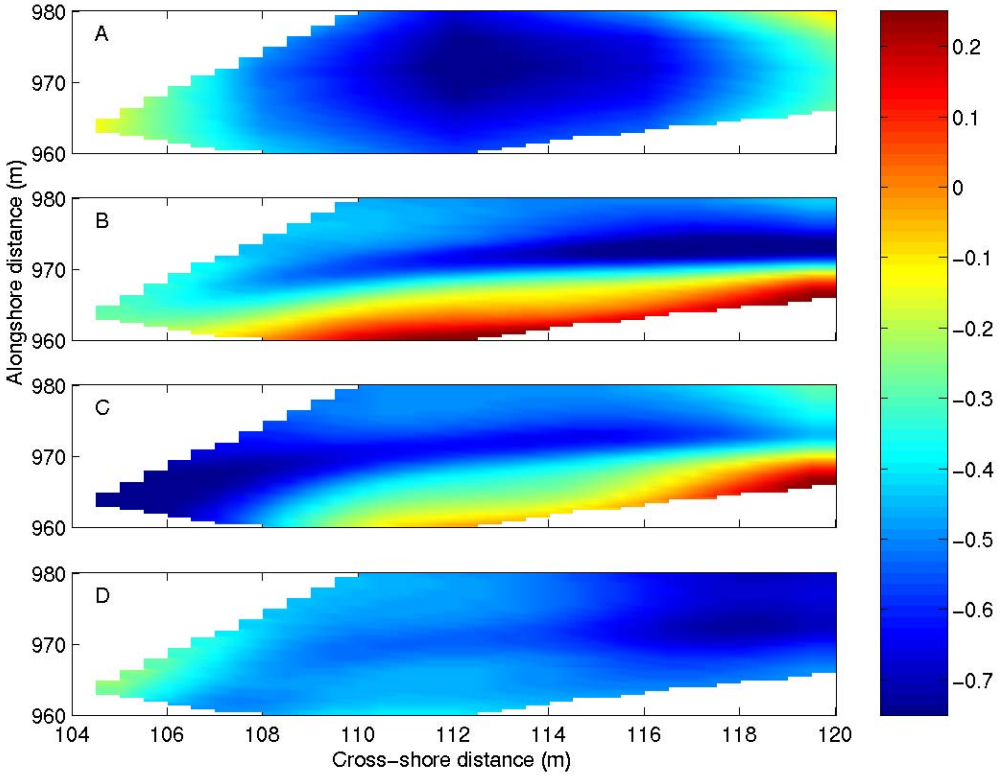

Figure 4-8. Foreshore elevation change (m) over the run duration (A), and corresponding predictions by the velocity-moment-based model (B), the extended model including an acceleration term (C) and the extended model including an acceleration skewness term (D).

The model using the acceleration extension is similar to the velocity-moment-based model, but predicts less accretion in the lower half of the foreshore region. Finally, the model using the acceleration skewness extension predicts erosion over the entire foreshore region in line with the observations resulting in a 50% error reduction over the velocity-moment-based model. Model skill (Table 4-1), defined as 1-var(residuals)/var(data) where var is the variance operating on either the residuals from the linear regression or the elevation change data, further demonstrates the increased predictive capability of the acceleration extensions, specifically the acceleration skewness.

Note that because the extended models have an additional free parameter, some of the increase in skill may be fortuitous. To test this, the data for acceleration and acceleration skewness was replaced with random noise and the correlations were again performed. Under these conditions, the overall root-mean-square differences between the predicted elevation change and the measured elevation change over the entire 5.25 hour period was 0.29 m and 0.29 m for the acceleration and acceleration skewness extension models respectively compared to 0.27 m and 0.17 m respectively for the actual field data. Similarly, the model skill was 0.72 and 0.73 for the random acceleration and acceleration skewness extension models respectively compared to 0.78 and 0.90 respectively for the actual field data. Based on this test, much of the increased skill and reduction of error for the acceleration skewness extension model is not attributed to the additional free parameter. In contrast, the acceleration extension model performed slightly better when real data versus random data was used suggesting that the small increase in predictive

capability using this model over the velocity-moment-based model was partially related to the inclusion of an additional free parameter.

Discussion

The results of our study indicate that higher order statistics such at the velocity and acceleration skewness can be used to qualitatively describe erosion/accretion patterns of the foreshore. Large positive values of low frequency cross-shore velocity skewness during the observed erosion period indicate a dominance of backwash motions on infragravity time scales that have been observed or postulated to be efficient offshore sediment transporting mechanisms [*Butt and Russell*, 1999 and *Puleo et al.*, 2000]. In contrast to the low frequency cross-shore skewness observed during the erosive period, high frequency skewness was always observed to be shore-directed. These motions result from the incident band bores representing a short duration onshore flow. Both the low frequency and high frequency velocity motions are included in the velocity-moment-based sediment transport model, but were unable to accurately predict the observed profile change through the erosive and stable periods.

Inclusion of flow acceleration in a sediment transport model is normally defended based on the phase lead of the bed shear stress with respect to the free stream velocity or because the bed shear stress is greater for a given velocity during accelerating flow [*King*, 1991]. The two methods used in here relied on functions of either the acceleration or acceleration skewness. A difficulty with the acceleration approach is the existence of a length scale in the formulation, but it was shown by *Puleo et al.* [2003] that allowing the length scale to be incorporated into k_a or using the water depth had little effect on predictive capability. It is not clear if some other length may be more appropriate. One difficulty with the acceleration skewness approach is there is no comprehensive study as

to what functional form of acceleration skewness sediment transport should depend on. Studies such as those by *Drake and Calantoni* [2001] and *Hoefel and Elgar* [2003] used a linear function of acceleration skewness which we adopted here, but it has yet to be determined if some other functional form is more appropriate.

Because observations from our study showed the high frequency onshore acceleration skewness was small and relatively constant during the erosive period potentially enhancing offshore transport and the time averaged flow acceleration showed spatial patterns similar to the observed beach change (Figure 4-5), we extended the velocity-moment-based model following previous works to include acceleration and acceleration skewness effects. Even though both extended models outperform the velocity-moment-based model and reduced the prediction error by up to 50%, they may only serve to obtain a better prediction without representing a detailed physical description of the swash motions. For instance, *Puleo et al.* [2003] suggests that the inclusion of an acceleration term in swash zone sediment transport models likely accounts for the bore effects such as turbulence and pressure gradients on the bed. The hope is that future studies will find the root causes of observed foreshore sediment transport patterns without having to overly parameterize or ignore potentially important processes.

Some of the potential processes that are lacking in the models presented here include infiltration/exfiltration effects, advection of pre-mobilized sediment and bore turbulence. The first has been assumed or shown to be minimal in sediment transport studies in the swash zone of sandy beaches [*Turner and Masselink,* 1998; *Masselink and Li*, 2001 and *Butt et al.*, 2001] whereas limited field data have found conflicting results

on the importance of advected pre-suspended sediment [*Puleo et al.*, 2000, *Jackson et al.,* 2004 and *Butt et al.*, in press] but the concept has been recently included in a numerical model *Kobayashi and Johnson* [2001] and warrants further study. Bore turbulence, however, is not thought to be negligible and actually may dominate the sediment suspension signal [*Puleo et al.*, 2000]. *Butt et al.* [in press] recently extended a velocity-moment-based model to include a term for turbulent kinetic energy and showed that near the bore, the extension yields a dramatic improvement in predictive capability similar to the improved predictive capability using energy dissipation rather than velocity moments to estimate sediment transport across the bore [*Puleo et al.*, 2000]. If these processes are truly important, then it is not surprising that the velocity-moment-based model originally proposed by *Bagnold* [1966] does not capture the effect of the bore as the model, in its original time-averaged formulation, was not meant to predict individual bursts of transported sediment potentially caused by processes occurring at the same time large flow accelerations are observed. The study here, however, has shown that the fluid acceleration and acceleration skewness increase predictive capability in swash zone sediment transport models but that further theoretical and physical justification for their use may be needed.

Conclusions

Measurements of two-dimensional swash zone surface velocities and foreshore morphology collected during an erosive event showed that severe foreshore erosion occurred during periods of large offshore-directed low frequency cross-shore velocity skewness (non-dimensional) associated with infragravity motions and small high frequency cross-shore velocity skewness potentially enhancing offshore transport. Onshore-directed non-dimensional acceleration skewness increased during the stable

period suggesting an increase in onshore transport during that time. Extending a two-dimensional velocity-moment-based sediment transport model to include a parameterization of the fluid acceleration reduced the root-mean-square prediction error by up to 50% over the model without any extensions, suggesting that processes associated with fluid acceleration in the swash zone should not be assumed insignificant.

CHAPTER 5
NUMERICAL SIMULATION OF INNER SURF AND SWASH ZONE HYDRODYNAMICS USING THE VOLUME OF FLUID TECHNIQUE

Introduction

The surf and swash zones compromise the area of the nearshore where wave breaking, current generation, turbulence and bed shear stresses occurring over shallow bathymetry influence and drive sediment transport and morphological evolution. To better understand the details of the complex fluid processes responsible for the bathymetric change, analytic solutions and/or numerical models based on the governing equations of fluid motion are required.

Swash hydrodynamics and runup are traditionally modeled using the nonlinear shallow water equations (NLSWE), a simplification to the full Navier-Stokes equations. Some of the first attempts to model these motions were performed by *Carrier and Greenspan* [1958] who focused on non-breaking waves climbing a planar sloping beach where it was shown that the wave shape and particle velocity distribution determine the breaking potential at the shoreline. Breaking waves and bore motions on a sloping beach were later investigated by *Keller et al.* [1960], *Shen and Meyer* [1963a], *Shen and Meyer* [1963b] and *Ho and Meyer* [1962] where the focus was on the collapse of the bore at the beach and the subsequent motion of the thin uprush tongue and backwash flows. These studies led to analytical descriptions of the location of the leading swash edge as a function of space and time through ballistic motion equations and the shape of the swash lens during its cycle.

While these early studies found analytical solutions for certain hydrodynamic cases, solutions over non-planar bathymetries require numerical procedures to study more generic inner surf and swash zone flows [*Hibberd and Peregrine*, 1979]. For instance, Kobayashi and his colleagues (see *Kobayashi et al.* [1989] and *Kobayashi and Poff* [1994]) developed a 1D depth averaged nonlinear shallow water model with quadratic friction known as RBREAK that has compared well to laboratory data. In terms of field data, RBREAK was able to reproduce the shape and horizontal excursion of runup, the total runup variance with less than 20% error, the decrease in incident and increase in infragravity energy for propagating waves from the surf to the swash zones and the third moments of the wave velocity in the inner surf zone [*Raubenheimer et al.*, 1995; *Raubenheimer and Guza*, 1996 and *Raubenheimer*, 2002]. There was, however, some discrepancy between the predicted depth averaged velocities and those measured *in situ* and it was found that RBREAK over predicts the sea swell asymmetry, the maximum uprush to backwash velocity ratio and the swash zone velocity skewness [*Raubenheimer*, 2002]. Still other work on smooth slopes using an RBREAK derivative showed that only runup levels and backwash velocities compared well with measurements [*van der Meer and Breteler*, 1990].

Although these formulations have generally shown good predictive skill, the depth-averaged formulation does not yield the detailed internal flow structure necessary for predictions of fluid vorticity or shear stresses derived from velocity gradients rather than a quadratic drag law formulation. Further, the models need to be forced in relatively shallow water, do not predict the vertical fluid velocity, and pressure is approximated as hydrostatic. Finally, broken waves are modeled as bores (shocks) and hence the sea

surface cannot be multi-valued in the vertical direction meaning that overturning, plunging breakers cannot be included. In addition to RBREAK, *Zelt* [1991] and *Titov and Synolakis* [1995] used other depth averaged finite element and finite difference models to address wave breaking in solitary waves but found that the models better predicted the runup maxima rather than the time history of breaking suggesting that more detailed models are required to simulate the wave breaking process.

More recently, the advent of faster personal computers and workstations has allowed for the modeling of the full Navier-Stokes equations without major simplifications. *Liu and Lin* [1997], *Lin and Liu* [1998a], *Lin and Liu* [1998b], and *Lin et al.* [1999] modified a volume of fluid (VOF) RANS model for use in the surf zone that also included a k-ε turbulence closure scheme to model the turbulence levels. They used the model to investigate the runup and rundown of solitary waves, turbulence transport under breaking waves and the propagation and evolution of a shoaling wave train across the surf zone. Their results showed good correlation with sea surface and velocity data collected in a laboratory flume. They determined that the mean particle velocity in the roller region of the breaking wave is at least 80% of the wave celerity, the pressure distribution under a spilling wave only deviates by up to 7% from hydrostatic and that the breaking wave process is a "local" process in that mean vorticity and turbulence are weak away from the wave front. It was also found that even for nonbreaking swash the shallow water assumption may be inaccurate due to occasionally large vertical variations in the horizontal velocity.

Several other Navier-Stokes solvers have been used to study breaking waves [*Lemos*, 1992; *Zhao and Tanimoto*, 1998; *Chen et al.*, 1999 and *Christensen and*

Deigaard, 2001], non-breaking wave runup [*Wood et al.*, 2003] and breaking wave, runup and swash processes [*Puleo et al.*, 2002]. These models have shown promise in predicting sea surface elevations, fluid velocities and other fluid motion descriptors including turbulence intensity and the 3D structure of turbulent eddies in the *Christensen and Deigaard* [2001] case (*Lin and Liu* [1998a] give a good review of recent numerical studies of turbulence and turbulence modeling associated with wave breaking). A major benefit to these types of models versus the depth-averaged NLSWE approach is the ability to distinguish the vertical flow structure, the time dependent evolution of the boundary layer, and wave breaking processes that may eventually assist in the difficult problem of sediment transport prediction in these regions. Yet, much of this past work has focused on the breaking process in the surf zone with little emphasis on the hydrodynamic processes occurring in the inner surf/swash zone for regular and irregular wave trains.

The purpose of this chapter is to describe a volume of fluid model known as RIPPLE that was originally developed by researchers at the Los Alamos National Laboratory [*Kothe et al.*, 1991] and show its predictive capability for inner surf and swash zone flows. The following section describes the model equations and turbulence closure scheme used. Then the model domain, numerical scheme, discretization methods, wave forcing, boundary conditions and modifications made to the original source code are addressed. The laboratory facility where inner surf and swash zone data was collected is described in the next section followed by model results, model-data comparisons, discussion and conclusions. Appendices are included at the end of this

dissertation to address numerical dissipation caused by the finite difference schemes used as well as the utility of the large eddy simulation subgrid scale closure scheme.

Ripple

Governing Equations

The RIPPLE model was developed by for incompressible flows with free surfaces [*Kothe et al.*, 1991] and has been utilized previously for breaking waves [*Liu and Lin*, 1997]. RIPPLE is derived from the mean 2D Navier-Stokes equations as

$$\frac{\partial u_i}{\partial x_i} = 0$$

$$\frac{\partial u_i}{\partial t} + u_j \frac{\partial u_i}{\partial x_j} = -\frac{1}{\rho}\frac{\partial p}{\partial x_i} + \frac{\partial}{\partial x_j}\left[\upsilon \frac{\partial u_i}{\partial x_j} + \upsilon \frac{\partial u_j}{\partial x_i}\right] + g_i + \frac{1}{\rho}\Gamma_{ij} \quad , \text{(5-1)}$$

where x_i and u_i are the spatial and mean velocity components, respectively, in the i direction (for 2D problems such as the one investigated here $i = 1$ is the cross-shore direction, $j = 2$ is the vertical direction), g_i is gravitational acceleration, p is the pressure, υ is the kinematic viscosity, and Γ_{ij} is a body force. The first relationship in equation 5-1 represents mass continuity and the second momentum conservation.

Turbulence Closure

Due to the temporally and spatially variable turbulence levels that are observed in the inner surf and swash zones, a turbulent eddy viscosity rather than solely a molecular viscosity can be used to incorporate an additional diffusion mechanism. In depth integrated model formulations, some studies have resorted to the inclusion of an eddy viscosity-type model [*Zelt*, 1991] or a roller model [*Schaffer et al.*, 1993] to account for the turbulence in the breaking portion of the wave. Rather than attempting either of the

above techniques used in the depth-integrated cases, a turbulence closure scheme is utilized to determine a turbulent eddy viscosity in conjunction with the molecular viscosity in equation 5-1.

A variety of turbulence closure schemes exist in the literature with the k-ε scheme being the most often used [*Wilcox* 2000]. This scheme and its numerous variations explicitly model the turbulent kinetic energy and dissipation rate of energy through two coupled equations by assuming that the Reynolds stresses follow the Boussinesq hypothesis and can be modeled by gradient diffusion. While the k-ε equations are often used, many difficulties can arise using them in complex flows such as those with boundary layer separation and adverse pressure gradients [*Rodi and Scheuerer*, 1986; *Pope*, 2000 and *Wilcox*, 2000]. In addition, five closure coefficients are needed for the model. While these coefficients have been investigated for flows like free shear turbulence (*Hwang and Jaw* [1998] provide a review) through comparisons to laboratory data and direct numerical simulations, they have not been rigorously determined for more complex flows like breaking waves. However, it should be noted that *Lin and Liu* [1998a] have successfully coupled a k-ε scheme using the common values for the closure coefficients into a model based on RIPPLE for breaking cnoidal waves and showed good comparison to laboratory data. Sensitivity tests, though, showed a 10% change in the coefficient on the production rate of turbulent dissipation term caused a 50% change in the total turbulent kinetic energy in the surf zone after wave breaking.

Instead of pursuing the k-ε closure scheme or derivative thereof, our approach is to adopt a large eddy simulation (LES). A LES results from calculating the stresses at the resolvable scales, and modeling them at the sub grid scales (SGS). LES has been

successfully used in many applications including two and three dimensional breaking wave volume of fluid models (*Zhao and Tanimoto* [1998] and *Christensen and Deigaard* [2001] respectively; see *Moin and Kim* [1982] ; *Ferziger and Peric* [1999] or *Zikanov et al*., 2002 for LES details) so its use here seems justified.

To proceed with LES, the Navier-Stokes equations 5-1 are filtered at the resolvable scales assuming that the SGS turbulence is isotropic leaving [*Wilcox* 2000]

$$\frac{\partial \overline{u}_i}{\partial x_i} = 0$$

$$\frac{\partial \overline{u}_i}{\partial t} + \overline{u}_j \frac{\partial \overline{u}_i}{\partial x_j} = -\frac{1}{\rho}\frac{\partial \overline{p}}{\partial x_i} + \frac{\partial}{\partial x_j}\left[\upsilon \frac{\partial \overline{u}_i}{\partial x_j} + \upsilon \frac{\partial \overline{u}_j}{\partial x_i}\right], \quad (5\text{-}2)$$

$$-\frac{\partial}{\partial x_j}\left(\overline{u_i u_j} - \overline{u}_i \overline{u}_j\right) + g_i + \frac{1}{\rho}\overline{\Gamma}_{ij}$$

where an overbar denotes a filtered quantity obtained by the volume-averaged (2D) box filter (example for u)

$$\overline{u}_i(x,z,t) = \frac{1}{\Delta^2}\int_{x-\frac{1}{2}\Delta x}^{x+\frac{1}{2}\Delta x}\int_{z+\frac{1}{2}\Delta z}^{z+\frac{1}{2}\Delta z} u_i(\xi,\eta,t)\,d\xi\,d\eta\,, \quad (5\text{-}3)$$

where Δ is a measure of the filter width (mesh size) defined as

$$\Delta = \sqrt{\Delta x \Delta z}\,. \quad (5\text{-}4)$$

The SGS velocity is then given as the difference between the fluid velocity and the filtered velocity as

$$u_i^{'} = u_i - \overline{u}_i\,. \quad (5\text{-}5)$$

Note that an extra term, the subgrid scale Reynolds stress, appears in equation 5-2 after the filter has been applied and is sometimes decomposed into individual stress terms [*Wilcox*, 2000]

$$\begin{aligned} L_{ij} &= \overline{\overline{u}_i \overline{u}_j} - \overline{u}_i \overline{u}_j \\ C_{ij} &= \overline{\overline{u}_i \overline{u}_j'} + \overline{\overline{u}_j \overline{u}_i'} \\ R_{ij} &= \overline{u_i' u_j'} \end{aligned} \quad . \text{(5-6)}$$

The physical significance of each of the terms was described by *Ferziger and Peric* [1999]. The first term is called the Leonard or outscatter term and represents the interaction of two resolved scale eddies to produce small scale (unresolved) turbulence. The second term is referred to as the cross term and represents the interaction between resolved and unresolved eddies. The last term is referred to as the true subgrid scale or backscatter term and represents the interaction between two unresolved eddies to produce a large scale (resolved) eddy. In this sense it produces energy transfer from the small scale back to the large scale.

It is possible to model the last two terms individually (the Leonard term can be calculated from the resolved field), but *Ferziger and Peric* [1999] point out that it is common to model the entire SGS Reynolds stress as a single unit

$$\tau_{ij} = L_{ij} + C_{ij} + R_{ij} \, . \text{(5-7)}$$

Smagorinsky [1963] proposed a simple SGS model for this stress term, equation 5-7, assuming the stresses follow the Boussinesq gradient diffusion hypothesis as

$$\tau_{ij} = -2\upsilon_T e_{ij} \, , \text{(5-8)}$$

where e_{ij} is the resolved strain rate given by

$$e_{ij} = \frac{1}{2}\left(\frac{\partial \overline{u}_i}{\partial x_j} + \frac{\partial \overline{u}_j}{\partial x_i} \right), \quad (5\text{-}9)$$

and ν_T is the turbulent eddy viscosity

$$\upsilon_T = \left(C_s \Delta\right)^2 \sqrt{e_{ij} e_{ij}} \ . \quad (5\text{-}10)$$

The constant C_s is known as the Smagorinsky coefficient and typically has values between 0.1 and 0.24 [*Rogallo and Moin*, 1984] for three-dimensional applications. Less attention has been paid to two-dimensional applications of LES where the turbulent eddy viscosity has to account for the individual stress terms previously mentioned due to the incapability of the 2D model to allow for vortex stretching [*Haas and Svendsen*, 2000]. For 2D applications, values of C_s both greater and less than those used in 3D applications have been used whereas *Haas and Svendsen* [2000] applied the typical values for all simulations in their 2D model. Often the Smagorinsky coefficient is tuned to better correlate observations with simulations, but without justification, only one typical value, 0.2, is used here.

Near a solid boundary, the Smagorinsky model overpredicts the turbulent eddy viscosity because it does not account for the effect of the wall on restricting the turbulent length scale. As such, wall damping functions are often used to smoothly bring the turbulent length scale and hence the turbulent eddy viscosity to zero at the wall (through multiplication with the length scale). Many wall damping functions exist (see *Hwang and Jaw* [1998] or *Piomelli and Balaras* [2002] for a review) and the widely used *van Driest* [1956] damping function is used here. This function has the form

$$D = \left[1 - \exp\left\{ -\left(\frac{z^+}{A^+} \right)^2 \right\} \right] \ , \quad (5\text{-}11)$$

where z^+ ($=zu^*/\upsilon$) is the distance from the wall in viscous wall units, u^* is the shear velocity at the wall and A^+ is a constant set to 25.

In addition, numerical viscosity could play a role in diffusion based on the numerical scheme used. *Liu and Lin* [1997], using their modified model based on the RIPPLE source code, performed an analysis to show that under non-breaking solitary waves the numerical dissipation is negligible. A similar test is also performed in our study (appendix-A).

Numerical Procedures and Solution Method

Model Domain

Model domains are divided into individual control volumes where the amount of fluid in each is specified by a volume of fluid function, *VOF*. The value of *VOF* is 0 in air, 1 in water and is between 0 and 1 at the free surface and near the boundaries of the model domain. Variables are defined following the marker and cell (MAC) staggered scheme [*Harlow and Welch*, 1965] such that horizontal velocities, u, are defined on the vertical volume faces while vertical velocities, w, are defined on the horizontal volume faces. Values of *VOF*, p and υ_T are defined at the mass control volume center. Momentum control volumes are also defined for fluxing x and z momentum and are centered about the horizontal and vertical mass control volume velocities (see diagram in *Kothe et al.* [1991]; page 9).

Discretization

The model is discretized using a finite difference scheme with central spatial differences and a forward time step. Care must be taken in the discretizations because the

staggered grid often means that values at a given location are not defined requiring linear interpolation. Representations of the individual finite differences are not given here as they are fully described elsewhere [*Liu and Lin*, 1997].

Past use of the model for breaking waves [*Liu and Lin*, 1997] utilized an interpolated donor cell method that combines both upwind donor cell and central differencing for the momentum advection terms. The donor cell method introduces numerical damping that tends to offset the numerical dispersion introduced by central differencing [*Kothe et al.* 1991]. Our usage relies on the *van Leer* [1979] method for upstream velocity estimation for the advection terms which purports to improve the accuracy by retaining second order terms to the Taylor series expansion. *Kothe et al.* [1991] also state that the Van Leer method forces weak monotonicity so that no new velocity extrema after momentum advection are introduced relative to those prior to advection.

Two–step projection method

RIPPLE is solved using a two-step projection method (further explained in *Kothe et al.* [1991] and *Slinn and Riley* [1998]) by defining an intermediate velocity, $\overline{U}$, which satisfies

$$\frac{\overline{U}_i^{n+1} - \overline{u}_i^n}{\delta t} = -\overline{u}_j \frac{\partial \overline{u}_i^n}{\partial x_j} + \frac{\partial}{\partial x_j}\left[\left(\upsilon + \upsilon_T\right)\left\{ \frac{\partial \overline{u}_i}{\partial x_j} + \frac{\partial \overline{u}_j}{\partial x_i} \right\} \right]^n + g_i + \frac{1}{\rho}\overline{\Gamma}_{ij} \quad , \text{(5-12)}$$

where δt defines the computational time step, and the superscript, n, denotes the time level. Equation 5-12 is the time discretized form of the Navier-Stokes equation with the removal of the pressure term. Hence, $\overline{U}_i$ is calculated from changes due to advection,

gravity, viscosity, shear stress and body forces only. The second step of the two-step method is to project the $\overline{U}_i$ velocity field onto a non-divergent vector field to obtain $\overline{u}_i$ at the new time level

$$\frac{\overline{u}_i^{n+1} - \overline{U}_i^{n+1}}{\delta t} = -\frac{1}{\rho^n}\frac{\partial \overline{p}^{n+1}}{\partial x_i} \quad (5\text{-}13)$$

$$\frac{\partial \overline{u}_i^{n+1}}{\partial x_i} = 0\,, \quad (5\text{-}14)$$

where equation 5-14 is the continuity equation satisfied at the n+1 time step. The pressure Poisson equation (PPE) is obtained by combining equation 5-13 and the divergence of equation 5-14 into a single equation to be solved

$$\frac{\partial}{\partial x_i}\left(\frac{1}{\rho^n}\frac{\partial \overline{p}^{n+1}}{\partial x_i}\right) = \frac{1}{\delta t}\frac{\partial \overline{U}_i^{n+1}}{\partial x_i}\,. \quad (5\text{-}15)$$

The density is retained inside the divergence operator even though RIPPLE solutions are for constant density fluids to accommodate the pressure solution at the free surface transition. Discretization of equation 5-15 results in a matrix equation that is solved via an incomplete Cholesky conjugate gradient method, a rapidly converging iterative technique.

Free Surface

Unlike many hydrodynamic models that explicitly track the free surface, RIPPLE uses the VOF technique instead [*Hirt and Nichols*, 1981]. The VOF function, the amount of fluid in each cell, is advected according to the total derivative on ρ and the mass continuity as

$$\frac{DF}{Dt} = 0\,, \quad (5\text{-}16)$$

where $F(x,z,t)=\rho(x,z,t)/\rho_{fluid}$. The free surface is then typically defined to reside in those fluid volumes where the VOF function is near 0.5. The slope of the free surface is reconstructed by calculating the gradient of the VOF field.

Internal Obstacles – An Impermeable Beach

Creating a beach surface in RIPPLE requires defining an internal solid obstacle in the model domain. The RIPPLE model treats obstacles as two-phase flow, such that the fluid occupies a volume fraction, θ, and the obstacle occupies a volume fraction of 1-θ. The fluid density inside the obstacle is given as infinite and the obstacle maintains zero velocity throughout a computation. Values for θ, vary from 0 (inside the obstacle) to 1 (inside the fluid domain). Near the obstacle boundary, values of 0 or 1 for θ manifest only when the obstacle is defined along the model mesh. Hence, for potentially curved boundaries, $0<\theta<1$. These values are necessary to avoid the jagged representation of a curved surface by discrete representation. *Kothe et al.* [1991] have termed these "partial flow cells" because only the θ portion of the cell volume is open to fluid and the remaining portion is closed to fluid flow. Two-phase flow equations are then prescribed near boundaries by incorporating θ into the mass and momentum equations, and thereby modeling flow near "smooth" boundaries.

Wave Forcing and Boundary Conditions

Waves have been forced in a VOF model in the past by way of a numerical wave maker [*Lin and Liu*, 1999]. That approach involved adding a source term to the continuity equation that was applied over a source region of a defined width and height. The source function was prescribed given an analytic solution for simple wave forms or for irregular wave forms using a Fourier series. In our study, we adopt a different

approach where we force both velocity components and the free surface at the seaward edge of the domain. By allowing the seaward boundary condition to be an inflow/outflow boundary, the horizontal and vertical velocity can be forced in a region that is only one computational cell wide (the limit of the *Lin and Liu* [1999] method, but for velocity and sea surface). Because measurements made for forcing the model are generally only collected at one of several locations in the vertical, we force the model with uniform horizontal and vertical velocities based on measurements and analogous to a piston-type wave maker. If the model is forced in sufficiently shallow water and the waves are small, this is not a great departure from linear theory. Alternatively, the model can be forced using a velocity measurement and some form of vertical decay, although this form becomes complicated in a random wave field such as that used in part of this study. Therefore, a uniform velocity profile is used in all cases presented here.

As mentioned above, in addition to forcing the velocity components at the seaward boundary, the free surface is also forced based on measurements. To do so, the grid locations spanning the measured free surface at the new time step are determined, all cells in the location below the measured free surface are completely filled and the cell containing the free surface is filled with the remaining volume. For instance, a measured free surface of 4.13 (arbitrary units) would be located between grid points 4 and 5 (free surface is located in cell 4) corresponding to the same arbitrary units. So, the fluid cells are filled (VOF set to 1.0) in cells 1, 2, 3 and the VOF function is set to 0.13 in cell 4. In other words, cell 4 is set to 13% full to coincide with the amount of the total cell volume occupied assuming cell sizes in this example are 1 unit by 1 unit.

Boundary conditions for the simulations used are given as rigid no slip along the bottom, top and landward side of the domain. As previously described, an inflow/outflow condition is used at the offshore boundary so that fluid can enter or leave the domain based on the forcing conditions described above. Boundary conditions at the bed are no slip, as specified using the partial flow method described above.

Model Modifications

Liu and Lin [1997] documented several changes that they made to the original RIPPLE source code to improve accuracy which we have adopted in our model. The first are the errors during the PPE computation that result in spurious velocity vectors. The errors arise because the tangential stress boundary condition in the PPE solution cannot be performed on an exact free surface because the free surface is not explicitly tracked in RIPPLE. Therefore, they suggested that the tangential stress boundary condition and the pressure be solved at the grid point just below the free surface where the PPE solution is known to be more accurate. Also, VOF advection can lead to the filling of cells that were empty in the previous time step. They state that RIPPLE does not apply the correct boundary condition when this happens and suggest following the method of *Chen et al.* [1995] to alleviate this error. That method basically states that the velocity at the free surface be forced to the velocity at the cell just below the free surface at the end of each computation time step replacing the potentially spurious vector at the free surface.

Data Collection

In July 2001 and June 2002, laboratory studies were carried out in the Large-scale Sediment Transport Facility (LSTF) at the Coastal Hydraulics Laboratory of the Army Corps of Engineers in Vicksburg, MS [*Hamilton and Ebersole*, 2001].

Figure 5-1. Snapshot of the Large-scale Sediment Transport Facility showing the instrumentation bridge, *in situ* sensors and surf zone waves.

The LSTF is a 30 m cross-shore by 50 m alongshore by 1.4 m deep wave basin with a nominal offshore slope of roughly 1:30 and a steeper foreshore (Figure 5-1). Median sediment grain size was 0.15 mm. Waves are forced at a shallow angle with four unidirectional spectral wave generators. A moveable instrumentation bridge spans the cross-shore expanse of the basin and is outfitted with twelve wave gages and acoustic Doppler velocimeter (ADV's) pairs separated by approximately 1.5 m. Four ADV sensors were also deployed at three locations in the swash zone. At the outer swash location, two ADV's were stacked vertically, separated by roughly 0.04 m.

Figure 5-2 shows a cross-shore profile of the inner surf and swash zones of the LSTF beach on July 10**,** 2001 and June 19, 2002. The actual beach extends out to a cross-shore location of about x = 20 m, but only the model domains are shown here. The vertical lines show the locations of the wave gages with the waves being forced at x = 0. Filled circles denote ADV's that are used for forcing and model to data comparisons.

The wave conditions on July 10, 2001 were monochromatic with a wave height (H) of 0.21 m and a period (T) of 3 s whereas on June 19, 2002 irregular waves were used with an H_{rms} = 0.16 m and a peak period of 1.5 s. During both configurations, surface elevations and cross-shore fluid velocities were recorded at 20 Hz (10 Hz in the swash zone).

Results

RIPPLE simulations were performed with and without LES for each test run. In all four simulations, the cross-shore grid spacing was 0.004 m and the vertical grid spacing was 0.002 m. The nominal time step is 0.02 s, but stability constraints often require smaller time steps and are automatically adjusted during the simulations.

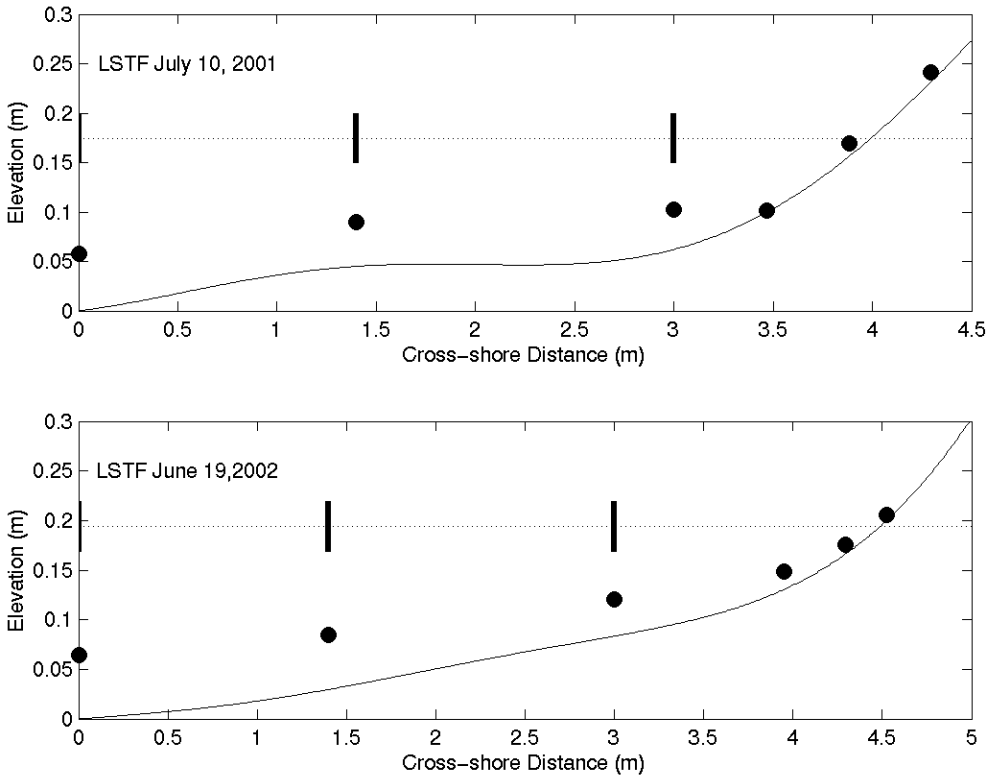

Figure 5-2. Cross-shore profiles in the model domain for July 10, 2001 and June 19, 2002. Vertical lines denote the location of wave gages and filled circles the location of ADV's.

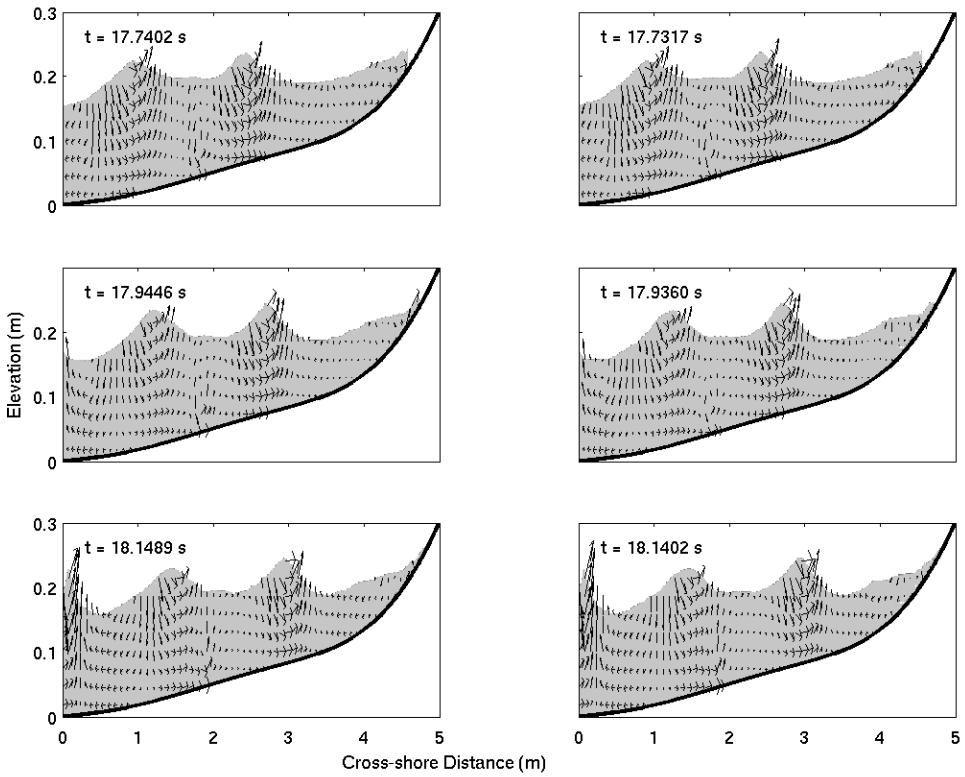

Figure 5-3. Sea surface and velocity vector comparison for June 2002 for non-LES (left) and LES (right) simulations.

Model output is written at 50 Hz. Because of the large number of grid points, 1202 x 162 (July, 2001) and 1352 x 162 (June, 2002), and the computational intensity required to run the model, only 40 s simulations are performed (requiring roughly 2 weeks of CPU time on a Sun Blade 1000 Processor).

Figure 5-3 shows six snapshots from the model including the velocity vectors and the volume of fluid (shaded region) for June 19, 2002. The time is given in the upper left of the images. The LES data are shown on the right and the closest corresponding data from the simulation without LES are shown on the left. Only every 20^{th} horizontal and every 15^{th} vertical vector are shown for clarity. In plots with exaggeration in one dimension, the vector direction can appear distorted. One option is to multiply the exaggerated vector component by the ratio of axis length scales (in this case vertical to horizontal) to show the true direction. This vector manipulation, however, will yield incorrect vector magnitudes. As such, we choose to show the velocity vectors in their true magnitudes but exaggerated directions and caution the reader to take the plot exaggeration into consideration when viewing Figure 5-3; specifically with respect to the vectors near the free surface and waves. The upper panels show a bore just about to collapse on the foreshore with the upper portion of the water column slightly landward of the lower part of the water column. This overturning feature is not possible in a 1D depth-averaged modeling simulation. The middle 2 panels occur approximately 0.2 s later and show the initial stages of uprush followed by later stages of uprush in the lower 2 panels. It is apparent that at this resolution there is little distinguishable variation in model output between the LES and non-LES simulations. This suggests that at this resolution the LES scheme has little effect in modifying the turbulent eddy viscosity

since at this scale the energy containing eddies are likely much larger. The LES, however, can be beneficial when the model is run at poorer grid resolution (appendix-B). Based on the similarity between LES and non-LES simulations only non-LES simulations are shown in the following figures and the LES is addressed in more detail in appendix-B.

Sea Surface Elevations

Sea surface elevation comparisons from the ADV locations in the inner surf zone show good overall correspondence (Figure 5-4). In all cases some transients are observed near the beginning of the run as the model spins up to forcing conditions and are not included in the root-mean-square error calculation (Table 5-1). However, by approximately 5 s into the simulation, the sea surface time series has begun to be well-predicted by the model. At times, though, the sea surface elevation is slightly under-predicted by the model and small phase lags are observed. While we have no exact explanation of these differences, we suspect that three-dimensionality that cannot be avoided in the wave basin plays some role in the mismatch. For instance, any directional variation in wave motion or interaction between reflected waves from basin walls or non-zero incidence reflected waves from the beach face could adversely affect our two-dimensional simulation.

Flow Velocity

Cross-shore velocity time series comparisons between the model and data show high visual correlation (Figure 5-5). In the inner surf zone, the model typically matches the measurement magnitudes but some phase shifting is visible.

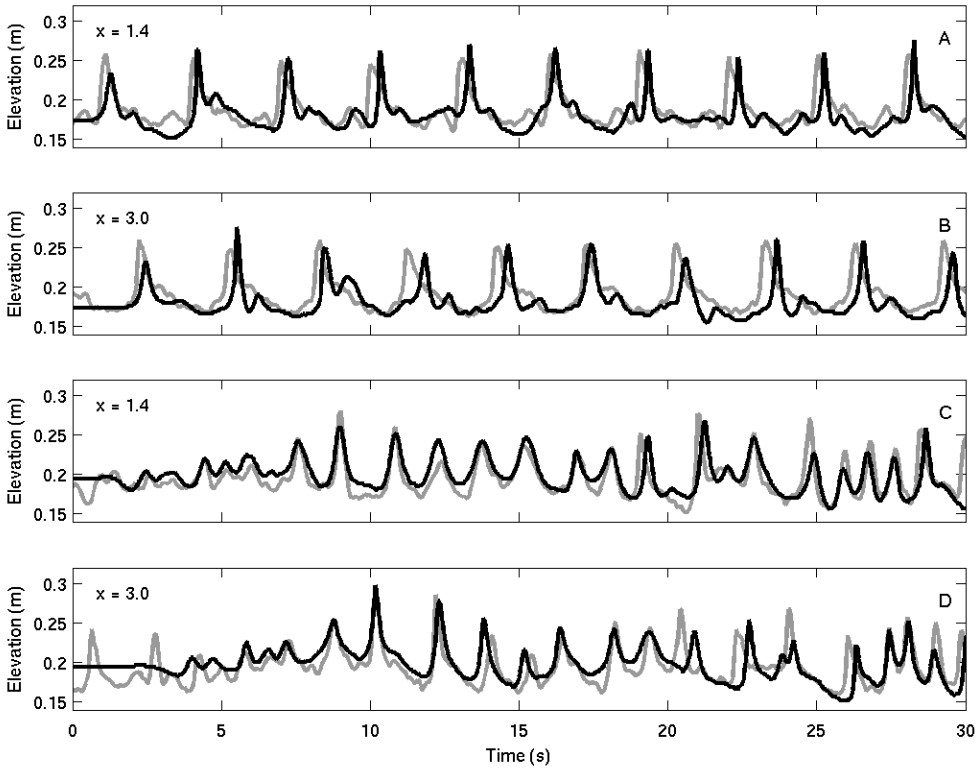

Figure 5-4. Sea surface elevation comparisons between model output (black) and data (gray) at 2 locations in the inner surf zone for July 2001 (A,B) and June 2002 (C,D).

Table 5-1. Root-mean-square errors between model and *in situ* measurements for sea surface (m) and horizontal velocity (m s^{-1}) in the inner surf zone.

	x = 3.0 m	x = 3.47 m		x = 3.0 m	x = 3.95 m
Sea surface elevation, July 2001 (monochromatic waves)	0.023	0.024	Sea surface elevation, June 2002 (irregular waves)	0.018	0.020
Cross-shore velocity, July 2001 (monochromatic waves)	0.17	0.18	Cross-shore velocity, June 2002 (irregular waves)	0.09	0.21

The comparisons are somewhat poorer in the monochromatic wave case, but are likely attributed to the ADV rather than the model as evidenced by the high number of culled data based on signal correlations (the gaps in the *in situ* time series). As the swash zone is approached, the velocity magnitudes are still well-predicted, but some phase shifting in the peaks in observed. The phase shifting is also partially responsible for some of the error as no temporal offset was utilized to align the time series (Table 5-1). The fact that only uprush velocities are seen in a few instances (Figure 5-5, x = 4.3m at 15 s) indicates that under these conditions the backwash depth was less than the height of the current meter, the vertical location of the time series extraction from the model. The high percentage of culled data in the swash zone also points to the difficulty in obtaining velocities in these thin flows. When *in situ* data is available in the swash zone it tends to match that extracted by RIPPLE, further suggesting that the model accurately predicts cross-shore fluid velocities across the inner surf and swash zones. The sections of swash zone time series with a constant zero velocity indicate periods when the collection location was unwetted or the water depth was below the elevation of the extraction location for the velocity time series. These periods could be more appropriately represented by replacing the zero velocity with a not-a-number, but for visual simplicity, zeroes remain in the time series.

Vertical velocities vary across the inner surf and swash zones with maximum magnitudes approaching 1/5 of their cross-shore counterparts (Figure 5-6). Only bi-directional ADV's were used in the inner surf and swash zones. Therefore, no comparison between model and *in situ* data can be made.

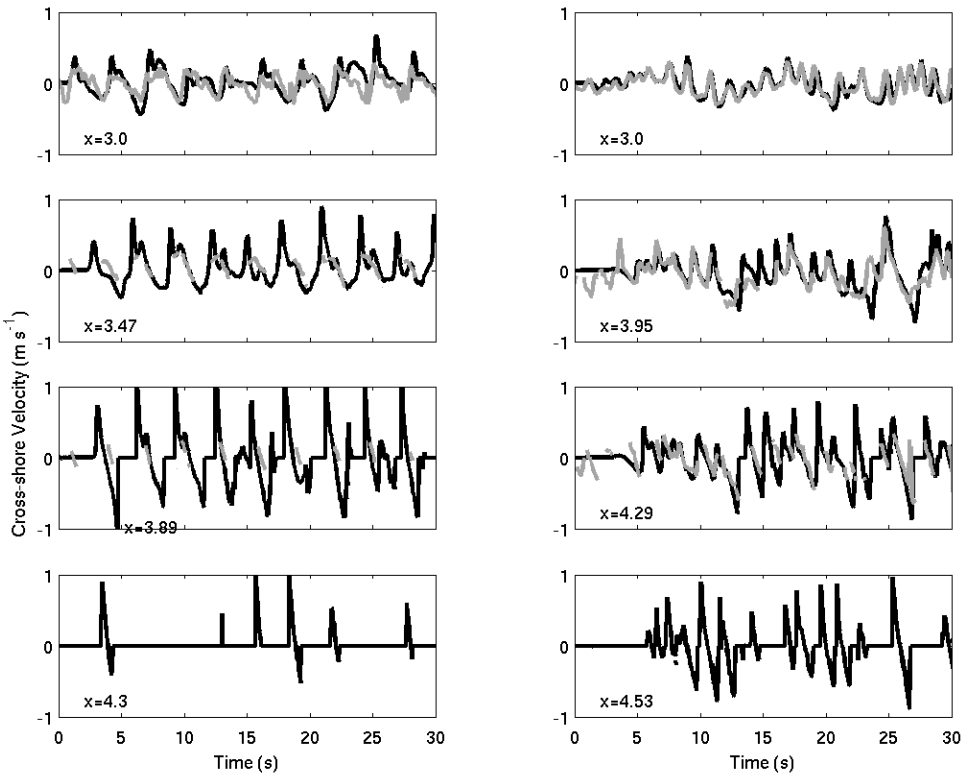

Figure 5-5. Horizontal velocity comparisons between model output (black) and data (gray) in the inner surf and swash zones for July 2001 (left) and June 2002 (right).

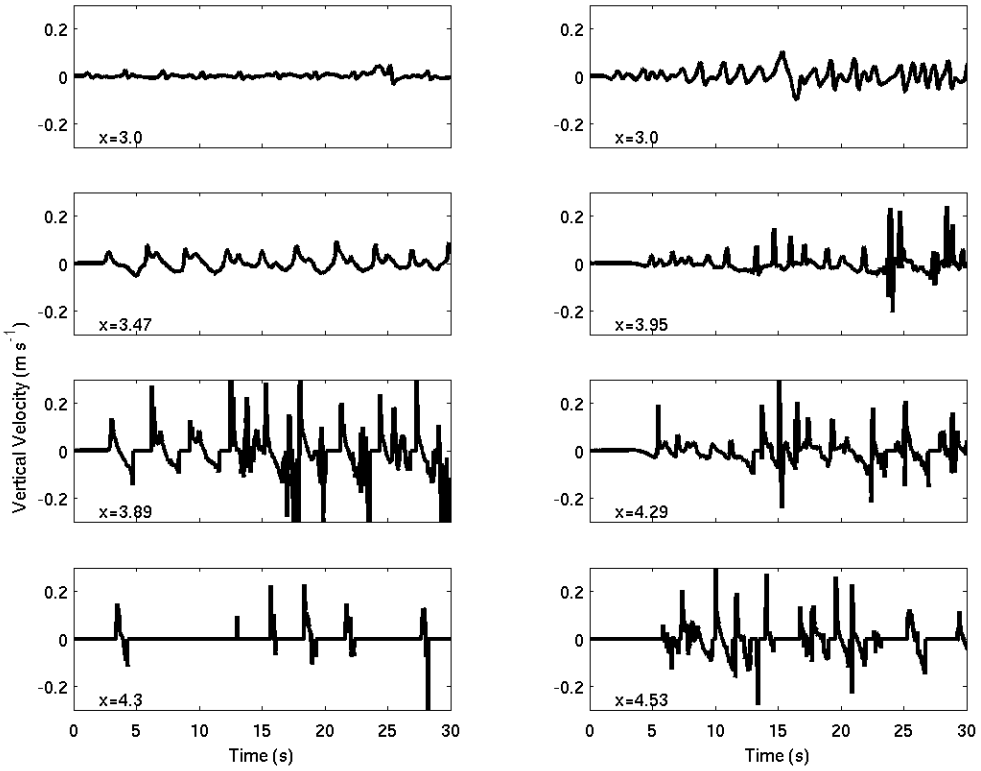

Figure 5-6. Vertical velocity model output in the inner surf and swash zones for July 2001 (left) and June 2002 (right).

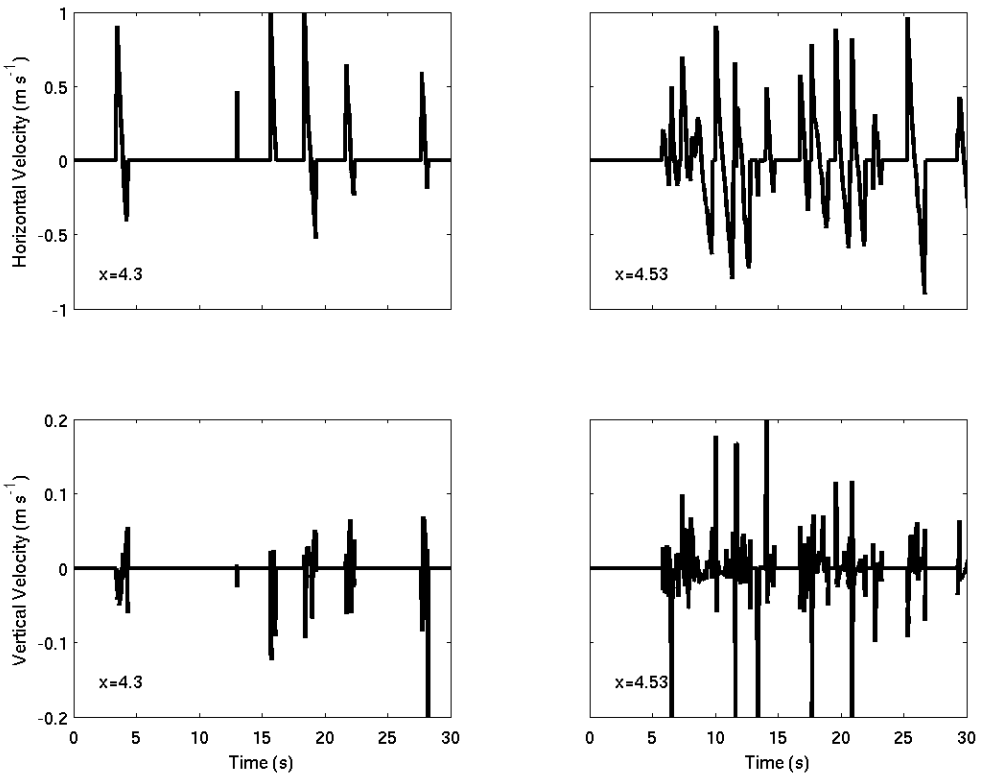

Figure 5-7. Horizontal and vertical velocity model output rotated into a bed parallel-bed orthogonal coordinate system. Locations from the swash zone on June 2002.

However, if the models predictive capability for sea surface elevation and cross-shore velocity are accepted, then it is reasonable to assume that the vertical velocities are also well-predicted. In the monochromatic case, the vertical velocities in the inner surf zone are only 0.05 to 0.1 m s^{-1}. In contrast, vertical velocities for the irregular wave case are nearly double. Large variations are observed in the swash zone with values greater than 0.2 m s^{-1} being observed close to the bed. It should be kept in mind when viewing these figures that vertical velocity is given with respect to the horizontal and vertical domain and not a beach normal coordinate system. Hence, if one wanted to rotate the coordinate system to be parallel and orthogonal to the beach face, the velocities normal to the bed would be reduced by roughly 2% in magnitude based on an approximate foreshore slope of 10° (Figure 5-7).

In the swash zone, vertical velocities on the order of 0.1 m s^{-1} are observed and not predicted by shallow water theory where the flow is assumed to be almost solely bed parallel. The downward vertical velocity predicted at bore collapse should supply a force to the bed that is not predicted or accounted for in simple boundary layer approximations of the swash flows. Yet, because the maximum vertical velocities are only 5-10% of the maximum horizontal velocities and are likely only important for a short portion of the swash cycle, much of the flow appears to conform to the shallow water criteria of being nearly bed parallel.

Velocity Profiles

Figure 5-8 shows velocity profiles for a short subsection of the June 2002 simulation. Each profile is offset by 0.5 m s^{-1} and the vertical gray line denotes zero velocity. Cross-shore positions are shown in the upper right heading onshore as x increases.

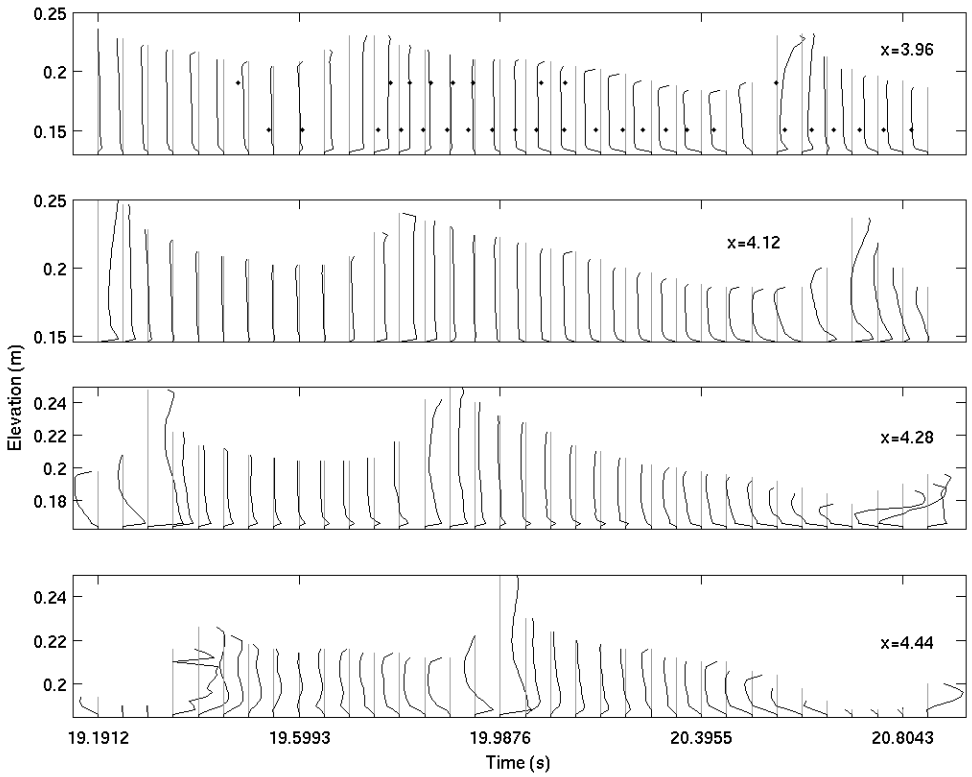

Figure 5-8. Velocity profiles from several locations across the inner surf and swash zones for June 2002. Profiles are offset by 0.5 m s^{-1} and zero velocities denoted by vertical gray line. Dots are data collected from the stacked ADV's.

In these cases from the inner surf and swash zones the boundary layer is observed to be on the order of 0.01 m or less throughout much of the bore propagation and swash cycle. In the swash zone, the model produces results similar to laboratory measurements [*Cowen et al.*, 2003] where the flow field had a high degree of depth uniformity during uprush. During backwash, a stronger boundary layer develops. Strong vertical gradients are predicted near the end of the backwash and beginning of the uprush phase during the collision process. At this time, high velocity backwash flows near the bed are over-taken by high velocity uprush flows near the surface (similar to undertow) causing vertical variations on the order of 1.5 m s^{-1} over distances as small as 0.01 m (Figure 5-8 near t = 20.0843). In contrast, at times backwash flows are observed higher in the water column, but the adverse pressure gradient supplied by the succeeding bore has caused the slower flow in the near bed boundary layer to reverse to the onshore direction (Figure 5-8 near t = 19.9876 s at x = 4.44 and slightly earlier at x = 4.28). This latter observation is more analogous to wave bottom boundary layer type flows where nearbed flows tend to reverse direction before flows above the boundary layer. At location x = 3.96, dots indicate the velocity measurements from the stacked ADV's 0.01 m away and show that the vertical structure predicted by the model is also typically observed in the *in situ* data.

Mean Flow

Mean flows for the simulations for both days are shown in Figure 5-9. The mean was taken by averaging a given cell only when it had fluid in it so the averaging is not biased by empty fluid volumes. In both instances, mean flow patterns show a dominance of shoreward motion in the upper water column near the propagating bores and small values of mean offshore flow below.

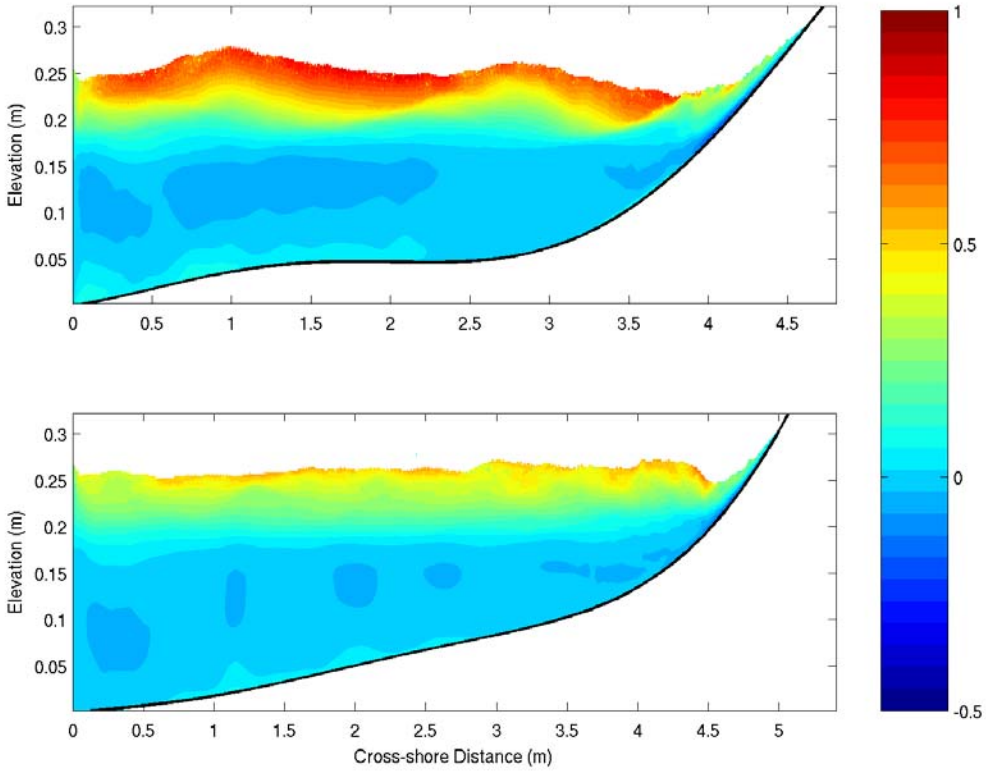

Figure 5-9. Mean horizontal velocity fields. Upper panel for July 2001. Lower panel for June 2002. Colorscale is the velocity in m s^{-1}.

It is also evident that an undertow is predicted by the model denoted by the thin region of offshore-directed flow landward of cross-shore locations x = 4.0 and x = 4.5 for July 2001 and June 2002 respectively. We find that the undertow feature extends up into the seaward portion of the swash zone and shows that the feature of uprush overriding backwash (observed in Figure 5-8) has some persistence.

Flow Acceleration

Flow accelerations have recently been reported to serve as a proxy for additional sediment transport mechanisms [*Drake and Calantoni*, 2001] and can be easily determined from the model output using second order differences. Note that care was taken in calculating the acceleration so that only one-sided differences were used at the first and last instance of a swash cycle. In this way, the acceleration is not biased by differencing with a zero velocity value when the location is unwetted**.** The cross-shore local, and convective acceleration for the June, 2002 simulation are shown in Figure 5-10 for locations at x = 3.95 m, x = 4.29 m and x = 4.53 m all at 4 mm above the bed. It is clear that local fluid accelerations (analogous to those that would be measured with a fixed instrument in the field) occur under broken waves. In addition, short-lived large onshore directed local fluid accelerations are also observed near the shoreline in the inner surf/swash zone where fluid collisions occur. Large shore-directed accelerations are not observed at the locations shown when they are landward of the initial start point for a swash cycle. The model also predicts backwash deceleration that has been observed in field data [*Puleo et al.*, 2003].

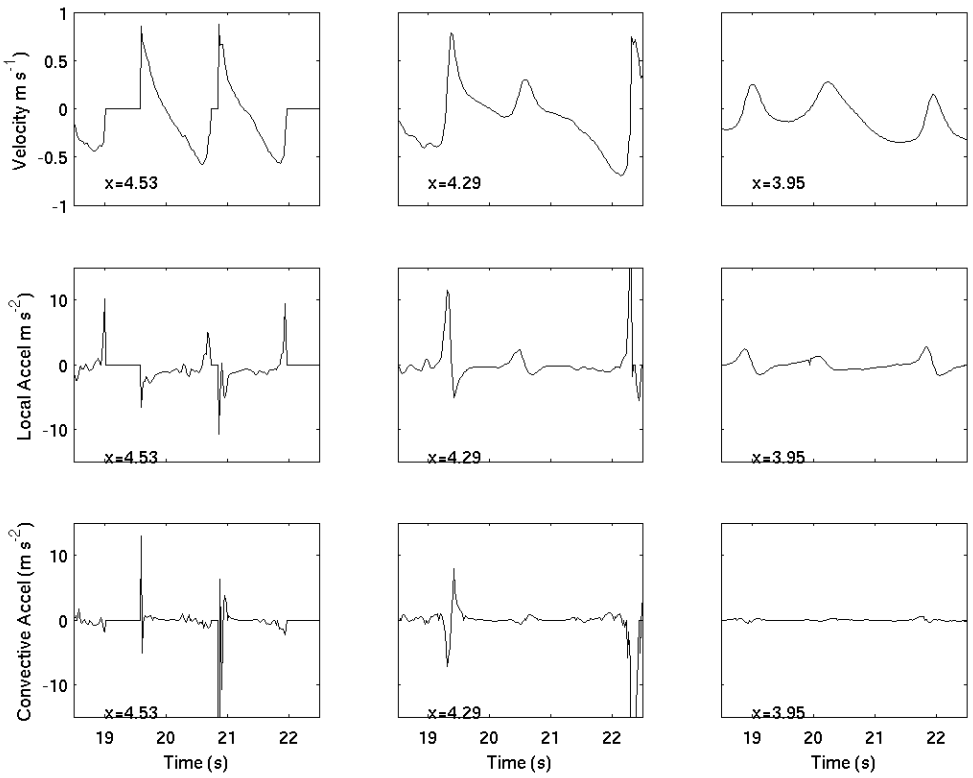

Figure 5-10. Velocity (upper panels), local acceleration (middle panels) and convective acceleration (lower panels) from 3 locations on June 2002.

While convective accelerations have been largely ignored in the inner surf and swash zones (see *Jensen et al.* [2003] for depth dependent acceleration measurements inside the swash front), it is evident from this model simulation (Figure 5-10) that they exist and can be the same order of magnitude as the local acceleration. Therefore, if acceleration is thought to affect sediment transport or is important to understanding of swash flows, both the local and convective acceleration should be considered.

Pressure fields

Shallow water theory predicts that the pressure at any location in the fluid is obtained via the hydrostatic approximation. Modeled pressure and hydrostatic approximation data from 3 cross-shore locations for the June 2002 simulation show that this approximation is typically valid (Figure 5-11) with greater than 94%, 84% and 69% of the estimates having smaller than 20% error at $x = 3.95$, $x = 4.29$ and $x = 4.53$ respectively. Under spilling breakers, *Liu and Lin* [1997] found the maximum deviation from hydrostatic pressure to be 7%, whereas some larger deviations were observed in our study under different forcing and bathymetric conditions. The fact that the hydrostatic approximation is typically in small error is not surprising given that the vertical velocities across these regions were shown to be small compared to the horizontal component (Figure 5-6). *Raubenheimer et al.* [1995] further suggest that the effect of the non hydrostatic assumption and lack of vertical flow information in using depth averaged non-linear shallow water models may be small based on qualitative agreement between field data and predictions on shallow sloping beaches.

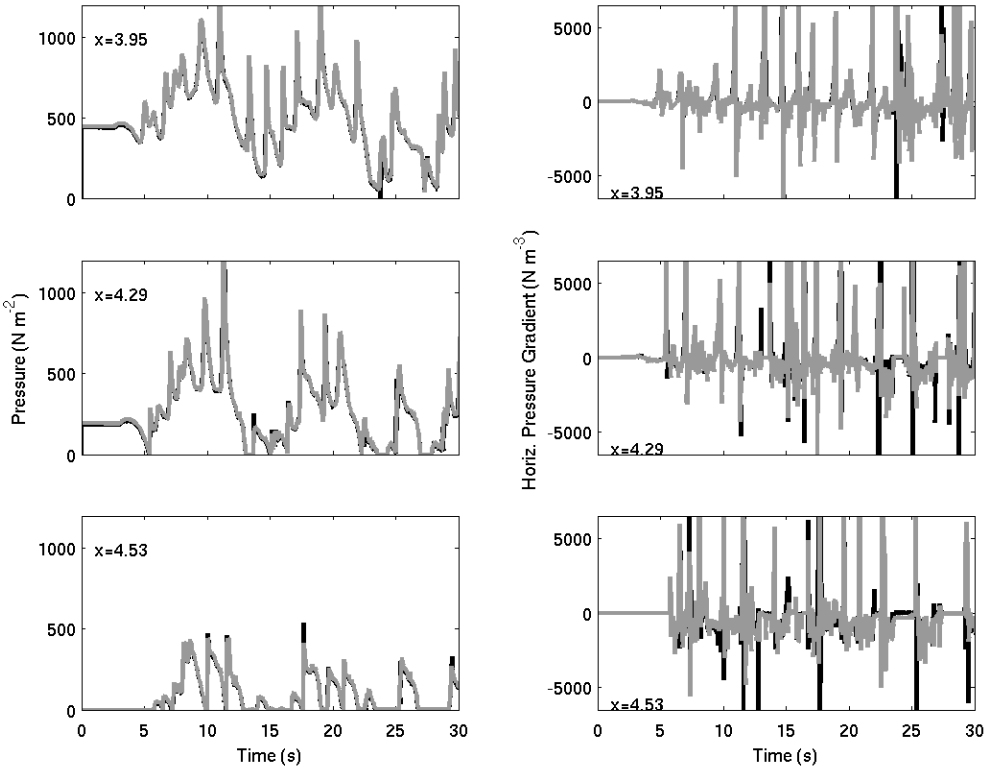

Figure 5-11. Modeled (black) and hydrostatic (gray) pressure (left panels). Modeled and hydrostatic pressure gradients (right panels; same color format). All time series for June 2002.

The modeled or hydrostatic approximation can be used to calculate the horizontal pressure gradient using finite differences. Some variation between the two may exist near the bore and in the swash region where some slight differences between the two pressure estimates were found. Onshore-directed pressure gradient forces up to 3 times that of the downslope component of gravity (~ -1700 N m^{-3} based on slope of 10°) are observed to occur under the passage of individual broken waves and swash. Interestingly, large off-shore directed pressure gradient forces are also observed. Large forces in this direction would tend to imply a deeper fluid column landward of a shallower fluid column. In the surf zone where crests and troughs exist, this is expected on the backside of the crest. In the swash zone, however a reverse sloping sea surface is not typically expected and prompted us to look deeper into the cause of these offshore directed pressure gradients. It was found that during the collision and collapse process the sea surface takes on an undulated form where the water depth landward of a location can be deeper than its seaward counterpart. In general these occurrences were for a very short duration and the water depth variations were only on the order of a few millimeters. However, the short horizontal distance over which the depth variations occurred caused the large observed offshore-directed pressure gradients.

Shear Stress

Bed shear stresses, τ, are determined from the gradients of the modeled flow field as

$$\tau = \rho(\upsilon + \upsilon_T)\left[\frac{\partial u}{\partial z} + \frac{\partial w}{\partial x}\right]. \quad (5\text{-}17)$$

Because of the damping in the calculation of the turbulent eddy viscosity, values for υ_T are zero at the bed. A simple means of visualizing the shear stress at each cross-shore

location for the simulation time is obtained through a bed shear stress time stack. The time stack is created by calculating the stresses at each cross-shore position and entering into a matrix where each column is a given time. Upon display, it is trivial to observe the bed shear stress for each passing wave and swash (Figure 5-12; for June, 2002). Here, narrow regions of high onshore directed stress are observed to occur alternately between broad regions of smaller magnitude offshore-directed stress provided by skewed wave motions in the surf zone. Variations in the stress magnitude are also observed along the wave propagation direction and are related to the variations in wave dissipation at the bed.

An additional benefit to the timestack is the ability to readily extract bed shear stress time series by taking a slice across the matrix. Figure 5-13 shows the time series for July, 2001 (A) and June, 2002 (B) from the location of the inner (black) and middle (gray) swash current meters. From this data, analysis of individual wave motions at a given location suggests that the net force applied to the bed varies on a wave by wave basis even under monochromatic conditions. Variations in the cross-shore stress at each location suggest that the net stress is offshore directed in all cases although net stresses for July 2001 only vary by about 2% whereas net stresses vary by about 35% for June 2002 (comparing the time series at $x = 4.29$ and 4.53). Finally, stress gradients between these two swash locations imply that the net stress gradient is strongly offshore directed for the June 2002 irregular wave case, while it is slightly onshore-directed for the July 2001 regular wave case.

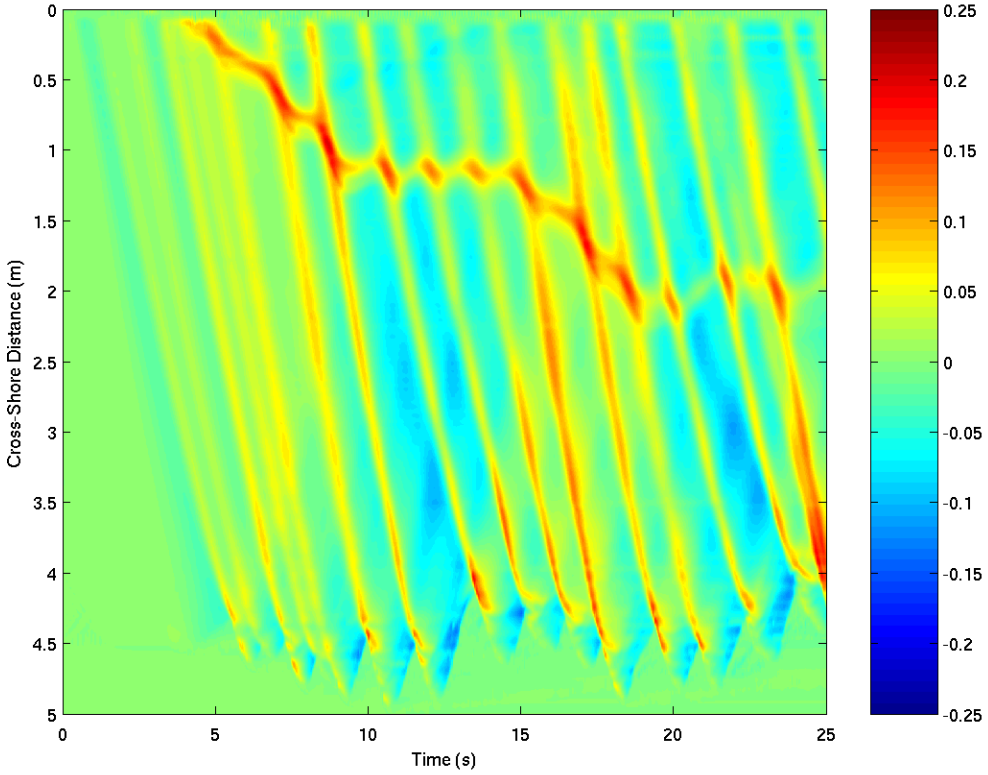

Figure 5-12. Shear stress time stack for June 2002. Color scale is the bed shear stress in N m^{-2}. Positive values are onshore-directed. Negative values are offshore-directed.

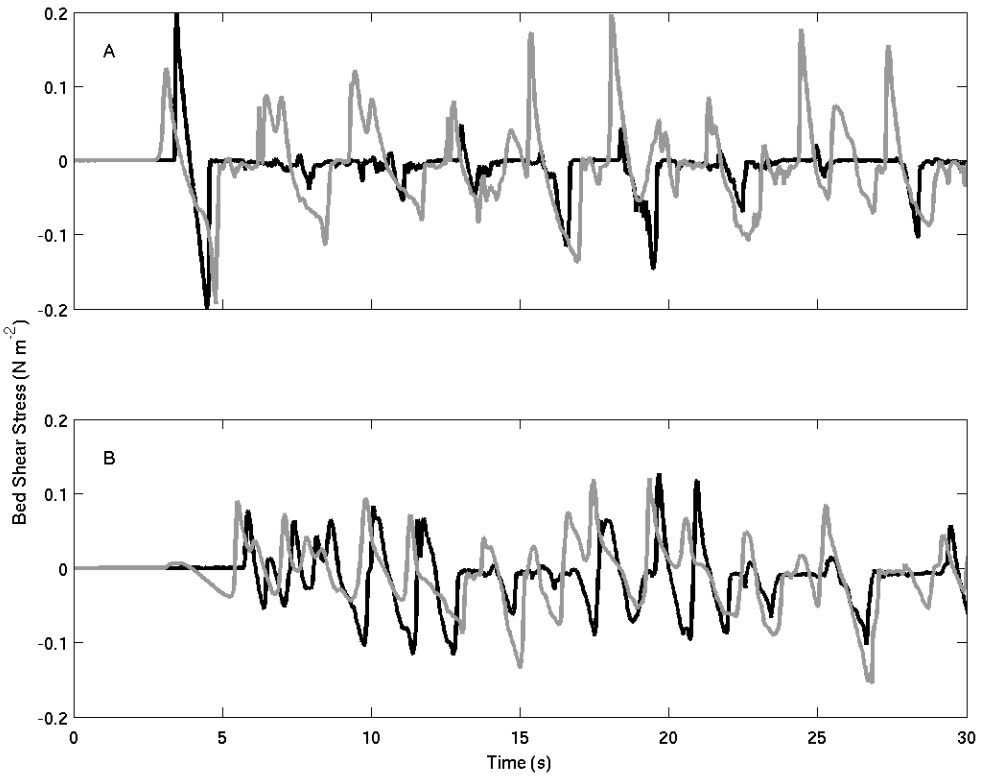

Figure 5-13. Shear stress time series extracted from a time stack at the locations of the landward swash zone ADV's for July 2001 (upper panel: gray from x = 3.89; black from x = 4.3) and June 2002 (lower panel: gray from x = 4.29; black from x = 4.53).

While no attempt is made to predict morphologic change based on this information due to lack of time-sequenced bathymetry measurements, it does suggest that the RIPPLE model is capable of supplying the required hydrodynamic parameters to investigate the effects of variable bed stresses during bore propagation and swash motions in relation to sediment transport.

Discussion and Conclusions

A large eddy simulation numerical model has been presented for simulating breaking waves in the inner surf and swash zones using the volume of fluid method. We have found the model to be capable of reproducing the observed sea surface elevations and typically fluid velocities in the inner surf and swash zones for regular and irregular wave trains. We found, similar to *Liu and Lin* [1997], that the shallow water approximations are nearly met in the inner surf and swash zones except at times in the vicinity of the bore. Vertical fluid velocities that scale out of the shallow water approximation, were found to be on the order of 5-10% of the horizontal velocities in these regions. The largest vertical velocities were observed to occur near the bore front and in the swash zone. It is important to note that the velocities reported here are with respect to the model domain and not in a beach parallel-orthogonal frame of reference. Yet, rotating the velocities at selected locations to lie in the beach parallel-orthogonal frame of reference suggested only a several percent decrease in the reported values. For steeper locations on the profile or for simulations on steeper profiles in general, the decrease in vertical velocities can be much larger.

The pressure field typically deviated from hydrostatic by less than 20% in the surf zone while some larger deviations were observed near the bore and in the swash zone. The often favorable comparison between the modeled pressure field and the hydrostatic

approximation again means that the assumptions in the depth averaged non-linear shallow water type models are typically valid in the inner surf and swash zones. Using these fields, we estimated both onshore and offshore-directed pressure gradient forces that exceeded the downslope component of gravity. The onshore-directed forces are supplied by the water depth variations across the bore face, while the offshore-directed forces occurred as a result of water depth variations on the backside of waves in the inner surf zone and the short lived surface irregularities in the swash zone as a result of the bore collapse.

Model simulations were performed over a smooth beach surface whereas the laboratory data were collected in a basin with 0.15 mm sediment and sand ripples everywhere seaward of the foreshore. The close correspondence between data and model simulations suggests that the lack of an additional friction term at the bed (viz the typical quadratic drag law formulation) to potentially account for these roughness elements did not adversely affect output. It is expected that under simulations where the grain size of the laboratory or field data is much larger or bed features such as megaripples exist would require a method to account for the additional near bed dissipation due to friction.

Horizontal velocity profiles in the inner surf and swash zones suggest that for much of the flow cycle, the boundary layer for the present simulations was only on the order of 0.01 m thick. Even more interesting was the variability of observations from the simulations. At times, the boundary layer appeared to respond similar to a boundary layer under adverse pressure gradients, where the nearbed flow reverses direction before flow in the upper portion of the water column does. Yet, in other instances near strong uprush/backwash collisions, flow in the lower portion of the water column was strongly

offshore whereas flow in the upper portion of the water column was strongly shore-directed. These opposing findings suggest that vertical structure in the swash cannot be described by simple boundary layer formulations for the entire swash duration at all locations on the foreshore. Rather, some additional processes related to interacting swash and bore propagation need to be considered.

Analysis of the fluid acceleration under these fairly benign conditions determined that shore-directed accelerations in the swash zone occur only near the bore and the swash interacting region or collapse point for the cases studied here. Further up the beach face, landward of the seaward edge of the swash zone, shore-directed accelerations appear to be non-existent suggesting, again, that at these locations the shallow water type model (ballistic motion) that suggests continual offshore-directed acceleration is justified. In contrast, shore-directed acceleration is often observed during the backwash phase of the swash cycle (a shore-directed acceleration during backwash implies a decelerating flow). This finding does not conform to the shallow water assumptions which would predict an accelerating flow during the backwash phase. Rather, the pressure gradient supplied by the fluid mass offshore in addition to the next incoming swash or bore causes the flow speed to slow. This flow deceleration may have important ramifications for sediment transport in this region as the adverse pressure gradient would cause the boundary layer to separate or dilate and potentially transport increased quantities of sediment higher into the water column [*Hanes and Huntley*, 1986].

Bed shear stress estimates are obtained from RIPPLE using velocity gradients rather than a drag law type formulation. These stress estimates were used to investigate the net stress at locations in the swash zone and additionally the net stress gradients. It

was found for the irregular wave case that the net stress gradient was offshore-directed while the net stress gradient for the monochromatic wave case was slightly onshore-directed. While these particular findings are only applicable to the bathymetry and conditions used in the present simulation, the ability to extract this information from RIPPLE data suggests that these analyses may be beneficial in the future in terms of estimating sediment transport patterns resulting from these gradients.

The goal of large eddy simulation is to calculate the turbulent eddy viscosity based on the resolved strain rates. Simulations using a fine grid showed that no additional predictive capability was obtained using the LES since both LES and non-LES simulations matched the laboratory data well (appendix-B). Rather, it was found that reducing the grid resolution caused the LES to absorb some of the resolution reduction through an increased eddy viscosity. In that sense, the LES inclusion performed as expected. Yet, turning the LES off in the reduced grid resolution simulations only caused a slight decrease in the model to data comparisons. Based on these findings, we conclude that the LES is beneficial for calculating the eddy viscosity, especially in regions near the free surface where strong vertical gradients exist, but that it did not substantially increase predictive capability at the scales of interest here. Future work, at larger prototype scales may prove the LES to be more beneficial.

CHAPTER 6
NUMERICAL PREDICTION OF SWASH ZONE VELOCITIES AND SHEAR STRESSES ON STEEP SLOPES

Introduction

Many field and laboratory studies have investigated cross-shore swash zone fluid velocities leading to the general consensus that, on steep beaches, peak uprush cross-shore velocity magnitudes tend to be nearly equivalent to [*Cowen et al.*, 2003 and *Puleo et al.* Submitted] or greater than [*Hughes et al.*, 1997b; *Masselink and Hughes*, 1998] peak backwash cross-shore velocities whereas the duration of backwash flow tends to exceed that of the uprush [*Hughes et al.*, 1997a; *Masselink and Hughes*, 1998; *Puleo et al.*, 2000; *Petti and Longo*, 2001; *Cowen et al.*, 2003]. Statements such as the previous need to be considered in a broad general context, however, since natural swash is typically irregular such that swash events can display characteristics opposite those mentioned above.

While cross-shore swash flows have often been addressed, fewer studies have investigated the vertical flow structure in this region. For incident band swash over smooth laboratory beds, [*Petti and Longo*, 2001 and *Cowen et al.*, 2003] found the velocities during uprush away from the bore had a high degree of vertical uniformity with a thin boundary layer whereas a slightly thicker boundary layer developed during backwash. Similar results can be inferred from *Cox and Hobensack* [submitted; Figure 7] over a fixed rough laboratory bed. Measurements from natural low frequency dominated beaches, also yielded somewhat similar results [*Raubenheimer et al.*, in review and

Masselink et al., in review]. Because the boundary layer in the backwash is partially controlled by flow duration, however, they observed a more notable boundary layer during the seaward phase of flow that was on the order of 0.05 m thick.

In contrast to the abundant swash zone velocity measurements in the literature, shear stress measurements are scarce. The only direct estimates of shear stresses in the swash zone, to our knowledge, have been presented by *Conley and Griffin* [2003]. They used a hot film probe mounted to a permeable brick that resembled the sediment characteristics of the field site where their study was undertaken. They found the uprush shear stress to be nearly double that during backwash but backwash duration to be approximately 1.5 times the uprush duration. Many other studies have inferred the bed shear stress by assuming a logarithmic velocity distribution using the friction velocity, near bed velocity gradients or through use of the quadratic drag law formulation with an empirical friction coefficient [*Archetti and Brocchini*, 2002; *Masselink et al.*, in review; *Cox and Hobensack*, submitted; *Puleo et al.*, submitted]. The latter method has been particularly abundant in swash zone sediment transport studies (*Evans et al.* [2003] and *Butt et al.* [submitted] among many others).

Both the fluid velocities and shear stresses are of paramount importance because their product is often used to describe sediment transport patterns through an energetics model [*Bagnold*, 1963; *Bailard*, 1981 and *Bowen*, 1980] leading to a velocity moment dependency. As previously mentioned, the general approach for the shear stress is to use a drag law formulation. Unfortunately, the embedded friction coefficients used have at least as order of magnitude range allowing for large variations in predictions [*Hughes*, 1995 *Puleo and Holland*, 2001, *Cowen et al.*, 2003; *Conley and Griffin*, 2003;

Raubenheimer et al., in review and *Cox and Hobensack*, submitted]. Even if the energetics transport models are accepted (recent works by *Drake and Calantoni* [2001], *Hoefel and Elgar* [2003], *Puleo et al.* [2003] and *Hsu and Hanes* [submitted] suggest parameters other than velocity moments may be important) difficulties in swash zone sediment transport modeling efforts are further exacerbated by incomplete field measurements because even during "extensive" studies only a few swash zone current meters are typically deployed often with minimal vertical coverage. Because of this limited coverage, bed shear estimates through the drag law tend to use whatever velocity is recorded regardless of location with respect to the boundary layer.

In this chapter, rather than address swash zone fluid velocities and bed shear stresses using field or laboratory measurements, numerical simulations using the two-dimensional (2D) Navier-Stokes (NS) solver are performed. The NS model and simulations are briefly described in the first section. Next, various hydrodynamic conditions including nearly spilling, plunging and surging waves of differing periods and heights are forced over a variety of foreshore slopes to determine the time dependent and mean shear stress at multiple locations on the foreshore and throughout a swash cycle. Stress values are compared to those determined from a drag law formulation, through the friction coefficient, using velocities from several vertical locations to mimic natural swash measurements. Conclusions are then provided.

Numerical Model and Methods

Navier-Stokes Solver: RIPPLE

The numerical model used in our study is a fully non linear volume of fluid (VOF) 2D Navier-Stokes solver for incompressible free-surface flows known as RIPPLE [*Kothe et al.*, 1991] that has been modified to include a large eddy simulation (LES) [The

model is fully described in *Kothe et al.* [1991], *Liu and Lin* [1997] and chapter 5]. RIPPLE solves the mass and momentum equations using a second order space, forward time differencing procedure. The model equations are modified by the LES leading to an additional stress term analogous to the stresses derived in a Reynolds averaged sense. The stresses are calculated at the resolvable scales and modeled at the subgrid scales through the additional term. We invoke the LES using Smagorinsky's method [*Smagorinsky*, 1963] and include a *van Driest* [1956] damping function to smoothly bring the subgrid scale turbulent stresses to the bed. Although, we have found that under the small grid scales considered in these studies, the subgrid scale stress does not alter the turbulent eddy viscosity from its kinematic molecular value enough to significantly affect model output.

The NS equations are solved using a pressure projection method. In short, intermediate velocities are obtained by solving the NS equations without the pressure term. These velocities are then projected onto a non-divergent vector field to obtain the velocities at the next time level. The equations in this second step are combined into a single pressure Poisson equation which is solved using an incomplete Cholesky conjugate gradient iterative technique.

Model Domain and Hydrodynamic Conditions

Model domains are rectangular with the bottom row of grid points located at the bed. Sloping beds are obtained by varying downslope gravity as a simple means to obtaining a grid field that is everywhere parallel and orthogonal to the bed. Therefore, the x coordinate is in the alongslope direction, rather than cross-shore, and the z coordinate normal to x, rather than vertical. Hydrodynamic conditions are carefully chosen to span a range of Iribarren numbers [*Iribarren and Nogales*, 1949]

$$\xi_O = \frac{\tan\beta}{(H/L)^{1/2}}, \quad (6\text{-}1)$$

where tanβ is the beach slope, H and L are the deep water wave height and length respectively, so that surging (ξ_o>3.3), plunging (0.5<ξ_o<3.3) and nearly spilling(ξ_o<0.5) breakers are generated (Table 6-1). Domain widths and heights vary depending on the hydrodynamic conditions but range between roughly 2 to 8 meters in the horizontal and 0.85 to 1.5 m in the vertical. Model runs are forced at the offshore boundary using the theoretical free surface and cross-shore and vertical velocities obtained from linear wave theory.

Grid spacing in the model is typically 0.02 m in the horizontal and 0.005 m in the vertical. Near the free surface at the offshore boundary, the bed and in the swash zone, the grid spacing is reduced to better resolve the boundary layer and wave forcing regions. In the domain interior, the grid spacing is enlarged to increase computational efficiency. In all cases, a minimum of 6 wave periods are run and only the last several swash cycles are retained for analysis. Because domains generally consist of between roughly 26,000 and 500,000 grid points typical model simulations take from approximately 1 to 14 days respectively on a 3.2 GHz Xeon processor under Linux. Model output is stored at 50 Hz.

Results

Figures 6-1 and 6-2 show the alongslope runup excursion about the still water shoreline for the 12 cases. The runup edge was determined from the most landward fluid cell just above the bed that had a fluid volume greater than 75% full.

Table 6-1. Hydrodynamic conditions used for the 12 cases.

	H=0.05m	H=0.1m
T= 1s, ξ_o= 0.75	Tanβ=1:7.5 (CASE1)	Tanβ=1:5.3 (CASE7)
ξ_o= 2.0	Tanβ=1:2.8 (CASE2)	Tanβ=1:2.0 (CASE8)
ξ_o= 3.5	Tanβ=1:1.6 (CASE3)	Tanβ=1:1.1 (CASE9)
T= 2s, ξ_o= 0.75	Tanβ=1:14.9 (CASE4)	Tanβ=1:10.5 (CASE10)
ξ_o= 2.0	Tanβ=1:5.6 (CASE5)	Tanβ=1:4.0 (CASE11)
ξ_o= 3.5	Tanβ=1:3.2 (CASE6)	Tanβ=1:2.3 (CASE12)

The variability in runup between the cases displays how a change in the bed slope, while holding other hydrodynamic values constant, can significantly alter the excursion. For instance, it is clear that lower frequency swash motions can arise even for monochromatic input waves. These motions result from an interaction between the incoming wave train and the swash flows that have a longer duration under less steep slopes. As the Iribarren number goes from surging to nearly spilling the runup begins to take on a more irregular pattern compared to the monochromatic forcing.

For comparison purposes, a single swash event was chosen from each runup record and is denoted by the gray areas in Figures 6-1 and 6-2. For our study a swash event is defined to begin when the runup edge starts its landward motion and ends when the runup edge has returned to the same position. This means that at times, the entire backwash motion will not be used in analyses in this paper (e.g. CASE5 and CASE11). The swash event was defined in this manner so that values are not unjustly skewed towards backwash flows when their duration exceeds that of the uprush.

In order to inter-compare events, the swash event width for each case, X, is determined based on the maximum and minimum alongslope runup levels for the chosen event as noted from Figures 6-1 and 6-2. This distance is then used to normalize the alongslope excursion between 0 and 1 based on a new coordinate system defined as,

$$x' = \frac{x - x_{start}}{X}, \quad (6\text{-}2)$$

where x and x_{start} are the time dependent and minimum alongslope runup level.

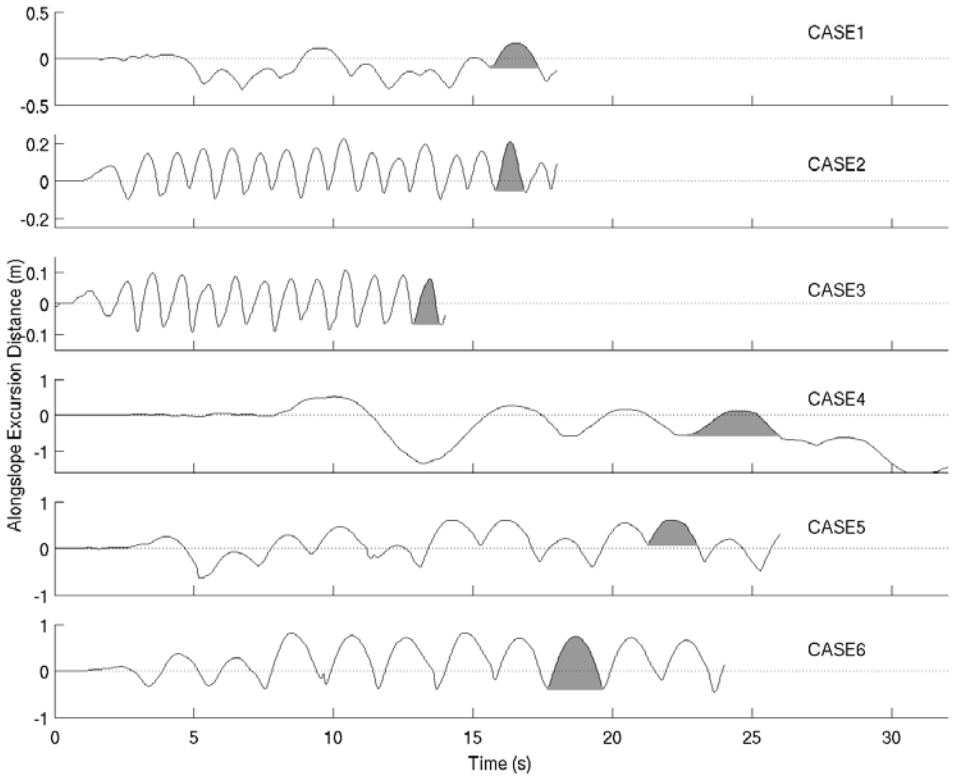

Figure 6-1. Alongslope runup excursions for CASES1-6. Grey areas denote regions to be used in velocity, friction coefficient and shear stress analysis.

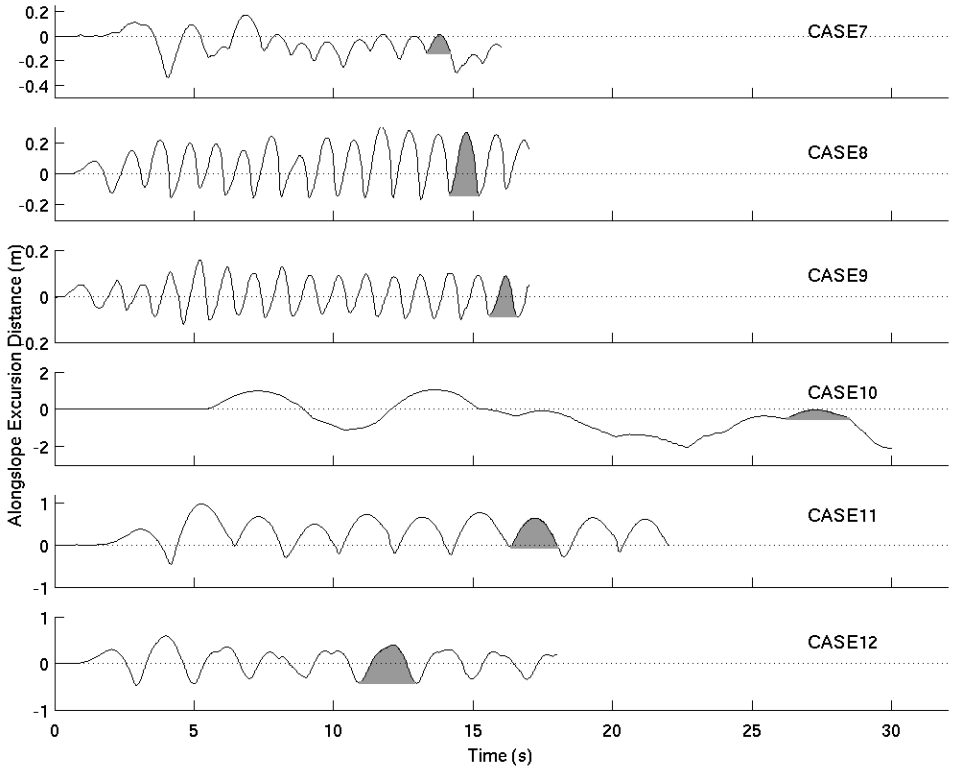

Figure 6-2. Alongslope runup excursions for CASES7-12. Grey areas denote regions to be used in velocity, friction coefficient and shear stress analysis.

In the same manner, t for each swash event is normalized using

$$t' = \frac{t - t_{start}}{D}, \quad (6\text{-}3)$$

where t_{start} is the start time of the uprush, and D is the total event duration.

Fluid Velocities

Alongslope fluid velocities for CASE11 for slightly more than a swash cycle show strong alongslope gradients depending on location as well as rapid variability in the velocity magnitude (Figure 6-3). Corresponding velocities normal to the bed are shown in Figure 6-4. The colorscale represents the fluid velocity with positive being directed onshore and away from the bed, but also shows the shape of the swash wedge and fluid elevations offshore. At t = 16.9389 s the swash has reached its most landward location and by t = 17.1393 s has started to head offshore. By t = 17.3394 s and t = 17.5395 s, backwash velocities on the order of 0.5 m s^{-1} are observed near the bed on the upper foreshore and are seen to interact with, but mostly flow beneath the incoming wave. Onshore fluid velocities near the surface are nearly 1 m s^{-1}. At the same time, velocities normal to the bed increase to about 0.25 m s^{-1}. The next several instances show the backwash thinning considerably but it is apparent, similar to findings by *Emery and Gale* [1951], that the leading edge maintains its location until much of the fluid mass has moved offshore. Onshore directed fluid velocities near the surface continue to increase as the wave front steepens and overturns, crashing on the foreshore (t = 17.7397 to t = 18.1402) reaching peak velocities of nearly 2 m s^{-1}. Just prior to the collapsing phase, velocities normal to, but directed away from, the bed increase to maximum values of 0.5 m s^{-1} as water rushes up the breaking wave face (Figure 6-4, t = 17.7397).

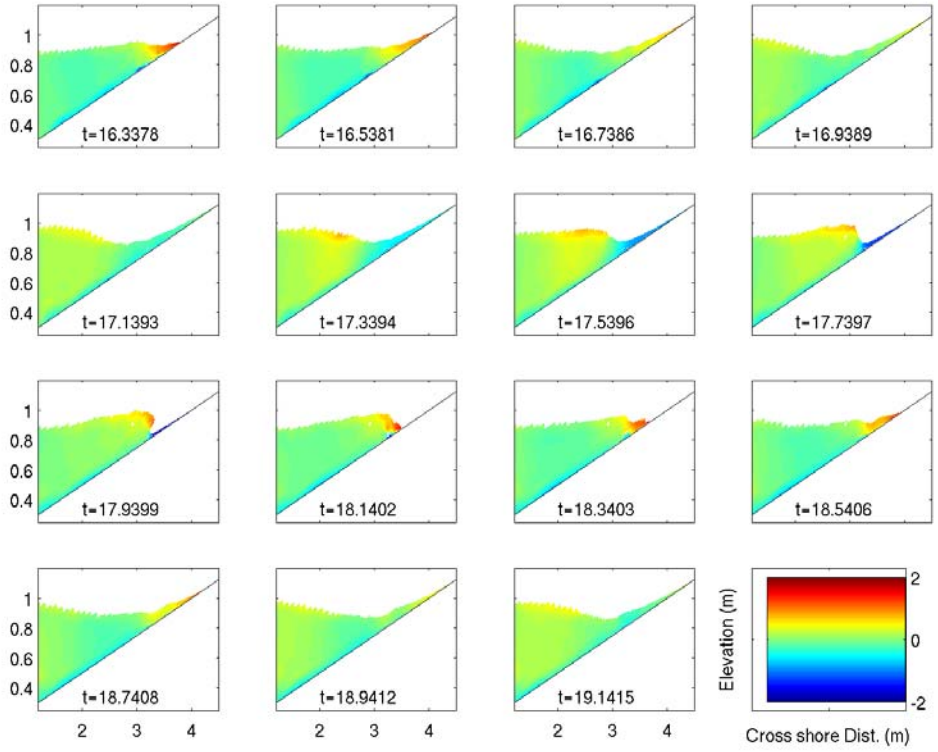

Figure 6-3. Alongslope fluid velocity for CASE11 as a function of time. Colorscale denotes the velocity (m s^{-1}) with positive values being upslope directed and negative values downslope directed.

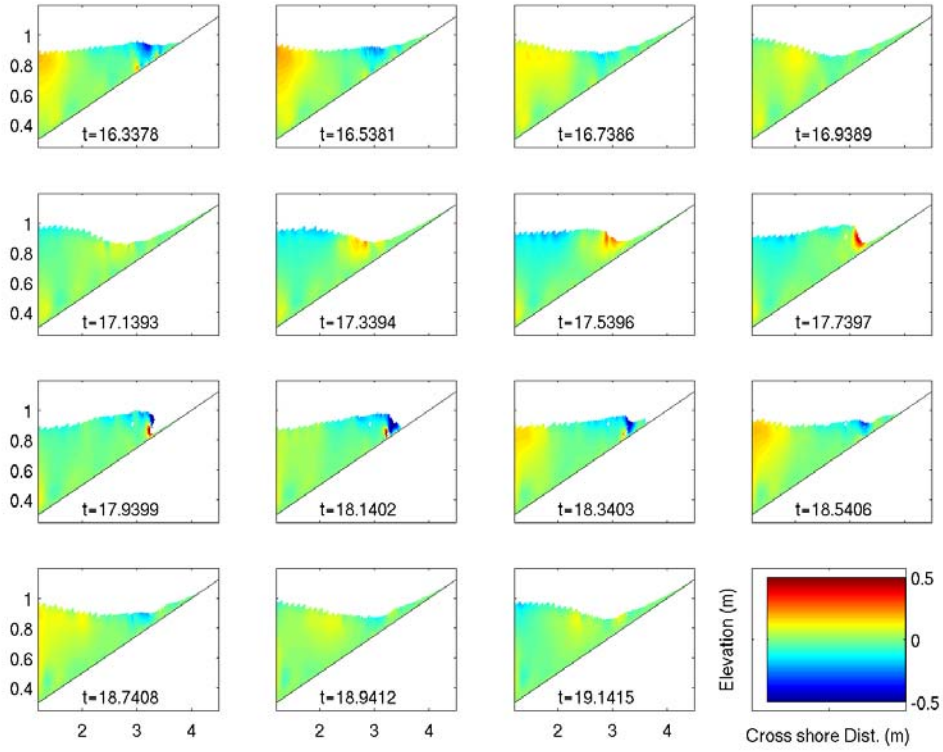

Figure 6-4. Bed normal fluid velocity for CASE11 as a function of time. Colorscale denotes the velocity (m s^{-1}) with positive values being directed away from the bed and negative values being directed towards the bed.

Afterwards, velocities are directed towards the bed during wave plunging, obtaining nearly similar velocity magnitudes. The rest of the uprush cycle shows alongslope fluid velocities reducing their speed and the bed normal velocities returning to relatively small values.

For comparison purposes, velocity fields from all cases near the initial stages of uprush are also shown (Figure 6-5). The plot is aligned such that the left panels are the nearly spilling cases, the middle panels, the plunging cases and the right panels are the surging cases. There is clearly a velocity dependence on wave period more so than wave height as evidenced by the larger velocities for CASE4-6 and CASE10-12 as compared to their 1 s counterparts. Alongslope velocities are also greatest for the plunging wave cases as compared to either surging or nearly spilling waves of the same hydrodynamic conditions. Unlike the surging cases, the plunging and nearly spilling cases tend to exhibit a very shallow backwash flow that attains alongslope velocities exceeding 1 m s^{-1}. Based on these characteristics we note that much of the energy contained in the wave form is expended before the breaking portion actually reaches the dry bed. Hence, the swash for these cases is not typically initiated by the initial breaking sequence near the shoreline but results from the corresponding landward flow after this breaking has occurred.

To get a better feel for the vertical variations in alongslope flow, velocity profiles spanning 2 swash events for CASE11 are displayed in Figure 6-6. Sequential velocity profiles are offset by 1 m s^{-1}. Based on this data, the boundary layer over the smooth model bed is on the order of 0.02 m thick during the initial stages of uprush.

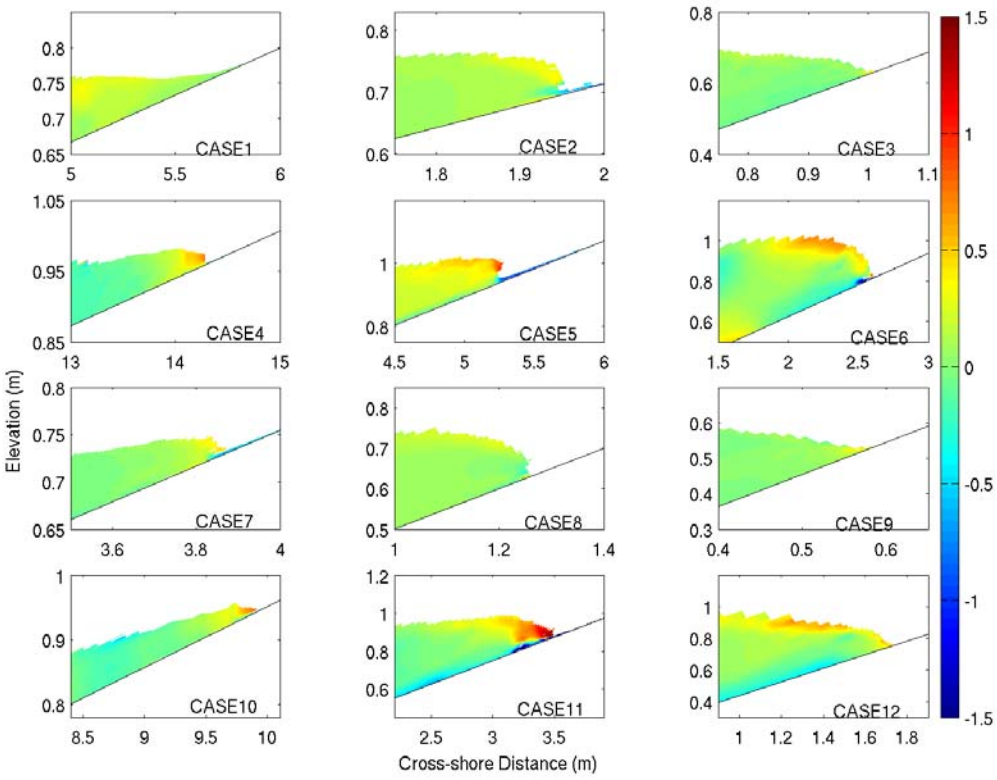

Figure 6-5. Alongslope fluid velocities near the start of uprush (near the beginning of the grey areas in Figures 6-1 and 6-2) for the 12 cases. Colorscale description is the same as Figure 6-3.

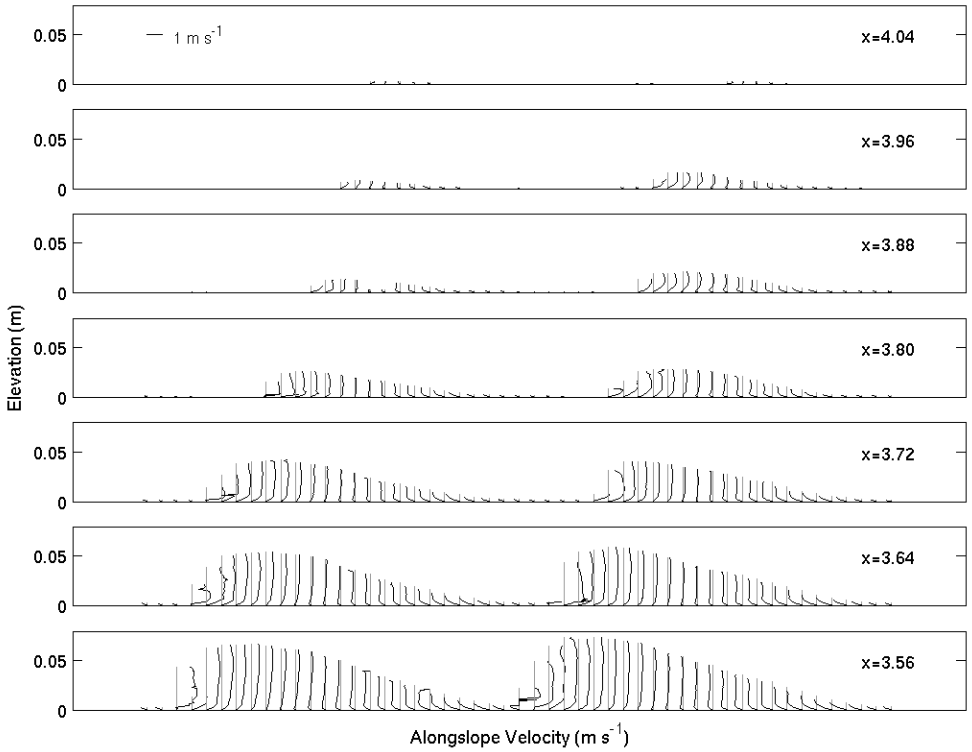

Figure 6-6. Alongslope velocity profiles for 2 swash events for CASE11. Values in upper right denote alongslope location with the still water shoreline located at x = 3.88 m. Sequential profiles are offset by 1 m s^{-1} (solid gray lines) and collected at 12.5 Hz.

These findings are similar to those by *Cowen et al.* [2003] over a glass laboratory beach and larger than findings by *Petti and Longo* [2001] over a smoothed concrete beach. In contrast, the boundary layer for the rest of the swash duration is smaller (< 0.01 m). The boundary layer appears to be most pronounced on the lower foreshore and reduced in thickness further up the beach face. Near the swash terminus, the water depths for this simulation are on the order of 0.005 m such that the 0.0005 m vertical model resolution near the bed may be incapable of accurately predicting the exact boundary layer structure. In addition, the boundary layer development during backwash is partially dependent on flow duration. Because the simulations are for short period waves, we do not expect considerable boundary layer development in the short period backwash simulated here. This expectation is confirmed where most of the backwash flows appear quite uniform over depth. The boundary layer thicknesses observed here are considerably smaller than those that have been observed on natural, rough bottoms that are predicted to be on the order of 0.05 m or larger [*Raubenheimer et al.*, in review and *Masselink et al.*, in review].

Unlike point measurements obtained in the field, it is not trivial to display the 3 dimensional alongslope velocity data (as a function of space and time) extracted from the model in a format similar to Figure 6-6 for multiple cases. Hence, we present the alongslope velocity time series in normalized coordinates for the 12 cases as obtained from 3 elevations (0.002, 0.005 and 0.01 m above the bed) from $x' = 1/8$ (Figure 6-7) and $x' = 1/2$ (Figure 6-8). As expected, in nearly all instances, the velocity near the bed is equivalent to or less than values above the bed except at the leading edge of the uprush suggesting that the boundary layer, similar to CASE11, is quite thin in most cases.

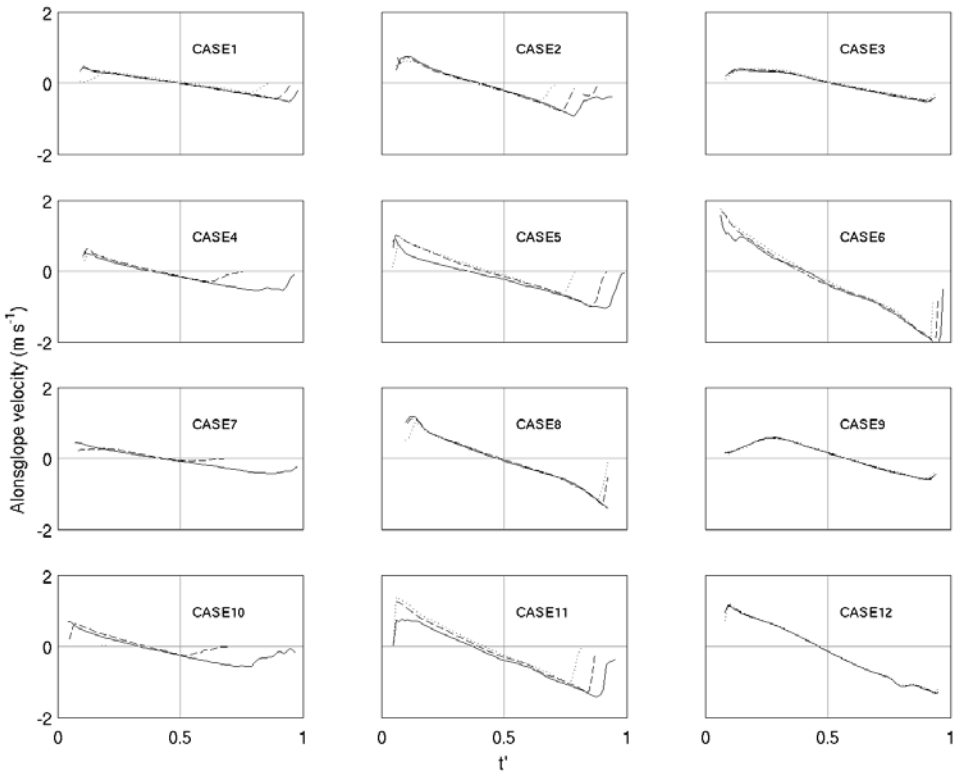

Figure 6-7. Alongslope velocity for the 12 cases extracted from normalized alongslope location x′=1/8 as a function or normalized time. Time series collected at distances of 0.002 m (solid line), 0.005 m (dashed line) and 0.01 m (dotted line).

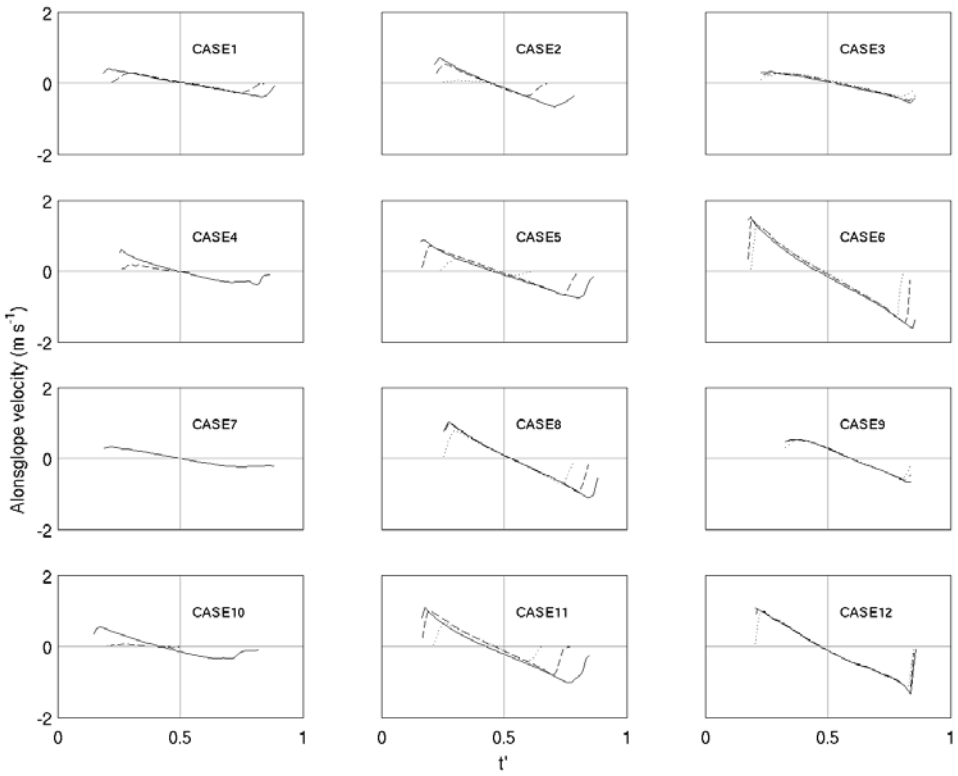

Figure 6-8. Alongslope velocity for the 12 cases extracted from normalized alongslope location x′=1/2 as a function or normalized time. Time series collected at distances of 0.002 m (solid line), 0.005 m (dashed line) and 0.01 m (dotted line).

We observe the most vertical structure in the 2 s plunging wave cases, again pointing to dependence on wave period as a key descriptor for distinguishing swash under varying hydrodynamic conditions.

Analogous to previous studies of swash zone flow we found the uprush velocity magnitudes tend to be slightly greater or nearly equal to backwash velocity magnitudes while the backwash duration tends to exceed that of the uprush. This is visually determined from the plots when the velocity time series crosses the zero axis (horizontal dotted line) before the mid swash event point (vertical dotted line). Some exceptions do occur, for instance for CASE8 and CASE9 and for several of the 1 s wave simulations, and are likely attributed to the specific set of hydrodynamic conditions and beach slope combinations. In comparing Figure 6-7 to Figure 6-8, the ratio of uprush to backwash duration decreases suggesting that this ratio is a function of cross-shore distance. The differing ratios result from well-documented observation of flow reversal behind the leading edge tending to occur before the uprush reaches its maximum landward extent [*Raubenheimer et al.*, 1995; *Raubenheimer and Guza*, 1996; *Hughes et al.*, 1997a; *Masselink and Hughes*, 1998; *Puleo et al.*, 2000 and *Cowen et al.*, 2003].

Estimated Swash Stress From Velocity Gradients

Shear stresses are estimated from the alongslope and bed-normal velocity data as

$$\tau = \rho(\nu + \nu_t)\left(\frac{\partial u}{\partial z} + \frac{\partial w}{\partial x}\right), \quad (6\text{-}4)$$

where ρ is the fluid density, ν and ν_t are the kinematic molecular and turbulent eddy viscosities respectively, x and z are the coordinates and u and w are the alongslope and bed normal velocities. In practice, except under violent or plunging swash the horizontal

gradient in vertical velocity is typically much smaller (<3%) than the vertical gradient in horizontal velocity. We still use both terms, however, in the stress estimation.

Calculating the shear stress at every cross-shore position within the swash and at each model output time enables the creation of a shear stress time stack; a compact way to visualize the time-space character of swash zone shear stresses (Figure 6-9; CASE11). For the CASE11 example, alternating colors of onshore and offshore stress are observed and coincide with the landward and seaward phases of swash motion. It is evident from the figure that in general, the uprush portion of swash stress (hot colors in Figure 6-9) are of larger magnitude but shorter duration than the backwash (cool colors in Figure 6-9). Of course there is some spatial variation to this pattern as well even within the narrow swash shown here.

One benefit of the shear stress time stack is the ability to extract shear stress time series by taking a horizontal slice through the matrix (Figure 6-9, bottom panel). Here, time series have been extracted at the 4 corresponding horizontal lines plotted on the time stack and are qualitatively similar to field [*Conley and Griffin*, 2003 and *Masselink et al.*, in review] and laboratory [*Cox and Hobensack*, submitted] observations. Shear stress values for a given time tend to decrease during uprush and increase during backwash. This feature results from the larger shear stresses being located near the leading edge as opposed to within the swash interior. Similarly, shear stress values during uprush show a broad range of values as a function of alongslope distance versus those during backwash suggesting that the boundary layer during backwash is more uniform in the alongslope direction (recall Figure 6-6).

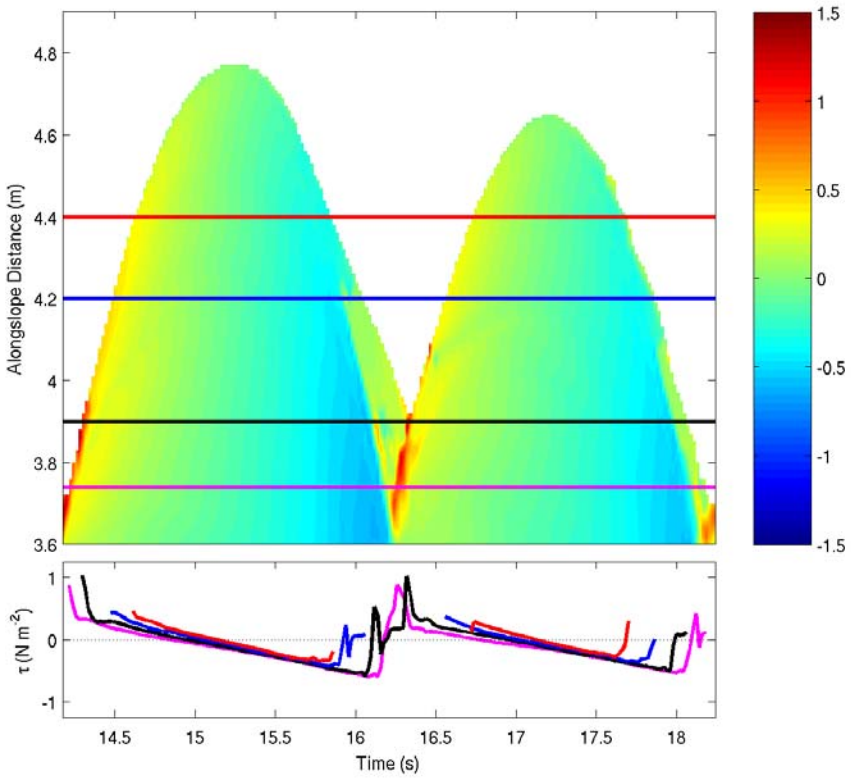

Figure 6-9. Bed shear stress time stack example for CASE11 (upper panel). Colorscale corresponds to bed stress with positive values directed upslope and negative values directed downslope. Bed shear stress time series extracted from the time stack (lower panel) corresponding to the lines in the upper panel.

Finally, the largest shear stresses are observed near the collision point between backwash and uprush and in the bore propagation region ($t \sim 16.25$ s in Figure 6-9). If sediment mobilization and suspension is related to shear stresses, then these large values should be expected to cause peaks in the amount of material in the water column. Furthermore, since the shear stress decays fairly rapidly away from these regions, it may be suspected that this potential region of sediment mobilization is responsible for a disproportionate amount of the overall sediment motion in the swash zone pointing to the potential for sediment advection to be a major contributor to the overall sediment transport budget in the lower swash zone [*Jackson et al.*, 2004].

Example shear stresses from the 12 cases at $x' = 1/8$, 1/4, 3/4 have the same typical shapes as those for the example in CASE11 (Figures 6-10 and 6-11). In general, the shear stress decreases in the landward direction and throughout the uprush cycle. Conversely, during backwash the shear stress tends to increase throughout much of the duration except at the last instance where the backwash begins to be significantly affected by the ensuing uprush. Shear stresses are often larger for the plunging wave cases than the surging or near spilling cases. The smallest shear stresses are predicted for the near spilling cases where much of the wave energy is dissipated outside the swash zone. Uprush and backwash shear stress maximum variability as a function of normalized cross-shore distance and Iribarren number are shown based on groupings defined by hydrodynamic conditions; CASE1-3, CASE4-6, CASE7-9 and CASE10-12 (Figure 6-12). Note that stress values in our study were only determined for $\xi_o = 0.75$, 2.0 and 3.5, but the curves are shown assist in visualizing the trends.

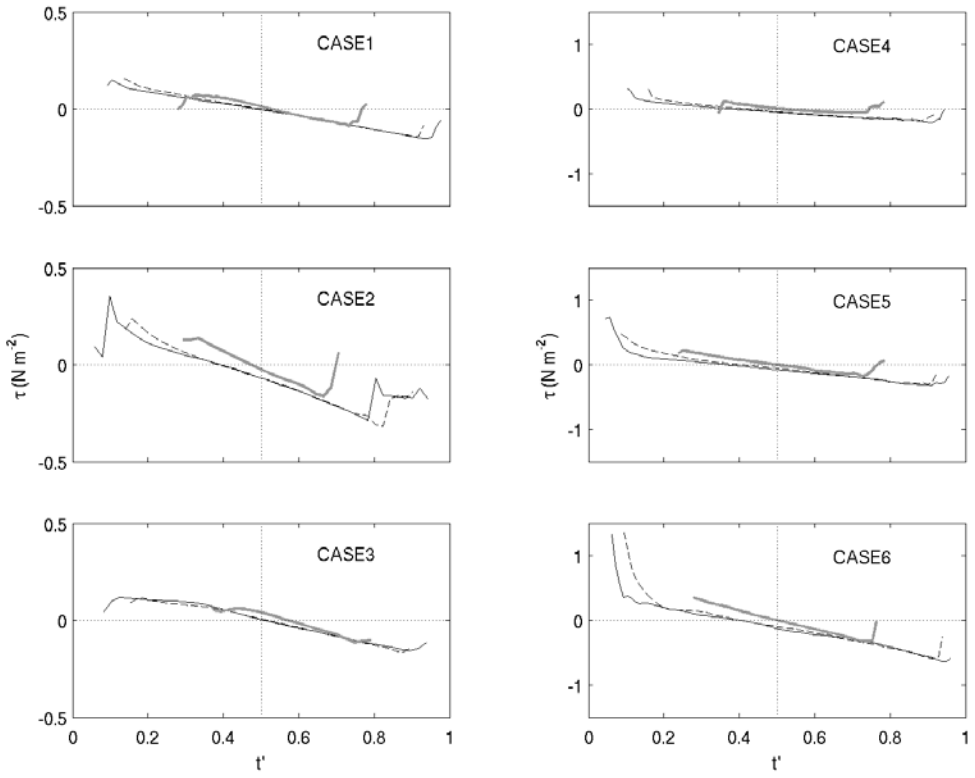

Figure 6-10. Bed shear stress time series for CASES1-6 extracted from normalized alongslope locations of $x' = 1/8$ (solid line), 1/4 (dashed line), and 3/4 (thick grey line).

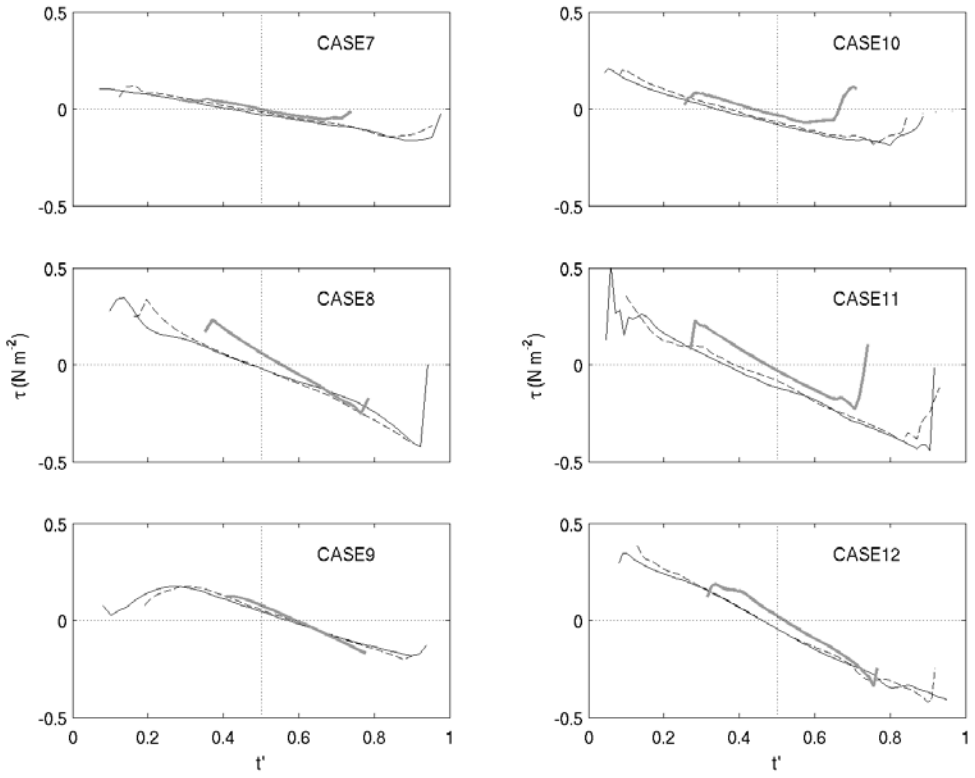

Figure 6-11. Bed shear stress time series for CASE7-12 extracted from normalized alongslope locations of $x' = 1/8$ (solid line), 1/4 (dashed line), and 3/4 (thick grey line).

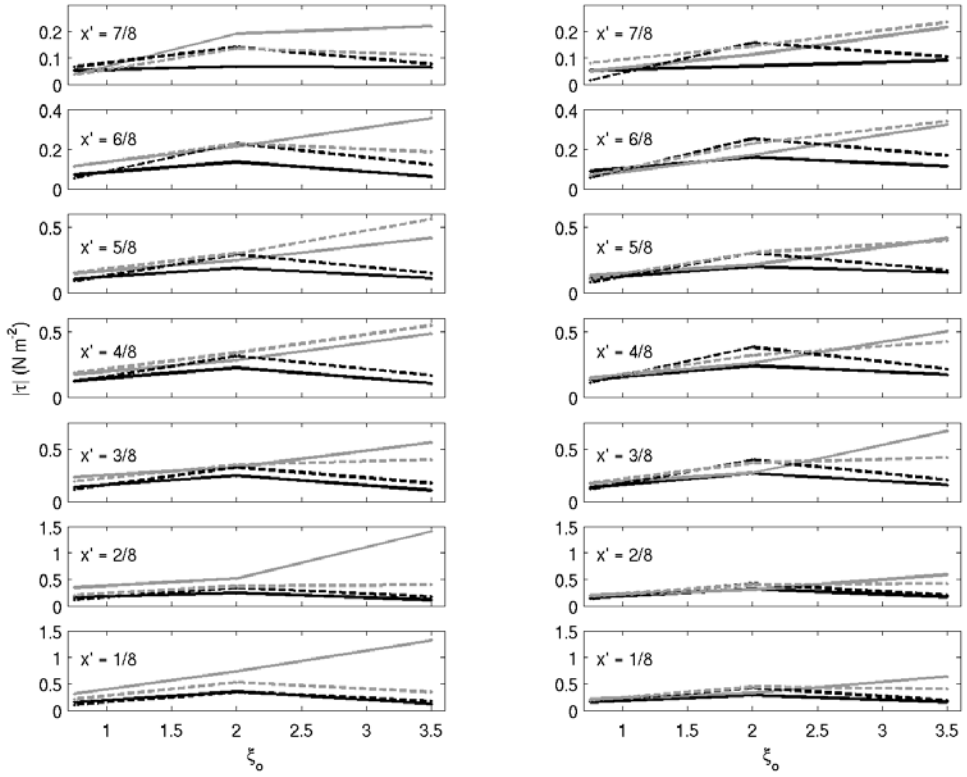

Figure 6-12. Bed shear stress as a function of Iribarren number for multiple normalized alongslope locations and grouped according to hydrodynamic conditions; CASE1-3 (solid black), CASE4-6 (dashed black); CASE7-9 (solid grey), CASE10-12 (dashed grey).

There is no drastic change in the trend (with respect to Iribarren number) in shear stress for uprush or backwash as a function of normalized cross-shore distance for any of the grouped cases. What is evident is that during uprush, the plunging cases have the largest shear stress for the 1 s waves. For the 2 s waves with 0.05 m wave height, however, the surging waves experience a larger maximum shear stress during uprush. In these instances, the plunging waves may expend much of their energy in the breaking process before the swash zone is reached, whereas the surging waves may release the bulk of their energy in the swash zone. Similar trends are observed in the backwash, with the plunging cases having the largest shear stresses for 1 s waves and the surging cases experiencing the largest maximum shear stresses for the 2 s waves. Overall, we do not find a definitive trend for shear stress as a function of Iribarren number. While in general we find that the shear stress tended to be larger for plunging waves, we also note that in some instances the simulated shear stresses were larger for surging waves and showed some dependence on wave period.

Mean stresses ($<\tau_{t'x'}>$; Table 6-2) are obtained from the time stack by summing over rows of the matrix and dividing by the number of points where data exists (the times when a particular region is wetted). Again the *x'* denotes the normalized location where the mean stress is obtained. Similarly, $<\tau>$ is the overall mean stress over both rows and columns of the entire event and represents the average force per unit supplied to the foreshore during the event. In general, the overall mean shear stress supplied to the bed is offshore for nearly all cases. One explanation is that in these simulations, the larger, short duration shear stress spike during uprush is not able to compensate for the smaller but longer duration backwash shear stresses.

Table 6-2. Mean stresses as a function of normalized alongslope distance and case number. Last column is the overall mean stress delivered to the foreshore during each swash event.

	$<\tau_{t',1/8}>$ (N m^{-2})	$<\tau_{t',2/8}>$ (N m^{-2})	$<\tau_{t',3/8}>$ (N m^{-2})	$<\tau_{t',4/8}>$ (N m^{-2})	$<\tau_{t',5/8}>$ (N m^{-2})	$<\tau_{t',6/8}>$ (N m^{-2})	$<\tau_{t',7/8}>$ (N m^{-2})	$<\tau>$ (N m^{-2})
CASE1	-1.49×10^{-2}	-9.20×10^{-3}	-5.30×10^{-3}	-2.20×10^{-3}	-9.00×10^{-4}	-9.00×10^{-4}	-2.00×10^{-4}	-4.87×10^{-3}
CASE2	-4.79×10^{-2}	-6.59×10^{-2}	-4.51×10^{-2}	-3.20×10^{-2}	-1.80×10^{-2}	-7.10×10^{-3}	1.50×10^{-3}	-2.42×10^{-2}
CASE3	-4.90×10^{-3}	-9.90×10^{-3}	-1.13×10^{-2}	-1.20×10^{-2}	-1.13×10^{-2}	-1.45×10^{-2}	-5.30×10^{-3}	-3.84×10^{-3}
CASE4	-4.40×10^{-2}	-3.60×10^{-2}	-2.64×10^{-2}	-1.00×10^{-2}	-5.50×10^{-3}	3.50×10^{-3}	-7.00×10^{-4}	-3.66×10^{-3}
CASE5	-5.34×10^{-2}	-3.41×10^{-2}	-1.86×10^{-2}	-1.05×10^{-2}	-4.00×10^{-4}	7.80×10^{-3}	1.63×10^{-2}	8.65×10^{-3}
CASE6	-1.02×10^{-1}	-7.27×10^{-2}	-8.02×10^{-2}	-4.48×10^{-2}	-2.78×10^{-2}	-1.47×10^{-2}	1.40×10^{-3}	-3.42×10^{-2}
CASE7	-2.91×10^{-2}	-2.44×10^{-2}	-1.45×10^{-2}	-1.04×10^{-2}	-2.70×10^{-3}	-2.30×10^{-3}	1.90×10^{-3}	-1.00×10^{-2}
CASE8	-2.67×10^{-2}	-4.26×10^{-2}	-5.53×10^{-2}	-3.58×10^{-2}	-1.36×10^{-2}	-1.28×10^{-2}	-5.30×10^{-3}	-1.42×01^{-3}
CASE9	1.15×10^{-2}	1.08×10^{-2}	1.13×10^{-2}	2.50×10^{-3}	-3.90×10^{-3}	-5.70×10^{-3}	-4.70×10^{-3}	1.15×10^{-2}
CASE10	-3.60×10^{-2}	-2.61×10^{-2}	-6.80×10^{-3}	2.40×10^{-3}	8.00×10^{-4}	4.80×10^{-3}	-3.50×10^{-3}	3.82×10^{-3}
CASE11	-8.44×10^{-2}	-8.74×10^{-2}	-6.44×10^{-2}	-4.28×10^{-2}	-3.11×10^{-2}	-1.37×10^{-2}	-3.50×10^{-3}	-3.28×10^{-2}
CASE12	-5.04×10^{-2}	-4.84×10^{-2}	-4.88×10^{-2}	-3.08×10^{-2}	-9.80×10^{-3}	-3.28×10^{-2}	-3.60×10^{-2}	-2.44×10^{-2}

The mean values tend to decrease in the alongslope direction, and occasionally change sign, due to decreased fluid velocities and duration of uprush vs. backwash as the swash reaches its maximum landward extent. Because sediment transport is dependent on bed shear stresses, the finding that mean and overall mean stress supplied to the bed is small compared to instantaneous values is consistent with the statement by *Osborne and Rooker* [1999] that the net sediment transport rate is the small difference between two large opposing quantities.

Estimated Friction Coefficients From The Drag Law Formulation

Multiple estimates of shear stresses in a boundary layer can be obtained using several different methods. In the previous section, bed shear stresses were estimated via the very near bed velocity gradients. Another method is to utilize the free stream velocity as a surrogate for the friction velocity by incorporating a friction coefficient as

$$\tau = \rho u^{*2} = \frac{1}{2}\rho f u^2, \quad (6\text{-}5)$$

where u^* is the friction velocity and f is an empirical friction coefficient. Normally values for u in this formulation are taken from a vertical location where a measurement happens to be made irrespective of its location with respect to the boundary layer as mentioned earlier. Utilizing this formulation to determine τ requires specifying f, normally based on the estimated bed roughness. Formulas do exist for estimating f on smooth slopes for laminar flow and have been estimated by experimentation as a function of Reynlolds number (see short overview by *Nielsen* [1992]). Here, rather than estimating the shear stress using an f value from experiment, we assume that the two shear stress formulations equations 6-4 and 6-5 are equivalent and solve for f via

$$\tau = \frac{1}{2}\rho f u^2 = \rho(\nu + \nu_t)\left(\frac{\partial u}{\partial z} + \frac{\partial w}{\partial x}\right) \Rightarrow f = \frac{2(\nu + \nu_t)\left(\left|\frac{\partial u}{\partial z} + \frac{\partial w}{\partial x}\right|\right)}{u^2}. \quad (6\text{-}6)$$

In this manner the friction coefficient can be solved using velocities from various vertical locations (Figure 6-13, example for CASE11). In this example, friction coefficients are estimated using alongslope fluid velocities from just above the bed, the mid water column and just below the free surface. Friction estimates range from 10^{-4} to > 1 with most predicted values being in the 10^{-4} to 10^{-2} range. The estimates are similar for the three vertical locations, but show that some variability (1.8×10^{-3} and -8.5×10^{-4} mean difference between the values using velocities near the free surface and bed as compared to those obtained using velocities from the mid water column respectively) can occur solely based on the location the velocity measurement is taken. Although the variability here is moderate, it is expected that under prototype conditions with larger fluid velocities the variability could be more substantial. The nearly vertical regions of large friction values (> 1) are a result of the square of small fluid velocities in the denominator of equation 6-6 and are likely unrealistic. Since the large *f* values are associated with flow reversal, the panels on the left side of Figure 6-13 also show how the uprush vs. backwash duration is a function of alongslope distance and reiterates that the backwash at lower locations on the foreshore begins before the uprush has reached its maximum landward extent.

Extracting time series across the friction panels (Figure 6-13 right side) further shows the inter-swash variability of *f*. The friction coefficient increases at the very beginning of uprush followed by a slight decay. As the velocity slows, the friction coefficient again increases slightly to drastically near flow reversal.

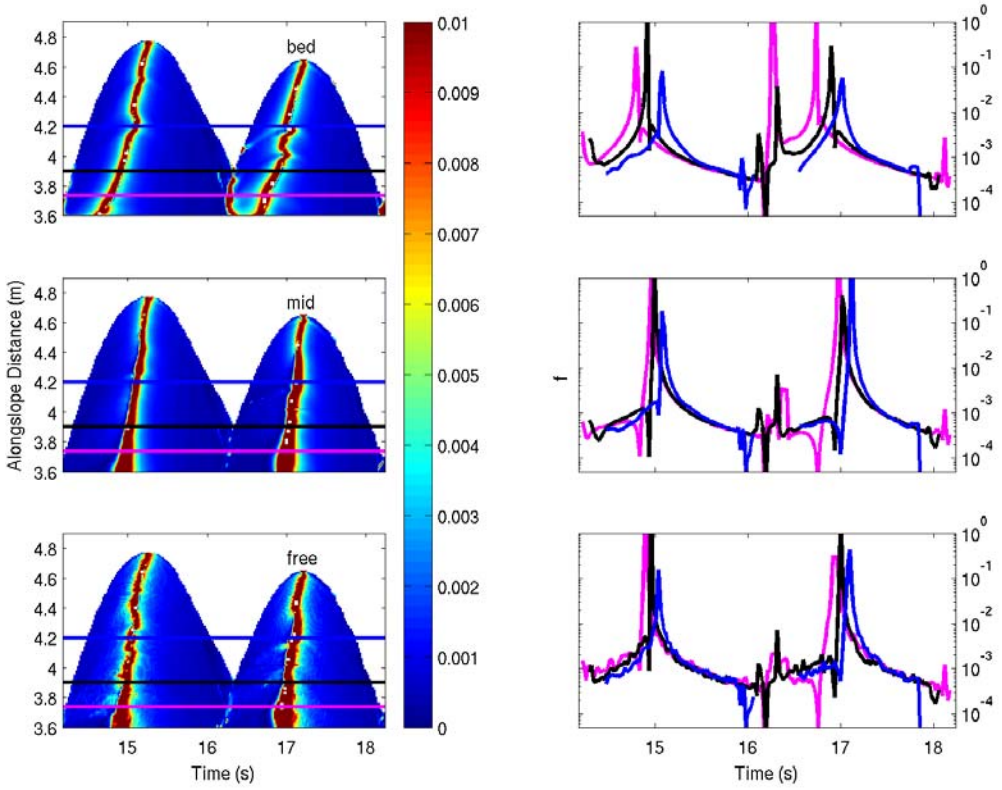

Figure 6-13. Estimated friction coefficients for CASE11 using the fluid velocity from just above the bed ('bed'), the mid water column ('mid'), and just below the free surface ('free'). Colorscale is the friction coefficient value. Time series of friction coefficients (right side) extracted from the corresponding horizontal lines in the left hand side plots.

Table 6-3. Friction coefficient estimates using equation 6-6 and the fluid velocity from mid water depth for each case based on the region shaded in Figures 6-1 and 6-2.

	5^{th} Percentile	50^{th} Percentile	95^{th} Percentile	Mean	Standard Deviation
CASE1	1.10×10^{-3}	3.00×10^{-3}	3.17×10^{-2}	1.19×10^{-2}	5.11×10^{-2}
CASE2	6.53×10^{-4}	1.75×10^{-3}	1.56×10^{-2}	5.63×10^{-3}	2.29×10^{-2}
CASE3	1.20×10^{-3}	2.41×10^{-3}	3.25×10^{-2}	1.38×10^{-2}	7.29×10^{-2}
CASE4	8.53×10^{-4}	1.76×10^{-3}	4.93×10^{-3}	2.16×10^{-3}	1.33×10^{-3}
CASE5	4.57×10^{-4}	1.18×10^{-3}	4.78×10^{-3}	1.72×10^{-3}	1.60×10^{-3}
CASE6	3.21×10^{-4}	7.09×10^{-4}	4.74×10^{-3}	1.39×10^{-3}	2.08×10^{-3}
CASE7	8.78×10^{-4}	2.61×10^{-3}	2.44×10^{-2}	8.64×10^{-3}	2.82×10^{-2}
CASE8	5.07×10^{-4}	1.31×10^{-3}	1.27×10^{-2}	5.66×10^{-3}	3.24×10^{-2}
CASE9	1.09×10^{-3}	1.87×10^{-3}	1.36×10^{-2}	8.54×10^{-3}	5.88×10^{-2}
CASE10	5.17×10^{-4}	1.58×10^{-3}	4.86×10^{-3}	2.01×10^{-3}	1.55×10^{-3}
CASE11	3.17×10^{-4}	8.73×10^{-4}	1.70×10^{-2}	8.06×10^{-3}	4.99×10^{-2}
CASE12	4.85×10^{-4}	8.68×10^{-4}	5.52×10^{-3}	1.65×10^{-3}	2.17×10^{-3}

At the start of backwash, the *f* values are still large and decrease for the remainder of the backwash duration until collision with the next uprush. Values tend to be slightly larger during uprush than backwash with the largest values occurring near flow reversal. The shapes of the friction curves are similar to those presented by *Cowen et al.* [2003] for simulations over a smooth glass beach, but the overall magnitudes are somewhat smaller. Friction coefficients for all cases using the fluid velocity from mid water depth for the regions shaded in Figures (6-1 and 6-2) are summarized in Table 6-3. Values greater than 1 have been removed from the analysis. Mean friction coefficients for all cases are on the order of 10^{-3} to 10^{-2}, which are slightly smaller than values typically used in the swash zone for rough beaches [*Puleo and Holland*, 2001; *Cox and Hobensack*, submitted and *Raubenheimer et al.*, in review]. Given the fact that the estimates here are for perfectly smooth beds while those mentioned above occurred over rough beds, it is not all that surprising that the estimated values are slightly smaller. What is interesting is that the values found here are slightly smaller than those obtained by *Cowen et al.* [2003] over a smooth bed. Differences can possibly be attributed to the hydrodynamic conditions and the method they used to estimate *f*, namely a slightly different strain rate formulation is used compared to this study.

Conclusions

The numerical simulations performed here analyzed variations between alongslope fluid velocities, bed shear stresses and friction coefficients for hydrodynamic conditions spanning Iribarren space for surging, plunging and nearly spilling waves. The main conclusions are as follows:

1) As the Iribarren number decreases causing waves to go from surging to spilling, the runup excursion becomes more irregular for monochromatic forcing. The

processes occurring in the swash zone operate at scales that are controlled by the initial uprush velocity, friction and in a large part to the downslope component of gravity. As the latter effect diminishes on shallow sloping beaches, swash overtake and interactions cause spatial variation in the uprush starting point and drive lower frequency oscillation of the shoreline.

2) Large backwash velocities are confined to the thin rundown wedge just prior to collision with the next uprush. Maximum uprush velocities are normally observed at the initiation of landward motion, but in the cases where the final wave breaking occurs landward of the shoreline, much of the incident energy is expended. Velocities normal to the bed are generally less than 5% of the alongslope flows except near the collapse point or leading edge where they can be of similar magnitude.

3) For the short period cases simulated here, the maximum uprush and backwash velocities were nearly equal. The uprush duration was nearly always less than the backwash duration. The difference between uprush and backwash duration decreased as a function of alongslope distance.

4) Alongslope fluid velocities showed some dependence on Iribarren number with the plunging wave cases generally having the largest velocity maxima. Alongslope velocity maxima also showed a correspondence to the wave period with 2 s waves having larger maximum values than their 1 s counterparts.

5) Swash zone boundary layers were observed to be on the order of 0.02 m during the initial stages of uprush and less than 0.01m during the rest of the uprush and backwash phases. The short duration backwashes simulated here did not have adequate time for the backwash boundary layer to experience significant development.

6) Swash zone shear stresses were found to generally be of slightly larger magnitude during the initial stages of uprush but of shorter duration than the backwash phase. As expected, shear stress magnitudes decrease in the alongslope direction but showed no drastic change in the trend with respect to Iribarren number as a function of alongslope distance. The 1 s waves experienced the largest shear stresses when they were plunging where the 2 s waves experienced the largest shear stresses when they were surging.

7) Friction coefficient estimates based on the near bed velocity gradients and the quadratic drag law yielded mean values in the 10^{-4} to 10^{-2} range for the perfectly smooth beach. The time history of the friction coefficient displayed a short duration peak during uprush followed by a decrease before the values increased drastically near flow reversal. The values during backwash started out large and decreased continually for the rest of the backwash duration.

CHAPTER 7
SUMMARY AND FUTURE DIRECTIONS

General Conclusions

The work contained herein investigated a range of processes and methodologies used in the swash zone. On the one hand, remote sensing methods were used to obtain surface flow fields over large spatial regions while on the other hand, a detailed hydrodynamic model was used to investigate small scale processes occurring within the water column at various phases of the swash cycle. Both of these extremes were linked by the common thread of trying to better understand swash processes with an aim towards improved sediment transport predictions.

In terms of understanding sediment transport, it was found that high suspended sediment concentrations occurred, as expected, during large velocities but also, not necessarily expected, during significant departures from gravitational acceleration. As a result of this finding, the typical sediment transport model was modified to include a parameterization of the flow acceleration. This new parameterization showed improved correlation over the typical model alone. It was interesting to find that the large accelerations in the swash zone occurred, during times of large horizontal pressure gradients and turbulent dissipation. Based on this nearly simultaneous occurrence, it was hypothesized that the acceleration serves as a proxy for these processes rather than its own physical sediment transport mechanism.

Armed with the ability to determine flow fields over large spatial domains and new sediment transport formulations, predictive capability on a field data set containing large and minimal foreshore elevation changes could be tested. It was found that using 2 separate acceleration parameterizations significantly reduced the prediction error over the standard velocity-moment-based (Bagnold-type) model. The modification developed as part of this work, performed more poorly than a previously published modification but still showed significant skill. In both cases, a portion of the increased skill was due to the addition of a free parameter, but did not override the benefit of the additional term. In addition to direct predictions, the velocity data was used to investigate links between flow field statistics and the observed change. In conjunction with past research, it was found that the largest erosion was observed under conditions of high offshore-directed low frequency velocity skewness associated with infragravity motions and relatively small values of onshore acceleration skewness associated with the offshore to onshore velocity transitions near the bore.

Finally, the small scale vertical flow structure and bed shear stresses were investigated via a Navier-Stokes solver. The model utilized here showed strong correspondence to laboratory observations for both free surface elevations and cross-shore fluid velocities. It was found, in support of the previous chapters, that a short-lived burst of onshore acceleration is observed during the collapse portion of a swash event with a deceleration phase predicted near the end of the backwash. Simulations showed that vertical flow structure is nearly depth uniform during much of the swash cycle but shows varied boundary layer structure near the initial stages and during the collision process. Departures from hydrostatic approximation tended to be small except near the

collision region between backwash and uprush suggesting that the non-linear shallow water assumptions often used in the swash region are typically valid. For the two laboratory cases simulated, the net bed shear stress for a swash cycle tended to be offshore-directed suggesting that the net force applied to the bed would enhance offshore motion of sediment.

The effect of varying swash motions on velocities and mean bed shear stresses was further investigated by testing the hydrodynamic model over a varied range of conditions. In almost all cases the maximum uprush and backwash velocities were nearly equal while the duration of the uprush to backwash was smaller. The difference between the duration of each phase decreased in the alongslope direction. In general it was found that the largest bed stresses occurred under plunging waves. It was also observed that surging waves with a 2 s period experienced larger stresses than the plunging wave cases suggesting that the shear stresses in the swash show some dependence on the wave period. Shear stresses in conjunction with the quadratic drag law were also used to estimate friction coefficients on the smooth model bed and yielded mean values between 10^{-2} and 10^{-4}, in the range observed in other smooth bed laboratory simulations.

Big Picture: Where to go from Here?

This dissertation and review of the recent swash zone literature has shed some light on the knowledge and lack thereof of swash zone fluid motions and sediment transport. Some general aspects of the swash zone are now becoming accepted such as: the difference in uprush and backwash dynamics, the importance of swash zone turbulence in driving sediment transport, and the overall importance of the swash zone to the sediment budget of the nearshore. Low and high frequency motions alike have been shown to be important on natural beaches with swash zones typically being low

frequency dominated even on steep beaches. Still, much more is to be gained through understanding of the vertical structure of swash flows, backwash/uprush collision, bore motion and hydraulic jump phenomena that occurs in the swash zone. The relatively shallow flows away from the bore have an extremely thin boundary layer that extends below the undisturbed bed requiring further knowledge into the dynamics of sheet flow [*Ribberink and Al-Salem*, 1994; *Ribberink and Al-Salem*, 1995; *Sumer et al.*, 1996 ;*Drake and Calantoni*, 2001; *Dohmen-Janssen and Hanes*, 2002 and*Nielsen and Callaghan*, 2003]; single phase (debris) flow [*Capart et al.*, 2001]; and/or two phase flows [*Jenkins and Hanes*, 1998 and *Hsu and Hanes*, submitted]. One instrument that may improve our understanding of high concentration, near bed flows is the conductivity concentration meter system (CCM; *Ribberink and Al-Salem* [1995] and *Dohmen-Janssen and Hanes* [2002]). The CCM consists of electrodes that measure the conductivity, related to the volume concentration, of the sand/water mixture in a flow. The CCM is placed beneath the sand surface with the electrodes located in the mobile bed layer with their elevation controlled by a vertical positioning system. At present this device has only been used in the surf zone in a laboratory setting, but its use in swash zone laboratory studies and potentially in a field exercise may lead to ground-breaking discoveries regarding near bed sediment transport in the swash zone.

Based on the present knowledge of swash motions, kinematic and numerical models have been developed to predict the fluid motions with varying degrees of success, but models based on the depth averaged non-linear shallow water equations and Navier-Stokes solvers are showing promise in terms of understanding both the medium scale fluid motions and the micro-scale fluid motions in the NS case even with respect to flow

just above the bed. In this regard, numerical models have fully outpaced our ability to collect thorough validation data. Instrumentation to monitor swash motions, however, is becoming more rugged and miniaturized so that the details in thin swash flows can be viewed and used as ground truth. Model verification will be further enhanced as remote sensing applications in the swash zone become more readily available.

Unlike our present capability to monitor and predict swash zone flows, capabilities regarding both modeling and collection of sediment transport in the swash zone is poor. The use of simple sediment transport models may need somewhat of an overhaul if the complex sediment dynamics in the highly turbulent swash are to be understood. For instance, a better understanding of sediment entrainment in hydraulic jumps, turbulent bores and thin flows with large shear stresses seems important and physically unaccounted for in the simple models. Recent extensions to the typically used energetics-type model may account for some of these more poorly understood phenomena but likely in a proxy form rather than explicitly describing the physical mechanisms.

Since swash zone research has ramped up in the past decade or so and with continued emphasis on its importance in nearshore research [*Thornton et al.*, 2000] it seems that knowledge, physical understanding and modeling capability are sure to improve. Ideally, future studies of the swash zone will consist of all the required measurements rather than trying to break down interconnected processes into individual pieces. To that end, it is suggested that when possible future studies of the swash zone incorporate sediment transport, three dimensional velocity, groundwater and/or pore pressure and water depth measurements, in at least several closely spaced locations on the

foreshore and at the “edge of the swash zone” in addition to video monitoring and foreshore profiling to hopefully capture as many of the potentially important processes simultaneously. These measurements can then be used as both forcing and validation for hydrodynamic and sediment transport models. While the costs of an expanded field study such as the one alluded to above are prohibitive for any single investigator, collaboration in a format analogous to the multi-investigator Duck set of field experiments or the recent MaST-III SASME (Surf and Swash Zone Mechanics) project seems warranted.

APPENDIX A
ACCURACY OF THE FORCING METHOD AND EFFECT OF NUMERCAL DISSIPATION

Because the forcing used in the numerical model, RIPPLE, was depth uniform for the velocity fields and because the numerical scheme is only second order accurate in space and first order accurate in time, the effect of numerical dissipation must be addressed. *Liu and Lin* [1997] used an interpolated donor cell method and showed that in their formulation, the numerical dissipation was roughly 2 orders of magnitude greater than the molecular viscosity. However, during breaking where large velocity gradients can occur, the turbulent eddy viscosity tended to be an order of magnitude larger than the numerical viscosity. In the case of non breaking waves where the flow is mostly irrotational, large velocity gradients do not exist such that the fluid viscosity plays a more limited role in dissipation.

Following *Lin and Liu* [1998] we test this model using a solitary wave traveling over a constant water depth. The free surface profile and velocities are given from the analytical Boussinesq solution as [*Lee et al.*, 1982]

$$\eta = H\left[\sec h\sqrt{\frac{3}{4}\frac{H}{h}}\frac{x-Ct}{h}\right]^2 \quad \text{(A-1)}$$

$$u = \sqrt{gh}\frac{\eta}{h} \quad \text{(A-2)}$$

$$w = \sqrt{gh}\frac{z}{h}\frac{1}{C}\frac{\partial \eta}{\partial t}, \text{(A-3)}$$

where η is the sea surface elevation, H is the solitary wave amplitude, h is the still water depth, x is the horizontal distance, z is the elevation above the bed and C is the wave phase speed given as

$$C = \sqrt{gh\left(1+\frac{H}{h}\right)} \quad . \text{(A-4)}$$

Note that in equations A-2 and A-3, only the lowest order terms are retained.

In this test, the LES and molecular viscosity are turned off such that we expect similar results to the test of *Lin and Liu* [1998] based on model similarity, but may vary slightly due to our forcing method and other small differences in model modifications. Therefore, we replicate the test case of their study using H =0.1 m, h = 1.0 m, dx = 0.1 m and dz = 0.01m. The model domain is 100 m long and the time step is allowed to vary based on stability criteria. The free surface and depth-independent velocities obtained at $z = h$ are forced at the left side of the domain. The right boundary is given as outflow so no reflection occurs. In the comparison, simulations are performed using the Van Leer discretization for advection as well as for values of α = 0.1, 0.3, 0.5, 0.7 and 0.9, where α controls the relative contribution of centered difference and donor cell discretization methods. A value of α = 0 is a centered difference scheme, whereas a value of α = 1 is a first order donor cell scheme. Values in between are interpolated donor cell methods. *Lin and Liu* [1998] used α = 0.3.

Free surface time series from x =10, 30, 50, 70 and 90 m are shown in Figure A-1. Numerical results are given by the dots whereas the analytical solution is given by the solid line. The numerical solutions match the analytical solution almost exactly at x = 10 and 30 m but starts to show slight leads and amplitude reduction by x = 70 and 90 m. This slight lead was also observed by *Liu and Lin* [1997] but they did not observe

noticeable amplitude reduction. Near the forcing region the van Leer method produces the most accurate results with respect to sea surface elevation with the error increasing as a function of α (Table A-1; showing root-mean-square elevation and mean percent error values for regions containing the solitary wave). Further away from the forcing region the error for the van Leer method becomes similar to the error using $\alpha = 0.3$ to 0.5 and the errors still tend to increase as a function of α. Possible reasons for the differences include numerical dissipation brought about by the various differencing schemes as evidenced by their relation to α. Another possibility for the discrepancies is potentially attributed to the fact that the vertical velocity, although small, was forced assuming a piston type (depth independent) mechanism rather than the analytical vertical profile. *Liu and Lin* [1997] further suggest that the use of the truncated Boussinesq formulation may not be sufficient to reproduce the original Navier-Stokes equations since higher order non-linear and dispersive terms are ignored. In the test here, though, this is likely mitigated due to the relatively small H/h ratio.

The test of numerical dissipation presented here is only partial because we have only addressed one condition. For instance, larger H/h ratios for the solitary waves or other tests under breaking waves or highly non-linear conditions may have shown the numerical dissipation to be larger than that determined by Table A-1. Hence, it should be expected that some numerical damping, as observed even in the solitary wave cases, does exist in these simulations but merely represents another form of sub grid scale dissipation.

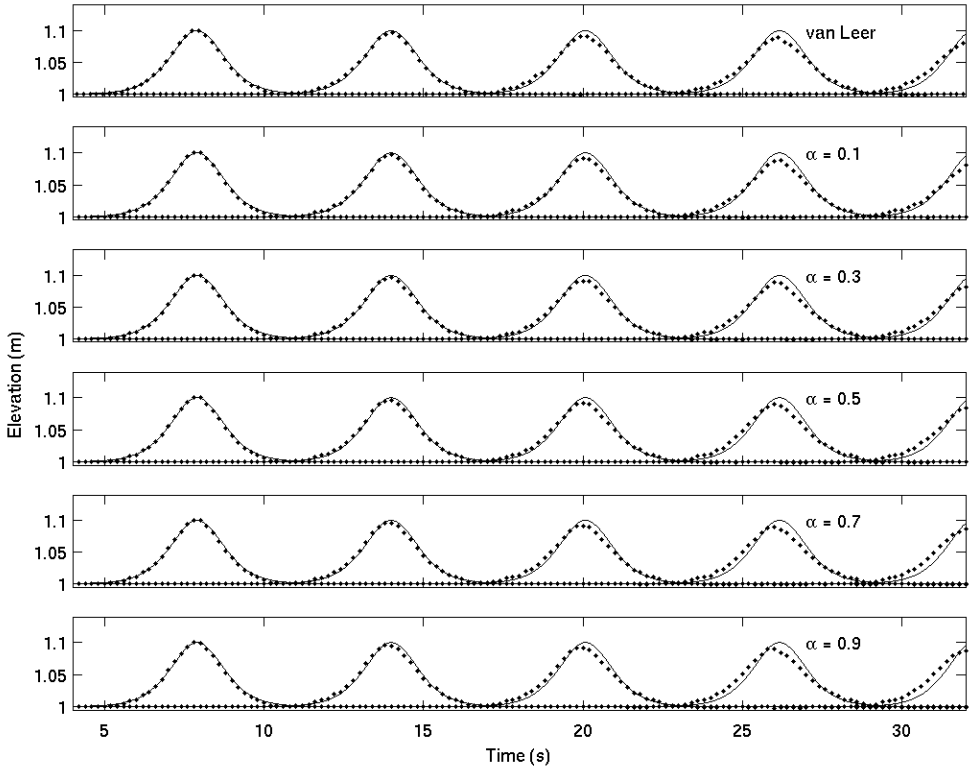

Figure A-1. Differencing scheme comparison for solitary waves over a flat bottom at distances of 10, 30, 50, 70 and 90 m from the boundary as shown by the successive peaks in each subplot. Comparisons are made for Van Leer differencing for the advection terms and several interpolated donor cell methods with various weights given by the alpha value as explained in the text.

Table A-1. Root mean square sea surface elevations errors as a function of distance for the solitary wave test for the various differencing schemes. Parenthetical values are mean percent errors between the theoretical solitary wave and that predicted by the model.

	x =10 m	x = 30 m	x = 50 m	x = 70 m	x = 90 m
van Leer	1.8×10^{-3} m (0.14)	2.5×10^{-3} m (0.18)	4.1×10^{-3} m (0.28)	5.8×10^{-3} m (0.40)	6.2×10^{-3} m (0.49)
$\alpha = 0.1$	1.9×10^{-3} m (0.15)	2.4×10^{-3} m (0.17)	3.8×10^{-3} m (0.26)	5.4×10^{-3} m (0.34)	4.9×10^{-3} m (0.37)
$\alpha = 0.3$	2.0×10^{-3} m (0.15)	2.6×10^{-3} m (0.18)	4.1×10^{-3} m (0.27)	5.6×10^{-3} m (0.36)	5.2×10^{-3} m (0.41)
$\alpha = 0.5$	2.0×10^{-3} m (0.15)	3.0×10^{-3} m (0.21)	4.6×10^{-3} m (0.31)	6.3×10^{-3} m (0.42)	6.4×10^{-3} m (0.50)
$\alpha = 0.7$	2.0×10^{-3} m (0.15)	3.3×10^{-3} m (0.23)	5.2×10^{-3} m (0.35)	7.1×10^{-3} m (0.47)	7.8×10^{-3} m (0.60)
$\alpha = 0.9$	2.1×10^{-3} m (0.16)	3.7×10^{-3} m (0.26)	5.8×10^{-3} m (0.40)	7.9×10^{-3} m (0.54)	9.2×10^{-3} m (0.70)

APPENDIX B
UTILITY OF THE LARGE EDDY SIMULATION

Comparison of the RIPPLE model with laboratory observations using LES showed little to no variation over the use of the model without a turbulence closure scheme. Several possibilities exist to explain this occurrence. The first is that, except near the free surface, the lack of strong velocity gradients precludes the necessity of a turbulence closure scheme such that the bulk of the flow is well described by the Navier-Stokes equations using molecular viscosity only. A second reason that the LES had no effect on the simulations performed here is potentially due to the grid resolution. Because the grid scales are 0.004 m x 0.002 m, it is likely that much of the small scale turbulence is already being resolved. If Kolmogorov's (1941) universal equilibrium theory is adopted, then the rate at which the "small" eddies dissipate energy into heat is governed by the transfer of energy from the "large" to the "small" eddies. This leads to a turbulence length scale dependent on the molecular viscosity and the dissipation rate as (see, for instance, *Tennekes and Lumley* [1972] or *Pope* [2000])

$$L = \left(\frac{\nu^3}{\varepsilon_{diss}} \right)^{1/4}, \text{(B-1)}$$

where ε_{diss} is the dissipation rate given by

$$\varepsilon_{diss} = 2\nu \left\langle s_{ij} s_{ij} \right\rangle, \text{(B-2)}$$

Brackets denote time averaging and the strain rate, s_{ij} is given by

$$s_{ij} = \frac{1}{2}\left(\frac{\partial u_i}{\partial x_j} + \frac{\partial u_j}{\partial x_i} \right). \quad \text{(B-3)}$$

Utilizing values of ε_{diss} from the cross-shore locations of the current meters in the irregular wave case yields estimates for L ranging between 8.1 x 10^{-5} and 1.6 x 10^{-3} m (Table B-1). Values in these calculations were included only when the region of interest was covered by water so that the mean and standard deviations were not biased by including zeroes. These estimated values of the smallest turbulence length scales range from roughly an order of magnitude smaller than and up to the resolvable scales for the present simulations and suggest that much of the small scale turbulence and energy containing eddies are being resolved.

To further test this notion, the irregular wave case is simulated again by reducing the resolution to one-half and one-quarter the former value in both the horizontal and vertical directions (dx = 0.008 m and dz = 0.004 m; dx = 0.016 m and dz = 0.008 m respectively). Although this will adversely affect the runup since a sparse grid cannot accurately capture the location of the leading edge, it will help determine the applicability of the LES when the turbulence is poorly resolved. The sea surface elevation at the two inner surf zone locations is essentially the same for the LES and reduced grid resolution LES simulations (Figure B-1, Table B-2). This implies that the model is typically capable of reproducing the sea surface elevation even at the reduced resolutions with or without LES. Yet, some amplitude reduction is observed at the one-quarter resolution grid. Hence, unless the grid resolutions are coarse with respect to the scales of interest, LES is not needed to accurately reproduce the sea surface in our 2D simulations.

Table B-1. Estimate of the turbulence length scales as a function of cross-shore distance for June 19, 2002.

Cross-shore Location (m)	Minimum (m)	Maximum (m)	Mean(m)	Std (m)
x = 1.4	1.1×10^{-4}	1.6×10^{-3}	6.8×10^{-4}	4.8×10^{-4}
x = 3.0	8.3×10^{-5}	1.3×10^{-3}	5.1×10^{-4}	4.1×10^{-4}
x = 3.95	8.6×10^{-5}	5.6×10^{-4}	2.4×10^{-4}	1.0×10^{-4}
x = 4.29	8.1×10^{-5}	4.5×10^{-4}	2.0×10^{-4}	5.7×10^{-5}
x = 4.53	1.1×10^{-4}	2.6×10^{-4}	1.7×10^{-4}	2.5×10^{-5}

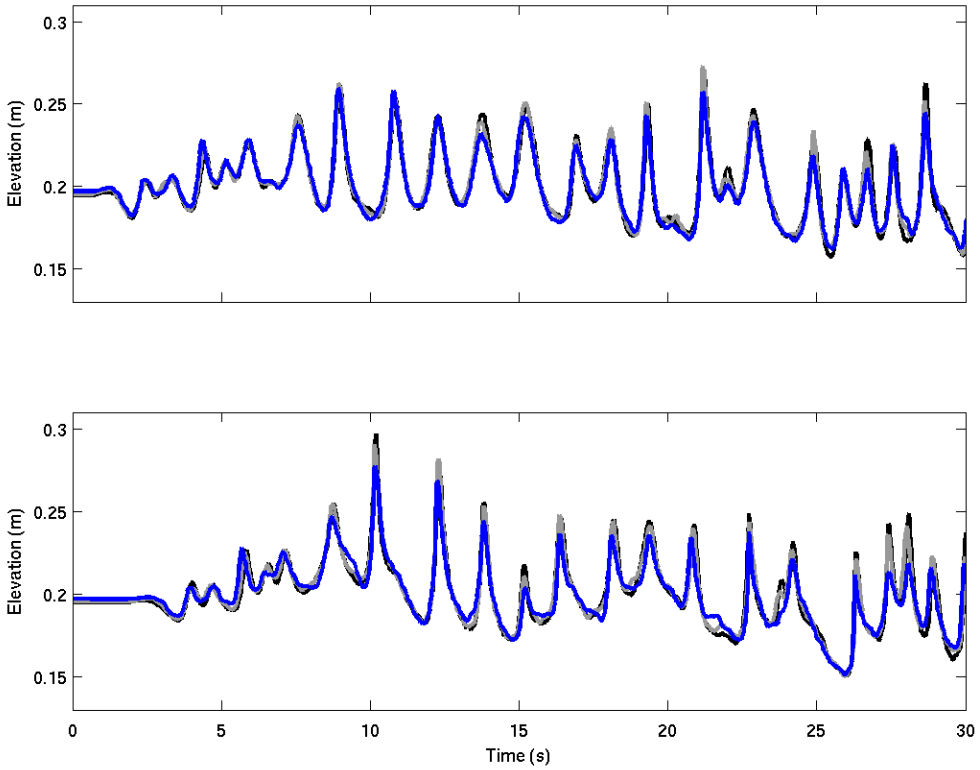

Figure B-1. Comparison of LES simulation (black) and LES simulations at reduced grid resolutions of 1/2 (gray) and ¼ (blue) for June 2002. Upper panel at cross-shore location x = 1.4 m. Bottom panel at cross-shore location x = 3.0 m.

Table B-2. Percent error for sea surface elevations in the inner surf zone for LES and all reduced resolution simulations as compared to the fine resolution non-LES simulation. Parenthetical values are R^2 correlation coefficients significant at the 99% level.

	Fine Resolution	One-half resolution	One-quarter resolution
LES (x = 1.4)	0.48 (0.996)	1.48 (0.963)	2.50 (0.902)
non-LES (x = 1.4)	------	1.50 (0.963)	2.49 (0.897)
LES (x = 3.0)	0.58 (0.994)	1.68 (0.952)	3.03 (0.841)
non-LES (x = 3.0)	------	1.64 (0.955)	3.00 (0.839)

Figure B-2 does verify that the LES is capable of predicting the increased eddy viscosity from the SGS turbulence as a result of the poorer grid resolution resulting in the similar model predictive capability. The comparisons show that the turbulent eddy viscosity is rarely much larger than the molecular viscosity ($1x10^{-6}$ m^{-2} s). During the LES, the turbulent eddy viscosity near the free surface and the forcing region is up to an order of magnitude larger than the molecular viscosity increasing the diffusion based on strong velocity gradients. We suspect that if the grid resolution is made fairly coarse, the turbulent eddy viscosity would continue to increases, but that the poor resolution would make forcing the model and individual waves and swash difficult to simulate based on the small scales of interest here. In prototype scale simulations, however, where wave lengths are on the order of tens of meters and wave heights on the order of meters, a coarser grid is expected to perform well with the inclusion of LES.

It should be noted that the reduced resolution simulations required roughly 3 hours and 3 days respectively of computation time compared to the roughly 2 weeks at the higher resolution. The similarity in model output between the simulations suggests that the reduced resolution simulation with or without the LES is capable of reproducing the sea surface measurements at nearly 5 times computational savings. The reduced resolution simulation accounts for the resolution reduction by increasing the values of SGS turbulence through the turbulent eddy viscosity that cannot be accounted for in the non-LES simulations.

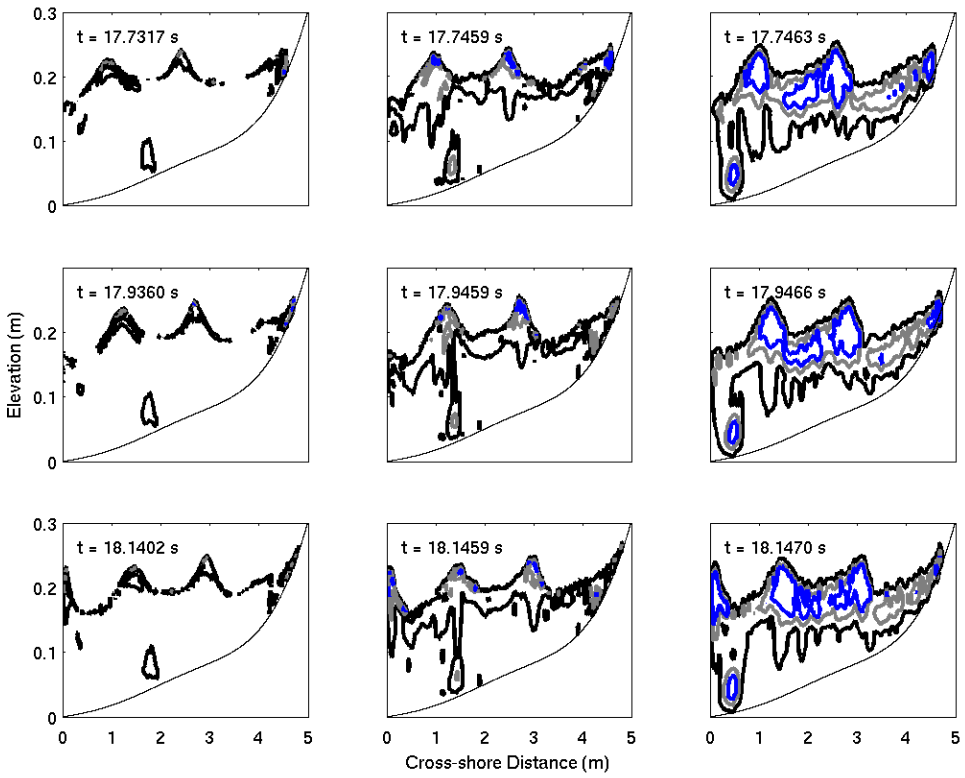

Figure B-2. Comparison of eddy viscosity for LES simulation (left panels) and LES simulation with reduced grid resolution (right panels) for June 2002 at different model times. Contours are 1 x 10^{-6} m^2 s^{-1} (black), 5 x 10^{-6} m^2 s^{-1} (gray) and 1 x 10^{-5} m^2 s^{-1} (blue).

LIST OF REFERENCES

Aagaard, T., and J. Holm, Digitization of wave run-up using video records, *Journal of Coastal Research*, *5* (3), 547-551, 1989.

Admiraal, D.M., M.H. Garcia, and J.F. Rodriguez, Entrainment response of bed sediment to time-varying flows, *Water Resources Research*, *36* (1), 335-348, 2000.

Amein, M., A method for determining the behavior of long waves climbing a sloping beach, *Journal of Geophysical Research*, *71* (2), 401-410, 1966.

Archetti, R., and M. Brocchini, An integral swash zone model with friction: an experimental and numerical investigation, *Coastal Engineering*, *45*, 89-110, 2002.

Asano, T., H. Suetomi, and J. Hoshikura, Measurements of current velocity generated in swash zone by obliquely incident waves, *Coastal Engineering in Japan*, *37* (2), 125-136, 1994.

Bagnold, R.A., Mechanics of marine sedimentation, in *The Sea*, edited by M.N. Hill, pp. 507-528, Wiley-Interscience, New York, 1963.

Bagnold, R.A., An Approach to the Sediment Transport Problem from General Physics, pp. 37, U.S. Geological Survey, Washington, DC, 1966.

Bailard, J.A., An energetics total load sediment transport model for a plane sloping beach, *Journal of Geophysical Research*, *86* (C11), 938-954, 1981.

Baird, A.J., and D.P. Horn, Monitoring and modeling groundwater behavior in sandy beaches, *Journal of Coastal Research*, *12* (3), 630-640, 1996.

Baird, A.J., T. Mason, and D.P. Horn, Validation of a Boussinesq model of beach ground water behaviour, *Marine Geology*, *148* (1-2), 55-69, 1998.

Baldock, T.E., A.J. Baird, D.P. Horn, and T. Mason, Measurements and modeling of swash-induced pressure gradients in the surface layers of a sand beach, *Journal of Geophysical Research*, *106* (C2), 2653-2666, 2001.

Baldock, T.E., and P. Holmes, Swash hydrodynamics on a steep beach, in *Coastal Dynamics Conference 1997*, edited by E.B. Thornton, pp. 784-793, ASCE, Plymouth, UK, 1997.

Baldock, T.E., and P. Holmes, Seepage effects on sediment transport by waves and currents, in *26th International Conference on Coastal Engineering*, ASCE, 1998.

Baldock, T.E., and P. Holmes, Simulation and prediction of swash oscillations on a steep beach, *Coastal Engineering*, *36* (3), 219-242, 1999.

Baldock, T.E., P. Holmes, and D.P. Horn, Low frequency swash motion induced by wave grouping, *Coastal Engineering*, *32* (2-3), 197-222, 1997.

Bascom, W.H., The relationship between sand size and beach face slope, *Transactions, American Geophysical Union*, *32* (6), 866-874, 1951.

Bascom, W.H., Characteristics of natural beaches, in *4th International Conference on Coastal Engineering*, pp. 163-180, ASCE, 1953.

Bauer, B.O., and J.R. Allen, Beach steps - An evolutionary perspective, *Marine Geology*, *123* (3-4), 143-166, 1995.

Beach, R.A., and R.W. Sternberg, Infragravity driven suspended sediment transport in the swash, inner and outer-surf zone, in *Coastal Sediments '91*, edited by N.C. Kraus, K.J. Gingerich, and D.L. Kriebel, pp. 114-128, ASCE, Seattle, 1991.

Beach, R.A., R.W. Sternberg, and R. Johnson, A fiber optic sensor for monitoring suspended sediment, *Marine Geology*, *103* (1-3), 513-520, 1992.

Bell, P.S., Shallow water bathymetry derived from an analysis of X-band marine radar images of waves, *Coastal Engineering*, *37*, 513-527, 1999.

Blewett, J.C., P. Holmes, and D.P. Horn, Swash hydrodynamics on sand and shingle beaches, in *27th International Conference on Coastal Engineering*, pp. 597-609, ASCE, Sydney, Australia, 2000.

Bodge, K.R., and R.G. Dean, Short-term impoundment of longshore transport, in *Coastal Sediments '87*, pp. 468-483, ASCE, 1987.

Bowen, A.J., Simple models of nearshore sedimentation; beach profiles and longshore bars, in *The Coastline of Canada*, edited by S.B. McCann, pp. 1-11, Geological Survey of Canada, 1980.

Bradford, S.F., Numerical simulation of surf zone dynamics, *Journal of Waterway Port Coastal and Ocean Engineering*, *126* (1), 1-13, 2000.

Bradshaw, M., Bores and swash on natural beaches, pp. 122, Sydney Univ. (Australia). Coastal Studies Unit, 1982.

Brenninkmeyer, B., Insitu measurements of rapidly fluctuating, high sediment concentrations, *Marine Geology*, *20* (2), 117-128, 1976a.

Brenninkmeyer, S.J., In situ measurements of rapidly fluctuating, high sediment concentrations, *Marine Geology*, *20*, 117-128, 1976b.

Brocchini, M., Eulerian and Lagrangian aspects of the longshore drift in the surf and swash zones, *Journal of Geophysical Research*, *102* (C10), 23155-23168, 1997.

Brocchini, M., and D.H. Peregrine, Integral flow properties of the swash zone and averaging, *Journal of Fluid Mechanics*, *317* (JUN), 241-273, 1996.

Broker-Hedegaard, I., J. Rolevink, H. Southagte, P. Pechon, J. Nicholson, and L. Hamm, Intercomparison of coastal profile models, in *Proc. 23rd International Conference on Coastal Engineering*, pp. 2108-2121, ASCE, 1992.

Broome, R., and P.D. Komar, Undular hydraulic jumps and the formation of backwash ripples on beaches, *Sedimentology*, *26*, 543-559, 1979.

Butt, T., and P. Russell, Suspended sediment transport mechanisms in high-energy swash, *Marine Geology*, *161* (2-4), 361-375, 1999.

Butt, T., and P. Russell, Hydrodynamics and cross-shore sediment transport in the swash-zone of natural beaches: A review, *Journal of Coastal Research*, *16* (2), 255-268, 2000.

Butt, T., P. Russell, G. Masselink, J. Miles, D. Huntley, D. Evans, and P. Ganderton, An integrative approach to investigating the role of swash in shoreline change, in *Proceedings of the American Society of Civil Engineers*, ASCE, Cardiff, Wales, UK, 2002.

Butt, T., P. Russell, J.A. Puleo, and G. Masselink, The application of Bagnold-type sediment transport models in the swash zone, *Journal of Coastal Research*, submitted.

Butt, T., P. Russell, J.A. Puleo, J. Miles, and G. Masselink, Observations of bore turbulence in the swash and inner surf zones, *Marine Geology*, in press.

Butt, T., P. Russell, and I. Turner, The influence of swash infiltration-exfiltration on beach face sediment transport: onshore or offshore?, *Coastal Engineering*, *42* (1), 35-52, 2001.

Capart, H., D.L. Young, and Y. Zech, Dam-break induced debris flow, in *Sediment Transport and Deposition by Particulate Gravity Currents*, edited by B. Kneller, B. McCaffrey, J. Peakall, and T. Druitt, pp. 149-156, 2001.

Carlson, C.T., Field studies of run-up generated by wind waves on dissipative beaches, pp. 194, SRI International, 1984.

Carrier, G.F., and H.P. Greenspan, Water waves of finite amplitude on a sloping beach, *Journal of Fluid Mechanics*, *4* (1), 97-109, 1958.

Chang, K.A., and P.L.-F. Liu, Velocity, acceleration and vorticity under a breaking wave, *Physics of Fluids*, *10* (1), 327-329, 1998.

Chen, G., C. Kharif, A. Zaleski, and J. Li, Two-dimensional Navier-Stokes simulation of breaking waves, *Physics of Fluids*, *11*, 121-133, 1999.

Chen, S., D.B. Johnson, and P.E. Raad, Velocity boundary conditions for the simulation of free surface fluid flow, *Journal of Computational Physics*, *115*, 262-276, 1995.

Chickadel, C., and R.A. Holman, Measuring longshore current with video techniques, *Transactions, American Geophysical Union, Fall Meeting Suppl.*, *82* (47), 2001.

Christensen, E.D., and R. Deigaard, Large eddy simulation of breaking waves, *Coastal Engineering*, *42*, 53-86, 2001.

Coco, G., D.A. Huntley, and T.J. O'Hare, Beach cusp formation: Analysis of a self-organization model, in *Coastal Sediments '99*, edited by N.C. Kraus, and W.G. McDougal, pp. 2190-2205, ASCE, Hauppauge, NY, 1999.

Conley, D.C., and J.G. Griffin, Direct measurements of bed stress under swash in the field, *Journal of Geophysical Research*, in review, 2003.

Conley, D.C., and D.L. Inman, Ventilated oscillatory boundary-layers, *Journal of Fluid Mechanics*, *273*, 261-284, 1994.

Cowen, E.A., I.M. Sou, P.L.-F. Liu, and B. Raubenheimer, PIV measurements within a laboratory generated swash zone, *Journal of Engineering Mechanics*, accepted, 2003.

Cox, D.T., and W.A. Hobensack, Temporal and spatial bottom stress variations in the swash zone, *Journal of Geophysical Research*, submitted.

Cox, D.T., W.A. Hobensack, and A. Sukumaran, Bottom stress in the inner surf and swash zone, in *Proccedings of the 27th International Conference on Coastal Engineering*, edited by B. Edge, pp. 108-119, ASCE, Sydney, AU, 2000.

Dean, R.G., and E.M. Maurmeyer, Beach cusps at Point Reyes and Drakes Bay Beaches, California, in *Proceedings of the 17th Coastal Engineering Conference*, edited by B.L. Edge, pp. 863-884, ASCE, Sydney, Australia, 1980.

Dohmen-Janssen, M., and D.M. Hanes, Sheet flow dynamics under monochromatic nonbreaking waves, *Journal of Geophysical Research*, *107*, 1-21, 2002.

Dominick, T.F., B. Wilkins Jr., and H. Roberts, Mathematical model for beach groundwater fluctuations, *Water Resources Research*, *7*, 1626-1635, 1971.

Doornkamp, J.C., and C.A.M. King, *Numerical Analysis in Geomorphology, An Introduction*, Arnold, London, 1971.

Drake, T.G., and J. Calantoni, Discrete particle model for sheet flow sediment transport in the nearshore, *Journal of Geophysical Research*, *106* (C9), 19859-19868, 2001.

Dubois, R.N., Inverse relation between foreshore slope and mean grain size a s a function of the heavy mineral content, *Geological Society of America Bulletin*, *83*, 871-876, 1972.

Dugan, J.P., G.J. Fetzer, J. Bowden, G.J. Farruggia, J.Z. Williams, C.C. Piotrowski, K. Vierra, D.C. Campion, and D.N. Sitter, Airborne optical system for remote sensing of ocean waves, *Journal of Atmospheric and Oceanic Technology*, *18* (7), 1267-1276, 2001a.

Dugan, J.P., C.C. Piotrowski, and J.Z. Williams, Water depth and surface current retrievals from airborne optical measurements of surface gravity wave dispersion, *Journal of Geophysical Research*, *106* (C8), 16,903-16,915, 2001b.

Dugan, J.P., H.H. Suzukawa, C.P. Forsyth, and M.S. Farber, Ocean wave dispersion surface measured with airborne IR imaging system, *IEEE Transactions on Geoscience and Remote Sensing*, *34* (5), 1282-1284, 1996.

Duncan, J.R., The effects of water table and tide cycle on swash-backwash sediment distribution and beach profile development, *Marine Geology*, *2*, 186-197, 1964.

Earnshaw, H.C., T. Bruce, C.A. Greated, and W.J. Easson, PIV measurements of oscillatory flow over a rippled bed, in *Proceedings of the 24th International Conference on Coastal Engineering*, edited by B.L. Edge, ASCE, Kobe, Japan, 1994.

Elfrink, B., and T.E. Baldock, Hydrodynamics and sediment transport in the swash zone: a review and perspectives, *Coastal Engineering*, *45*, 149-167, 2002.

Elgar, S., E.L. Gallagher, and R.T. Guza, Nearshore sandbar migration, *Journal of Geophysical Research*, *106* (C6), 11623-11627, 2001.

Eliot, I.G., and D.J. Clarke, Semi-diurnal variation in beach face aggradation and degradation, *Marine Geology*, *79*, 1-22, 1988.

Emery, K.O., and J.F. Foster, Water tables in marine beaches, *Journal of Marine Research*, *VII* (3), 644-654, 1948.

Emery, K.O., and J.F. Gale, Swash and swash mark, *Transactions, American Geophysical Union*, *32* (1), 31-36, 1951.

Ericksen, N.J., Measurement of tide induced change to water table profiles in coarse and fine sandy beaches along Pegasus Bay, Canterbury, *Earth Science*, *4*, 24-31, 1970.

Evans, D., G. Masselink, P. Russell, T. Butt, J. Miles, and P. Ganderton, Application of Bagnold's model in the swash zone using field data, in *Coastal Sediments '03*, ASCE, Clearwater Beach, FL, 2003.

Ferziger, J.H., and M. Peric, *Computational Methods for Fluid Dynamics*, 389 pp., Springer, 1999.

Flick, R.E., and R.A. George, Turbulence scales in the surf and swash, in *Proceedings of the 22nd International Conference on Coastal Engineering*, 1990.

Frasier, S.J., Y. Liu, D. Moller, R.E. McIntosh, and C. Long, Directional ocean wave measurements in a coastal setting using focused array imaging radar, *IEEE Transactions on Geoscience and Remote Sensing*, *33* ((2)), 428-440, 1995.

Frasier, S.J., and R.E. McIntosh, Observed wavenumber-frequency properties of microwave backscatter from ocean surface at near-grazing angles, *Journal of Geophysical Research*, *101* (C(8)), 18391-18407, 1996.

Freeman, J.C., and B. Le Méhauté, Wave breakers on a beach and surges on a dry bed, *Journal of the Hydraulics Division*, *90* (HY2), 187-216, 1964.

Gallagher, E.L., S. Elgar, and R.T. Guza, Observations of sand bar evolution on a natural beach, *Journal of Geophysical Research*, *103* (C2), 3203-3215, 1998.

Gourlay, M.R., Wave set-up, wave run-up and beach water-table: Interaction between surf zone hydraulics and groundwater hydraulics, *Coastal Engineering*, *17* (1-2), 93-144, 1992.

Graber, H.C., D.R. Thompson, and R.E. Carande, Ocean surface features and currents measured with synthetic aperature radar interferometry and HF radar, *Journal of Geophysical Research*, *101* (C11), 25813-25832, 1996.

Grant, U.S., Influence of the water table on beach aggradation and degradation, *Journal of Marine Research*, *VII* (3), 655-660, 1948.

Gray, C., and C.A. Greated, The application of PIV to the study of water waves, *Optics and Lasers in Engineering*, *9*, 265-276, 1988.

Guza, R.T., and D.L. Inman, Edge waves and beach cusps, *Journal of Geophysical Research*, *80* (21), 2997-3012, 1975.

Guza, R.T., and E.B. Thornton, Swash oscillations on a natural beach, *Journal of Geophysical Research*, *87* (C1), 483-491, 1982.

Haas, K.A. and I.A. Svendsen, Three-dimensional modeling of rip current systems, pp. 250, University of Delaware, 2000.

Hamilton, D.G., and B.A. Ebersole, Establishing uniform longshore currents in a large-scale sediment transport facility, *Coastal Engineering*, *42* (3), 199-218, 2001.

Hanes, D.M., and D.A. Huntley, Continuous measurements of suspended sand concentration in a wave dominated nearshore environment, *Continental Shelf Research*, *6* (4), 585-596, 1986.

Hardisty, J., A morphodynamic model for beach gradients, *Earth Surface Processes and Landforms*, *11* (3), 327-333, 1986.

Hardisty, J., A note on suspension transport in the beach gradient model, *Earth Surface Processes and Landforms*, *15* (1), 91-96, 1990.

Hardisty, J., J. Collier, and D. Hamilton, A calibration of the Bagnold beach equation, *Marine Geology*, *61* (1), 95-101, 1984.

Harlow, F.H., and J.E. Welch, Numerical calculation of time-dependent viscous incompressible flow, *Physics of Fluids*, *8*, 2182-2189, 1965.

Harrison, W., Empirical equations for foreshore changes over a tidal cycle, *Marine Geology*, *7* (6), 529-551, 1969.

Harrison, W., C.S. Fang, and S.N. Wang, Groundwater flow in a sandy tidal beach 1. One-dimensional finite element analysis, *Water Resources Research*, *7*, 1313-1322, 1971.

Hart, D.P., High-speed PIV analysis using compressed image correlation, *Journal of Fluids Engineering - Transactions of the ASME*, *120* (3), 463-470, 1998.

Hegge, B.J., and G. Masselink, Groundwater-table responses to wave run-up: An experimental study from western Australia, *Journal of Coastal Research*, *7* (3), 623-634, 1991.

Hibberd, S., and D.H. Peregrine, Surf and run-up on a beach: a uniform bore, *Journal of Fluid Mechanics*, *95* (2), 323-345, 1979.

Hirt, C.W., and B.D. Nichols, Volume of fluid (VOF) method for the dynamics of free boundaries, *Journal of Computational Physics*, *39*, 201-225, 1981a.

Hirt, C.W., and B.D. Nichols, Volume of fluid (VOF) moethod for dynamics of free boundaries, *Journal of Computational Physics*, *39*, 201-225, 1981b.

Ho, D.V., and R.E. Meyer, Climb of a bore on a beach: Part 1, Uniform beach slope, *Journal of Fluid Mechanics*, *14* (20), 305-318, 1962.

Hoefel, F., and S. Elgar, Surfzone sandbar migration and wave acceleration induced sediment transport, *Science*, *299*, 1885, 2003.

Holland, K.T., Application of the linear dispersion relation with respect to depth inversion and remotely sensed imagery, *IEEE Transactions on Geoscience and Remote Sensing*, *39* (9), 2060-2072, 2001.

Holland, K.T., and R.A. Holman, Video estimation of foreshore topography using trinocular stereo, *Journal of Coastal Research*, *13* (1), 81-87, 1997.

Holland, K.T., R.A. Holman, T.C. Lippmann, J. Stanley, and N. Plant, Practical use of video imagery in nearshore oceanographic field studies, *IEEE Journal of Oceanic Engineering*, *22* (1), 81-92, 1997.

Holland, K.T., T.R. Keen, J.M. Kaihatu, and J. Calantoni, Understanding coastal dynamics in heterogeneous sedimentary environments, in *Coastal Sediments '03*, pp. 1-10, Clearwater Beach, Fl., 2003.

Holland, K.T., and J.A. Puleo, Variable swash motions associated with foreshore profile change, *Journal of Geophysical Research*, *106* (C3), 4613-4623, 2001.

Holland, K.T., J.A. Puleo, and T. Kooney, Quantification of swash flows using video-based particle image velocimetry, *Coastal Engineering*, *44*, 65-77, 2001.

Holland, K.T., B. Raubenheimer, R.T. Guza, and R.A. Holman, Runup kinematics on a natural beach, *Journal of Geophysical Research*, *100* (C3), 4985-4993, 1995.

Holland, K.T., A.H. Sallenger, Jr., B. Raubenheimer, and S. Elgar, Swash zone morphodynamics and sediment transport processes, in *Proceedings of the 26th International Conference on Coastal Engineering*, edited by B.L. Edge, pp. 2799-2811, ASCE, Copenhagen, 1998.

Holman, R.A., Infragravity energy in the surf zone, *Journal of Geophysical Research*, *86* (C7), 6442-6450, 1981.

Holman, R.A., and R.T. Guza, Measuring run-up on a natural beach, *Coastal Engineering*, *8* (2), 129-140, 1984.

Holman, R.A., T.C. Lippmann, P.V. O'Neill, and K. Hathaway, Video estimation of subaerial beach profiles, *Marine Geology*, *97* (1-2), 225-231, 1991.

Holman, R.A., and A.H. Sallenger, Jr., Setup and swash on a natural beach, *Journal of Geophysical Research*, *90* (C1), 945-953, 1985.

Holman, R.A., A.H. Sallenger, Jr., T.C. Lippmann, and J.W. Haines, The application of video image processing to the study of nearshore processes, *Oceanography*, *6* (3), 78-85, 1993.

Horn, D.P., and T. Mason, Swash zone sediment transport modes, *Marine Geology*, *120* (3-4), 309-325, 1994.

Howd, P.A., and R.A. Holman, A simple model of beach foreshore response to long period waves, *Marine Geology*, *78* (1-2), 11-22, 1987.

Hsu, T.J., and D.M. Hanes, The effects of waves induced pressure gradient on sheet flow sediment transport, *Journal of Geophysical Research*, submitted.

Hughes, M., G. Masselink, D. Hanslow, and D. Mitchell, Towards a better understanding of swash zone sediment transport, in *Coastal Dynamics*, edited by E.B. Thornton, pp. 804-823, ASCE, Plymouth, U.K., 1997a.

Hughes, M.G., Application of a non-linear shallow water theory to swash following bore collapse on a sandy beach, *Journal of Coastal Research*, *8* (3), 562-578, 1992.

Hughes, M.G., Friction factors for wave uprush, *Journal of Coastal Research*, *11* (4), 1089-1098, 1995.

Hughes, M.G., J.B. Keene, and R.G. Joseph, Hydraulic sorting of heavy-mineral grains by swash on a medium- sand beach, *Journal of Sedimentary Research*, *70* (5), 994-1004, 2000.

Hughes, M.G., G. Masselink, and R.W. Brander, Flow velocity and sediment transport in the swash zone of a steep beach, *Marine Geology*, *138* (1-2), 91-103, 1997b.

Huntley, D.A., Long-period waves on a natural beach, *Journal of Geophysical Research*, *81* (36), 6441-6449, 1976.

Huntley, D.A., M. Davidson, P. Russell, Y. Foote, and J. Hardisty, Long waves and sediment movement on beaches: Recent observations and implications for modelling, *Journal of Coastal Research*, *SI* (15), 215-229, 1993.

Huntley, D.A., R.T. Guza, and A.J. Bowen, A universal form for shoreline run-up spectra?, *Journal of Geophysical Research*, *82* (18), 2577-2581, 1977.

Hwang, R.R., and S. Jaw, Second-order closure turbulence models: Their achievements and limitations, *Proceedings of the National Science Council*, *22* (6), 703-722, 1998.

Inman, D.L., and R.A. Bagnold, Littoral Processes, in *The Sea*, edited by M.N. Hill, pp. 529-553, Wiley-Interscience, New York, 1963.

Iribarren, C.R., and C. Nogales, Protection des ports, in *XVIIth Int. Nav. Congress*, pp. 31-80, Lisbon, 1949.

Jackson, N.L., G. Masselink, and K.F. Nordstrom, The role of bore collapse and local shear stresses on the spatial distribution of sediment load in the uprush of an intermediate-state beach, *Marine Geology*, *203*, 109-118, 2004.

Jaffe, B.E., and D.M. Rubin, Using nonlinear forecasting to learn the magnitude and phasing of time-varying sediment suspension in the surf zone, *Journal of Geophysical Research*, *101* (C6), 14283-14296, 1996.

Jago, C.F., and J. Hardisty, Sedimentology and morphodynamics of a macrotidal beach, Pendine Sands, SW Wales, *Marine Geology*, *60* (1-4), 123-154, 1984.

James, C.P., and B.M. Brenninkmeyer, Sediment entrainment within bores and backwash, in *Geoscience and Man : Research in Coastal Environments*, pp. 61-68, 1977.

Jenkins, J.T., and D.M. Hanes, Collisional sheet flows of sediment driven by a turbulent fluid, *Journal of Fluid Mechanics*, *370*, 29-52, 1998.

Jensen, A., G.K. Pedersen, and D.J. Wood, An experimental study of wave run-up at a steep beach, *Journal of Fluid Mechanics*, *486*, 161-188, 2003.

Johnson, R.S., *A Modern Introduction to the Mathematical Theory of Water Waves*, 445 pp., Cambride University Press, New York, 1997.

Kamphuis, J.W., Alongshore sediment transport rate distribution, in *Coastal Sediments '91*, pp. 170-183, ASCE, 1991.

Kang, H.Y., P. Nielsen, and D.J. Hanslow, Watertabel overheight due to wave runup on a sandy beach, in *24th International Conference on Coastal Engineering*, ASCE, Kobe, Japan, 1994.

Karambas, T.V., Modelling of infiltration-exfiltration effects of cross-shore sediment transport in the swash zone, *Coastal Engineering Journal of Japan*, *45*, 63-82, 2003.

Keller, H.B., D.A. Levine, and G.B. Whitham, Motion of a bore over a sloping beach, *Journal of Fluid Mechanics*, *7*, 302-316, 1960.

Kemp, P.H., Wave asymmetry in the nearshore zone and breaker area, in *Nearshore Sediment Dynamics and Sedimentation*, edited by J. Hails, and A. Carr, pp. 47-67, Wiley-Interscience, London, 1975.

Kemp, P.H., and D.T. Plinston, Beaches produced by waves of low phase difference, *Journal of the Hydraulics Division - ASCE*, *94*, 1183-1195, 1968.

King, D.B.J., Studies in oscillatory flow bedload sediment transport, PhD thesis, University of California (SIO), San Diego, 1991.

Kirkgöz, M.S., A theoretical study of plunging breakers and their run-up, *Coastal Engineering*, *5* (4), 353-370, 1981.

Kobayashi, N., D.T. Cox, and A. Wurjanto, Irregular wave reflection and run-up on rough impermeable slopes, *Journal of Waterway, Port, Coastal, and Ocean Engineering*, *116* (6), 708-726, 1990a.

Kobayashi, N., and G.S. DeSilva, Motion of sediment particles in swash zone, in *Coastal hydrodynamics; proceedings*, edited by R.A. Dalrymple, pp. 715-730, Am. Soc. Civ. Eng. New York NY United States, Newark, 1987.

Kobayashi, N., G.S. DeSilvia, and K.D. Watson, Wave transformation and swash oscillation on gentle and steep slopes, *Journal of Geophysical Research*, *94* (C1), 951-966, 1989.

Kobayashi, N., and B.D. Johnson, Sand suspension, storage, advection, and settling in surf and swash zones, *Journal of Geophysical Research*, *106* (C5), 9363-9376, 2001.

Kobayashi, N., and E.A. Karjadi, Obliquely incident irregular waves in surf and swash zones, *Journal of Geophysical Research*, *101* (C3), 6527-6542, 1996.

Kobayashi, N., A.K. Otta, and I. Roy, Wave reflection and run-up on rough slopes, *Journal of Waterway, Port, Coastal, and Ocean Engineering*, *113* (3), 282-300, 1987.

Kobayashi, N., and M.T. Poff, Numerical model RBREAK2 for random waves on impermeable coastal structures and beaches, pp. 165, University of Delaware, 1994.

Kobayashi, N., A. Wuranto, and D.T. Cox, Irregular waves on rough permeable slopes, *Journal of Coastal Research*, *SI* (7), 167-184, 1990b.

Kobayashi, N., and A. Wurjanto, Numerical model for waves on rough permeable slopes, *Journal of Coastal Research*, *SI* (7), 149-166, 1990.

Kobayashi, N., and A. Wurjanto, Irregular wave setup and run-up on beaches, *Journal of Waterway, Port, Coastal, and Ocean Engineering*, *118* (4), 368-386, 1992.

Komar, P.D., Selective grain entrainment by a current from a bed of mixed sizes: A reanalysis, *Journal of Sedimentary Petrology*, *57* (2), 203-211, 1987.

Komar, P.D., *Beach Processes and Sedimentation*, 544 pp., Prentice-Hall, Englewood Cliffs, N.J., 1998.

Kothe, D.B., R.C. Mjolsness, and M.D. Torrey, RIPPLE: A computer program for incompressible flows with free surfaces, Los Alamos National Laboratory, 1991.

Kraus, N.C., R.S. Farinatom, and K. Horikawa, Field experiments on longshore sand transport in the surf zone, *Coastal Engineering in Japan*, *24*, 171-94, 1982.

Kraus, N.C., R.S. Farinto, and K. Horikawa, Field experiments on longshore sand transport in the surf zone, *Coastal Engineering in Japan*, *24*, 171-194, 1981.

Kroon, A., Suspended sediment concentrations in a barred nearshore zone, in *Coastal Sediments '91*, pp. 371-384, ASCE, 1991.

Lanyon, J.A., I.G. Eliot, and D.J. Clarke, Groundwater-level variation during semi-diurnal spring tidal cycles on a sandy beach, *Australian Journal of Marine and Freshwater Research*, *33* (3), 377-400, 1982.

Larson, M., Model of beach profile change under random waves, *Journal of Waterway Port Coastal and Ocean Engineering*, *122* (4), 172-181, 1996.

Larson, M., and N.C. Kraus, Prediction of cross-shore sediment transport at different spatial and temporal scales, *Marine Geology*, *126* (1-4), 111-127, 1995.

Larson, M., and T. Sunamura, Laboratory experiment on flow characteristics at a beach step, *Journal of Sedimentary Petrology*, *63* (3), 495-500, 1993.

Larson, M.A., and N.C. Kraus, SBEACH: Numerical model for simulating storm-induced beach change, Report 1: Empirical foundation and model development, USACE Waterways Experiment Station Coastal Engineering Research Center, Vicksburg, MS, 1989.

Larson, M.A., and N.C. Kraus, Mathematical modeling of the fate of beach fill, *Coastal Engineering*, *16*, 83-114, 1991.

Lee, M., J.E. Skjelbreia, and F. Raichlen, Measurement of velocities in solitary waves, *Journal of Waterway Port Coastal and Ocean Engineering*, *108*, 200-218, 1982.

Lemos, C.M., A simple numerical technique for turbuelnt flows with free surfaces, *International Journal of Numerical Methods in Fluids*, *15*, 127-146, 1992.

Li, L., D.A. Barry, J.Y. Parlange, and C.B. Pattiaratchi, Beach water table fluctuations due to wave run-up: Capillarity effects, *Water Resources Research*, *33* (5), 935-945, 1997a.

Li, L., D.A. Barry, C. Pattiaratchi, and G. Masselink, BeachWin: modeling groundwater effects on swash sediment transport and beach profile changes, *Environmental Modelling and Software*, *17*, 313-320, 2002.

Li, L., D.A. Barry, and C.B. Pattiaratchi, Numerical modelling of tide-induced beach water table fluctuations, *Coastal Engineering*, *30* (1-2), 105-123, 1997b.

Li, L., D.A. Barry, F. Stagnitti, and J.Y. Parlange, Groundwater waves in a coastal aquifer: A new governing equation including vertical effects and capillarity, *Water Resources Research*, *36*, 411-420, 2000.

Lin, P., and P.L.-F. Liu, A numerical study of breaking wave in the surf zone, *Journal of Fluid Mechanics*, *359*, 239-264, 1998a.

Lin, P., and P.L.-F. Liu, Turbulence transport, vorticity dynamics, and solute mixing under plunging breaking waves in surf zone, *Journal of Geophysical Research*, *103*, 15677-15694, 1998b.

Lin, P., and P.L.-F. Liu, Internal wave maker for Navier-Stokes equatins models, *Journal of Waterway Port Coastal and Ocean Engineering*, *125*, 207-215, 1999.

Lin, P.Z., K.A. Chang, and P.L.F. Liu, Runup and rundown of solitary waves on sloping beaches, *Journal of Waterway Port Coastal and Ocean Engineering*, *125* (5), 247-255, 1999.

Lippmann, T.C., and R.A. Holman, Quantification of sand bar morphology: A video technique based on wave dissipation, *Journal of Geophysical Research*, *94* (C1), 995-1011, 1989.

Lippmann, T.C., and R.A. Holman, The spatial and temporal variability of sand bar morphology, *Journal of Geophysical Research*, *95* (C7), 11,575-11,590, 1990.

Lippmann, T.C., and R.A. Holman, Phase speed and angle of breaking waves measured with video techniques, in *Coastal Sediments '91*, edited by N.C. Kraus, K.J. Gingerich, and D.L. Kriebel, pp. 542-556, ASCE, New York, 1991.

Liu, P.L.-F., and P. Lin, A numerical model for breaking waves: The volume of fluid method, pp. 54, University of Delaware, 1997.

Longo, S., M. Petti, and I. Losada, J, Turbulence in the surf and swash zones: a review, *Coastal Engineering*, *45*, 129-147, 2002.

Luccio, P.A., S.I. Voropayev, H.J.S. Fernando, D.L. Boyer, and W.N. Houston, The motion of cobbles in the swash zone on an impermeable slope, *Coastal Engineering*, *33* (1), 41-60, 1998.

Madsen, P.A., and I.A. Svendsen, Turbulent bores and hydraulic jumps, *Journal of Fluid Mechanics*, *129*, 1-25, 1983.

Marom, M., L. Shemer, and E.B. Thornton, Energy density directional spectra of nearshore wave field measured by interferometric synthetic aperature radar, *Journal of Geophysical Research*, *96* (C12), 22125-22134, 1991.

Martin, C.S., and M.M. Aral, Seepage force on interfacial bed particles, *Journal of the Hydraulics Division*, *7*, 1081-1100, 1971.

Mase, H., Spectral characteristics of random wave run-up, *Coastal Engineering*, *12*, 175-189, 1988.

Mase, H., Frequency down-shift of swash oscillations compared to incident waves, *Journal of Hydraulic Research*, *33* (3), 397-411, 1995.

Masselink, G., D. Evans, M.G. Hughes, and P. Russell, Suspended sediment transport in the swash zone of a dissipative beach, *Marine Geology*, in review.

Masselink, G., and M. Hughes, Field investigation of sediment transport in the swash zone, *Continental Shelf Research*, *18* (10), 1179-1199, 1998.

Masselink, G., and L. Li, The role of swash infiltration in determining the beachface gradient: a numerical study, *Marine Geology*, *176* (1-4), 139-156, 2001.

Matsunaga, N., and H. Honji, The backwash vortex, *Journal of Fluid Mechanics*, *99* (AUG), 813-&, 1980.

Matsunaga, N., and H. Honji, The steady and unsteady backwash vortices, *Journal of Fluid Mechanics*, *135* (OCT), 189-197, 1983.

Mayer, S., and P.A. Madsen, Simulation of breaking waves in the surf zone using a Navier-Stokes solver, in *Proceedings of the International Conference on Coastal Engineering*, pp. 928-941, ASCE, Sydney, Australia, 2000.

McGregor, J.A., E.M. Poulter, and M.J. Smith, Ocean surface currents obtained from microwave sea-echo Doppler spectra, *Journal of Geophysical Research*, *102* (C11), 25227-25236, 1997.

McGregor, J.A., E.M. Poulter, and M.J. Smith, S band Doppler radar measurements of bathymetry, wave energy fluxes, and dissipation across an offshore-bar, *Journal of Geophysical Research*, *103* (C9), 18779-18789, 1998.

McIntosh, R.E., S.J. Frasier, and J.B. Mead, FOPAIR: A focused phased array imaging radar for ocean remote sensing, *IEEE Transactions on Geoscience and Remote Sensing*, *33* (1), 115-124, 1995.

McLachlan, A., I.G. Eloit, and D.J. Clarke, Water Filtration through reflective microtidal beaches and shallow sublittoral sands and its implications for an inshore ecosystem in Western Australia, *Estuarine, Coastal and Shelf Science*, *21*, 91-104, 1985.

Metcalf, W.L., H.J. Bokuniewicz, and A.V. Terchunian, Water table variations on a reflective ocean beach: Quogue, New York, *Northeastern Geology and Environmental Science*, *17*, 61-67, 1995.

Meyer, R.E., Run-up on beaches, in *Waves on Beaches*, edited by R. Meyer, pp. 357-411, Academic Press, New York, 1972.

Meyer-Peter, E., and R. Muller, Formulas for bed-load transport., in *Proceedings 3rd Meeting of the International Association for Hydraulic Research*, pp. 39-64, Stockhold, Sweden, 1948.

Miche, R., Le pouvoir réfléchissant des ouvrages maritimes exposés à l'action de la houle, *Annales des Ponts et Chaussées*, *121*, 285-319, 1951.

Miller, K.S., and M.M. Rochwarger, A covariance approach to spectral moment estimation, *IEEE Transactions on Information Theory*, *18* (5), 588-596, 1972.

Miller, R.L., Experimental determination of run-up of undular and fully developed bores, *Journal of Geophysical Research*, *73* (14), 4497-4510, 1968.

Miller, R.L., and J.M. Zeigler, A model relating dynamics and sediment pattern in equilibrium in the region of shoaling waves, breaker zone, and foreshore, *Journal of Geology*, *66* (4), 417-441, 1958.

Moin, P., and J. Kim, Numerical investigation of turbulent channel flow, *Journal of Fluid Mechanics*, *118*, 341-377, 1982.

Moller, D., S.J. Frasier, D.L. Porter, and R.E. McIntosh, Radar-derived inferometric surface currents and their relationship to subsurface current structure, *Journal of Geophysical Research*, *103* (C6), 12839-12852, 1998.

Nelson, C.L., and R.L. Miller, The interaction of fluid and sediment on the foreshore, pp. 176, University of Chicago, 1974.

Nielsen, P., Tidal dynamics of the water table in beaches, *Water Resources Research*, *26*, 2127-2134, 1990.

Nielsen, P., *Coastal Bottom Boundary Layers and Sediment Transport*, 324 pp., World Scientific Publishing Co., River Edge, NJ, 1992.

Nielsen, P., Coastal groundwater dynamics, in *Coastal Dynamics '97*, pp. 546-555, ASCE, 1998.

Nielsen, P., Shear stress and sediment transport calculations for swash zone modelling, *Coastal Engineering*, *45*, 53-60, 2002.

Nielsen, P., and D.P. Callaghan, Shear stress and sediment transport calculation for sheet flow under waves, *Coastal Engineering*, *47*, 347-354, 2003.

Nielsen, P., and P.J. Cowell, Calibration and Data Correction Procedures for Flow Meters and Pressure Transducers Commonly Used by the Coastal Studies Unit, pp. 33, 1981.

Nordstrom, K.F., and N.L. Jackson, Migration of swash zone, step and microtopographic features during tidal cycles on an estuarine beach, Delaware Bay, New Jersey, USA, *Marine Geology*, *92* (1-2), 147-154, 1990.

Oldenziel, D.M., and W.E. Brink, Influence of suction and blowing on entrainment of sand particles, *Journal of the Hydraulics Division*, *1000*, 935-949, 1974.

Osborne, P.D., and G.A. Rooker, Surf zone and swash zone sediment dynamics on high energy beaches: West Auckland, New Zealand, in *Coastal Dynamics*, edited by E.B. Thornton, pp. 814-823, ASCE, Plymouth, UK, 1997.

Osborne, P.D., and G.A. Rooker, Sand re-suspension events in a high energy infragravity swash zone, *Journal of Coastal Research*, *15* (1), 74-86, 1999.

Packwood, A.R., The influence of beach porosity on wave uprush and backwash, *Coastal Engineering*, *7*, 29-40, 1983.

Packwood, A.R., and D.H. Peregrine, The propagation of solitary waves and bores over a porous bed, *Coastal Engineering*, *3*, 221-242, 1980.

Peregrine, D.H., and S.M. Williams, Swash overtopping a truncated plane beach, *Journal of Fluid Mechanics*, *440*, 391-399, 2001.

Petit, H.A.H., M.R.A. van Gent, and P. van den Bosch, Numerical simulation and validation of plunging breakers using a 2D Navier STokes model., in *Proceedings of the 24th International Conference on Coastal Engineering*, pp. 511-524, ASCE, 1994.

Petti, M., and S. Longo, Hydrodynamics in the swash zone, *International Journal of Offshore and Polar Engineering*, *11* (5), 202-210, 2001a.

Petti, M., and S. Longo, Turbulence experiments in the swash zone, *Coastal Engineering*, *43* (1), 1-24, 2001b.

Piomelli, U., and E. Balaras, Wall-layer models for large eddy simulations, *Annual Review of Fluid Mechanics*, *34*, 349-374, 2002.

Plant, N., K.T. Holland, and J.A. Puleo, Analysis of the scale of errors in nearshore bathymetric interpolation, *Marine Geology*, *191*, 71-86, 2002.

Plant, N., K.T. Holland, J.A. Puleo, and E. Gallagher, Prediction skill of nearshore profile evolution models, *Journal of Geophysical Research*, *109* (C01006), doi:10.1029/2003JC001995, 2004.

Plant, W.J., E.A. Terray, R.A.J. Petitt, and W.C. Kellar, The dependence of microwave backscatter from the sea on illuminated area: correlation times and lengths, *Journal of Geophysical Research*, *99* (C5), 9705-9723, 1994.

Pope, S.B., *Turbulent Flows*, 771 pp., University Press, Cambridge, UK, 2000.

Poulter, E.M., M.J. Smith, and J.A. McGregor, S-band FMCW radar measurements of ocean surface dynamics, *Journal of Atmospheric and Oceanic Technology*, *12* (6), 1271-1286, 1995.

Puleo, J.A., R.A. Beach, R.A. Holman, and J.S. Allen, Swash zone sediment suspension and transport and the importance of bore-generated turbulence, *Journal of Geophysical Research*, *105* (C7), 17021-17044, 2000.

Puleo, J.A., T. Butt, and D.M. Hanes, Instantaneous energetics sediment transport model calibrations, *Journal of Coastal Research*, submitted.

Puleo, J.A., G. Farquharson, S.J. Frasier, and K.T. Holland, Comparison of optical and radar measurments of surf and swash zone velocity fields, *Journal of Geophysical Research*, *108* (C3), 45-1 - 45-12, 2003a.

Puleo, J.A., and K.T. Holland, Field observations of three-dimensional swash flow patterns and morphodynamics, in *Proceedings of the 27th International Conference on Coastal Engineering*, edited by B.L.Edge, pp. 637-650, ASCE, Sydney, Australia, 2000.

Puleo, J.A., and K.T. Holland, Estimating swash zone friction coefficients on a sandy beach, *Coastal Engineering*, *43* (1), 25-40, 2001.

Puleo, J.A., and K.T. Holland, Swash zone flow fields and foreshore morphodynamics on a steep beach, *Marine Geology*, submitted.

Puleo, J.A., K.T. Holland, N. Plant, D.N. Slinn, and D.M. Hanes, Fluid acceleration effects on suspended sediment transport in the swash zone, *Journal of Geophysical Research*, *108*, 2003b.

Puleo, J.A., D.N. Slinn, and K.T. Holland, Numerical simulation of inner surf and swash zone hydrodynamics using the volume of fluid technique, *Journal of Fluid Mechanics*, Submitted.

Puleo, J.A., D.N. Slinn, K.T. Holland, E. Smith, and B.M. Webb, Numerical modelling of swash zone hydrodynamics, in *Proceedings of the American Society of Civil Engineers*, ASCE, Cardiff, Wales, UK,, 2002.

Quick, M.C., Onshore-offshore sediment transport on beaches, *Coastal Engineering*, *15*, 313-332, 1991.

Rakha, K.A., R. Deigaard, and I. Broker, A phase-resolving cross shore sediment transport model for beach profile evolution, *Coastal Engineering*, *31* (1-4), 231-261, 1997.

Raubenheimer, B., Observations and predictions of fluid velocities in the surf and swash zones, *Journal of Geophysical Research*, *107* (C11, 3190, doi:10.1029/2001JC001264), 2002.

Raubenheimer, B., S. Elgar, and R.T. Guza, Swash zone velocities, turbulent dissipation and friction coefficients, *Journal of Geophysical Research*, In review.

Raubenheimer, B., and R.T. Guza, Observations and predictions of run-up, *Journal of Geophysical Research*, *101* (C11), 25575-25587, 1996.

Raubenheimer, B., R.T. Guza, and S. Elgar, Wave transformation across the inner surf zone, *Journal of Geophysical Research*, *101* (C11), 25589-25597, 1996.

Raubenheimer, B., R.T. Guza, and S. Elgar, Tidal water table fluctuations in a sandy ocean beach, *Water Resources Research*, *35* (8), 2313-2320, 1999.

Raubenheimer, B., R.T. Guza, S. Elgar, and N. Kobayashi, Swash on a gently sloping beach, *Journal of Geophysical Research*, *100* (C5), 8751-8760, 1995.

Rector, R.L., Laboratory study of equilibrium profiles of beaches, pp. 38, U.S. Army Corps of Engineers, Beach Erosion Board, 1954.

Ribberink, J.S., and A.A. Al-Salem, Sediment transport in oscillatory boundary layers in cases of rippled bed ans sheet flow, *Journal of Geophysical Research*, *99*, 12707-12727, 1994.

Ribberink, J.S., and A.A. Al-Salem, Sheet flow and suspension in oscillatory boundary layers, *Coastal Engineering*, *25*, 205-225, 1995.

Rodi, W., and G. Scheuerer, Scrutinizing the k-ε turbulence model under adverse pressure gradients, *ASME Journal of Fluid Engineering*, *108*, 174-179, 1986.

Rodriguez, A., A. Sanchez-Arcilla, J.M. Redondo, and C. Mosso, Macroturbulence measurements with electromagnetic and ultrasonic sensors: a comparison under highly turbulent flows, *Experiments in Fluids*, *27*, 31-42, 1999.

Rogallo, R.S., and P. Moin, Numerical simulation of turbulent flows, *Annual Review of Fluid Mechanics*, *16*, 99-137, 1984.

Ruessink, B.G., P.S. Bell, I.M.J. van Enckevort, and S.G.J. Aarninkhof, Nearshore bar crest position quantified from time-averaged X-band radar images, *Coastal Engineering*, *45*, 19-32, 2002.

Ruessink, B.G., M.G. Kleinhans, and d.B.P.G.L. van, Observations of swash under highly dissipative conditions, *Journal of Geophysical Research*, *103* (C2), 3111-3118, 1998.

Sabeur, Z.A., N.W. Allsop, R.G. Beale, and J.M. Dennis, Wave dynamics at coastal structures: development of a numerical model for free surface flows, in *Proceedings of the 25th International Conference on Coastal Engineering*, pp. 393-402, ASCE, 1996.

Sallenger, A.H., Jr., and B.M. Richmond, High-frequency sediment-level oscillations in the swash zone, *Marine Geology*, *60* (1-4), 155-164, 1984.

Schaffer, H.A., P.A. Madsen, and R. Deigaard, A Boussinesq model for waves breaking in shallow-water, *Coastal Engineering*, *20* (3-4), 185-202, 1993.

Schiffman, A., Energy measurements in the swash-surf zone, *Limnology and Oceanography*, *10*, 255-260, 1965.

Schoonees, J.S., and A.K. Theron, Evaluation of 10 cross-shore sediment transport morphological models, *Coastal Engineering*, *25* (1-2), 1-41, 1995.

Senet, C.M., J. Seemann, and F. Ziemer, The near-surface current velocity determined from image sequences of the sea surface, *IEEE Transactions on Geoscience and Remote Sensing*, *39* (3), 492-505, 2001.

Shah, A.M., and J.W. Kamphuis, The swash zone: A focus on low frequency motion, in *Proceedings of the 25th International Conference on Coastal Engineering*, edited by B.L. Edge, pp. 1431-1442, ASCE, Orlando, 1996.

She, K., C.A. Greated, and W.J. Easson, Experimental of 3 dimensional breaking wave kinematics, *Applied Ocean Research*, *19* (5-6), 329-343, 1997.

Shemer, L., M. Marom, and D. Markman, Estimates of currents in the nearshore ocean region using interferometric synthetic aperature radar, *Journal of Geophysical Research*, *98* (C4), 7001-7010, 1993.

Shen, M.C., and R.E. Meyer, Climb of a bore on a beach: Part 2, Non-uniform beach slope, *Journal of Fluid Mechanics*, *16* (8), 108-112, 1963a.

Shen, M.C., and R.E. Meyer, Climb of a bore on a beach: Part 3, run-up, *Journal of Fluid Mechanics*, *16* (8), 113-125, 1963b.

Shephard, F.P., Beach Cycles in Southern California, U.S. Army Corp of Engineers, Beach Erosion Board, 1950.

Shephard, F.P., and R. Young, Distinguishing between beach and dune sands, *Journal of Sedimentary Petrology*, *31*, 196-214, 1961.

Shyy, W., H.S. Udaykumar, M.M. Rao, and R.W. Smith, *Computational Fluid Dynamics With Moving Boundaries*, 284 pp., Taylor & Francis, 1996.

Slinn, D.N. and J.J. Riley, A model for the simulation of turbulent boundary layers in an incompressible stratified flow, *Journal of Computational Physics*, 144, 550-602, 1998.

Smagorinsky, J., General circulation experiments with primitive equations, *Monthly Weather Review*, *91*, 99-165, 1963.

Smith, A.W., Slope of the swash zone of an ocean beach, *Shore & Beach*, *58* (3), 26-29, 1990.

Smith, E., P. Wang, and J. Zhang, Evaluation of the CERC fromula using large-scale model data, in *Coastal Sediment '03*, pp. 1-13, Clearwater Beach, FL, 2003.

Sonu, C.J., N. Pettigrew, and R.G. Fredericks, Measurement of swash profile and orbital motion on the beach, in *Proceedings of the International Symposium on Ocean Wave Measurement and Analysis*, pp. 621-638, ASCE, New Orleans, Louisiana, 1974.

Speranskiy, N.S., Some kinematic features of the surf swash, *Oceanology*, *12* (5), 714-718, 1972.

Stockdon, H.F., and R.A. Holman, Estimation of wave phase speed and nearshore bathymetry from video imagery, *Journal of Geophysical Research*, *105* (C9), 22015-22033, 2000.

Stoker, J.J., The formation of breakers and bores, *Communications on Applied Mathematics*, *1* (1), 1-87, 1948.

Strahler, A.N., Tidal cycle of changes in an equilibrium beach, Sandy Hook, New Jersey, *Journal of Geology*, *74* (3), 247-268, 1966.

Suhayda, J.N., Standing waves on beaches, *Journal of Geophysical Research*, *79* (21), 3065-3071, 1974.

Sumer, B.M., A. Kozakiewicz, J. Fredsoe, and R. Deigaard, Velocity and concentration profiles in sheet-flow layer of movable bed, *Journal of Hydraulic Engineering*, *122* (10), 549-558, 1996.

Sunamura, T., Quantitative predictions of beach-face slopes, *Geological Society of America Bulletin*, *95* (2), 242-245, 1984.

Svendsen, I.A., and P.A. Madsen, A turbulent bore on a beach, *Journal of Fluid Mechanics*, *148*, 73-96, 1984.

Symonds, G., D.A. Huntley, and A.J. Bowen, Two-dimensional surf beat: Long wave generation by a time-varying breakpoint, *Journal of Geophysical Research*, *87* (C1), 492-498, 1982.

Tennekes, H., and J.L. Lumley, *A First Course In Turbulence*, 300 pp., MIT Press, Cambridge, Massachusetts, 1972.

Thorne, P.D., and D.M. Hanes, A review of acoustic measurements of small-scale sediment processes, *Continental Shelf Research*, *22*, 603-632, 2002.

Thornton, E.B., and S. Abdelrahman, Sediment transport in the swash due to obliquely incicdent wind waves modulated by in fragravity waves, in *Coastal Sedimaents '91*, edited by Kraus, Gingerich, and Kriebel, pp. 100-113, ASCE, 1991.

Thornton, E.B., R.A. Dalrymple, T.G. Drake, E. Gallagher, R.T. Guza, A. Hay, R.A. Holman, J. Kaihatu, T.C. Lippmann, and H.T. Ozkan-Haller, State of Nearshore Processes Research: II, Naval Postgraduate School, Monterey, 2000.

Thornton, E.B., and R.T. Guza, Transformation of wave height distribution, *Journal of Geophysical Research*, *88* (C10), 5925-5938, 1983.

Thornton, E.B., R.T. Humiston, and W. Birkemeier, Bar/trough generation on a natural beach, *Journal of Geophysical Research*, *101* (C5), 12097-12110, 1996.

Titov, V.V., and C.E. Synolakis, Modeling of breaking and nonbreaking long-wave evolution and runup using Vtcs-2, *Journal of Waterway Port Coastal and Ocean Engineering*, *121* (6), 308-316, 1995.

Trenhaile, A.S., L.V. Vandernol, and P.D. Lavalle, Sand grain roundness and transport in the swash zone, *Journal of Coastal Research*, *12* (4), 1017-1023, 1996.

Turner, I.L., The total water content of sandy beaches, *Journal of Coastal Research*, *SI* (15), 11-26, 1993.

Turner, I.L., Simulating the influence of groundwater seepage on sediment transported by the sweep of the swash zone across macro-tidal beaches, *Marine Geology*, *125* (1-2), 153-174, 1995.

Turner, I.L., Monitoring groundwater dynamics in the littoral zone at seasonal, storm, tide and swash frequencies, *Coastal Engineering*, *35* (1-2), 1-16, 1998.

Turner, I.L., and G. Masselink, Swash infiltration-exfiltration and sediment transport, *Journal of Geophysical Research*, *103* (C13), 30813-30824, 1998.

Turner, R.J., The effects of a mid-foreshore groundwater effluent zone on tidal-cycle sediment distribution in Puget Sound, Washington, *Journal of Coastal Research*, *6* (3), 597-610, 1990.

van der Meer, J.W., and M.K. Breteler, Measurement and computation of wave induced velocities on a smooth slope, in *22nd International Conference on Coastal Engineering*, pp. 191-204, ASCE, The Netherlands, 1990.

van Driest, E.R., On turbulent flow near a wall, *Journal of the Aeronautical Sciences*, *23*, 1007, 1956.

van Leer, B., Towards the ultimate conservative difference scheme. V. A second-order sequel to Godunov's method, *Journal of Computational Physics*, *32*, 101-136, 1979.

Van Wellen, E., A.J. Chadwick, and T. Mason, A review and assessment of longshore sediment transport equations for coarse-grained beaches, *Coastal Engineering*, *40* (3), 243-275, 2000.

Voulgaris, G., and M.B. Collins, Sediment resuspension on beaches: response to breaking waves, *Marine Geology*, *167*, 167-187, 2000.

Waddell, E., Dynamics of swash and implication to beach response, pp. 49, Coastal Studies Institute, Louisiana State University, 1973.

Waddell, E., Swash-groundwater-beach profile interactions, in *Beach and Nearshore Sedimentation*, edited by R.A. Davis, Jr., and R.L. Ethington, pp. 115-125, SEPM, Tulsa, OK, 1976.

Wang, P., B.A. Ebersole, and E.R. Smith, Longshore sand transport - Initial results from large scale sediment transport facility, pp. 1-10, USACE, 2002.

Wang, P., N.C. Kraus, and R.A. Davis, Total longshore sediment transport rate in the surf zone: Field measurements and empirical predictions, *Journal of Coastal Research*, *14* (1), 269-282, 1998.

Watters, G.Z., and M. Rao, Hydrodynamic effect of seepage on bed particles, *Journal of the Hydraulics Division*, *3*, 421-439, 1971.

Werner, B.T., and T.M. Fink, Beach cusps as self-organized patterns, *Science*, *260* (May 14 '93), 968-971, 1993.

Whitham, G.B., On the propagation of shock waves through regions of non-uniform area or flow, *Journal of Fluid Mechanics*, *4*, 337-360, 1958.

Wilcox, D.C., *Turbulence modeling for CFD*, 539 pp., DCW Industries, Inc., La Canada, CA, 2000.

Williams, A.T., The transport of sediment particles in the swash zone, *Malaysian Journal of Tropical Geography*, *5*, 82-94, 1982.

Wilson, K.C., Analysis of bed-load motion at thigh shear stress, *Journal of the Hydraulics Division*, *113*, 97-103, 1987.

Wolf, J., and P.S. Bell, Waves at Holderness from X-band radar, *Coastal Engineering*, *42*, 247-263, 2001.

Wood, D.J., G.K. Pedersen, and A. Jensen, Modelling of run up of steep non-breaking waves, *Ocean Engineering*, *30*, 625-644, 2003.

Wright, J.W., A new model for sea clutter, *IEEE Transactions on Antenna Propagation*, *16*, 217-223, 1968.

Wright, L.D., and A.D. Short, Morphodynamic variability of surf zones and beaches: A synthesis, *Marine Geology*, *56* (1-4), 93-118, 1984.

Wright, P., A cine-camera technique for process measurement on a ridge and runnel beach, *Sedimentology*, *23*, 705-712, 1976.

Wurjanto, A., and N. Kobayashi, Numerical model for random waves on impermeable coastal structures and beaches, Center for Applied Coastal Research, University of Delaware, Newark, Del., 1991.

Yeh, H.H., A. Ghazali, and I. Marton, Experimental study of bore run-up, *Journal of Fluid Mechanics*, *206*, 563-578, 1989.

Young, I.R., W. Rosenthal, and F. Ziemer, A 3-dimensional analysis of marine radar images for the determination of ocean wave directionality and surface currents, *Journal of Geophysical Research*, *90* (C1), 1049-1059, 1985.

Zelt, J.A., The run-up of nonbreaking and breaking solitary waves, *Coastal Engineering*, *15*, 205-246, 1991.

Zhao, Q., and K. Tanimoto, Numerical simulation of breaking waves by large eddy simulation and the VOF method, in *Proceedings of the 26th International Conference on Coastal Engineering*, pp. 892-905, ASCE, 1998.

Zikanov, O., D.N. Slinn and M. R. Dhanak, Turbulent convection driven by surface cooling in shallow water, *Journal of Fluid Mechanics*, 464, 81-111, 200.

BIOGRAPHICAL SKETCH

I have been an employee at the Naval Research Laboratory at Stennis Space Center for the last 6 years working on a variety of nearshore projects generally focused on the swash zone and optical remote sensing techniques. I obtained my undergraduate degrees from Humboldt state university in Oceanography and Mathematics. I then obtained a Masters of Science degree in Oceanography from Oregon State University. I have been a member of AGU for the last 9 years and have served as a reviewer for four scientific journals. My interests include nearshore processes with specific focus on sediment transport, computational fluid dynamics and video-based remote sensing.